FEDERAL UNIVERSITY OF SÃO CARLOS
CENTER FOR EXACT SCIENCES AND TECHNOLOGY
GRADUATION PROGRAM IN MATERIALS SCIENCE AND ENGINEERING

TAILORING THE COMPOSITION OF THE AA2017 TO REDUCE ITS HOT CRACKING SUSCEPTIBILITY DURING LPBF

Nicolas Rojas Arias

São Carlos-SP
2024

FEDERAL UNIVERSITY OF SÃO CARLOS
CENTER FOR EXACT SCIENCES AND TECHNOLOGY
GRADUATION PROGRAM IN MATERIALS SCIENCE AND ENGINEERING

TAILORING THE COMPOSITION OF THE AA2017 TO REDUCE ITS HOT CRACKING SUSCEPTIBILITY DURING LPBF

Nicolas Rojas Arias

Doctoral Thesis presented to the Graduation Program in Materials Science and Engineering as a partial requirement to obtain the title of DOCTOR IN MATERIALS SCIENCE AND ENGINEERING

Supervisor: Prof. Dr. Ing. Piter Gargarella
Co-supervisor: Dr. Francisco Gil Coury
Cotutelle Supervisor: Prof. Dr. Sergio de Traglia Amâncio Filho
Funding agency: FAPESP (Grant n° 2020/01426-5) and FAPESP/BEPE (Grant n° 2022/00896-3)

São Carlos-SP
2024

UNIVERSIDADE FEDERAL DE SÃO CARLOS

Centro de Ciências Exatas e de Tecnologia
Programa de Pós-Graduação em Ciência e Engenharia de Materiais

Folha de Aprovação

Defesa de Tese de Doutorado do candidato Nicolas Rojas Arias, realizada em 06/09/2024.

Comissão Julgadora:

Prof. Dr. Piter Gargarella (UFSCar)

Prof. Dr. Claudemiro Bolfarini (UFSCar)

Prof. Dr. José Eduardo Spinelli (UFSCar)

Prof. Dr. Kahl Dick Zilnyk (ITA)

Prof. Dr. Sergio de Traglia Amancio Filho (TU Graz)

O Relatório de Defesa assinado pelos membros da Comissão Julgadora encontra-se arquivado junto ao Programa de Pós-Graduação em Ciência e Engenharia de Materiais.

ACKNOWLEDGMENTS

This study was financed in part by the Coordenação de Aperfeiçoamento de Pessoal de Nível Superior - Brasil (CAPES) - Finance Code 001.

FAPESP is acknowledged for financial support within the FAPESP projects with the following grants: FAPESP (n° 2017/27031-4), FAPESP (n° 2020/01426-5), and FAPESP/BEPE (n° 2022/00896-3).

This project was partially financed by the Austrian Ministry for Climate Action, Environment, Energy, Mobility, Innovation, and Technology, BMK (TAKE-OFF grant number 852796, 208).

ABSTRACT

Laser Powder Bed Fusion (LPBF) holds significant importance and research interest because of its capability to fabricate metallic components with intricate geometries that are challenging to replicate using traditional manufacturing methods. However, only a limited number of alloys are commercially viable for LPBF due to the processing conditions and characteristics of the alloys. This issue is particularly critical for alloys with wide solidification ranges such as wrought aluminum alloys, which may exhibit poor LPBF processability. For instance, previous experiments with the AA2017 alloy revealed its unsuitability for LPBF due to susceptibility to hot cracking. This study aimed to alter this alloy composition by incorporating additional elements that reduce the solidification range, facilitate grain refinement, and prevent crack formation during LPBF. The impact of different alloy element additions on the solidification range and phase formation was assessed via thermodynamic calculations. Compositions based on AA2017 were designed using the CALPHAD method and subsequently produced via gas atomization. The Design of Experiments methodology guided the selection of appropriate processing parameters to achieve crack-free parts with optimal structural integrity. Various characterization techniques were employed to examine the microstructural and mechanical properties. A new composition based on AA2017 was produced, enabling the construction of high-density, crack-free LPBF parts. X-ray diffraction analysis and microscopy techniques revealed that the improved processability of the new composition is attributed to its shorter solidification interval and a more fraction of liquid in the final stage of solidification with the presence of eutectic Al+Al_3CeCu regions, which not only help to prevent crack formation but also enhanced the material's mechanical strength, as confirmed by the mechanical tests.

Keywords: additive manufacturing; laser powder bed fusion; wrought aluminum alloys; AA2017; composition design; hot cracking susceptibility.

ZUSAMMENFASSUNG

ANPASSUNG DER ZUSAMMENSETZUNG DES AA2017 ZUR VERRINGERUNG SEINER HEISSRISSANFÄLLIGKEIT WÄHREND DES LPBF

Das „Laser Powder Bed Fusion“, kurz LPBF (oder auch „das pulverbettbasierte Schmelzen von Metall mittels Laserstrahl“ genannt) stellt einen vielversprechenden Ansatz zur Herstellung metallischer Bauteile mit komplexen Geometrien dar. Aufgrund seiner vielseitigen Einsatzmöglichkeiten und der daraus resultierenden hohen Forschungsrelevanz erfährt dieses Fertigungsverfahren eine zunehmend große Bedeutung. Aufgrund der Verarbeitungsbedingungen und Eigenschaften der Legierungen sind allerdings nur eine begrenzte Anzahl von Legierungen kommerziell für LPBF geeignet. Dieses Problem ist besonders kritisch für Legierungen mit breiten Erstarrungsbereichen wie gewalzte Aluminiumlegierungen, die eine schlechte LPBF-Verarbeitbarkeit aufweisen können. Beispielsweise zeigten frühere Experimente mit der Legierung AA2017 hinsichtlich ihrer Anfälligkeit für Heißrissbildung ihre Ungeeignetheit für LPBF. Diese Studie hatte zum Ziel, die Legierungszusammensetzung durch die Einbeziehung zusätzlicher Elemente zu verändern, die den Erstarrungsbereich verringern, die Kornfeinung erleichtern und Rissbildung während des LPBF verhindern. Der Einfluss verschiedener Legierungselemente auf den Erstarrungsbereich und die Phasenbildung wurde mittels thermodynamischer Berechnungen bewertet. Zusammensetzungen basierend auf AA2017 wurden unter Verwendung der CALPHAD-Methode entworfen und anschließend mittels Gasverdüsung hergestellt. Die Methode des Versuchsdesigns ermöglichte die Auswahl geeigneter Prozessparameter, um rissfreie Teile mit optimaler struktureller Integrität zu erzielen. Verschiedene Charakterisierungstechniken wurden eingesetzt, um die mikrostrukturellen und mechanischen Eigenschaften zu untersuchen. Im Rahmen dieser Studie wurde eine neue chemische Pulverzusammensetzung entwickelt, die auf AA2017 basiert. Daraufhin wurde das Pulver hergestellt. Dies ermöglichte die Fertigung von hochdichten, rissfreien LPBF-bauteilen. Die Ergebnisse der Röntgenbeugungsanalyse und der Mikroskopietechniken deuten darauf hin, dass die verbesserte Prozessierbarkeit der neuen Pulverzusammensetzung auf ihr kürzeres Erstarrungsintervall und einen höheren Anteil von flüssigem Material im Endstadium der Erstarrung mit der Präsenz von eutektischen Al+Al_3CeCu-Regionen zurückzuführen ist. Dies führt nicht nur zur Verhinderung der Rissbildung, sondern auch zu einer Verbesserung der mechanischen Festigkeit des Materials, wie durch die mechanischen Tests bestätigt wurde.

Schlüsselwörter: Laserpulverbettfusion; AA2017; Heißrissanfälligkeit; eutektische Zonen

RESUMO

ADAPTAÇÃO DA COMPOSIÇÃO DO AA2017 PARA REDUZIR SUA SUSCETIBILIDADE A TRINCAS A QUENTE DURANTE A LPBF

A Fusão a Laser em Leito de Pó (LPBF) tem uma importância significativa e desperta interesse de pesquisa devido à sua capacidade de fabricar componentes metálicos com geometrias complexas que são desafiadoras de replicar usando métodos de fabricação tradicionais. No entanto, apenas um número limitado de ligas é comercialmente viável para LPBF devido às condições de processamento e características das ligas. Esse problema é particularmente crítico para ligas com amplas faixas de solidificação, como as ligas de alumínio forjado, que podem apresentar uma baixa processabilidade no LPBF. Por exemplo, experimentos anteriores com a liga AA2017 revelaram sua inadequação para LPBF devido à susceptibilidade à fissuração a quente. Este estudo teve como objetivo alterar a composição desta liga incorporando elementos adicionais que reduzem a faixa de solidificação, facilitam o refinamento de grãos e previnem a formação de fissuras durante o LPBF. O impacto de diferentes adições de elementos de liga na faixa de solidificação e na formação de fases foi avaliado por meio de cálculos termodinâmicos. Composições baseadas em AA2017 foram projetadas usando o método CALPHAD e subsequentemente produzidas por atomização de gás. A metodologia de Design de Experimentos guiou a seleção de parâmetros de processamento adequados para alcançar peças livres de fissuras com integridade estrutural ótima. Várias técnicas de caracterização foram empregadas para examinar as propriedades microestruturais e mecânicas. Uma nova composição baseada em AA2017 foi produzida, possibilitando a construção de peças LPBF de alta densidade e livres de fissuras. Análises de difração de raios X e técnicas de microscopia revelaram que a melhor processabilidade da nova composição é atribuída ao seu intervalo de solidificação mais curto e fração de líquido maior na etapa final de solidificação com a presença de regiões eutéticas Al+Al3CeCu, que não apenas ajudam a prevenir a formação de fissuras, mas também melhoram a resistência mecânica do material, conforme confirmado pelos testes mecânicos.

Palavras-chave: Fusão a laser em leito de pó; AA2017; suscetibilidade ao trincamento a quente; regiões eutéticas

x

PUBLICATIONS

Patent process:

- **Rojas-Arias, N**.; Coury, F.G.; Gargarella, P. *Liga de Alumínio-Cobre-Terra rara, seu uso e peça obtida em processo de fabricação por manufatura aditiva* [in portugues]. **Patent process No.** BR 10 2023 012773 8. Patent of Invention (PI – 10) owned by the Federal University of São Carlos, SP, Brazil.

Scientific papers:

- **Rojas-Arias, N.**, Coury, F.G., Vanmeensel, K., Amancio-Filho, S.T. & Gargarella, P. (2024). Heat treating additive-manufactured alloys: A comprehensive review. ***Journal of Alloys and Compounds***, *1005*, 176035. Doi: 10.1016/j.jallcom.2024.176035.

- **Rojas-Arias, N.**, Silva, A.S., de Albuquerque Sousa, S.M., de Gouveia, G.L., Amancio-Filho, S.T., Coury, F.G., Spinelli, J.E. & Gargarella, P. (2024). Effect of Ce and solidification cooling rate on the microstructure and mechanical properties of AA2017 aluminum alloy. ***Journal of Alloys and Compounds***, *998*, 174848. Doi: 10.1016/j.jallcom.2024.174848.

- Mathias, Laura E. T. ; Pinotti, Vitor E. ; Batistão, Bruna F. ; **Rojas-Arias, Nicolas** ; Figueira, Gustavo ; Andreoli, Angelo F. ; Gargarella, Piter . Metal powder as feedstock for laser-based additive manufacturing: From production to powder modification. **Journal of Materials Research**, v. 39, p. 19-47, 2024. Doi: 10.1557/s43578-023-01271-8.

Conference presentation:

- **Rojas-Arias, N**.; Coury, F.G.; Amancio-Filho, S.T; Gargarella, P. *A literature review of the heat treatments applied in aluminum alloys processed by additive manufacturing*. **LightMat 2023 conference,** Jun. 21th – 23th, 2023, Trondheim, Norway.

- **Rojas-Arias, N**.; Coury, F.G.; Amancio-Filho, S.T; Gargarella, P. *A Literature Review of the Heat Treatments Applied in Metallic Parts Processed by Additive Manufacturing*. **FEMS EUROMAT 2023 conference,** Sept. 3rd – 7th, 2023, Frankfurt am Main, Germany.

- **Rojas-Arias, N.**; Soares Silva, A.; de Albuquerque Sousa, S.M.; Lisboa de Gouveia, G.; Spinelli, J.E.; Amancio-Filho, S.T.; Gargarella, P.; Gil Coury, F. *Study of the Effect of the Cooling Rate on the Microstructure and Mechanical Strength of an AA2017 Alloy*. **FEMS EUROMAT 2023 conference,** Sept. 3rd – 7th, 2023, Frankfurt am Main, Germany.

- **Rojas-Arias, N**.; Coury, F.G.; Amancio-Filho, S.T; Gargarella, P. Influence of the cooling rate on the hot tearing susceptibility of a modified AA2017 aluminum alloy. **RQ and ISMANAM conference**, Aug. 20th – 25th, 2023, Warsaw, Poland.

- **Rojas-Arias, N.**; Coury, F.G.; Amancio-Filho, S.T; Gargarella, P. *A review of the modification of aluminum powders for processing by LPBF*. **FEMS XXI B-MRS Meeting (SBPMat) conference**, Oct. 1st – 5th, 2023, Maceió-AL, Brazil.

- **Rojas-Arias, N.**; Coury, F.G.; Amancio-Filho, S.T; Gargarella, P. Influence of the cooling rate on the hot tearing susceptibility of a modified AA2017 aluminum alloy. **FEMS XXI B-MRS Meeting (SBPMat) conference**, Oct. 1st – 5th, 2023, Maceió-AL, Brazil.

INDEX

TABLE CAPTIONS

FIGURE CAPTIONS

SYMBOLS AND ABBREVIATIONS

ASTM	American Standard for Testing of Materials
AA	Aluminum alloy
AM	Additive Manufacturing process
AMI	As-melted ingot
AR	Aspect ratio
ANOVA	Analysis of Variance
BSE	backscattered electrons
CAD	Computer-Aided Design
COD	Crystallography Open Database
C_0	Concentration of interest
C_L	Concentration of the liquid phase
CR	Circularity ratio
C_S	Concentration of the solid phase
d	**I**ndentation size
DED	Direct Energy Deposition
DA	Direct aging
DoE	Design of Experiments
DSC	Differential Scanning Calorimetry
Ɛ	Ductility
EBSD	Electron Backscatter Diffraction
EDX	energy dispersive X-ray spectroscopy
F	Applied Load
FCC	Face Center Cubic
fs	Solid fraction
G	Temperature gradient
GS	Grain Size
h	Hatching
$\boldsymbol{H_0}$	Absolute hardness
HCS	Hot Cracking Susceptibility
HIP	Hot Isostatic Pressing
HT	Heat treatment

HV	Vicker Hardness
ICP–OES	Inductively Coupled Plasma Optical Emission Spectrometry
ICSD	Inorganic Crystal Structure Database
IDR	**I**nter Decis Ratio
IPF	Inverse Pole Figure
K	coefficient
L	Length
LOD	Loss of Drying
LR	Laser remelting
M	Metal
m	Meyer index
M1_0Ce	AA2017 modified composition without adding Ce
M1_3Ce	AA2017 modified composition with 3wt.% of Ce added
N	Newton
Nb:YAG	Neodymium-Doped Yttrium Aluminium Garnet
OM	Optical microscopy
P	Laser power
ppm	Parts per millon
R	Solidification rate
RE	Rare earth
rpm	Revolutions per minute
SAED	Selected Area Electron Diffraction
SC	Scution Casting
SE	Secondary Electrons
SEM	Scanning Electron Microscopy
SHAT	Solution Heat Treatment
T	Temperature
$\dot{T}$	Cooling rate
T_E	Eutectic temperature
TEM	Transmission electron microscopy
T_M	Melting temperature
UTS	Ultimate Tensile Strength

V	Scanning laser speed
v	Solidification speed
W	Wide
WAAM	Wire Arc Additive Manufacturing
wt.	Weight
XRD	X-ray Diffraction
YS	Yield Strength
%	Percentage
α	alfa
Δ	delta
μ	micrón
Ψ	Sphericity

1. INTRODUCTION

The additive manufacturing (AM) of metals is a relatively recent process presented in the 1980s to produce parts with complex geometries and highly refined microstructure that enhances the mechanical properties of the built parts [1-4]. AM has several techniques that are applied to produce metallic parts; nevertheless, Laser Powder Bed Fusion (LPBF) is one of the main techniques used for metals. LPBF produces parts layer-by-layer, using metallic powders as raw material and a laser as a heat source [5, 6]. This technique involves different processing parameters related to the laser characteristics, laser scanning strategies, temperatures (e.g. intrinsic heat treatment and the temperature of the substrate), and the raw material features, which may influence the processability of an alloy and the quality of the as-built parts [7].

Few alloys are commercially available to be used in LPBF, highlighting some Ti, Fe, and Al-based alloys [8-10]. For aluminum alloys, the cast aluminum alloys (Al-Si(Mg)-based compositions) are the most used in LPBF due to their reduced solidification interval and suitable fluidity, reducing the probability of cracking during solidification (hot craking). In contrast, wrought aluminum alloys (e.g. 2xxx, Al-Cu alloys) present a wide solidification interval, low fluidity, and poor weldability that increase the hot-cracking susceptibility (HCS) [11-14].

The alloy modification by adding inoculants produces an equiaxed microstructure that reduces the formation of hot cracks in wrought aluminum alloys processed in AM. Different inoculants such as borides or carbides have shown an improvement in the processability of aluminum alloys and an improvement in the mechanical properties of the as-built parts [15]. Nevertheless, employing inoculants in additive manufacturing (AM) processes poses various challenges. One issue is that particles may not evenly disperse across the deposited layers, leading to agglomeration. Consequently, this may result in an uneven solidification microstructure and localized fluctuations in material strength that can be detected by localized tests, e.g. microhardness measurements [16]. Furthermore, these agglomerates have a greater capacity to absorb the energy supplied by the laser, favoring the formation of porosity due to evaporation of

alloying elements, e.g. Mg. While these issues can be alleviated by using nanoparticles [16, 17], it also raises concerns about potential health risks from inhaling metallic and ceramic nanoparticles, as well as exposure through the eyes and skin [18].

Another strategy to reduce the hot cracking in AM parts is by reducing the solidification interval of the alloy. The addition of some metallic elements such as rare earths or Si into the compositions enhances the processability of wrought aluminum alloys in AM processes [19-26].

Although new compositions based on wrought aluminum alloys have been successfully designed and applied in AM processes, e.g. Scalmalloy® [27], several aluminum alloys have not shown good processability within this process. For example, AA2022 and AA2024 also have shown their limited processability into AM due to their wide solidification interval that increases the HCS [25]. The processability of another Al-Cu-based alloy, AA2017, has been studied by the Additive Manufacturing research group of DEMa-UFSCar [28]. The effect of Al-NbB inoculant addition on formed microstructure and mechanical properties was investigated [28]. Although the results showed a reduction in the density of cracks, they were not totally removed, which suggests that further studies are needed to improve its processability.

Considering the above, within the co-tutelle agreement between UFSCar – Brazil and TU Graz – Austria, **this work aimed to tailor the AA2017 composition to reduce its HCS and, thus, improve its processability during LPBF.** For this purpose, the research was divided into different stages related to 1) thermodynamic calculations and preliminary tests to define some candidate compositions to be tested by LPBF; 2) the production and characterization of raw material, i.e. metal powder, requested to produce LPBF parts; 3) the use of the design of experiments (DoE) and analysis of variance (ANOVA) methodologies to evaluate the effect of the process parameters on microstructural characteristics and mechanical properties of as-built parts; and 4) a deep microstructural and mechanical characterization by different techniques.

2. LITERATURE REVIEW

2.1. Additive manufacturing of metals

Additive manufacturing (AM) processes allow building parts layer-by-layer from a computer-aided design (3D-CAD). The processing of metallic materials by additive manufacturing has gained great interest due to its versatility in the construction of parts of high geometric complexity and with a highly refined microstructure. The rapid cooling rates achieved in some additive manufacturing processes, around ~10^6 °C·s^{-1}, enable the creation of a finely tuned microstructure, enhancing the material mechanical strength. Additionally, the freedom for intricate design and topological optimization enables the fabrication of parts with highly complex geometries, thereby minimizing the reliance on subsequent processing stages and expensive tools typically associated with conventional methods like machining [29-31].

Although AM is offered as a novel technology to design and build metallic parts, it suffers from a lack of alloys that can be successfully processed; highlighting some alloys based on Ti, Fe, and Al [32]. TiAl6V4, Inconel 718, stainless steels, and cast aluminum alloys (Al-Si-(Mg)) have shown good physical and mechanical properties that, in several cases, can be superior to parts obtained by conventional manufacturing processes [8, 9, 33]. Nevertheless, some metallic materials such as conventional high-strength aluminum alloys are highly susceptible to hot cracking, which difficult their application in AM. Likewise, the intrinsic characteristics of the raw material, such as high reflectivity and thermal conductivity, reduce the processability of these alloys. Due to this, the design and modification of alloys to facilitate their processability within AM have become a topic of great interest.

There are different techniques within AM destined to metals processing, e.g. Wire Arc Additive Manufacturing (WAAM) and Direct Energy Deposition (DED); nevertheless, LPBF is the most popular technique to process metallic materials, standing out mainly due to its ability to obtain parts with a high relative density and good surface finishing, compared to other AM techniques [34]. LPBF allows obtaining parts with a highly refined and textured microstructure and with

the versatility to process different alloys (reactive or non-reactive) [35]. Considering the nature and main objective of this work, this technique, focused mainly on aluminum alloys, shall be described in more detail.

2.2. Laser Powder Bed Fusion (LPBF) technique

2.2.1. Working principle

LPBF technique consists of the selective melting of a powder bed by using a laser beam following a 3D-CAD model [36]. By repeating this process layer by layer, customized parts with complex shapes and a high density can be obtained. **Figure 2.1** shows a schematic figure of this process. LPBF is subject to several processing parameters that affect the quality of a part. Aboulkhair *et al.* [7] have classified these parameters into four groups related to the characteristics of metallic powders, laser, scanning, and temperature.

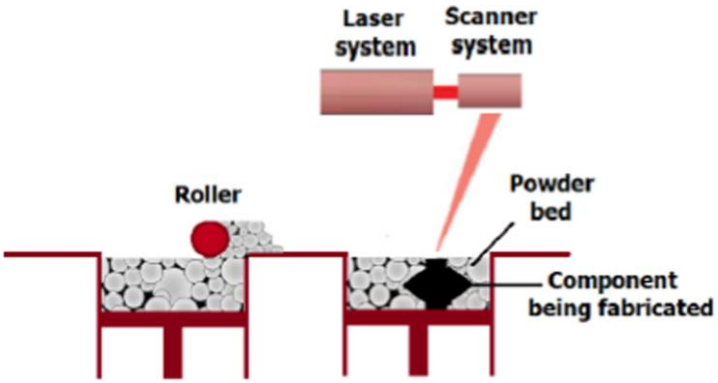

Figure 2. 1 – Schematic image of the LPBF technique. Figure reproduced under Creative Commons CC-BY International License from [36].

The characteristics of the metallic powders play a crucial role in the quality of the LPBF parts. The metallic powders must present a spherical morphology, with an adequate distribution of particle size and good fluidity; with the absence of surface impurities, satellites, and other morphological irregularities that generate some defects such as agglomeration, uneven thermal gradients, a poor union between layers, low density, low resistance, and undesired roughness in

the built parts [37][38][39][40]. The application of metallic powders with a mostly spherical morphology can significantly improve the mechanical properties of the part [7, 41].

Another characteristic of metallic powders to consider is the ability of the particles to absorb the radiation energy emitted by the laser. This parameter affects the melting and welding of the powder layers. Absorbance is an intrinsic material property for any given laser source. Materials such as copper and nickel show high absorbance in Nd-YAG (L_λ = 1.06 μm) and CO_2 (10.6 μm) lasers [42]. In contrast, aluminum alloys show a high reflectivity that difficult their application in LPBF, require high laser powers and low scanning speeds to compensate for the energy that metal powders cannot absorb, as well as to minimize defects in the built parts [43, 45].

AlSi10Mg and AA6061 alloys can present reflectivity values of 91% using a Nd:YAG laser source [46]. On the other hand, AISI 316L shows a reflectivity of 41% [47] and Ti6Al4V 53-59% [48, 49]. Furthermore, aluminum alloys also exhibit high thermal conductivity (for example, 146 $W \cdot m^{-1} \cdot K^{-1}$ for AlSi10Mg and 172 $W \cdot m^{-1} \cdot K^{-1}$ for AA6061 [50]) compared to AISI 316L steel (21.4 $W \cdot m^{-1} \cdot K^{-1}$ [50]) and Ti6Al4V (6.7 $W \cdot m^{-1} \cdot K^{-1}$ [51]), which increases the difficulty of melting powders efficiently, since the little energy transferred to the metal tends to dissipate rapidly through the substrate [52, 53].

The laser power and the laser scanning speed have a great influence on the depth and length of the molten pool [54]. The dimensions of the molten pool are governed by the power and absorptive capacity of the material [55]. The accumulated heat in deep and steep melt pools, especially at the start and end points of the laser scan, generates keyholes that affect the mechanical properties [56]. Other parameters, such as spacing between the scan lines (hatching) and the scanning strategies also play a fundamental role during the melting, welding, and solidification of the powder layers and the final microstructure [57, 58]. There are different scanning strategies, as shown in **Figure 2.2**. The application of a complex scanning strategy, varying the scanning direction (**Figure 2.2**(**a**)) in a layer allows to obtain higher densification because this strategy can melt the powder bed more homogeneously, in addition to reducing the residual internal

stresses. Instead, a simple scanning strategy (e.g., **Figure 2.2**(**c**)) can produce a lack of fusion and welding between the layers, favoring the presence of porosities and non-welded areas that affect the mechanical behavior in the as-built parts [44, 59].

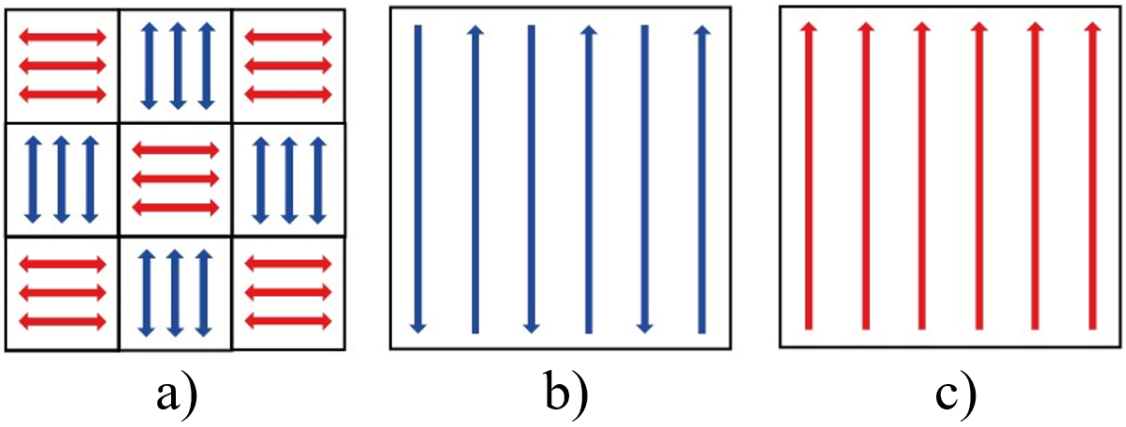

Figure 2. 2 – Scanning strategies commonly used in LPBF. In a) chessboard scanning strategy, b) bidirectional traks scanning strategy, and c) one-way traks scanning strategy.

2.2.2. Physical Metallurgy of alloys produced by LPBF technique

The inherent dynamics of LPBF, caused by the process conditions, allow for obtaining unique microstructural characteristics. The high cooling rates and the heat concentrated in a reduced area during the material processing, favor a microstructural refinement [60], in addition to promoting the formation of metastable phases and a supersaturated solid solution [8]. A poor selection of processing parameters can generate changes in the thermal history of the as-built part and, consequently, affect the integrity of the part due to the formation of porosity, poor weldability, and non-melting zones, including spatter and/or partial evaporation of the metal [61, 62].

The heat applied by the laser in the powder layers is dissipated through the substrate homogeneously, promoting directional grain growth [63, 64]. In this sense, the grains grow in the heat flux direction, typically leading to a columnar structure. The grain growth direction of LPBF parts also depends on the grain

orientation of the substrate [9]. The heat transfer occurs mainly by conduction to the substrate, convection through the melt pool, and radiation on the surfaces irradiated with the laser beams [65]. The crystals usually grow in preferential directions, e.g. aluminum (FCC structure) tend to have the <100> crystallographic directions nearly parallel to the local heat flux direction [37, 58]. The deposition and melting of a new layer of powder generate a heat input on the previous layer, which promotes the occurrence of an intrinsic cyclic heat treatment [66]. As the number of layers deposited increases, the efficiency of the substrate as a heat dissipator decreases [35, 67].

The morphology and size of the solidification microstructure are affected by the direction and scanning strategy of the laser, as well as the relationship between the temperature gradient (G, in $k \cdot mm^{-1}$) and the solidification rate (R, in $mm \cdot s^{-1}$) at the solid-liquid interface. Depending on G/R, a certain solidification structure can be obtained as shown in **Figure 2.3**. For instance, additive manufacturing techniques like LPBF, when there is an overcooling (G/R), it promotes the formation of a cellular microstructure. Nevertheless, the G/R is not sufficiently high to poduce a planar microstructure. Similarly, when we increase the cooling rate (G·R), it leads to the development of a more refined microstructure. The scanning strategy influences the direction of heat flow, thus defining the solidification direction [68]. Applying a unidirectional strategy can generate uniform growth on the different deposited layers as seen in **Figure 2.4**(**a** – **b**), maintaining the growth direction along the built direction. In contrast, a bidirectional scanning strategy favors the growth of the grains in a zig-zag (**Figure 2.4**(**c** – **d**)) [58, 69].

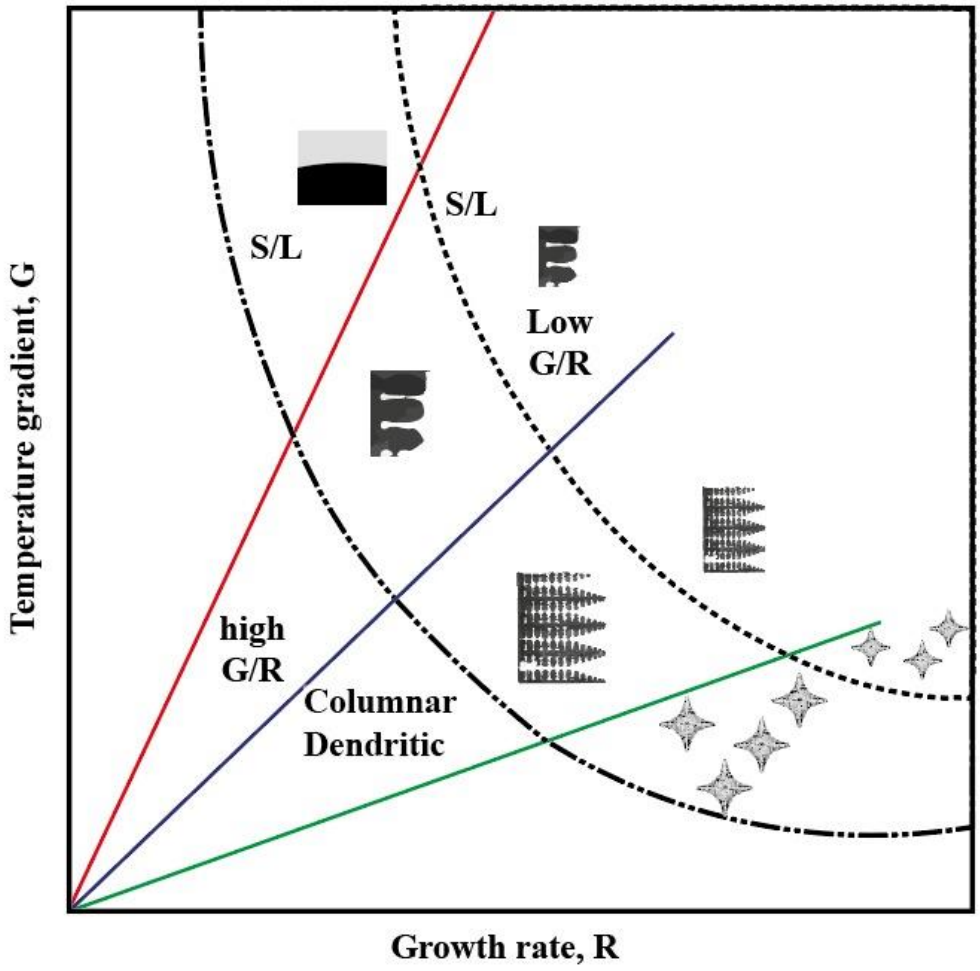

Figure 2. 3 – Effect of temperature gradient G and growth rate R on the morphology and size of solidification microstructure. Schematic figure based on [68].

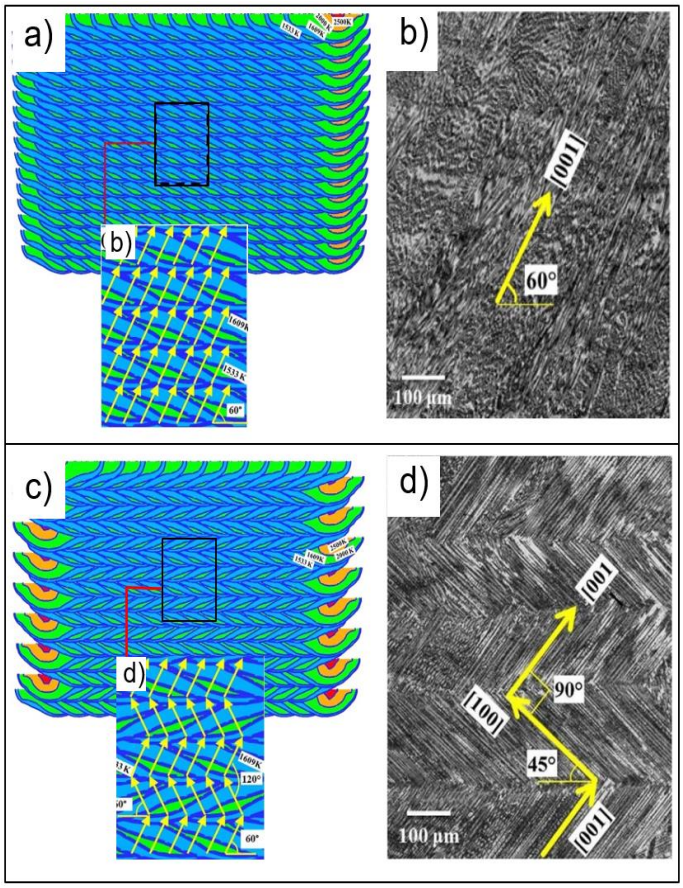

Figure 2. 4 – Thermal gradient calculations and optical micrographs of the longitudinal sections of Ni AM parts, showing the heat flow and grain growth directions: a, b) unidirectional and c, d) bidirectional laser scanning. Figure reproduced under Creative Commons Attribution 4.0 International License from [58].

The variations of G and R in the LPBF process allow for obtaining unique microstructures, characterized by presenting a highly refined structure and a columnar grain growth in the direction of heat extraction, i.e. towards the substrate, resulting in a high hot cracking susceptibility (HCS) [62, 70]. The residual stress generated during the solidification and contraction of the material may promote cracking [65]. The use of low scanning speeds and high-energy input usually favors high thermal stresses. If the residual stress exceeds the local YS of the material, plastic deformation can be generated. Instead, if the residual stress exceeds UTS, the molten material may crack [65]. The columnar structure obtained in LPBF parts reduces the strain accommodation in the grains and the

internal tensions generated during the solidification, in addition to hindering the permeability of liquids between the grains formed, contributing to a higher HCS [71, 72]. For wrought aluminum alloys, this problem increases due to a lack of liquid during the final stage of solidification avoiding filling the voids between grains [73].

2.3. Aluminum alloys in AM

2.3.1. Aluminum alloys processed by AM

Aluminum and its alloys have become strategic materials due to its low density (2.7 $g \cdot cm^{-3}$), approximately one-third of steel (7.83 $g \cdot cm^{-3}$), its ductility, optimal thermal and electrical conductivity, and good corrosion resistance, making this material attractive for several applications [74-76]. The Al-Si and Al-Si-Mg alloys (cast aluminum alloys) are the most studied aluminum alloys in AM processes due to their short solidification range and good fluidity that reduce the HCS [7, 29, 77]. Nevertheless, cast aluminum alloys do not have the best mechanical properties, including yield strength (YS), ultimate tensile stress (UTS), and uniform strain (Ɛ), compared with wrought aluminum alloys, which exhibit improved mechanical properties through heat treatments. Unfortunately, wrought aluminum alloys are not an optimal candidate for AM processes such as LPBF [78-80]. The heat transfer and melt pool dynamics during the deposition of the different layers, i.e. producing a high GxR, results in a microstructure with columnar grains arranged in the direction of heat extraction (perpendicular to substrate) that favor a high HCS. Furthermore, the wide solidification interval, low permeability, and low liquid availability during the final stages of solidification in wrought aluminum alloys favor an increase in HCS [72, 81].

For this reason, some wrought aluminum alloys from the 2xxx, 5xxx, and 7xxx series have been modified by adding other elements or compounds to reduce their cracking susceptibility and reach the processing requirements in AM [9]. In essence, the reduction of HCS in AM parts is aided by 1) heterogeneous nucleation through the incorporation of dispersoid phases and 2) reducing its alloy solidification interval by modifying the alloy composition.

The first route favors a greater grain refinement through heterogeneous nucleation, which allows the accommodation of internal stresses, a higher resistance to cracking, and an increase in mechanical properties through the formation of a reinforced matrix [82]. Nevertheless, it has been verified that an excessive content of inoculants in alloys can affect the mechanical properties and promote cracking [83, 84]; therefore, it is necessary to determine optimal inoculant concentrations that allow grain refinement without affecting the part integrity [85].

The second route, focused mainly on wrought aluminum alloys, consists in modifying the alloy composition, which favors a reduction in the solidification interval and promotes the formation of eutectic regions that allow reducing the HCS, similar to the behavior of cast aluminum alloys [73, 86]. Both routes favor greater processability of aluminum alloys, as well as an improvement in their mechanical properties due to the microstructural changes and formation of new phases.

2.3.2. Modification of aluminum alloys in AM

2.3.2.1. Heterogeneous nucleation by adding ceramic particles

The addition of ceramics in aluminum alloys is widely used in conventional manufacturing processes to promote grain refinement by heterogeneous nucleation [87]. In AM, obtaining a highly refined equiaxed structure can favor an increase in mechanical strength and the prevention of cracking. Several authors have studied the application of different ceramics such as borides [88-90], carbides [91-93], nitrides [94-97], and oxides [98-101] to modify the microstructural characteristics and mechanical strength of Al parts processed by LPBF. Nevertheless, most of these works are focused on cast aluminum alloys.

The development of new alloys such as the A205 alloy (Al-Cu-Mg-Ag-(TiB_2)) can be highlighted, which corresponds to an A201 modification through the addition of Ti (3 – 3.85 wt. %) and B (1.25 – 1.55wt. %) to produce TiB_2 by in-situ reaction [102]. It has been reported that as-built A205 LPBF parts can obtain values of YS = 322-440 MPa, UTS = 100-650 MPa, and ε = 9.5 – 17.7% [102-

104]. The incorporation of TiB_2 by in-situ reaction has also been studied in AA2024 LPBF parts [105]. The in-situ reaction guarantees uniform distribution of TiB_2 nanoparticles (0.5 μm), which promote grain refinement and act as reinforcing particles, improving the mechanical properties in as-built parts (YS = 250 – 400MPa, UTS = 400 – 520MPa, and Ɛ = 3 - 9%), compared to TiB_2-free or AA2024 parts produced by conventional methods (*see* ***Figure 2.5***) [105].

The incorporation of ceramics can also be done ex-situ. The mixture of AA2024 powders with CaB_6 [106, 107] and TiH_2-TiC [92, 108] powders to reduce cracking in LPBF parts has been reported. The addition of 2 wt. % CaB_6 allows an increase in YS, UTS, and Ɛ values from 53 MPa, 53 MPa, and 0.3 % to 457 MPa, 482 MPa, and 12 % [106]. Likewise, the parts composed of AA2024/TiC-TiH_2 have reported an increase in the UTS and Ɛ values from 240 MPa and 0.3 % to 390 and 12 %, respectively. Likewise, the application of subsequent heat treatment allows an increase in UTS to 490 MPa and Ɛ to 16% [108].

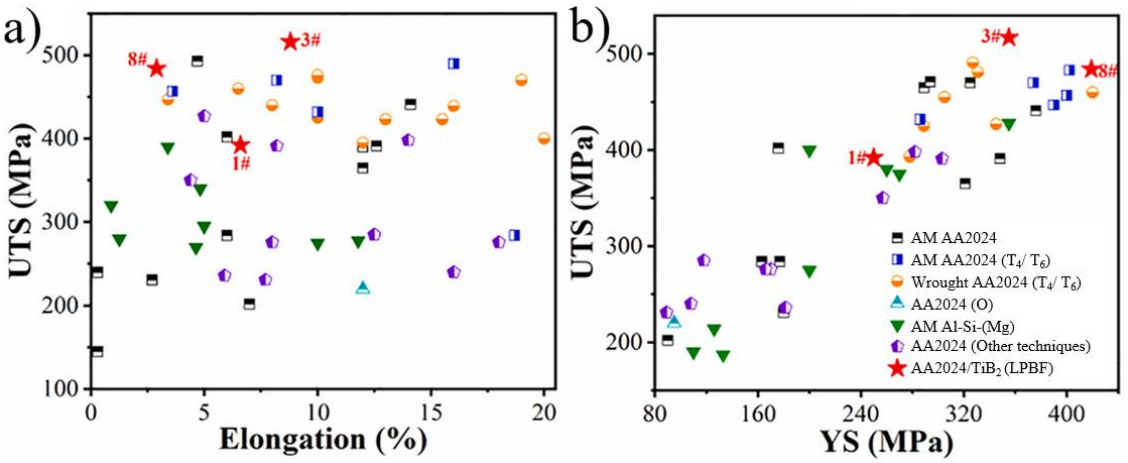

Figure 2. 5 – Relationship between mechanical properties a) elongation / UTS and b) YS / UTS of AA2024/TiB_2 parts produced by LPBF and its comparison with other aluminum alloys processed by different manufacturing techniques (including AM). The red starts refers to the AA2024/TiB_2 LPBF parts. Image reproduced and adapted from [105] with permission of Elsevier.

2.3.2.2. Heterogeneous nucleation by adding metallic elements

The addition of metallic elements that promote heterogeneous nucleation by forming $L1_2$ primary trialuminides (Al_3M, M = metal), which present a low lattice parameter-misfit with relation to the α-aluminum, is also presented as an alternative to reduce the probability of cracking of aluminum LPBF parts. The continuous interest in designing and applying new AM printable compositions using added inoculants has allowed the development of alloys such as Scalmalloy® (5xxx(Sc–Zr) [27]), Scancromal® [109], and Calciscal® [110]. Nevertheless, the addition of elements such as Cr can generate the formation of primary phases such as $Al_{11}Cr_2$ (Monoclinic [111]), which do not behave as a dispersoid particle due to a large phase mismatch with the matrix [112]. Likewise, the incorporation of other elements such as Sc and Zr, although effective for grain refinement, they are significantly expensive to apply in new alloys [113, 114].

A new alloy, known as Scantital®, has recently been reported, which consists of a modification of Scalmalloy® by the addition of Ti [112]. The addition of Ti can partially replace the required Sc content in alloys intended for LPBF by forming Al_3Ti [112, 115]. The use of Ti to modify the microstructure by heterogeneous nucleation of Al-Cu parts processed by LPBF has been reported [116]. Al-2.25Cu-1.8Mg LPBF parts with 1.5 wt. % Ti obtained a highly refined structure that reduces the probability of cracking as observed in **Figure 2.6** [116].

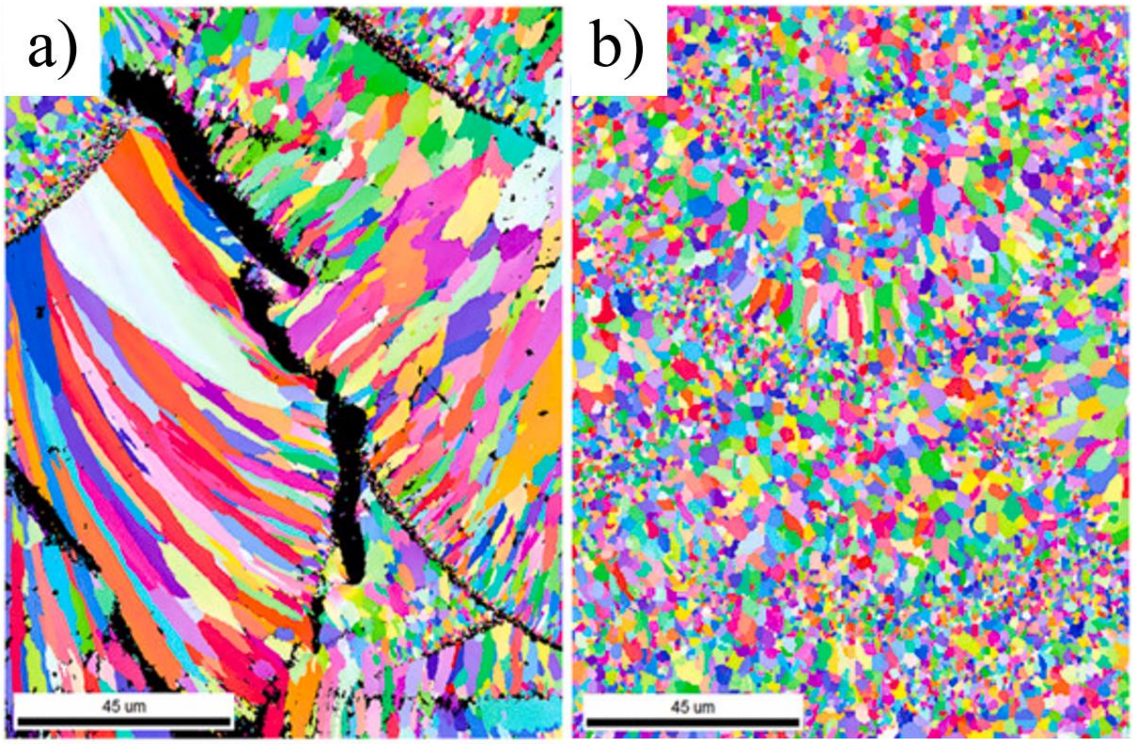

Figure 2. 6 – IPF – EBSD images of Al-2.25Cu-1.8Mg-xTi (wt.%) parts built by LPBF and the effect of Ti on the microstructural refining and hot-cracks elimination. In a) Al-2.25Cu-1.8 and b) Al-2.25Cu-1.8Mg-1.5Ti. Image reproduced and adapted from [116] with permission of Elsevier.

2.3.2.3. Modification by reducing the solidification interval

Applying aluminum compositions with short solidification range, i.e. with a eutectic / near-to-eutectic composition,is presented as a useful strategy to improve printability in LPBF. The Al-Si [117,118], Al-Ni [119, 120], and Al-Ce [19, 121, 122] based aluminum alloys have been widely studied within LPBF. Their short solidification range and the presence of a eutectic solidification region during the final stage of solidification guarantee an HCS reduction.

HCS is caused during the final stage of solidification (Fraction of solid, f_s = 0.98 – 1), in which the deformations induced by solidification and contraction of the material prevent the grains from accommodating properly within the microstructure, resulting in the fracture of the material. Moreover, the low ductility of the grains and the scarcity of liquid during the terminal stage of solidification in

wrought aluminum alloys reduce the possibility of filling the cracks formed [72, 123, 124].

The addition of elements such as Ce, Si, and Ni to promote eutectic compositions guarantees a greater amount of liquid during the final stage of solidification in wrought aluminum alloys. Montero *et al.* [125] have mixed AA7075 powders with Si powders (4 wt. %) to improve their printability by LPBF, obtaining crack-free LPBF parts with a high density (approx. 99%). Likewise, the addition of Si allows a refinement of the microstructure. Nevertheless, the mixture of AA7075 and Si powders generates a microstructure with poor homogeneity.

EBSD images of Si-free AA7075 LPBF parts shown in **Figure 2.7** reveal a microstructure with columnar grains parallel to the direction of solidification and no apparent appearance of melt pools. In contrast, an increase in the Si concentration reduce the solidification interval of the AA7075 alloy and, in addition, leads to a refinement of the solidification structure, resulting in the formation of finer columnar and equiaxed grains [125]. The difference in the density and the particle distribution between different powder compositions complicates the mixing of the raw material, as well as the optimal distribution of Si in as-built parts, due to the high cooling rates offered in LPBF [125]. Similar behavior has been reported during the mixture of Mo and TiGr5 powders by LPBF [126]. The production of pre-alloyed powders favors a greater homogeneity of the microstructure compared with parts produced by mixing powders as reported by Guichuan *et al.* [127] for AA7075 - 3.74 wt.% Si parts built by LPBF.

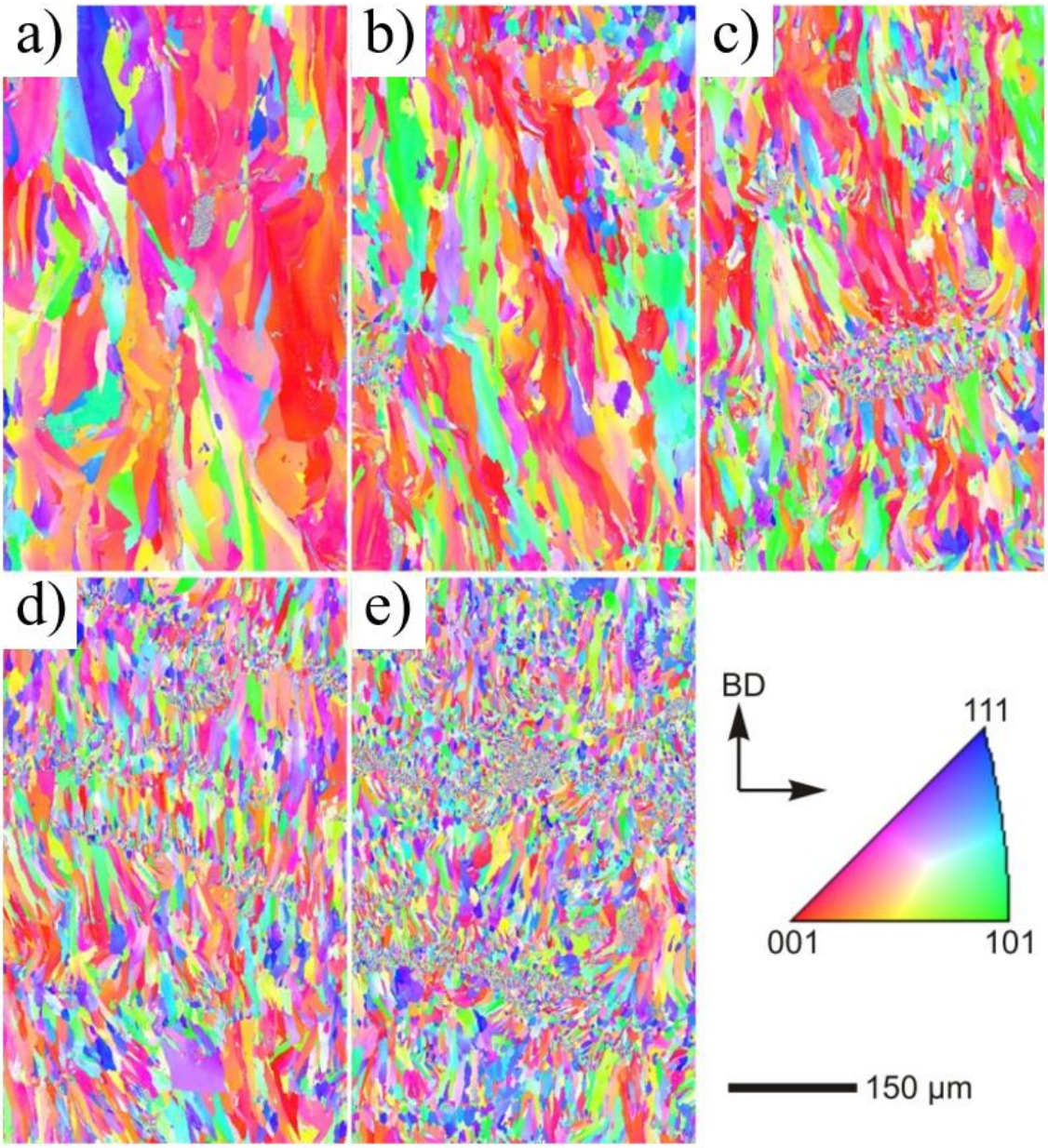

Figure 2. 7 – IPF – EBSD maps of AA7075 LPBF parts modified with a) 0 wt.% Si, b) 1 wt.% Si, c) 2 wt.% Si, d) 3 wt.% Si, and e) 4 wt.% Si. The incorporation of Si in the AA7075 composition helps to obtain highly refined microstructures with some equiaxial zones between the melt pools. Image reproduced and adapted from [125] with permission of Elsevier.

Ruidi *et al.* [128] have developed a variant of Scalmalloy by adding Si to improve its processability by LPBF. Even if Scalmalloy® alloys (Al-Mg-Sc-Zr) [129, 130] and Al-Mn-Sc-based alloys [131] present optimum processability within the AM process, these alloys require a minimum scandium content of 0.66

wt.%, which considerably increases the costs of the alloy. A reduction in the Sc content generates an increase in HCS due to grain coarsening [132]. The addition of 1.3 wt. % Si to the composition Al-8Mg-1.3Si-0.5Mn-0.5Sc-0.3Zr allowed to eliminate the formation of cracks in LPBF parts. However, a decrease in the Si content can have the opposite effect, as shown in **Figure 2.8** [128]. The concentration and interaction between the alloying elements also play a crucial role in the HCS. The development of maps by thermodynamic calculations to estimate the HCS of Al-Cu-Mg, Al-Si-Mg, Al-Si-Cu, and Al-Mg-Zn base alloys has been reported [133, 134].

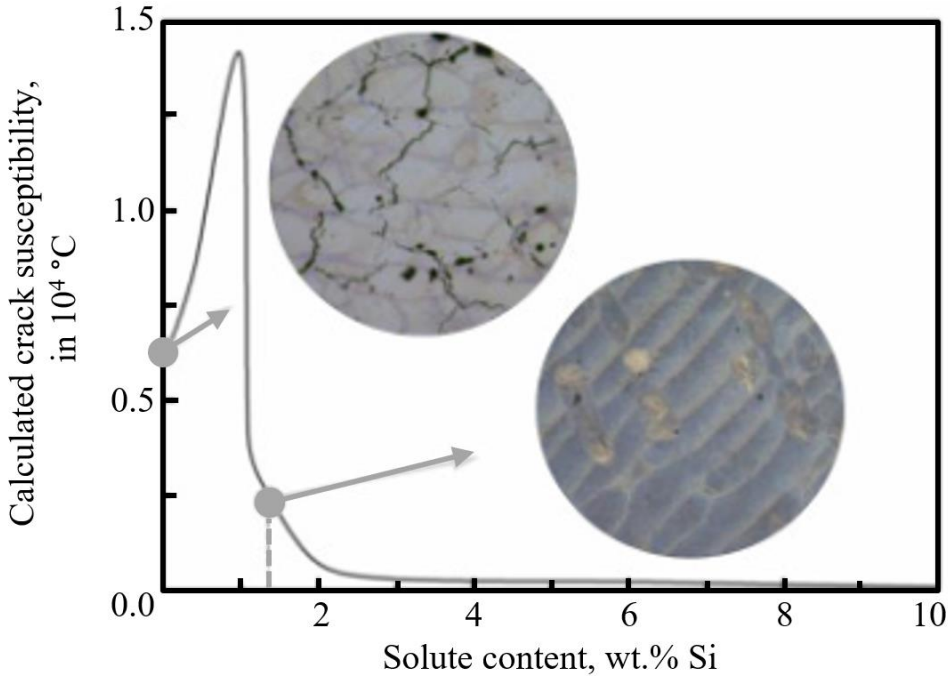

Figure 2. 8 – Effect of Si content in an Al6Mg-xSi (wt.%) alloy during the design of Scalmalloy® for its application in LPBF. Image reproduced and adapted from [128] with permission of Elsevier.

Currently, the use of rare earths (RE) has been presented as an optimal option for the design and modification of aluminum alloys to improve their processability by LPBF. The use of RE such as La and Y has been studied to improve the printability of Al-La-Mg-Mn [135] and AA2024/Y [136] allowing a HCS reduction due to the formation of eutectic regions in the form of Al + $Al_{11}La_3$ and Al + Al_8Cu_4Y, respectively. However, most of the recently reported works position

Ce as an optimal candidate for the modification of aluminum alloys intended for AM processing [19, 121, 122, 137, 138]. Among the RE, cerium (Ce) stands out as the most abundant and cheapest element [139]. Likewise, Ce-modified aluminum alloys are characterized by high thermal stability and high processability due to their high fluidity and optimal mechanical properties [20, 137, 140, 141].

Perrin *et al.* [122] have studied the effect of Ce addition in Al-Cu base alloys processed by LPBF. Compositions close to a eutectic composition revealed the formation of binary eutectic regions composed of Al+Al_4Ce, Al+Al_8Cu_3Ce, and Al+Al_8Cu_4Ce, as well as the identification of a ternary eutectic composed by Al+Al_8Cu_4Ce+Al_2Cu. The Al-7Cu-3Ce (in wt.%) parts presented values of YS = 257 MPa and UTS=349 MPa, which are higher than the Al-10Ce alloy parts processed by the same technique (YS = 222 MPa and UTS = 319 MPa) [138]. However, a substantial reduction in ductility is observed (11 % to 1.1 % from Al-10Ce to Al-7Cu-3Ce). Manca *et al.* [19] have reported the formation of eutectic zones composed of $Al_{11}Ce_3$ and $Al_{6.5}CeCu_{6.5}$ phases in Al–7Cu–3Ce parts processed by LPBF. The application of an annealing treatment (540 °C for 3 h and subsequent aging at 190 °C for 8 h) generates an increase in the size of the $Al_{6.5}CeCu_{6.5}$ particles from 16.8 nm to 100 nm, which causes a decrease in the hardness values from 159 HV to 95 HV.

Although important advances have been made in the design and modification of wrought aluminum alloys to improve their printability by LPBF, these works have focused on a few commercially applied wrought aluminum alloys. For 2xxx series alloys, most of these works are related to the AA2024 [89, 106, 108, 142]. Nevertheless, other alloys in this series are currently widely used in the industry, so their adjustment to the LPBF process can represent a contribution to the design and production of parts using this technique. Considering the above, some of the basic characteristics of the AA2017 alloy shall be mentioned, which is an alloy widely used in the automotive and aeronautical industries [143, 144].

2.3.3. AA2017

The AA2017 aluminum alloy is one of the most used aluminum alloys in aeronautics and automotive applications, showing higher mechanical properties than AA2024 [143]. Some of the physical characteristics and mechanical properties offered by the AA2017 in annealed condition are presented in **Table 2.1** [74]. The chemical composition of the AA2017 presented by Kissell [76] is shown in **Table 2.2**.

Table 2. 1 – Physical and mechanical properties of the AA2017 [74].

Property	Unit	Value
Density	$g \cdot cm^{-3}$	2.79
Melting point	°C	513 – 641
UTS	MPa	427
YS	MPa	275
Elongation	%	22
Elastic modulus	MPa	72
Shear strength	MPa	124
Thermal conductivity	W·mk	193
Thermal expansion	C^{-1} (at 20 – 300°C)	$23.6 \cdot 10^{-6}$

Table 2. 2 – AA2017 chemical composition in wt. % [76].

Si	Fe	Cu	Mn	Mg	Cr	Ni	Zn	Ti	Be	Others	Al
0.2-0.8	0.7	3.5-4.5	0.4-1.0	0.4-0.8	0.1	-	0.25	0.15	0.05	0.15	Bal.

The AA2017 parts produced by conventional routes usually are treated by a solution annealing, carried out at 500°C, followed by water quenching and artificial aging at 160°C during 18h (also known as T6 heat treatment or “temper”) [145], promoting the formation of Al_2CuMg (σ) and Al_2Cu (θ) intermetallic phases mainly, leading to an increment in the mechanical strength [146]. The θ phase

formation follows the sequence: supersaturated solid solution (SSSS) → GP zones → θ´´ → θ´ → θ [31, 82]. An increase in the heat treatment temperature tends to reduce and almost eliminate most phases, a process known as solubilization [147]. The increment in the Cu content allows a higher mechanical strength and hardness. Extended aging heat treatments shall generate an over-aging where a drop-in strength is seen as shown in stage IV for Al-Cu alloys with an addition of 1.66 – 2.18 at. %Cu (**Figure 2.9**). The formation of other types of precipitates, e.g. Cu_2FeAl, reduces the amount of copper available for generating the θ and σ intermetallic phases [148].

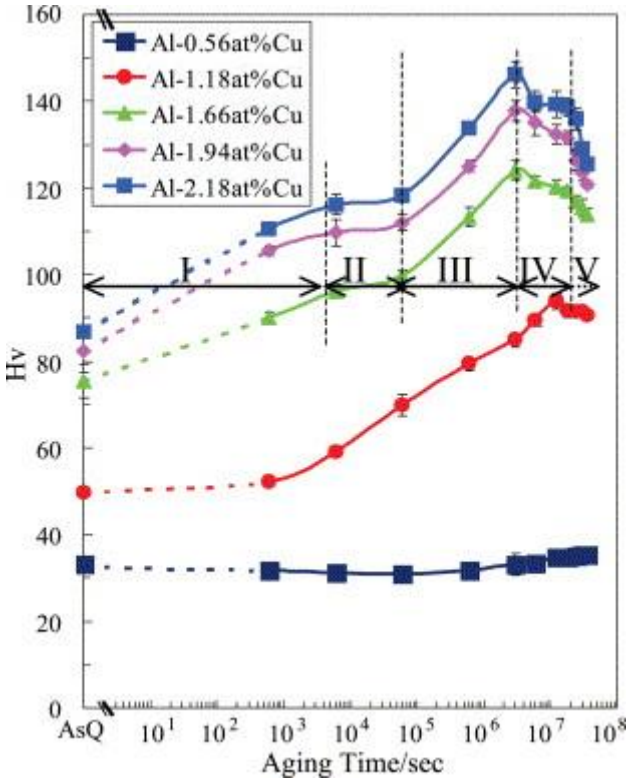

Figure 2. 9 – Schematic of the effect of heat treatment time and temperature on the precipitation sequence and hardness behavior in Al-Cu alloys. In a) θ precipitation sequence according to the temperature and, in b) effect of the addition of Cu (in at. %) and aging time on the hardness. Image reproduced from [147] with permission of Elsevier.

The as-cast AA2017 parts usually are formed by a faced-centered cubic (FCC α-Al) matrix often together with intermetallic phases, depending on the

solidification condition [148, 149]. The microstructure of parts produced by low cooling rates is heterogeneous and coarse as shown in **Figure 2.10**(**a**–**c**). The low cooling rates allow the formation and growth of θ phases with a needle-shape morphology, which can embrittle the part, along with $Al_5Cu_6Mg_2$, Al_2CuMg, and others phases, which have a coarse size [149, 150]. On the other hand, at high cooling rates, such as obtained in suction casting processes (10^2 – 10^3 °C·s^{-1}), a more refined and homogenously microstructure is seen. In addition, eutectic aglomerates can occur as observed in **Figure 2.10**(**d** – **f**), promoting the eutectic formation around the dendrites and generating a structure that resembles a net (*see **Figure 2.10(d)***) *at low magnification*). The microstructure of parts produced by suction casting shows more refined and homogenously distributed precipitates and eliminates the presence of needle-shaped precipitates, allowing to enhance the mechanical properties such as hardness [150].

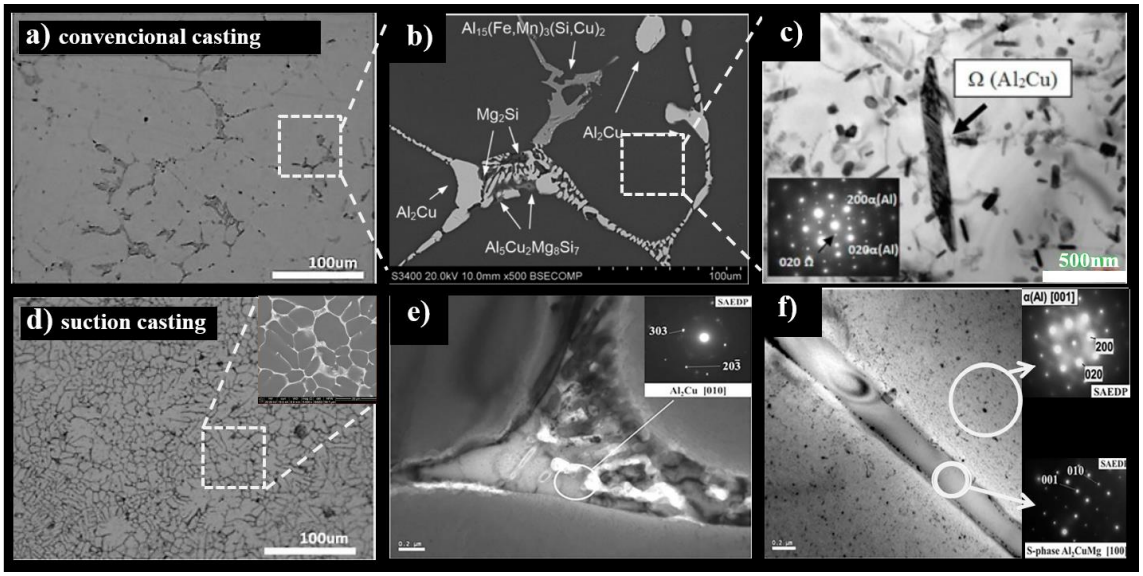

Figure 2. 10 – Microstructure of AA2017 parts produced by conventional casting (ingot solidified in an alumina crucible in ar) (a-c) and by vacuum suction casting (d-f). The alloys produced with a low cooling rate show a coarser and heterogenous microstructure and the presence of needle-shaped θ precipitates. In contrast, parts produced by suction casting show a more refined microstructure with a minor proportion of precipitates, which are more refined and homogeneously distributed. Image reproduced and adapted from [149] and [150] with permission of Elsevier and Jonh Wiley and Sons.

A recent study reported the LPBF of the AA2017 alloy [151]. The authors showed that the constructed parts present a high density of intergranular hot cracks but they do not propose alternatives to improve the processability of this alloy. Furthermore, other studies related to Al-Cu base alloys processed by AM, e.g. AA2024 [89, 106, 108, 142], have demonstrated their poor ability to be applied efficiently in this type of process due to its wide solidification interval that increases the HCS. Considering the above, this research focused on tailoring the AA2017 composition to improve its processing by LPBF. Details of the experimental procedure carried out, as well as the results and analyzes carried out are presented in ***Session 3***.

3. EXPERIMENTAL PROCEDURE

This work aimed to tailor the AA2017 composition to decrease its hot cracking susceptibility and, therefore, improve its processability by LPBF. This chapter describes the different experimental techniques used for the composition design, production, and subsequent characterization of the metallic powders and parts produced by LPBF and conventional manufacturing processes. Figure 3.1 summarizes the experimental procedure.

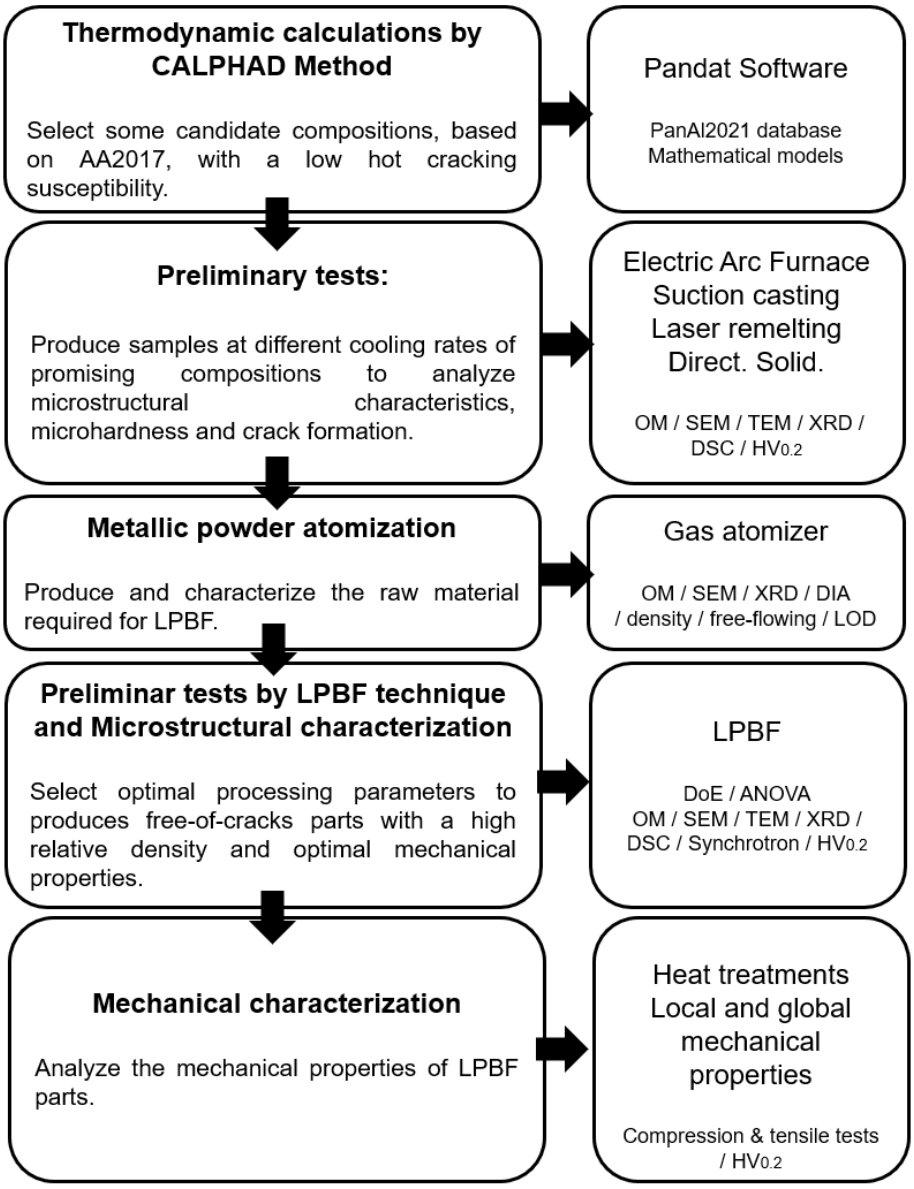

Figure 3. 1 – Flowchart of the experimental procedure developed in this work.

3.1. Thermodynamic calculations and preliminary tests

CALPHAD method via COMPUTHERM/Pandat thermodynamic software and the PanPhaseDiagram tool was used to carry out thermodynamic calculations and produce different pseudobinary phase diagrams, varying the concentration of the elements that make up the AA2017 within the standardized ranges. The variation of the solidification interval of the constructed diagrams was observed, and the best AA2017-based composition was determined. Next, the effect of adding other elements, different from those that constitute the AA2017, was studied and an optimal percentage was selected to be applied to further reduce the solidification interval. The main goal of this step was to generate optimal modifications of the AA2017 with a reduced solidification interval. The elements tested in this step were those included on the PanAl2021 database (Ag, B, Be, Bi, C, Ca, Ce, Co, Dy, Er, Gd, Ge, Hf, Ho, K, Li, Lu, Na, Nb, Nd, Ni, Pb, Pm, Pr, Sb, Sc, Sm, Sr, Tb, Tm, V, W, Y, Yb, Zn, Zr).

Promising compositions, obtained from the CALPHAD calculations, were produced in an Electric Arc Furnace in a vacuum atmosphere. The arc-melted ingots (AMI) with an approximate weight of 15 g and plates of 2mm*4mm*30mm produced by copper-mold suction casting (SC) were processed in a Bühler GmbH MAM 1 Arc melter. Some SC samples were subsequently laser remelted (LR) in an AURORA S-Titanium Pro Additive Manufacture device with a CO_2 laser source. Single tracks were produced using a laser power of 300 W and scanning speed of 15 $m \cdot s^{-1}$ in an argon atmosphere (± 1000 ppm O_2). The selection of these parameters were chosen through preliminary tests carried out in the additive manufacturing group of the DeMa/UFSCar. In addition, the samples produced in this stage were microstructurally analyzed according to the descriptions in the ***Section 3.5***. The samples produced in the three conditions, i.e. AMI, SC, and LR, were analyzed in the transverse region. For each case, a minimum of three replicates per condition were analyzed.

In order to have a better understanding of the microstructural evolution during solidification, it was carried out an exploratory study of directional solidification for promising compositions chosen from preliminary tests. For this,

the promising compositions were cast and subsequently poured into an AISI 310 stainless steel mold to produce metallic cylinders 160 mm in height and 60mm in diameter [152]. The evolution of the temperatures along the length of the casting was monitored using fine K-type thermocouples, whose tips were distributed longitudinally along the casting. When the melt temperature reached 5% above the liquidus temperature during the directional solidification (DS) tests, the electric heaters were turned off, and the water flow at the bottom of the container was initiated. For this reason, the cooling system was started as soon as the melt reached the correct temperature.

The water-cooled base promoted the onset of solidification and kept the system running until the casting was fully solidified. The solidification cooling rates were calculated concerning the movement of the liquidus α-Al isotherm throughout the casting length. After each thermocouple had passed the liquidus isotherm, the cooling rate ($\dot{T}$) was calculated by taking the local time (t) derivative of each cooling curve (dT/dt).

These tests of directional solidification allowed extracting different information such as mathematical models to determine the influence of the cooling rate and solidification speed on dendritic spacing, grain size, phase formation, and mechanical properties (microhardness in this case). The microstructural characterization was carried out by optical microscopy, scanning electron microscopy, and X-ray diffraction. Details of the characterization process will be given in ***Section 3.5***.

3.2. Powder production and characterization

Ingots of the modified AA2017 alloys were produced using a Power Trak 50-30R VIP induction furnace. The chemical composition of the produced ingots were analyzed by Inductively Coupled Plasma Optical Emission Spectrometry (ICP-OES). The ingots produced were used to prepare metallic powders by gas atomization in a HERMIGA 75/5VI(EAC) equipment. The atomization process for both M1_0Ce and M1_3Ce compositioins was carried out at 800 °C, applying a pressure of 20 bar, and using a nozzle of 1.5 mm.

Particle size distribution was performed by sieving and dynamic image analysis. Considering the operating characteristics of the LPBF equipment used in this work, the powders produced were sieved to obtain samples with a useful particle size between 20 µm – 63 µm.

Topographical features of the particles were analyzed by optical microscopy (OM, Carl Zeiss Observer Z1m microscope), scanning electron microscopy (SEM, TESCAN Mira 3, Tescan) equipped with an EDAX Octane Plus energy dispersive X-ray spectroscopy (EDX) detector and a Hikari Plus electron backscattered diffraction (EBSD) camera, and dynamic image analysis using a particle size analyzer (Sympantec PAQXOS 4.3) according with ISO 13320, 13322, and 9276. For this work, the particle analysis was focused on the measurement of anisotropy, circularity, and sphericity in dried samples. Details of the preparation of the samples will be detailed in ***Section 3.5***

The physical characteristics of the gas-atomized powders were also considered. The tapping density was measured according to the ASTM B527 standard. The apparent density was carried out by the Arnold method according to the ASTM B703 standard. Likewise, the bulk density and fluidity of the powder were measured using Hall and Carney funnels, according to ASTM B212 and ASTM B417 standards, respectively. Finally, the skeletal density was measured by pycnometry test in a Accupyc 1330-Micromeritics and following the ASTM B923 standard. Free-flowing tests were performed using the Hall and Carney funnels. Additionally, the Carney funnel was also used to measure the (static) angle of repose of the powder samples.

The moisture measurement of the material was carried out using the loss on drying (LOD) method in a controlled atmosphere oven, varying the temperature from 80 °C to 200 °C at 24 h. The remaining moisture content in samples was determined using the Karl-Fischer method in a Xylem-TL® 7500KF-trace device. The measurements were carried out at a constant temperature (21°C), using dried samples of 2 g. The powders were also characterized by OM, XRD, and DSC as will be detailed in ***Section 3.5***.

3.3. Optimization of LPBF processing parameters

The selection of an optimal combination of parameters to produce LPBF parts with a high density and free of cracks occurred by the application of design of experiments (DoE) and analysis of variance (ANOVA). The response surface method was selected through the application of a face-centered cubic design (FCC, k = 3) to determine the influence of the laser power (W), scanning speed of the laser (v), and Hatching (h) on the microstructural characteristics of the parts built by LPBF. The selected factors and levels are presented in **Table 3.1**.

The range of parameters was chosen based on preliminary tests, determining the minimum and maximum values suitable for fabricating parts using LPBF technology without jeopardizing the printer's integrity. The LPBF parts were built in a ORLAS-Creator® printer machine.

Table 3. 1 – Processing parameters used to produce LPBF parts in this work.

DoE (FCC, K=3)				
Parameter	**Unit**	**-1**	**0**	**1**
Laser power	W	100	175	250
Scanning speed	$mm \cdot s^{-1}$	200	1100	2000
Hatching	µm	50	100	150
Constant parameters				
Rotation angle	°		67	
Spot diameter	µm		80	
Powder bed thickness	µm		25	
Scanning strategy	--		bidirectional	
Powder size distribution	µm		20 – 63	

In total, 15 combinations were analyzed for each DoE, using 6 central points to determine the variability of the process. Likewise, 3 runs were carried out for each composition to increase the reliability of the data acquired. The LPBF samples were subjected to a metallographic process as described in section 3.5.1. The microstructure obtained was analyzed under OM and SEM according

to ***Section 3.5***. The images obtained were used to determine the relative density of the parts, the density and length of the cracks, and the aspect ratio of the melt pools. The measurements were carried out using the free software ImageJ [153]. In addition, the mechanical behavior by microhardness tests was investigated according to ***Section 3.6***. The results obtained were used to establish adequate processing conditions to obtain parts with optimal mechanical properties, high relative density, and free of cracks.

3.4. Heat treatments

Considering that one of the main properties that characterize the 2xxx series aluminum alloys (Al-Cu base alloys) is their ability to be precipitation hardenable, LPBF cubes of 5 cm^3 were subjected to aging heat treatment. The heat treatment conditions were defined through the analysis of DSC curves. From the DSC curves, the appropriate temperatures were determined to apply homogenization, annealing and aging treatments on parts produced by LPBF. Details of the heat treatments applied shall be shown in ***Section 4.6***. The effect of applying heat treatments was observed by microhardness measurements according to ***Section 3.6***.

3.5. Microstructural characterization

3.5.1. Metallography

The different parts produced in this work, i.e. processed by different manufacturing processes, were metallographically prepared as follows: The samples were embedded in cold-mounting acrylic resin (Struers VersoCit-2, Denmark). The resin-embedded samples were ground in a Struers–Tegramin grinding and polishing machine (Denmark) using SiC paper from #320 to #3000 grift. The first grinding stage, using #320 grift, was carried out until both faces of the specimen were parallel. Subsequently, the following grinding stages were

carried out during 1 min intervals between the different sandpapers, applying a force of 5 N, a rotation speed of 240 rpm, and a co-rotation of 150 rpm.

The polishing process was performed using 3 µm and 1 µm diamond pastes using the same grinding parameters, followed by colloidal silica for 5 minutes and reducing the rotation speed to 60 rpm. Finally, a final polishing was carried out in water during 5 minutes at 60 rpm to remove the colloidal silica retained within the sample. Between each polishing stage, the samples were cleaned with distilled water and isopropyl alcohol by ultrasound for 15 min. For microstructural analysis by OM, a chemical etching was then performed by applying a Keller reagent (2.5 mL HNO_3 1.5 mL HCl 1 mL HF 95 mL Distilled Water) during 2 – 6 seconds and electro-etching in barker reagent using 25V and 0.8-1.4 A between 30 – 45 seconds at 17 – 21°C.

3.5.2. Optical and electron microscopy

The samples produced in the preliminary tests and the LPBF parts were analyzed by optical microscopy (OM; Carl Zeiss Observer Z1m microscope and Olympus BX41M-LED microscope), scanning electron microscopy (SEM; Tescan Mira 3 microscope and a Quanta 400 microscope) with an energy dispersive X-ray spectroscopy (EDX; EDAX Octane Plus) detector, and transmission electron microscopy (TEM; FEI TECNAI G² F20 HRTEM with a FEG source operating at 200 kV). The samples produced in the preliminary tests, i.e. AMI, SC, and LR, as well as directionally solidified samples were analyzed on the transverse and longitudinal midsection. The samples produced by LPBF were sectioned into several parts in relation to the solidification direction in order to have a larger analysis area and better statistics.

Analyzes using SEM and TEM techniques were reserved for promising samples obtained using different processing conditions, i.e. samples of candidate compositions manufactured with the best processing parameters or with microstructural characteristics that are relevant to be analyzed in this study, e.g. regions with the intermetallic formation and possible defects such as cracks and porosities.

These techniques allowed the analysis of the microstructural variation in LPBF parts as well as the fractography analysis of parts subjected to tensile tests. The SEM-EDX technique was used to determine the composition of intermetallic phases and the distribution of the alloy elements within the microstructure. Electron backscatter diffraction (EBSD) measurements were carried out to define the microstructural characteristics like the texture and misorientation of grains in LPBF parts.

In addition, TEM analysis was applied to study and determine the crystal structure of the intermetallic phases and their coherence with the matrix. The samples were cut into sheets just over 1 mm thick. Subsequently, the samples were roughened with #1200 and #2000 SiC paper until obtaining a thickness close to 0.05 mm. Subsequently, a final finishing using 1 µm diamond paste and colloidal silica of 0.25 µm was carried out. Between each stage, the samples were cleaned by ultrasound for 5 - 10 min. Next, the samples were drilled in a precision ion polishing system (PIPS, gatan 691) using a beam energy of 5 KeV, a current of 0.1 µA and a sample rotation speed of 1 rpm.

3.5.3. Density and presence of defects

The relative density/porosity and length/density of cracks in the parts built by LPBF and conventional methods were determined from image analysis using the free software ImageJ [153]. For this, the cubes produced by LPBF were cut into different sections and the entire area of the sections was analyzed. During the density/porosity measurement, the presence of cracks was not considered, only the presence of pores and lack-of-fusion defects.

3.5.4. X-ray diffraction

The phase constitution of the parts produced in this work was evaluated by X-Ray Diffraction (XRD), using a Bruker – D8 Advance ECO diffractometer equipped with Cu-Kα radiation (Kα, λ = 1.5418 Å) and 2θ = range of 20 °– 90 °, stepsize of 0.02 ° and 1 second per step. The database used to analyze the XRD patterns was obtained from COD (Crystallography Open Database) and ICSD (Inorganic Crystal Structure Database). Additionally, the most relevant samples

for this research, e.g. gas atomized powder samples or LPBF samples, were analyzed by XRD–synchrotron (PETRA III, beamline P02.1, Deutsches Elektronen-Synchrotron (DESY), Germany). The measurements were carried out applying an energy density of 60 keV and the beam wavelength was 0.207363 nm. The sample–detector distance was set up at 1010 mm. The data were processed using DAWN Software (Diamond Data Analysis Workbench). This technique allows for obtaining XRD patterns with a lower noise density, facilitating the characterization of the phases present in the samples.

3.5.5. Differential Scanning Calorimetry

Differential Scanning Calorimetry (DSC) measurements were also performed in a Netzsch DSC-404 equipment under an N_2 atmosphere and using alumina crucibles. Samples of approximately 10 mg were heated from 25 to 780 °C at a heating rate of 10°C·min^{-1}.

3.6. Mechanical tests

The samples produced in this work were analyzed by microhardness tests in an EMCO-TEST Durascan machine (Zwick/Roell, Austria) applying a force of 200 gf for 15 seconds. The results obtained helped to determine a combination of parameters that favors building parts with high density and high mechanical strength. From the selection of the ideal processing parameters, compression test specimens were built with inclinations of 0 °, 45 °, and 90 ° concerning the build direction. Due to insufficient raw material, according to the LPBF machine requirements, the samples for tensile testing were built only horizontally (0°). The tensile and compression tests were carried out on Instron 5500R and 5900R universal machines, respectively, using a video extensometer in both cases. For both mechanical tests, it was applied a crosshead speed of 3 mm·min^{-1} according to ASTM E8-16 and ASTM E9-09, respectively. At least 3 replicates were carried out for each sample/condition.

Apart from the LPBF samples designed for compression and tensile testing, we also fabricated samples through directional solidification and

graphite/copper mold casting for comparison purposes. Due to the dimensions of certain samples from these processes, cylindrical samples were exclusively produced for the parts made via LPBF and cast in a graphite mold for tensile tests. Furthermore, rectangular geometry samples were generated for tensile testing across all conditions. The dimensions of the compression and tensile specimens (with a rectangular and cylindrical geometry) are presented in **Figure 3.2**.

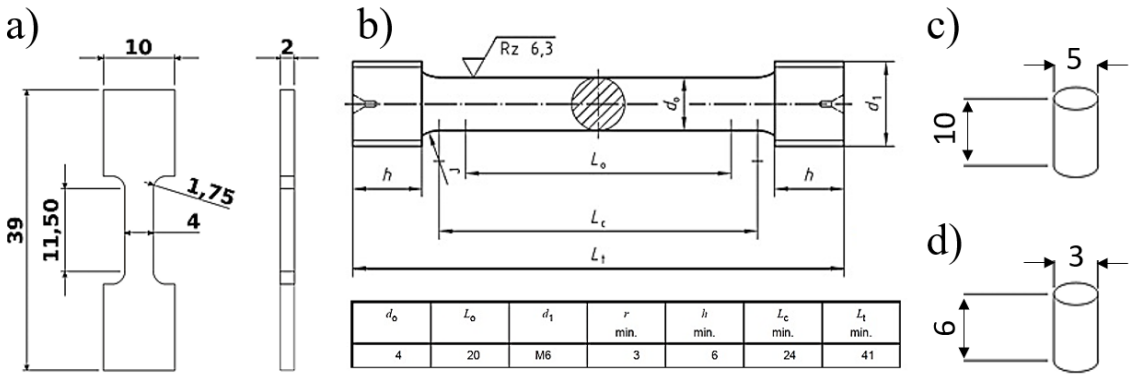

d_o	L_o	d_1	r min.	h min.	L_c min.	L_t min.
4	20	M6	3	6	24	41

Figure 3. 2 – Dimensions of the samples used for tensile and compression tests. In a, b) tensile test and c, d) compression test samples geometries. All the dimensions are represented in milimeters (mm).

4. RESULTS AND DISCUSSION

4.1. Preliminary tests

4.1.1. CALPHAD calculations

The thermodynamic calculations allowed to observe the influence of the different elements that make up the AA2017 alloy (*see* ***Table* 2.2**), as well as the addition of other alloying elements, on the solidification range of the alloy. The construction of phase diagrams as presented in **Figure 4.1**(**a**, **b**) facilitated the process of the selection of promising compositions for this work. Candidate compositions are shown in **Table 4.1**.

Table 4. 1 – Candidate compositions (in wt.%) obtained from thermodynamic calculations.

Alloy (wt.%Ce)	Cu	Si	Mg	Mn	Cr	Fe	Ti	Ce	Al
AA2017_0Ce *	4.0	0.6	0.6	0.7	0.1	0.35	0.15	0.0	bal.
AA2017_1Ce	4.0	0.6	0.6	0.7	0.1	0.35	0.15	1.0	bal.
AA2017_3Ce	4.0	0.6	0.6	0.7	0.1	0.35	0.15	3.0	bal.
M0_0Ce	3.75	0.4	0.8	0.6	0.0	0.0	0.0	0.0	bal.
M0_1Ce	3.75	0.4	0.8	0.6	0.0	0.0	0.0	1.0	bal.
M0_3Ce	3.75	0.4	0.8	0.6	0.0	0.0	0.0	3.0	bal.
M1_0Ce	3.75	0.4	0.8	0.6	0.0	0.0	0.1	0.0	bal.
M1_1Ce	3.75	0.4	0.8	0.6	0.0	0.0	0.1	1.0	bal.
M1_3Ce	3.75	0.4	0.8	0.6	0.0	0.0	0.1	3.0	bal.

* Original composition based in [76].

M0 and M1 based compositions were produced solely by modifying the concentration of each of the different elements that form the AA2017 alloy within the range established in **Table 2.2**, i.e. without adding any other element. In this sense, both M0 and M1 can still be considered as the AA2017 alloy. The difference between M0 and M1 is the addition of Ti, where M0 is Ti-free, while M1 presents an addition of 0.1 wt. %Ti. The three base compositions, AA2017,

M0, and M1, were modified with the addition of 1 and 3 wt. %Ce. The addition of this element allowed an optimal reduction of the solidification range as observed in **Figure 4.1**(**c**, **d**).The different candidate compositions were named according to their Ce concentration (in wt.%), e.g. for AA2017-based compositions, they were differentiated as AA2017_0Ce, AA2017_1Ce, and AA2017_3Ce when 0, 1, and 3 wt. %Ce is added, respectively. The same nomenclature was applied to proposed compositions M0 and M1. Next, the methodology used to select each of the compositions presented in **Table 4.1** will be explained.

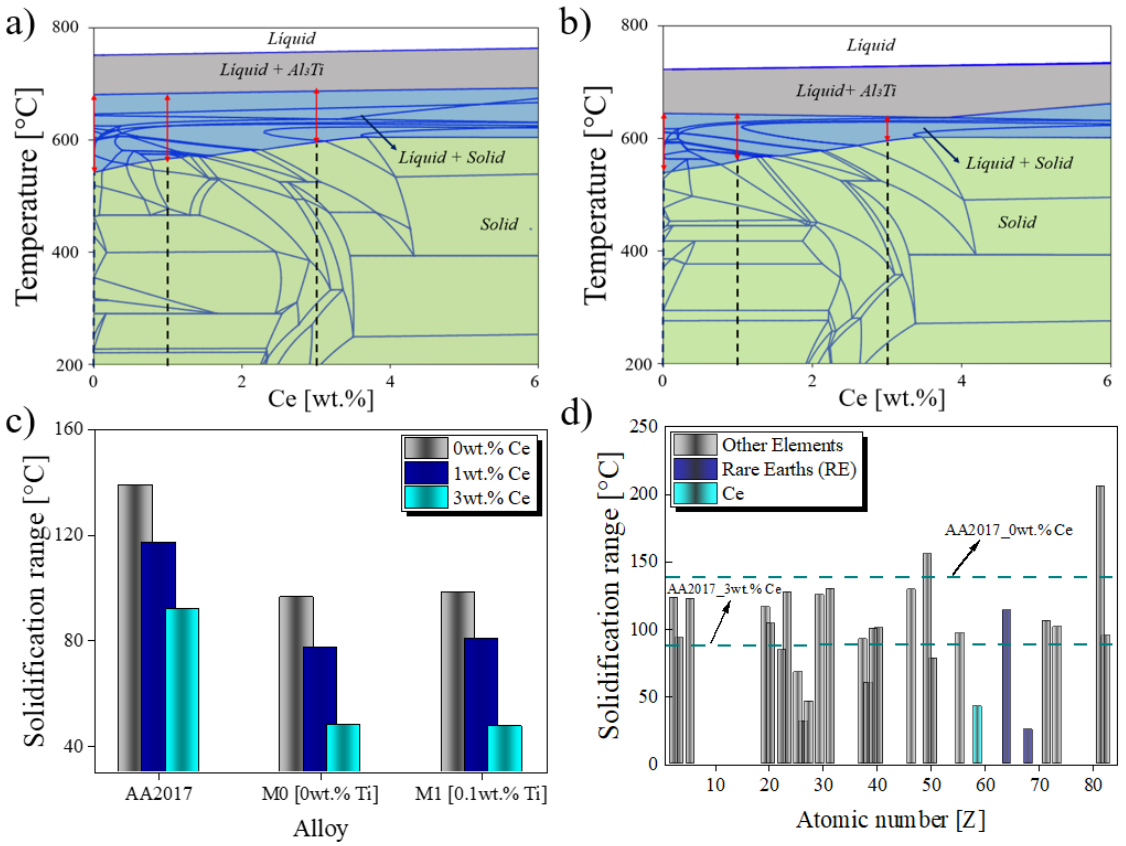

Figure 4. 1 – Pseudo-binary diagrams AA2017 / M1 vs Ce (in wt.%) and solidification ranges obtained from thermodynamic calculations by the CALPHAD method. In Figure 4.1(a) Pseudobinary phase diagram AA2017 vs Ce and Figure 4.1(b) Pseudobinary phase diagram M1 vs Ce. In Figure 4.1(c) the solidification range obtained for the alloys AA2017, M0, and M1, modified with 0, 1, and 3 wt.%Ce, were defined disregarding the formation of the Al_3Ti phase (dispersoid). In Figure 4.1(d) a comparative bar graph of the influence of the addition of 3 wt.%Ce in the alloy M1 in comparison with adding 3 wt.% of other elements

presented in the PanAl2021 database, including Er and Gd (dark blue) as rare earth (RE). For Figure 4.1(a, b): the gray area represents the zone where only the liquid + Al_3Ti phases coexist; the area highlighted in dark blue shows the zone where liquid + other phases (including α-Al FCC phase) occur; and the area highlighted in green is the free-liquid zone.

It was observed that by varying the percentage of each element that form the AA2017 alloy, the solidification range can be decreased from 140°C to 90°C. The presence of elements such as Si and Cu in the alloy increases the solidification range and increases the HCS as reported by Yan and Lin [154] for the binary Al-Cu and Al-Si alloys.

The presence of Fe and Cr promotes phases in the form of $Al_{13}M_2$ and $Al_{13}M_4$ (M = Cr, Fe) with a higher melting point than α-Al FCC, as observed in **Figure 4.2**. Althought these crystalline phases have been considered dispersoids in AA6061 parts processed by conventional casting [155], in this work, these phases are unable to act as inoculant agents, mainly due to their proximity to the formation temperature of the α-Al FCC phase and its dissolution during solidification process, favoring the formation of new secondary phases [156-158]. Therefore, the removal of these elements favors a reduction in the HCS.

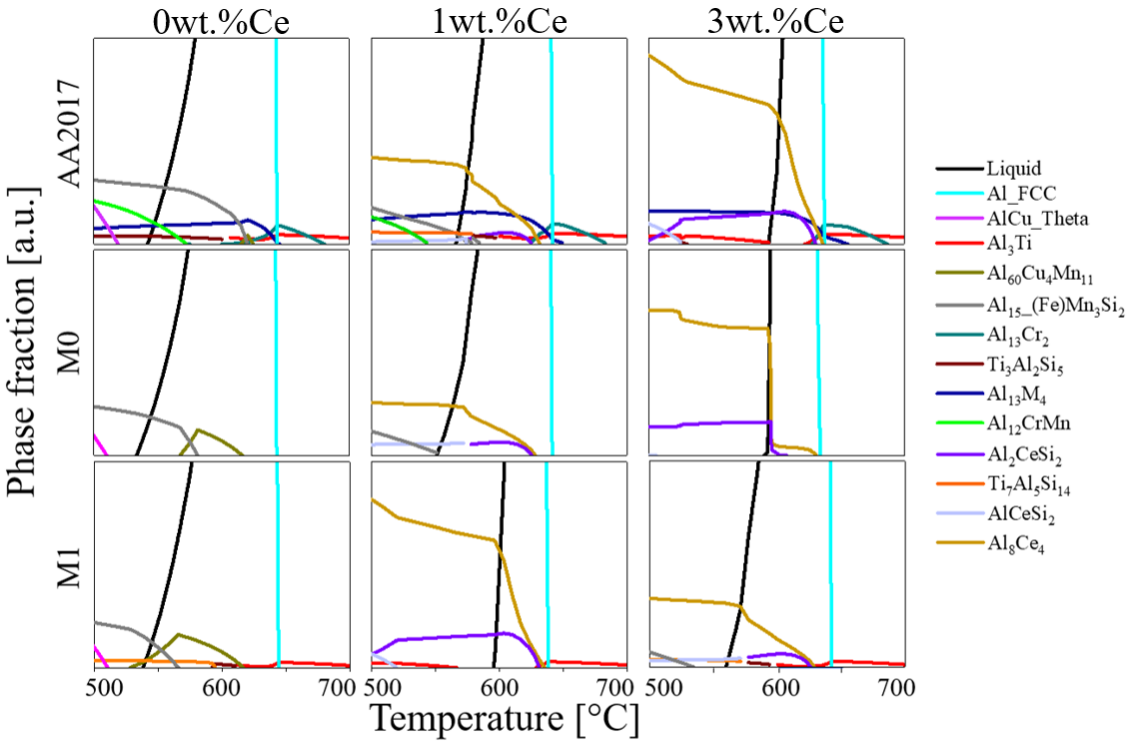

Figure 4. 2 – Equilibrium volume phase fraction calculated between 500 °C and 700 °C using Pandat software and the PanAl2021 database. The thermodynamic calculations were developed for the AA2017–, M0–, and M1–based compositions with the addition of 0, 1, and 3 wt. %Ce.

The addition of other elements, external to the original composition of AA2017, can favor a further reduction in the solidification range. The data obtained bia Pandat software show Ce is an optimal candidate to modify the AA2017 composition. The addition of 3 wt. %Ce in the modified AA2017 composition exhibits a solidification range of up to 45 °C (**Figure 4.1**(**c**-**d**)) and promotes a “eutectic–like” solidification during the final stage of solidification. Although Gd favored a much smaller interval (25 °C, as shown in **Figure 4.1**(**d**)), Ce is the most abundant and cheapest element among the rare earth [159]. The total abundance in the Earth's crust of Ce (63 ppm) exceeds the concentrations of other alloying elements such as Cu (28 ppm), making it an excellent candidate to be applied in the modification of aluminum alloys [159]. For this reason, this element was selected to be added to the compositions of this work in concentrations of 0, 1, and 3 wt. %Ce.

Figure 4.3 shows the Scheil-Gulliver curves for the nine (9) compositions proposed. The AA2017 composition usually has a maximum content of 0.15 wt.%Ti [76]. The presence of Ti in the AA2017– and M1–based compositions favor the formation of the Al_3Ti phase in the initial solidification stage and promotes solidification by heterogeneous nucleation, which allows for obtaining a more refined structure and reduces the residual stresses caused during solidification, minimizing cracking probability [160]. Nevertheless, as seen in **Figure 4.3**(**a**, **c**), the fraction of Al_3Ti produced is minimal due to the low Ti content in the alloy. Likewise, it has been reported that the addition of Ce can inhibit the refining effect of Ti during the solidification process [161]. For this reason, this work established two base compositions (M0 and M1) to determine if there is any effect on the microstructure that can be generated by the interaction of these elements.

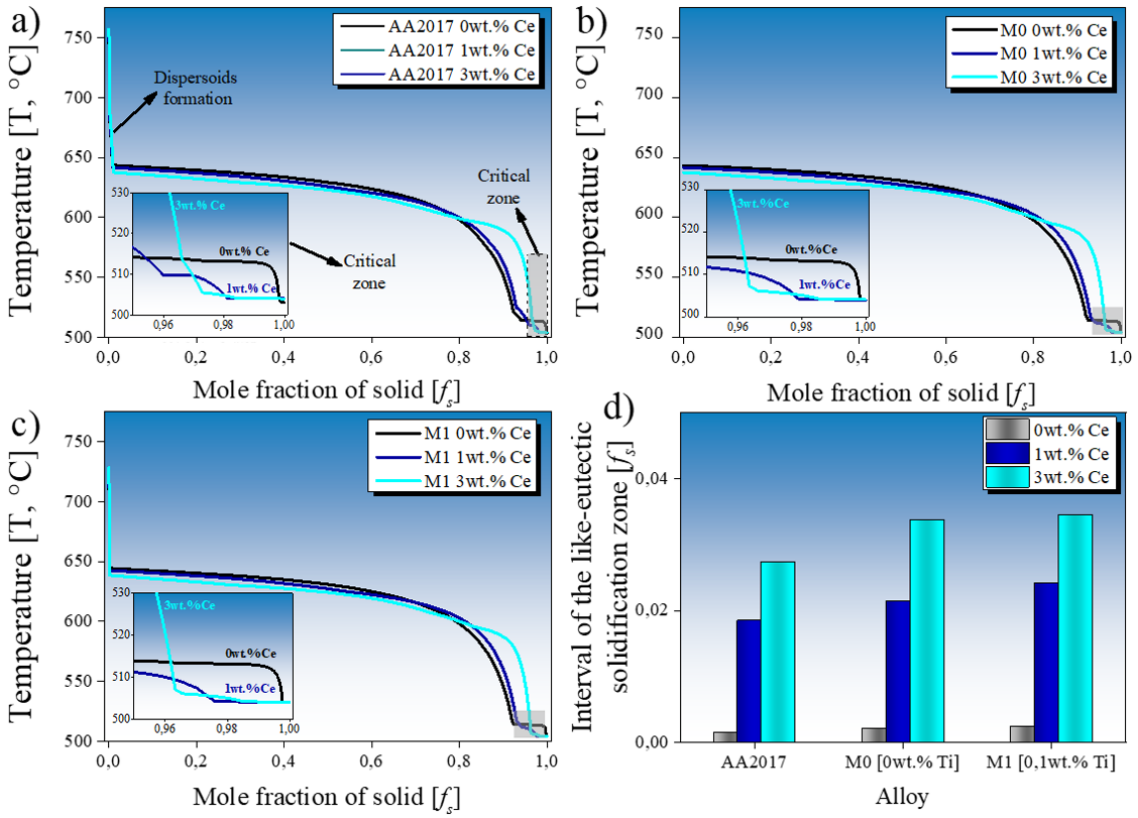

Figure 4. 3 – Scheil–Gulliver curves of the AA2017 (Figure 4.3(a)), M0 (Figure 4.3(b)), and M1 (Figure 4(c)) alloys with the addition of 0, 1, and 3 wt.%Ce. The insets at the bottom left of the Figures 4.3(a – c) show the critical solidification

zone. The solidification range of the eutectic-like zone in solid fraction [f_S] is shown in (Figure 4.3(d)).

The modification of the AA2017 alloy by adding Ce allows obtaining a reduction of the temperature range during the final stage of solidification, due to the formation of a "eutectic–like" solidification zone in the final stage of solidification, composed of phases α-Al FCC +Al_8RM_4 (RM = Ce; i.e. Al_2Ce, space group $Fd\bar{3}mS$ (227), structure type Cubic $MgCu_2$ [162]) according to thermodynamic calculations (*see* ***Figure 4.3***). An increase in the concentration of Ce within the compositions favors an increase in the range of the " eutectic–like" solidification zone (**Figure 4.3**(**d**)), increasing the amount of liquid to fill cracks. The literature reports that adding Ce in aluminum alloys favors the formation of other eutectic promoter phases, such as $Al_{11}Ce_3$ [121], Al_8Cu_3Ce [122, 163], and Al_4Ce [122, 163]. Nevertheless, these phases were neglected in the thermodynamic calculations due to the presence of Si, favoring the formation of secondary Al-Ce-Si phases.

The Scheil-Gulliver curves allow the HCS of an alloy to be determined. For instance, the effect of Si and Cu on the HCS for the AA2017 composition is shown in **Figure 4.4**. A useful index to determine the HCS of an alloy has been proposed by Sindo-Kou [79], which can be extracted from the Scheil-Gullive curves through the following mathematical relationships:

$$\left|\frac{\delta T}{\delta (f_S)^{\frac{1}{2}}}\right| = \frac{2\cdot(1-k)\cdot(T_M-T_E)\cdot\sqrt{f_S}}{1-f_S} \quad (1),$$

$$k = \frac{C_S}{C_L} \quad (2),$$

$$C_L = C_0(1-f_S)^{k-1} \quad (3).$$

Where C_L, C_S, and C_0 are the concentration of liquid, solid and the nominal composition, respectively; T is the analyzed temperature; T_M is the *liquidus*

temperature of the alloy, T_E is the eutectic temperature, and k is the partition coefficient.

Figure 4.4 shows the interaction of Cu and Si on the HCS of the AA2017 alloy. The solubility range of both elements (3.5 - 4.5 wt. %Cu and 0.2 - 0.8 wt. %Si) in aluminum favors an increase in the solidification range and increases the HCS as shown in **Figure 4.4**(**a**). A composition rich in Cu (4.1–4.3 wt.%) shall favor a higher HCS as observed in **Figure 4.4**(**b**). In contrast, the application of 0.2–0.5 wt. %Si and 3.6–3.8 wt. %Cu, **Figure 4.4**(**b**), favors a significant reduction of HCS, still maintaining sufficient content of these elements to form secondary phases that allow reinforcing the matrix by applying heat treatments (Al_2Cu). This behavior has also been observed in the alloys AA2024 [164], Al-4Cu-2Si [165], and AA6000 [166].

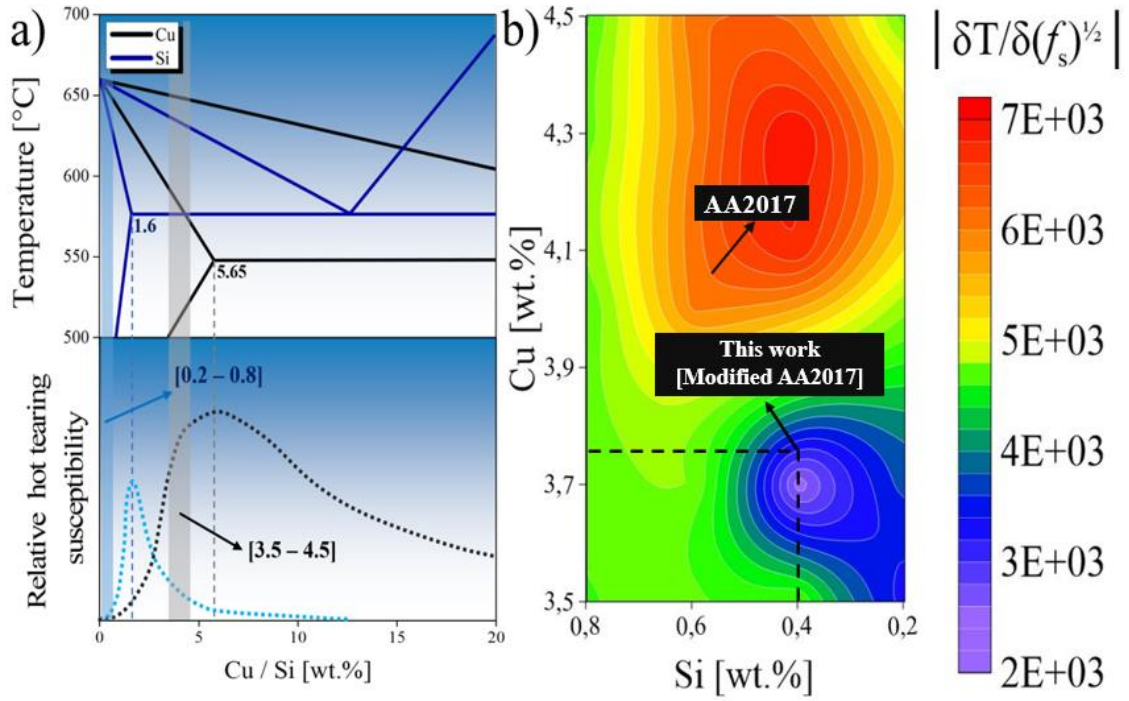

Figure 4. 4 – Effect of Cu and Si on the HCS of the AA2017. In a) a schematic figure of the influence of Cu (in black) and Si (in blue) on the relative HCS. In b) the HCS behavior for the AA2017 alloy (composition based on Table 4.1, AA2017_0Ce*), when the Cu/Si concentration is varied, considering the Al as the balance element.

Figure 4.5 shows that the initial modification of the composition of AA2017 and the subsequent addition of Ce allow a significant HCS reduction compared with other 2xxx alloys.

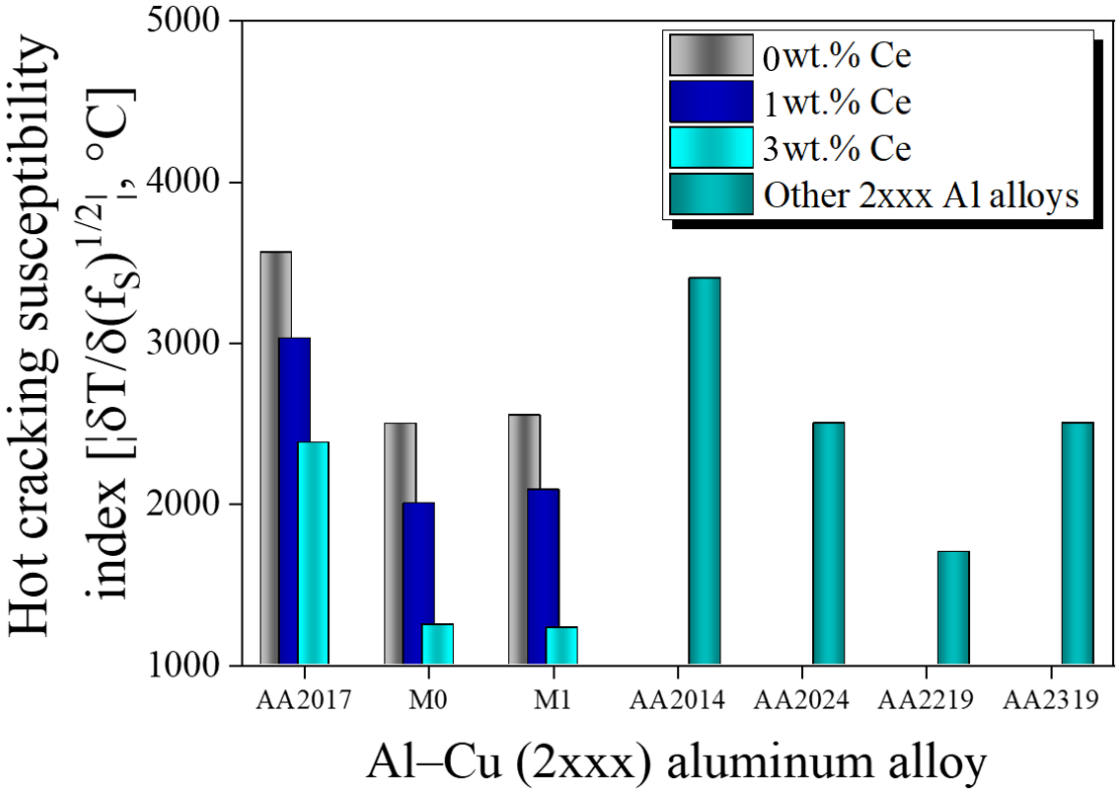

Figure 4. 5 – Hot tear susceptibility of Al–Cu-based aluminum alloys (2xxx series). The maximum steepness |dT/d(fs)½| was obtained from Scheil – Gulliver curves calculated by the CALPHAD method. The values of the AA2017, M0, and M1 aluminum alloys modified with 0, 1, and 3 wt. %Ce was calculated in this work. The values for the AA2017, AA2024, AA2219, AA1319 were obtained from [79, 167].

4.1.2. Validation of promising compositions

The nine proposed compositions, selected from the thermodynamic calculations, were produced using the AMI, SC and LR techniques, ensuring

different cooling rates, as explained in ***Section 3.1***. The results of the samples' characterization are presented below.

4.1.2.1. Samples produced in AMI and SC condition

Figure 4.6 shows the OM images for samples subjected to a relatively low cooling rate (AMI samples, <100 °C·s^{-1} [168, 169]). The microstructural characteristics of the samples are presented in **Table 4.2**. In this work, the upper part of the ingot was analyzed, which presents a lower cooling rate since it is not in contact with the copper base of the furnace. The samples present coarse microstructure of solidification heterogeneously distributed due to the low cooling rates applied during solidification.

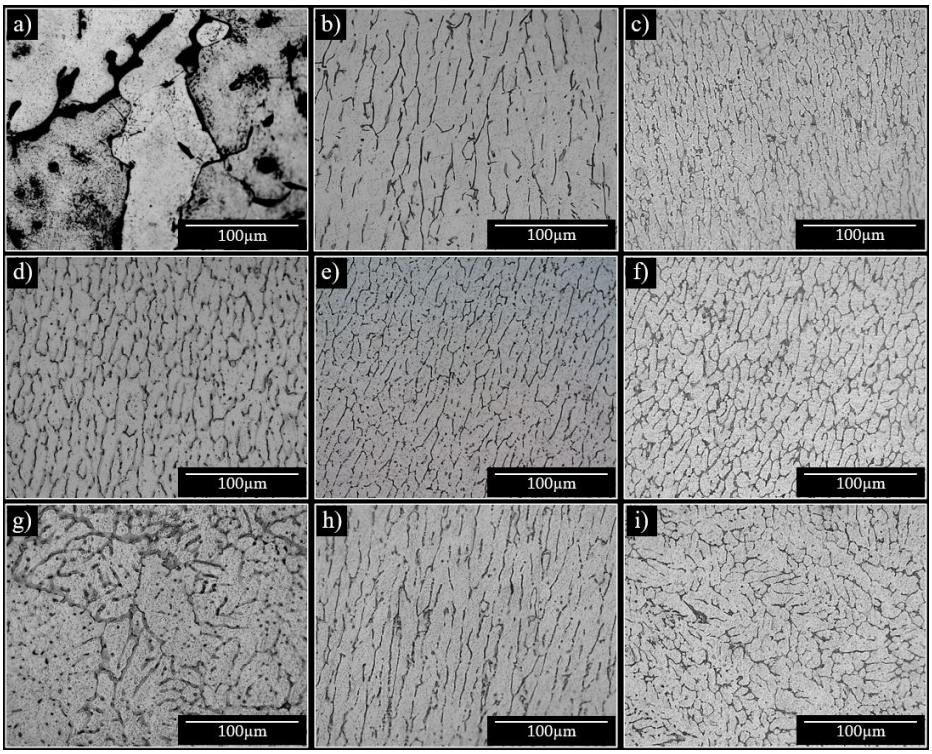

Figure 4. 6 – Optical microscope images at 500X of the solidification microstructure obtained for the AA2017 (a–c), M0 (d – f), and M1 (g – i) alloys under low cooling rate in AMI condition. The alloys were modified by adding Ce in 0 wt.% (a, d, g), 1 wt.% (b, e, h), and 3 wt.% (c, f, i).

Table 4. 2 – Mean grain size of alloys processed by low (AMI) and moderate (SC) cooling rates.

Composition	Grain size [µm]		Internal structure size [µm]	
	AMI	SC	AMI	SC
AA2017_0Ce	786±76	414±188	113±64	35±13
AA2017_1Ce	491±106	316±197	51±11	21±2
AA2017_3Ce	375±36	284±174	22±4	18±3
M0_0Ce	468±95	285±119	56±7	23±4
M0_1Ce	321±37	269±86	25±5	18±2
M0_3Ce	327±11	261±84	11±3	14±2
M1_0Ce	284±59	96±90	58±23	25±7
M1_1Ce	232±23	107±43	42±9	20±3
M1_3Ce	128±15	94±54	28±9	16±6

The AA2017_0Ce sample presents a predominant dendritic structure, with an average grain size of 786 ± 76.1 µm. In contrast, the M0_0Ce and M1_0Ce samples present dendrites with smaller secondary arms and with growth in the direction of heat extraction (copper baseplate). The addition of Ti in the M1 composition favors obtaining a more refined microstructure compared to the M0 samples, demonstrating the effectiveness of Ti as a refining agent due to the formation of Al_3Ti [112].

The addition of 1 wt. %Ce in the different compositions makes it possible to obtain a structure of elongated and slightly more refined columnar grains that grow in the direction of heat extraction with some secondary arms in the same direction. When the addition of Ce increased to 3 wt. %, the microstructure becomes more refined, with smaller columnar dendrites and more secondary arms compared to samples modified with 1 wt. %Ce.

Figure 4.7 shows the microstructure obtained in samples processed by SC (10^2 -10^3 °C·s^{-1} [150]). The microstructural characteristics are presented in **Table 4.2**. An increase in the cooling rate favors obtaining a more refined microstructure and the formation of microstructured with a mixture of cells and

dendrites. Ce-free samples produced by SC show a refinement between 40 – 50 % in relation to samples produced by AMI, while the refinement observed in samples with 1 wt. %Ce (9.8 – 35.6 %) and 3 wt. %Ce (20.3 – 24.3 %) is significantly lower. This may be because the Ce-containing samples already had a considerably refined microstructure. The microstructure of the candidate compositions is characterized by being of the dendritic columnar type with growth in the direction of heat extraction (walls of the copper mold).

The grain refinement in the compositions with the addition of Ce is attributed to the formation of the $Al_{11}Ce_3$ phase, which can act as a dispersoid during the solidification of the material [170, 171]. Likewise, the increase in constitutional undercooling at the solid-liquid interface due to an enrichment of Ce in the solidification front, inhibits the growth of α-Al grains. The supercooled liquid favors generating a greater number of nucleation points due to the difficulty of releasing the latent heat generated during the formation of dendrites, which are forced to contract and melt [170]. The formation of a eutectic liquid allows the α-Al phase to form within it to act as nucleation points for the primary phase in a similar way to that reported in A356 samples modified with La-Ce and processed by electromagnetic stirring [172].

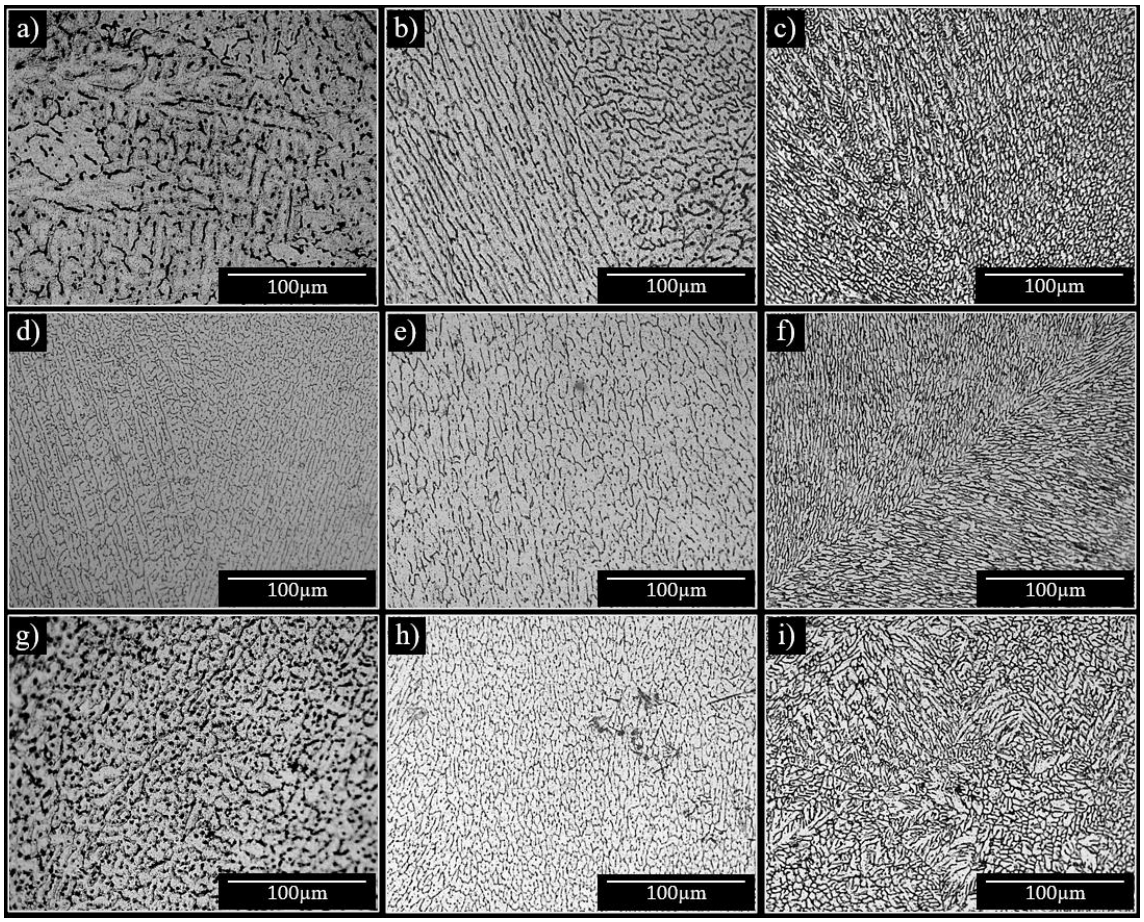

Figure 4. 7 – Optical microscope images of the solidification microstructure obtained for AA2017 (a–c), M0 (d – f), and M1 (g – i) alloys processed by suction casting. The alloys were modified by adding Ce in 0 (a, d, g), 1 (b, e, h), and 3 wt.% (c, f, i).

4.1.2.2. Samples produced in LR condition

In order to simulate the inherent dynamic conditions of the LPBF process, samples processed by SC were laser remelted. The single-track samples obtained by LR underwent high cooling rates (10^5 – 10^8 °C·s^{-1} [173]), which favors obtaining a highly refined structure. Unlike the samples processed in AMI and SC conditions, the samples processed by LR show the formation of intergranular cracks within the remelted area and around the heat-affected zone. The microstructure obtained in each of the 9 candidate compositions is presented in **Figure 4.8**. Likewise, the values of the mean grain size and the crack density are presented in **Table 4.3**.

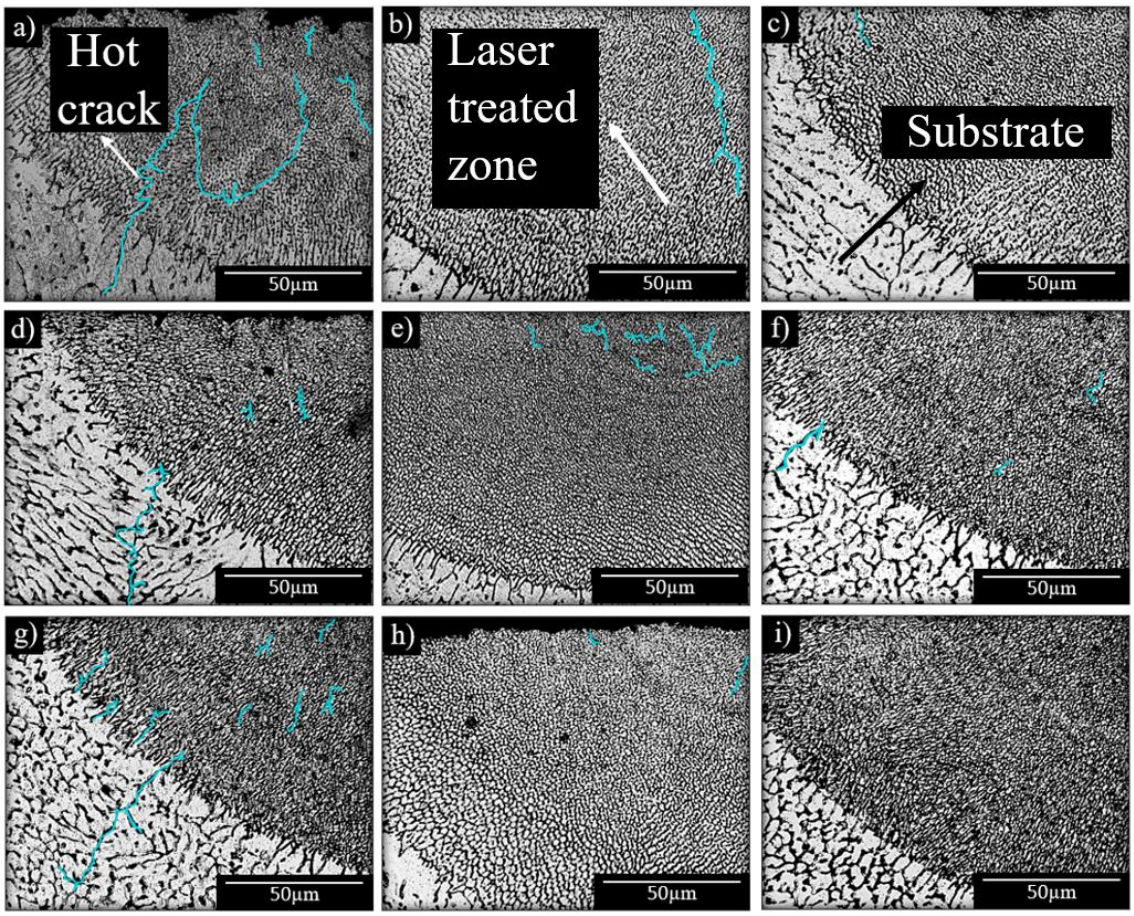

Figure 4. 8 – Optical microscope images of the solidification microstructure obtained for AA2017 (a–c), M0 (d – f), and M1 (g – i) –based compositions after laser remelting. The alloys were modified by adding Ce in 0 wt.% (a, d, g), 1 wt.% (b, e, h), and 3 wt.% (c, f, i). The cracks are highlighted in blue.

Table 4. 3 – Mean grain size and hot cracking density of alloys processed in the LR condition.

Composition	**Grain size** [**μm**]	**crack density** [**μm·μm^{-2}**]
AA2017_0Ce	6.43±0.3	49.84±1.12
AA2017_1Ce	5.81±0.2	25.71±0.98
AA2017_3Ce	3.92±0.2	10.22±0.78
M0_0Ce	3.88±0.1	12.13±1.00
M0_1Ce	2.90±0.8	6.63±0.90
M0_3Ce	1.65±0.4	4.00±0.71
M1_0Ce	3.61±0.9	7.24±0.90
M1_1Ce	3.17±0.9	2.74±0.70
M1_3Ce	2.07±0.5	No cracks

The high cooling rates achieved by the laser remelting process induce 27 to 198 times greater grain refinement compared to the grain size of samples in AMI condition, or 3.5 to 22 times more refined than AMI and SC samples. The histogram of the grain size distribution for each sample is shown in **Figure 4.9**. The initial modification of the composition of AA2017 allows for obtaining more homogeneous and refined microstructures. The grain refinement is increased by the addition of Ce and allows a reduction of the HCS. For the composition M1_3Ce, the samples did not show cracks, as observed in **Figure 4.8**(**i**). Therefore, this alloy was analyzed in greater detail.

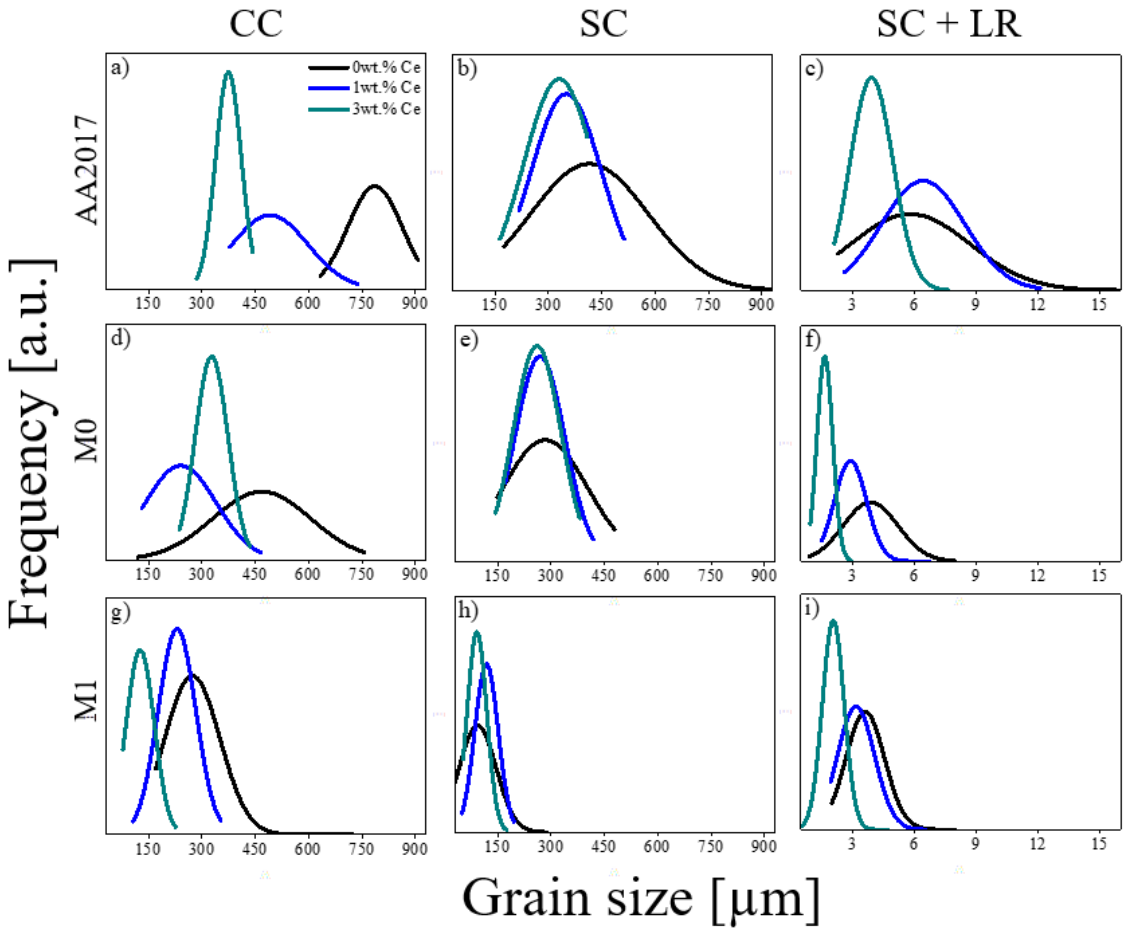

Figure 4. 9 – Distribution of the grain size of the AA2017 (a–c), M0 (d – f), and M1 (g – i) compositions processed in AMI (a, d, g), SC (b, e, h), and LR (c, f, i) condition.

4.1.3. Thermal, microstructural and mechanical characterization of samples produced in AMI, SC, and LR conditions

4.1.3.1. DSC analysis

Figure 4.10 shows the DSC cooling and heating curves obtained for the compositions proposed in **Table 4.1**. No significant differences were observed in the DSC curves for samples processed in different conditions, for which reason only the DSC curves for SC samples are presented.

The Ce-free compositions show the presence of a single peak between 652 °C and 650 °C, corresponding to the solid-liquid transition due to the

formation of the α-Al FCC phase. The composition AA2017_0Ce shows a second exothermic peak between 517 °C and 525 °C, which corresponds to the formation of Al-Cu-type precipitates. The presence of this peak was observed only during the cooling process. This is mainly because the high cooling rates used in the SC process can prevent the formation of precipitates from [149][150], favoring the presence of a more saturated matrix. The formation of two peaks in the samples contaminated with 1 and 3 wt.% Ce reflects the presence of a "eutectic–like" region, which is crucial in this work since it guarantees the presence of a greater amount of liquid during the final stage of solidification that reduces the HCS.

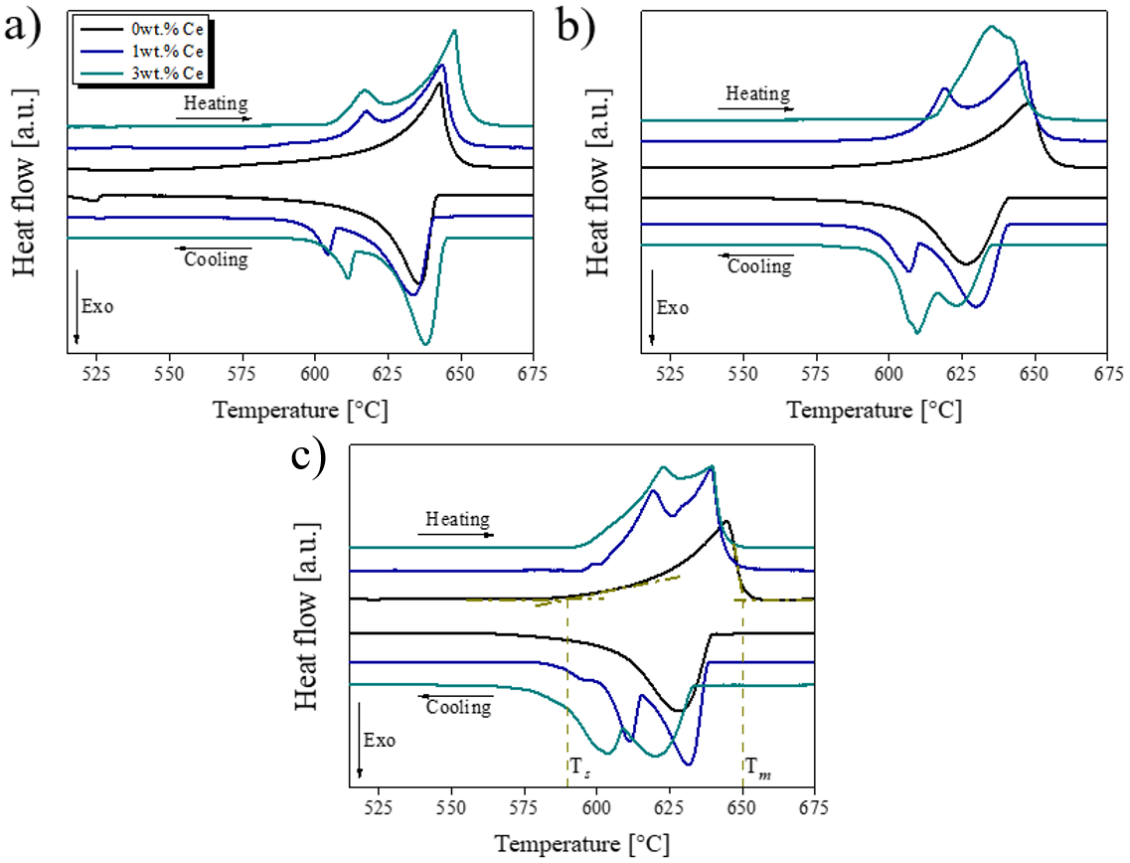

Figure 4. 10 – DSC curves of the AA2017 (Figure 13(a)), M0 (Figure 13(b)), and M1 (Figure 13(c)) compositions modified by adding 0, 1, and 3 wt.%Ce and processed by suction casting.

4.1.3.2. XRD analysis

The phases formed in the 9 proposed compositions, produced using the three different processes, were analyzed by XRD. Considering that single-track LR samples have an insufficient area to be analyzed by XRD, superficially remelted samples were produced and analyzed. The laser remelted tracks in the LR samples presents a negligible area to be able to be analyzed by XRD. For this reason, samples in SC condition were laser remelted in a 4 mm x 10 mm area with a 100 µm hatch between laser tracks. This allowed obtaining enough area to be correctly analyzed by XRD. The results are shown in **Figure 4.11**.

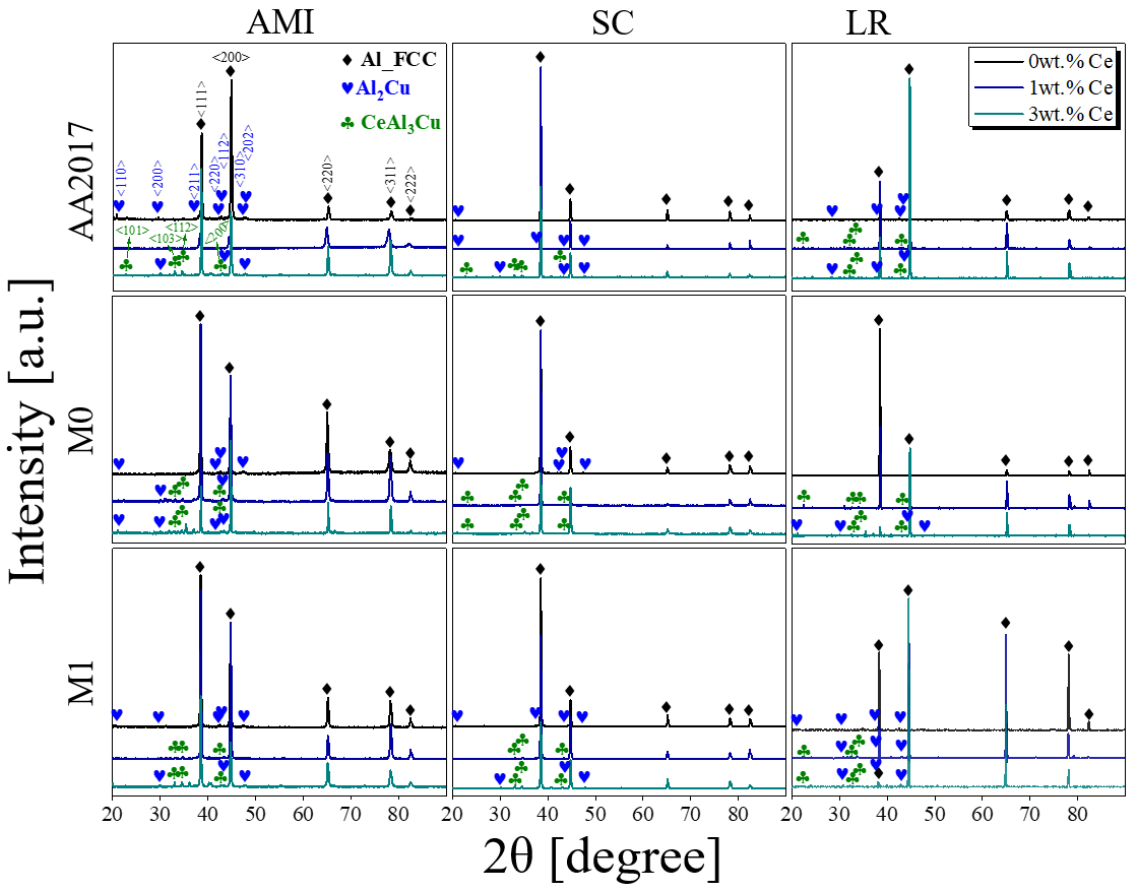

Figure 4. 11 – XRD patterns for AA2017 (a–c), M0 (d – f), and M1 (g – i) compositions modified with 0, 1, and 3 wt.%Ce. The compositions were processed in AMI (a, d, g), SC (b, e, h), and LR (c, f, i) conditions. The graph is plotted on a logarithmic scale.

All diffraction patterns show the main characteristic peaks of the α-Al FCC phase (ICSD n° 18839, space group $Fm\bar{3}m$ (225), Face Centered Cubic [174]).

The second phase peaks vary according to the Ce content and can be indexed as Al_2Cu_θ (ICSD no. 42517, space group I4/mcm (140), Tetragonal [175]) and Al_3CeCu (ICSD no. 190993, space group I4mm (107), structure type Tetragonal BaNiSn3 [176]) phases.

The data obtained do not show the presence of the phases predicted by thermodynamic calculations, nor the formation of other common phases in Al 2xxx alloys such as S (Al_2CuMg [30]), β″ (Mg_5Si_6 or $Mg_5Al_2Si_4$ coherent needles [177, 178]), β′ (semi-coherent $Al_3Mg_9Si_7$ rods [177, 178]), β (incoherent plate of Mg_2Si [177-179]), β* (Al_3Mg_2 [107, 180]), Q ($Al_5Mg_8Si_6Cu_2$, acicular or elliptical shape (2D) [179, 181]), and π ($Al_8FeMg_3Si_6$ [181]), which are quite common in Al-Cu base alloys processed by conventional manufacturing methods [149].

Although the thermodynamic calculations carried out establish that the eutectic region should be composed mainly of the Al + Al_8RM_4 phases, various authors report that the eutectic region can be composed of other phases formed from the addition of Ce, as shown in **Table 4.4**. Likewise, the presence of Si offers the possibility of producing a second eutectic in the form of α-Al FCC + Si or α-Al FCC + Mg_2Si, typical of Al-Si and Al-Mg-Si alloys [182], as well as the formation of the $CeAl_4Cu_2Si$ [183].

In order to analyse the crystalline phases that make up the eutectic region, as well as the possible formation of other secondary phases, samples of the composition M1_3Ce were analyzed by SEM and TEM. Only the composition M1_3Ce was analyzed by these techniques because this composition showed the best behavior in this work since hot cracks were not observed.

Table 4. 4 – Eutectic compositions in aluminum alloys with Ce processed by LPBF.

Eutectic	**Alloy**	**Reference**
Al-$Al_{11}Ce_3$	Al-12Ce*	[121]
	Al–8Ce-10Mg	[184]
	AlCe10MgSi	[185]
	Al-7Ce-8Mg	[186]

	Al–3Ce–7Cu	[19]
	Al-10Ce	[138]
	Al–Ce–Mg	[187]
	Al–8Ce-10Mg	[188]
Al-Al_4Ce	Al-3.5Cu-1Ce-(0.27Zr)	[163]
	Al-9Cu-6Ce	[122]
Al-Al_8Cu_3Ce	Al-3.5Cu-1Ce-(0.27Zr)	[163]
	Al-9Cu-6Ce	[122]
	Al-9Cu-6Ce-(1Zr)	[189]
Al-Al_8Cu_4Ce	Al-9Cu-6Ce	[122]
	Al-3.5Cu-1Ce-(0.27Zr)	[163]
Al-$Al_{20}Mn_2Ce$	Al–10Ce-8Mn	[190]
	$Al_{92}Mn_6Ce_2$ (at. %)	[191]
Al-$Al_{13}CeMg_6$	Al-7Ce-8Mg	[186]
Al-$Al_{6.5}CeCu_{6.5}$	Al–3Ce–7Cu	[19]
Al-$Al_{20}Mn_2Ce$-$Al_{11}Ce_3$	Al–10Ce-8Mn	[190]
Al-$Al_{6.5}CeCu_{6.5}$-$Al_{11}Ce_3$	Al–8Ce-10Mg	[184]
Al-Al_8Cu_3Ce-Al_2Cu	Al-9Cu-6Ce-(1Zr)	[189]
Al-$Al_{11}Ce_3$-$Al_{13}Mg_6Ce$	Al–8Ce-10Mg	[188]
Al-Al_8Cu_4Ce-Al_8Cu_3Ce-Al_4Ce	Al-9Cu-6Ce	[122]
M1_3Ce	**Al-Al_3CuCe**	**This work**

*Processed in Laser Remelting condition

4.1.3.3. SEM analysis

Figure 4.12 shows the SEM EDX maps of the composition M1_3Ce processed in AMI condition. The formation of eutectic regions rich in Cu and Ce can be observed. Correlating this results with the XRD patters, the eutectic regions can be constituted mainly by Al + Al_3CeCu.

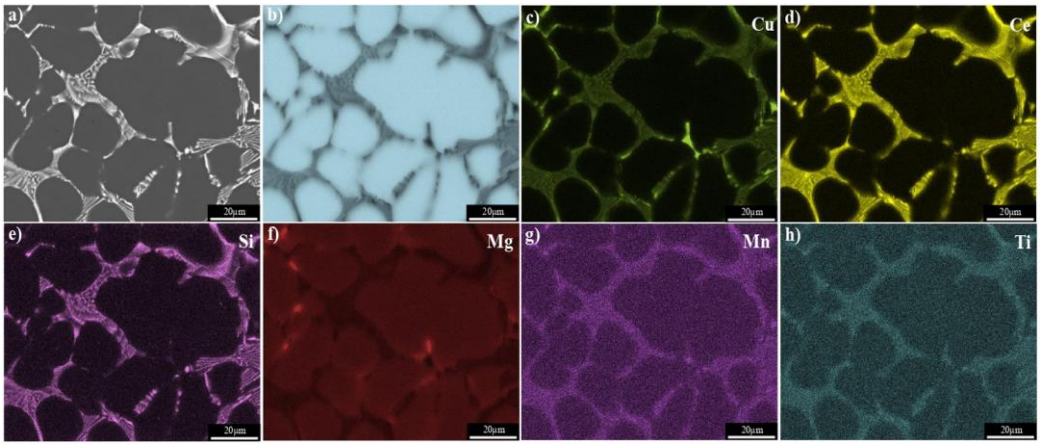

Figure 4. 12 – EDX mapping analysis of the M1_3Ce sample processed in AMI condition.

The EDX point analysis (**Figure 4.13**) reveals the possible formation of the Al_2Cu secondary phase. The presence of secondary phases glimpses the possibility of improving the mechanical properties of the alloy through the application of heat treatments [145]. EDX analyses show that the dendrites are mainly composed of the Al phase, while most of the alloying elements remain within the eutectic region. The dark region is composed mainly of Al, Mn, and Ti with a homogeneous distribution. On the other hand, the bright regions are mainly composed of Cu, Ce, and Si. The formation of other possible phases within the analyzed region was not observed.

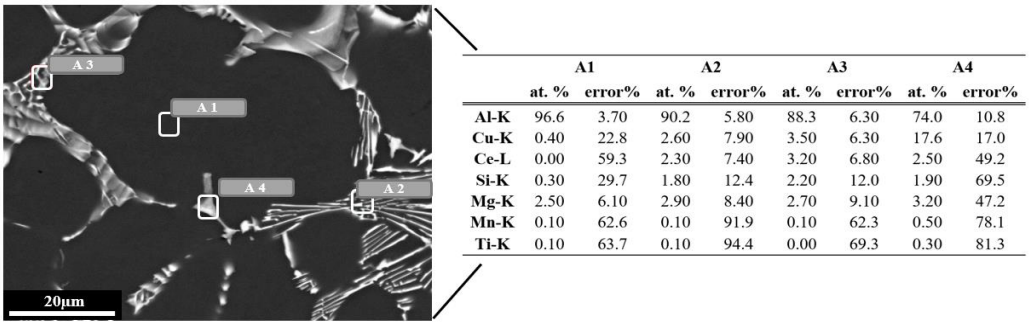

	A1		A2		A3		A4	
	at. %	error%	at. %	error%	at. %	error%	at. %	error%
Al-K	96.6	3.70	90.2	5.80	88.3	6.30	74.0	10.8
Cu-K	0.40	22.8	2.60	7.90	3.50	6.30	17.6	17.0
Ce-L	0.00	59.3	2.30	7.40	3.20	6.80	2.50	49.2
Si-K	0.30	29.7	1.80	12.4	2.20	12.0	1.90	69.5
Mg-K	2.50	6.10	2.90	8.40	2.70	9.10	3.20	47.2
Mn-K	0.10	62.6	0.10	91.9	0.10	62.3	0.50	78.1
Ti-K	0.10	63.7	0.10	94.4	0.00	69.3	0.30	81.3

Figure 4. 13 – EDX measurements in different regions of the area shown in Figure 4.12. The A1 zone corresponds to an Al-rich dendrite surrounded by eutectic regions rich in Cu, Ce, Mg, and Si according to the EDX measurements in the A2 and A3 zones. In the A4 zone can be observed an Al-Cu rich region.

4.1.3.4. TEM analysis

Bright-field TEM images and SAED patterns obtained for the M1_3 sample are presented in **Figure 4.14**. The results obtained revealed the presence of the quaternary phase $Al_{24}Cu_8Ce_3Mn$ (ICSD n° 1531015, space group $Pm\bar{3}m$ (221), type of Tetragonal structure $BaHg_{11}$ [192]), which was not previously detected by XRD, probably due to its low amount. Likewise, the Al3CeCu phase was detected by XRD and also by SAED, as shown in **Figure 4.14**(**a**, **b**). The detection of this phase by SEM-EDX, SAED-TEM, and XRD in the eutectic region, confirms that this region is mainly composed of Al + Al_3CeCu.

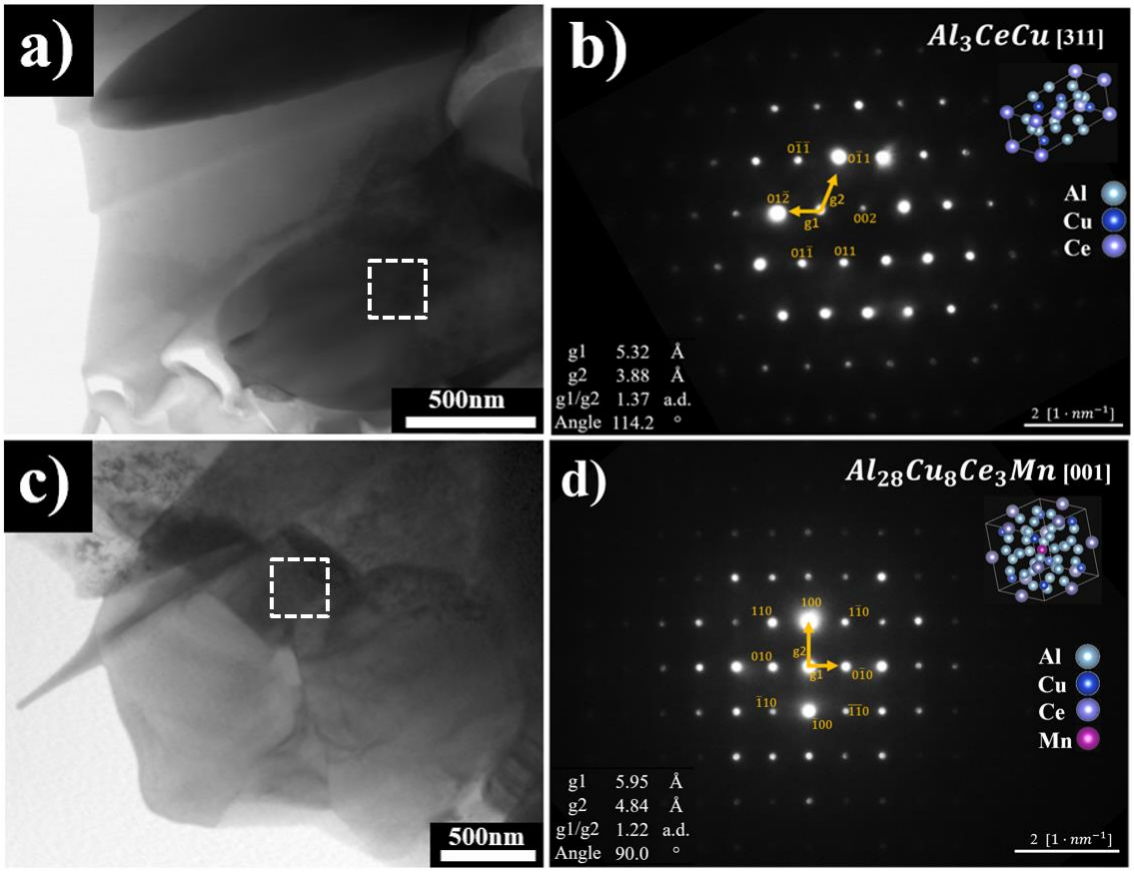

Figure 4. 14 – TEM images in bright field (BF) condition and select area diffraction patterns (SAED – TEM) obtained from the M1_3Ce samples processed by suction casting. In a, b) Al_3CeCu (ICSD n° 190993) and c, d) $Al_{28}Cu_8Ce_3Mn$ (ICSD n° 1531015) phases.

4.1.3.5. Microhardness behavior

The microhardness of the different compositions is presented in **Table 4.5**. It can be observed that the grain refinement caused by an increase in the cooling rate and the addition of Ce in the different compositions favors an increase in the hardness values. According to the Hall-Petch equation (**eq. 4**), YS (σ_y) for polycrystalline materials is inversely proportional to the grain size ($\sqrt{d}$) and directly proportional to the material constant (*k*). The friction stress (σ_0) depends on the material and not on the grain size [193].

$$\sigma_y = \sigma_0 + \frac{k}{\sqrt{d}} \quad (4)$$

Although it has been reported the formation of reinforcing secondary phases addition by adding low concentrations of Ce (between 0.2 and 0.45 wt.%) in Al-Cu-Mg-Ag base alloys [194], a higher concentration of Ce produce eutectic regions were a large part of Ce is concentrated (*see* ***Figure 23*** *and* ***Figure 24***), generating a reinforcement by Orowan's strengthening mechanism. The intermetallic phases produced during the solidification process act as pinning points for mobile dislocations, which surround the particle and increase the strength of the material [195]. Similar behavior has been reported in Al-Ce-Mn parts produced by additive manufacturing [190]. The addition of Ce also favors a grain refinement effect that improves the mechanical properties due to the larger grain boundary area and its interaction with dislocations. Likewise, the formation of eutectic regions and reinforcement secondary phases, mentioned in ***Section 4.1.3.3***, also generate a contribution to the increase in mechanical resistance [170-172].

Table 4. 5 – Microhardness values of AA2017, M0, and M1 modified with 0, 1, and 3 wt.% Ce and processed by AMI, SC, and LR. The microindentations were carried out applying a charge of 200 gf during 15 seconds.

Composition	Processing condition		
	AMI	SC	LR
AA2017_0Ce	84±5	96.5±6	124.2±4
AA2017_1Ce	84±4	98.5±8	126.9±9
AA2017_3Ce	98±5	102.3±4	136.8±7
M0_0Ce	79±12	74.4±3	124.7±9
M0_1Ce	82±9	87±3	126.9±6
M0_3Ce	83±3	92.4±3	131.3±4
M1_0Ce	76±7	74.2±5	115.9±8
M1_1Ce	79±8	77.5±7	116.6±8
M1_3Ce	79±9	82.4±5	129.1±7

4.1.4. Selection of compositions to be processed by LPBF

The application of different characterization techniques such as OM, SEM-EDX, SAED-TEM, DSC, XRD, and microhardness tests, allowed to establish the effect of composition and cooling rate on the microstructural characteristics, mechanical strength and, more importantly, determine the response of the new compositions towards HCS. The results obtained showed that only the composition M1_3Ce presented a crack-free microstructure. The addition of Ce in the different compositions guaranteed a decrease in the solidification interval that reduces the HCS values, promotes grain refinement, and increases hardness values. The microstructural characterization carried out by SEM-EDX, XRD, and SAED-TEM allowed us to establish that the eutectic region formed is mainly composed of Al and Al_3CeCu. Considering these results, the M1_3Ce was selected to be further investigated. For the sake of comparison, the M1_0Ce alloy was also selected to be investigated. This alloy can still be considered as the AA2017 because its composition is still within the range established by Kissel [76], as shown in **Table 2.2**.

4.2. Directional solidification

In order to have a better understanding of the behavior during the solidification process of the candidate compositions selected to be processed by LPBF, directional solidification tests were performed. The results obtained at this stage allowed us to correlate in greater detail the influence of Ce in the M1 composition on the microstructural characteristics and hardness in samples solidified at cooling rates between 0.5 °C·s^{-1} and 20 °C·s^{-1}.

4.2.1. Thermal profiles and solidification parameters

The macrographic images and thermal profiles of the M1_0Ce and M1_3Ce cylinders, which underwent directional solidification, are presented in **Figure 4.15** and **Figure 4.16**, respectively. The macrographs allow to observe a growth of columnar grains arranged preferentially on the vertical axis (direction of heat extraction). From the data presented in **Figure 4.16**, it is possible to determine the solidification kinetics of both compositions, as previously published by [152, 196].

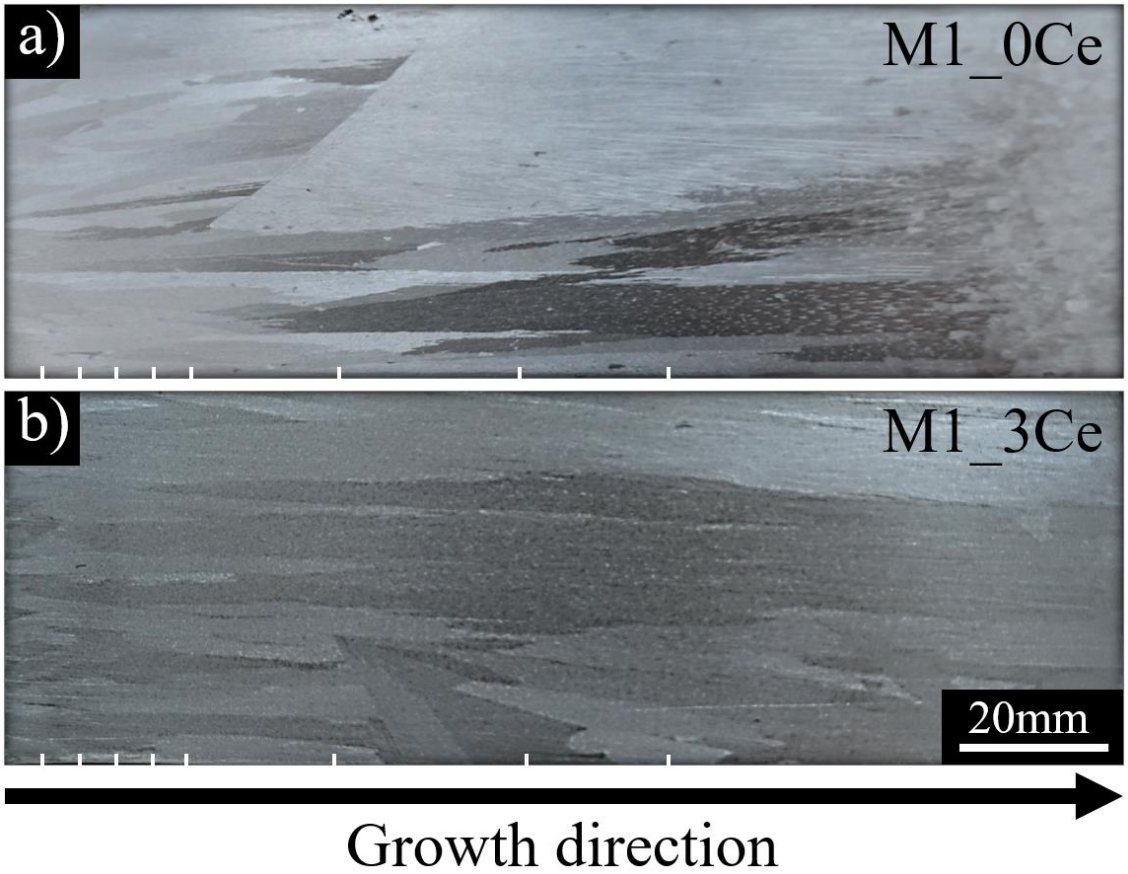

Figure 4. 15 – Macrographs of a) M1_0Ce and b) M1_3Ce cylinders produced by directional solidification. The images allow us to observe the formation of columnar grains. Likewise, the marks presented in the bottom part of each figure show the position where the different thermocouples were inserted.

The cooling rate curves ($\dot{T}=\Delta T/\Delta t$, in °C·s^{-1}) and thermal gradient ($G=\dot{T}/V_L$, in °C·mm^{-1}) are presented in **Figure 4.17**. It is not possible to perceive any relevant change/effect of the solidification kinetics of the M1_3Ce due to the addition of Ce, maintaining a similar solidification kinetic with M1_0Ce composition. Although some grains were sedimented by gravity from the upper surface of the AA2017 casting, the positions where the thermocouples were inserted present a columnar solidification structure for both cylinders, i.e. no column-to-equiaxial transition (CET) was observed, making it easier to establish a correlation between the microstructures obtained between both compositions. Furthermore, despite a higher solute content in the M1_3Ce composition, the development of a complete columnar macromorphology in the cylinder

demonstrates that Ce could not act as a refiner under the solidification conditions used in this stage of the work. Siqueira *et al.* [197] propose cooling rates higher than 0.2°C·s^{-1} in Al-Cu base alloys to obtain a CET. Due to this, the cooling rates applied in this work (0.55 – 0.65 °C·s^{-1}) prevent the formation of defined columnar to equiaxed transition zones as shown in **Figure 4.15**.

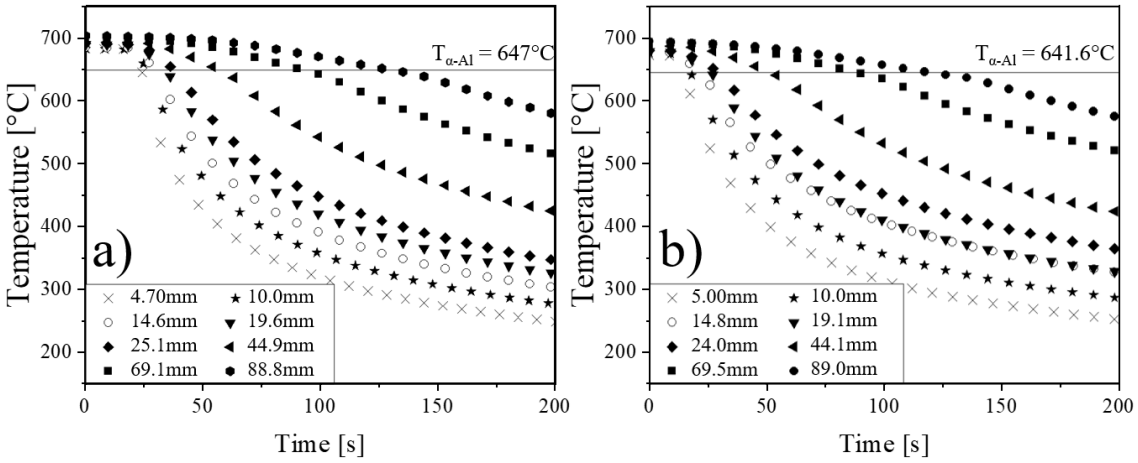

Figure 4. 16 – Experimental cooling curves for eight thermocouples at different positions inside the cast cylinders shown in **Figure 4.15** for a) M1_0Ce and b) M1_3Ce compositions.

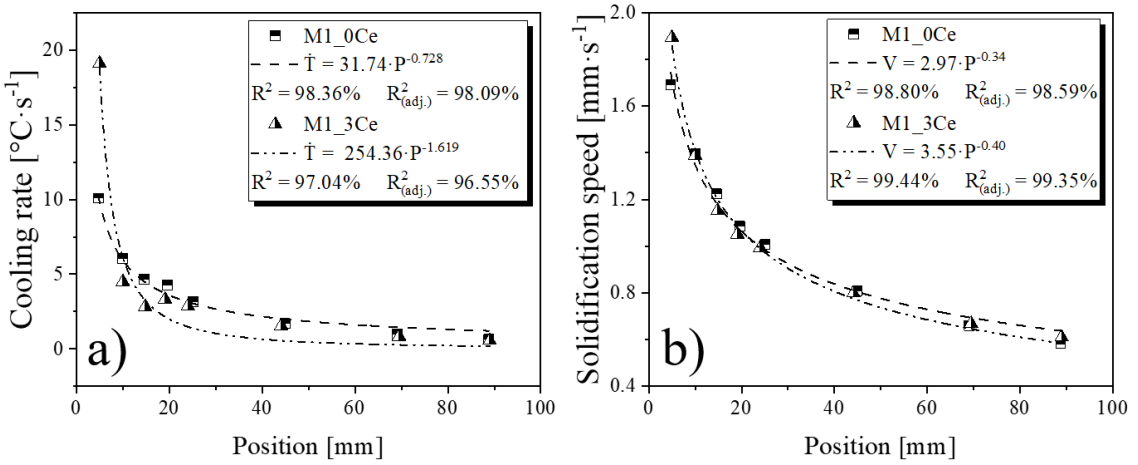

Figure 4. 17 – a) Cooling rate and b) solidification speed variations along the directionally solidified cylinders for the M1_0Ce and M1_3Ce compositions.

4.2.2. Microstructural characterization by optical microscopy

The correlation between the microstructural characteristics, i.e. dendritic spacing and grain size, and solidification kinetics were investigated using OM. Considering that the samples present an anisotropic microstructure, the analysis was performed transversely and longitudinally concerning the direction of solidification. **Figure 4.18** and **Figure 4.19** show the variation of the primary dendritic spacing to the cooling rate and the variation of the secondary dendritic spacing to the solidification speed for both compositions.

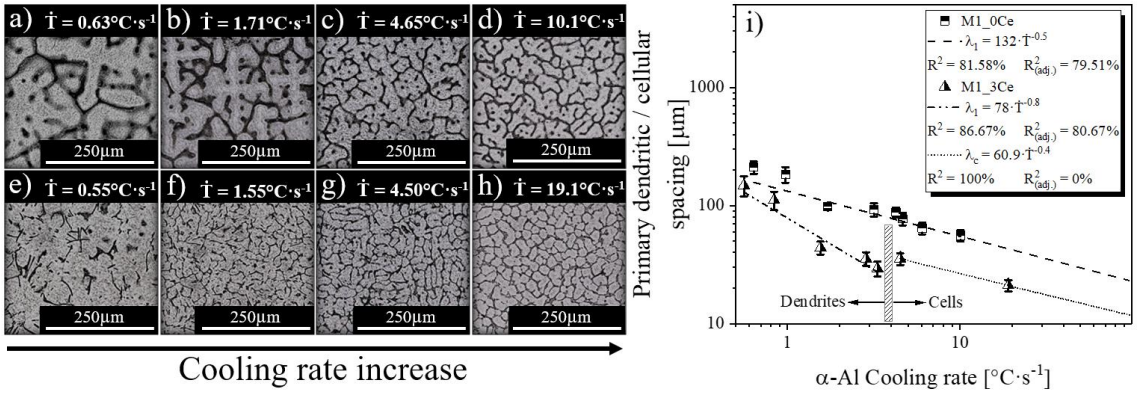

Figure 4. 18 – Correlation between primary dendritic/cellular spacing and the cooling rate of M1_0Ce (a – d) and M1_3Ce (e – h) compositions. In (**a** – **h**) show some representative microstructures in the transverse direction and in (**i**) the secondary dendrite arm spacing as a function of the cooling rate.

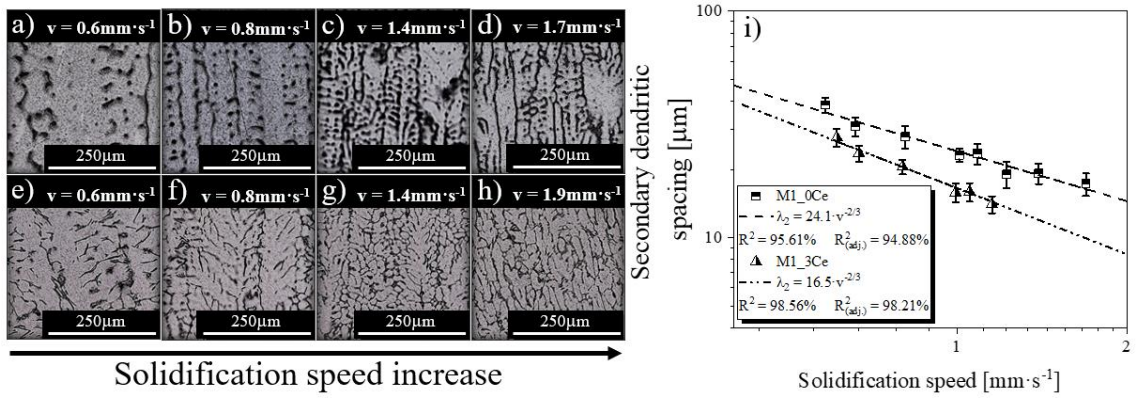

Figure 4. 19 – Correlation between secondary spacing and the solidification speed of M1_0Ce (a – d) and M1_3Ce (e – h) compositions. In (a – h) shows

some representative microstructures in the longitudinal direction and (i) the secondary dendrite arm spacing as a function of the solidification speed.

The microstructural analysis allows us to observe that, unlike the M1_0Ce sample, which presented a predominantly dendritic microstructure in all positions analyzed, the addition of Ce in the M1_3Ce sample promoted a refinement of dendrites towards the bottom of the cylinder (cooling rates above 4.5°C·s^{-1}), favoring a microstructure composed of a cellular and dendritic matrix in the lower part of the cylinder, while in the upper part, only the formation of dendrites occurs after the transition region. The addition of Ce in aluminum alloys generates different microstructural changes. The possible formation of dispersoid phases ($Al_{11}Ce_3$) and an increase in the constitutional supercooling degree inhibit the capacity for growth and thickening of the secondary arms that form the dendrite [170-172]. Nevertheless, the presence of $Al_{11}Ce_3$ could not be corroborated in this work.

In turn, the cooling rates generated in the lower part of the cylinder favor the obtaining of a predominantly cellular microstructure due to a more thermodynamically stable liquid [196, 198]. A more thermodynamically stable eutectic liquid caused by the addition of Ce and, consequently a more stable solid-liquid interface, helps to avoid the dissipation of the latent heat for dendrite growth through the material, raising the temperature towards the dendrite arms, and generating new nucleation points that shall favor obtaining a microstructure more refined and with the presence of cell and dendrites with thin ramifications [172]. In addition, it is presumed that during the solidification process, both alloys have a similar G; however, the eutectic composition of M1_3Ce may present a lower cooling rate due to a greater amount of solute, favoring the material to present a less dendritic solidification tendency. A schematic illustration of this behavior is shown in **Figure 4.20**.

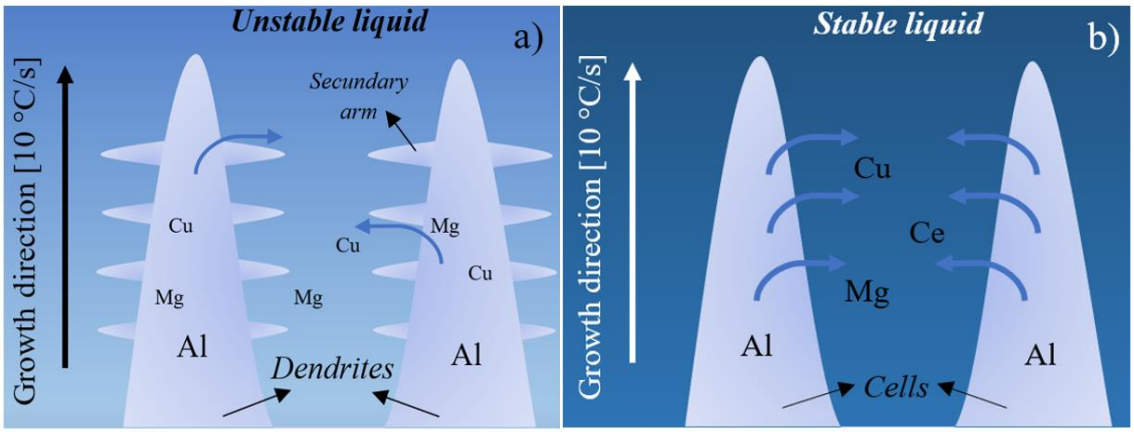

Figure 4. 20 – Schematic of the growth of cells and dendrites in a) M1_0Ce and b) M1_3Ce compositions. The addition of Ce generates a more stable eutectic liquid and, thus, a greater stability of the solid-liquid interface.

Although the literature has reported that the addition of Ce favors a refinement in the grain size, which was verified for the samples manufactured by AMI, SC, and LR, the directional solidification tests did not show a representative change in grain size as shown in **Figure 4.21**. This may be due to the fact that the presence of Ce in the proposed composition does not exert a refining effect, i.e. from the formation of Al_3Ce or $Al_{11}Ce_3$ phases, promoting heterogeneous nucleation. On the other hand, Ce allows the reduction of the solidification interval and promotes the formation of eutectic regions.

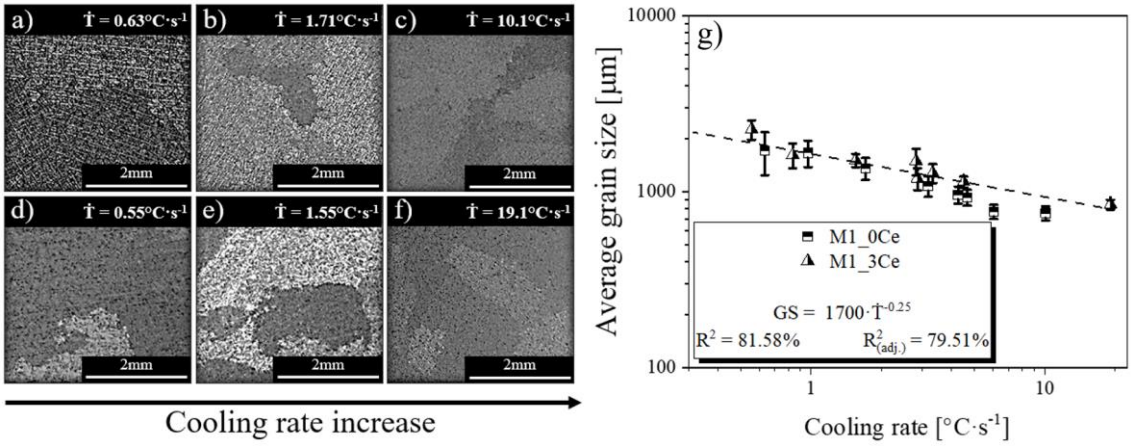

Figure 4. 21 – Effect of the cooling rate on the average grain size for M1_0Ce and M1_3Ce compositions. In (**a** – **f**) shows some representative microstructures

revealing the grains for both alloys solidified at different cooling rates and in (**g**) shows the average grain size values obtained as a function of the cooling rate.

4.2.3. Microstructural characterization by SEM-EDX and XRD

The microstructural characterization by SEM-EDX was carried out with two samples solidified under different cooling rates of the M1_0Ce (0.63°C·s^{-1} and 10 °C·s^{-1}) and M1_3Ce (19.1 °C·s^{-1} and 0.55 °C·s^{-1}) compositions, these corresponding to 5 mm and 90 mm samples from the base of the cylinder. The EDX-mapping images are presented in **Figure 4.22** and **Figure 4.23**.

The collected images allow us to observe the formation of small eutectic regions with a globular morphology for the M1_0Ce composition, which is mainly composed of Al + Al_2Cu, according to the EDX analysis. The formation of small eutectic regions is consistent with the Scheil-Gulliver curve presented in **Figure 4.3**(**c**). In contrast, the M1_3Ce composition presents a larger eutectic-rich region with a lamellar morphology, caused by the addition of Ce [199][200], as shown in **Figure 4.23**.

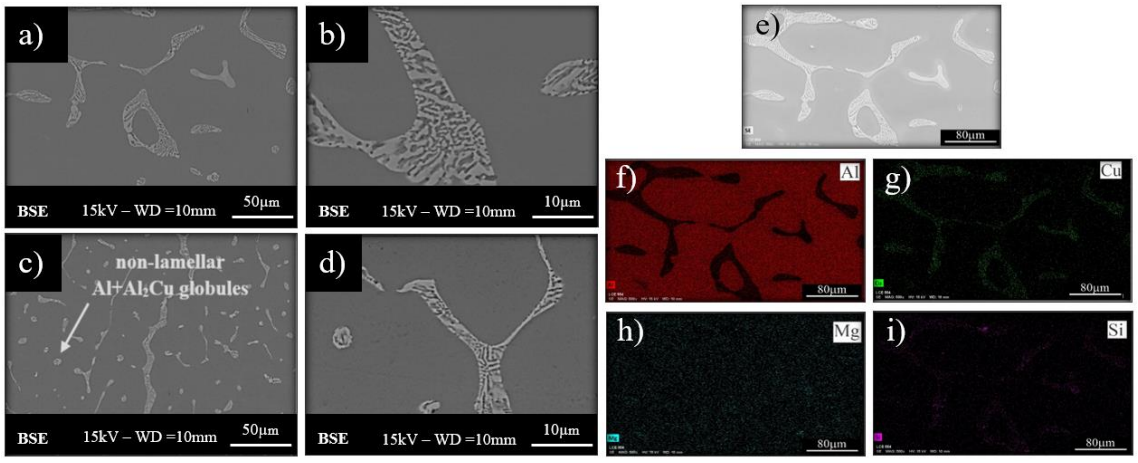

Figure 4. 22 – SEM – BSE images for low (0.63°C·s^{-1}, (a, b)) and high (10°C·s^{-1}, (c, d)) cooling rate samples for the M1_0Ce composition. The eutectic region shown in Fig. 4.22(a) was analyzed by EDX-mapping as shown in (e – i).

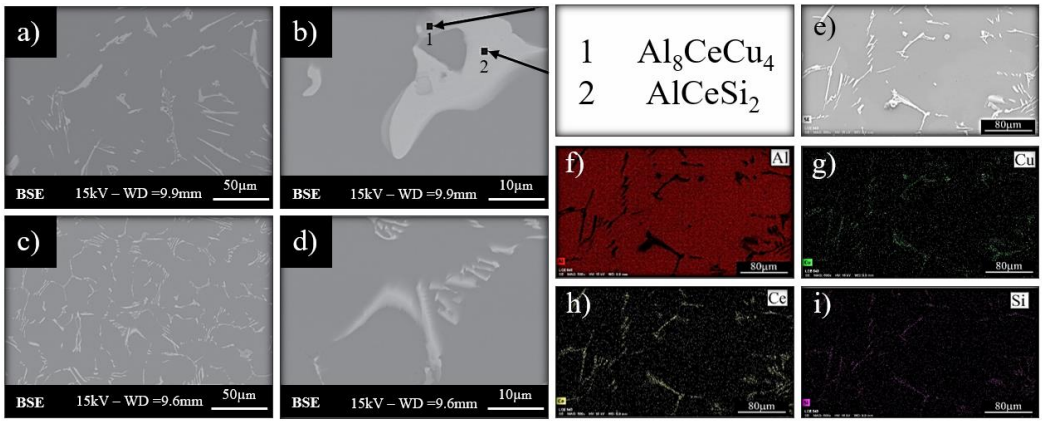

Figure 4. 23 – SEM – BSE images for low (0.55 °C·s^{-1}, (a, b)) and high (19.1 °C·s^{-1}, (c, d)) cooling rate samples for the M1_3Ce composition. The eutectic region shown in Fig. 4.23(a) was analyzed by EDX-mapping as shown in (e – i).

The EDX analysis allowed to identify the formation of the Al_8CeCu_4 and $AlCeSi_2$ phases within the eutectic region. The XRD patterns shown in **Figure 4.24** allowed us to identify the Al_2Cu phase (ICSD n° 42517, space group I4/mcm (140, Tetragonal) for the composition M1_0Ce while the Al_8CeCu_4 (ICSD n° 169061, space group I4/mmm (140), Tetragonal) and Al_3CeCu (ICSD n° 190993, space group I4mm (107)) phases were identified for the M1_3Ce composition. Nevertheless, it was not possible to verify the formation of $AlCeSi_2$ phase, which may be in a low amount and could not be detected by this technique.

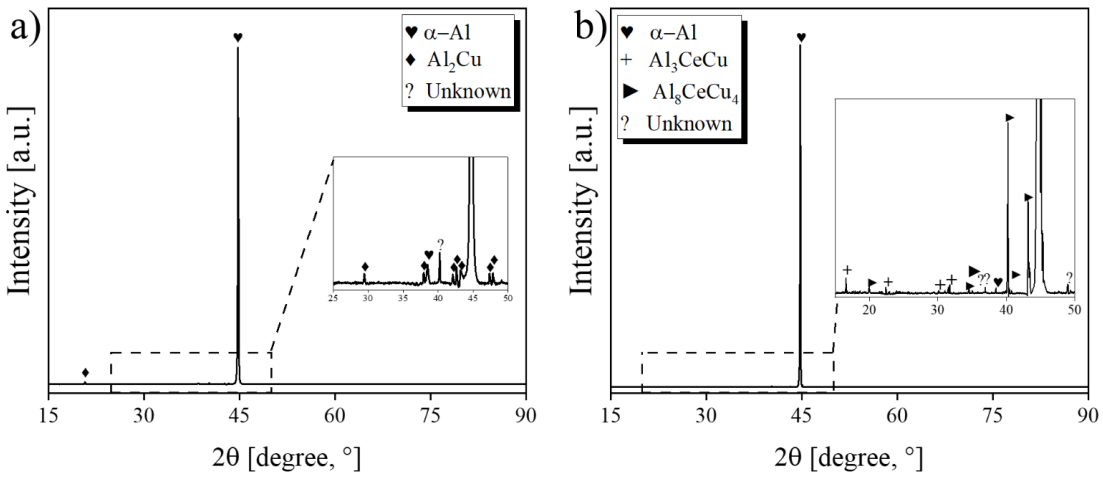

Figure 4. 24 – XRD patterns for a) M1_0Ce and b) M1_3Ce samples directly solidified with a cooling rate of 0.63 °C·s^{-1} and 0.55 °C·s^{-1}, respectively.

These results allowed to observe the solidification kinetics at low cooling rates for both compositions. Likewise, it was possible to produce mathematical relationships that can later be extrapolated to analyze the material when subjected to other processes with higher cooling rates.

4.2.4. Microhardness behavior in directly solidified samples

Microhardness measurements allow verifying the effectiveness of Ce in increasing the mechanical strength of the composition M1_3Ce compared to M1_0Ce. The results are shown in **Figure 4.25**. Although a visible grain refinement was not obtained due to the addition of Ce, a refinement of the internal solidification structure was observed through the formation of cells and dendrites with the spacing of the secondary and primary arms smaller for the M1_3Ce. The decrease in dendritic spacing results in an increase in the mechanical strength of the material due to a better distribution of the intermetallic phases present within the interdendritic regions. Likewise, as reported in section 4.1.3.5., the addition of Ce allows 1) the formation of secondary phases that reinforce the matrix; 2) the formation of eutectics that increase the resistance of the material through the Orowan reinforcement mechanism; and 3) the possible formation of dispersoid phases that favors maintaining a more refined microstructure with improved mechanical strength [170-172, 190, 194, 195].

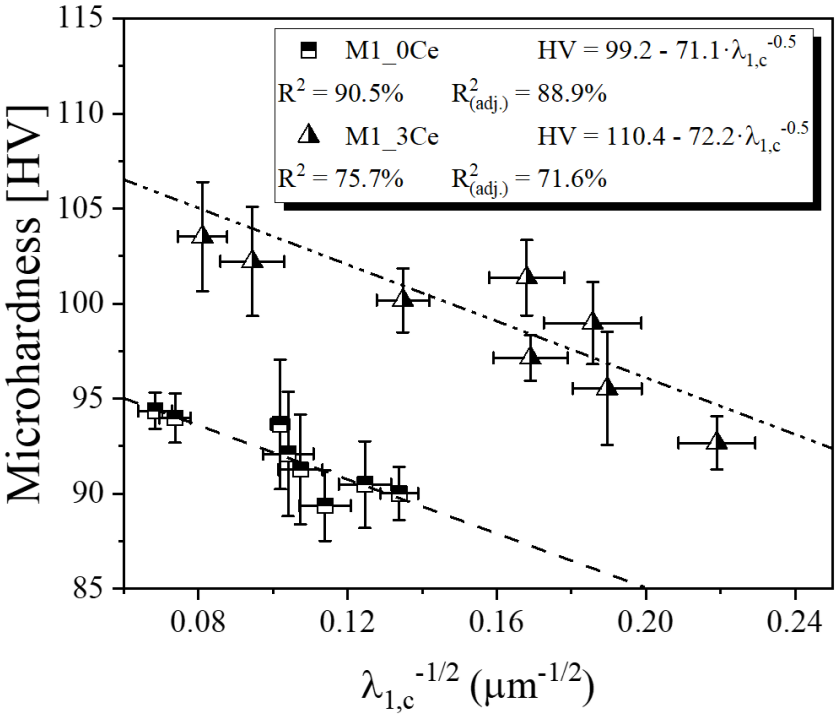

Figure 4. 25 – Microhardness values of the M1_0Ce and M1_3Ce direct solidified parts as a function of $\lambda_{1,c}$.

Figure 4.26(**a**, **b**) shows examples of compressive stress-strain curves for the different samples taken from directionally solidified castings based on their dendritic/cellular primary spacing for M1_0Ce and M1_3Ce compositions. The corresponding yield strength (YS), elastic modulus (E), elongation at fracture (ε_F), and the compressive strength (σ_F) values extracted from these curves are depicted in **Figure 4.27**(**a** – **d**). The YS (**Figure 4.27**(**a**)) and E (**Figure 4.27**(**b**)) values exhibit a behavior akin to what's observed in Vickers microhardness tests, as shown in **Figure 4.27**. Here, an increase in $\lambda_{1,c}$ leads to an improvement in mechanical strength but at the expense of ductility (**Figure 4.27**(**c**)). Ductility was slightly reduced with the insertion of Ce, with the ductility increasing as the dendritic spacing decreased for both alloys. In contrast, the addition of Ce in the proposed composition leads to a significant 13% improvement in compressive stress values, and this remains unaffected by $\lambda_{1,c}$ (**Figure 4.27**(**d**)). The relationship between mechanical properties and solidified microstructure exhibits a behavior oposited that set by the Hall-Petch law, which suggests that finer grains should result in stronger mechanical resistance. This deviation can be

attributed to changes in the volume of eutectic formations. When the cooling rate decreases, dendrites grow larger, accompanied by an increase in the volume of eutectic regions. This, in turn, enhances the material's mechanical resistance. Conversely, samples with finer grain sizes and dendrites exhibit a lower proportion of eutectic, diminishing its impact on the material's mechanical strength.

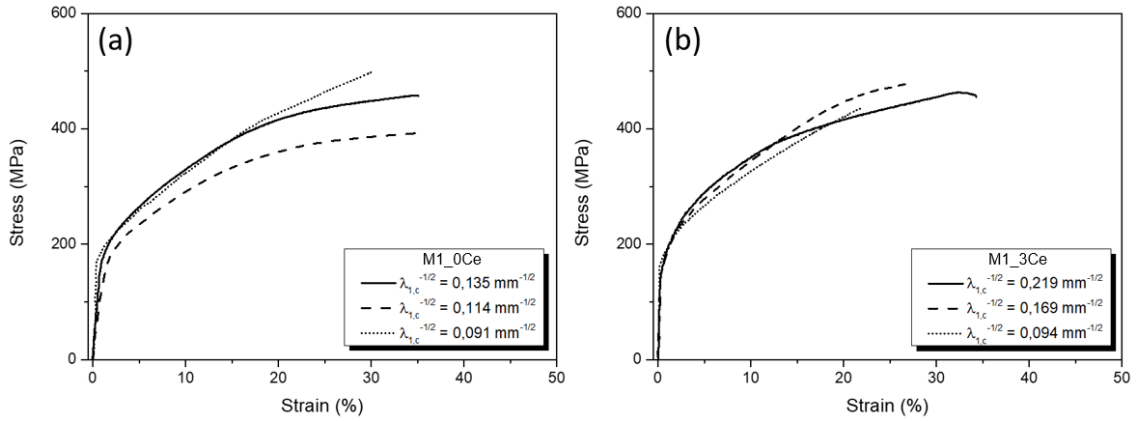

Figure 4. 26 – Typical compression curves registered for the **a**) M1_0Ce and **b**) M1_3Ce compositions.

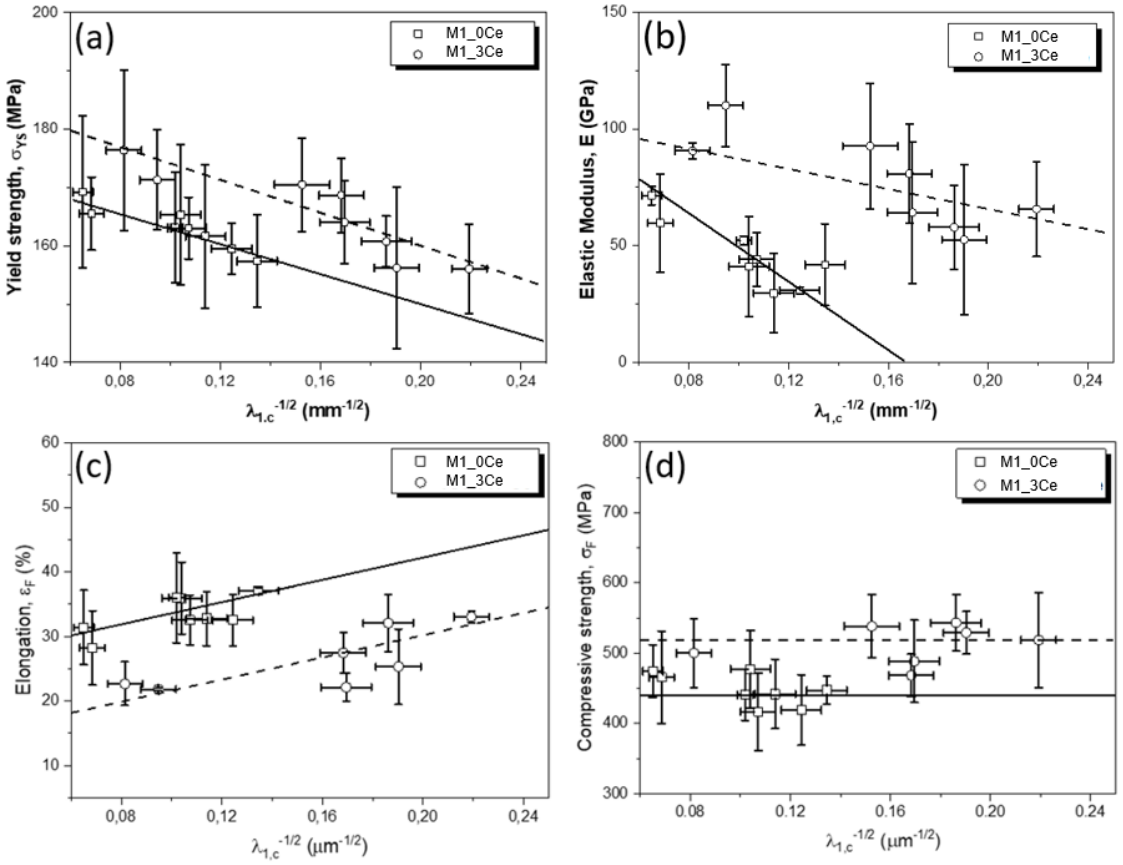

Figure 4. 27 – Experimental correlations between the (**a**) yield strength; (**b**) elastic modulus; (**c**) elongation at fracture; and (**d**) compressive strength as a function of $\lambda_{1,c}$ for the M1_0Ce and M1_3Ce compositions.

4.3. Metallic powder characterization

Powders of the M1_0Ce and M1_3Ce were produced by gas atomization at DEMa/UFSCar aiming for their use in the LPBF process. The results of their characterization are given in this section.

4.3.1. Particle size distribution

The particle size distribution for gas-atomized powders analysis was performed by sieving and the results are depicted in **Figure 4.2**. The atomization process of composition M1_0Ce produced 85.4% of powder deposited in the lower chamber of the atomizer, while for composition M1_3Ce this value was 83.8%. The remaining powder for both compositions was deposited in the cyclone chamber.

Both compositions present a particle size distribution where where the largest fraction is between 53 µm and 75 µmand the inter decis ratio (IDR) for compositions M1_0Ce and M1_3Ce is 51 µm and 43 µm, respectively. Nevertheless, the d50 varies significantly, with values of d50 = 81 µm for M1_0Ce and d50 = 57 µm for M1_3Ce, which influence the amount of powder that can be used during the construction of parts by LPBF (the ideal particle size range for this process is 20 µm – 63 µm). In this sense, 71% of the M1_3Ce powder sample can be used in this work, while only 19.5% of the M1_0Ce powder sample is useful for the production of parts by LPBF.

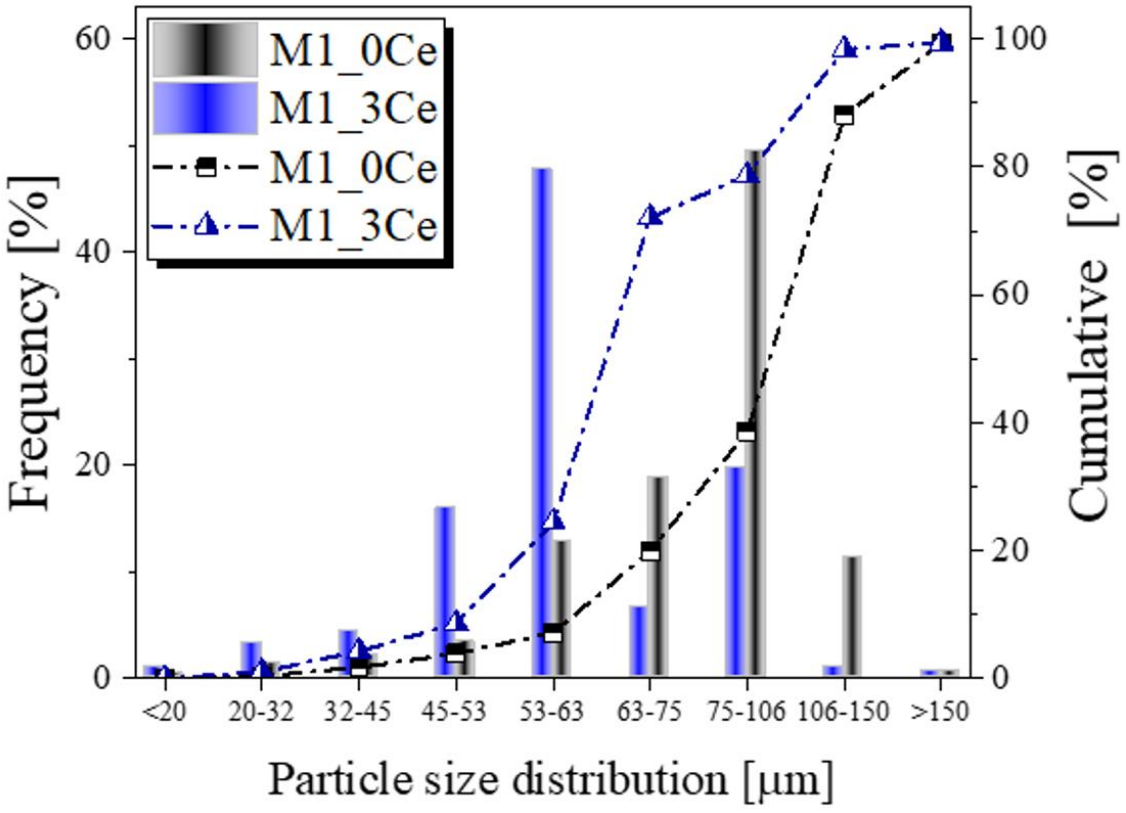

Figure 4. 28 – Particle size distribution of the metal powders used in this work. The analysis was carried out by sieving technique.

Although in this work the same selected parameters were used to produce the powders of both compositions, the difference in the percentage of useful powder for both compositions is significantly different. Despite the reason for this difference is not exactly known, it is suggested that this could be due to:

1) The addition of Ce, which could affect the fluidity of the molten metal and, consequently, influence the atomization process.

2) Process factors, e.g. variation of the liquid viscosity inside the guide tube in the nozzle or variation of the atomization gas pressure.

4.3.2. Morphological characteristics of metallic powders

The morphological, microstructural, and compositional characteristics of metallic powders intended for application in AM are of great importance. In general, efforts are made to obtain spherical powders free of defects such as porosity, satellites, and superficial oxide layers, among others, to guarantee optimal fluidity and printability. Considering the above, a detailed analysis of the microstructural, morphological, and physical characteristics of the powders produced in this work was carried out.

4.3.2.1. SEM Characterization

SEM-SE images of the powders used in this work are presented in **Figure 4.29** and **Figure 4.30**. The application of this technique allows to obtain a general view of the morphological condition of the powders. Both compositions present a predominantly spherical morphology with the presence of satellites in some of the particles. Within AM processes, the use of spherical powders favors a greater fluidity of the powders and a better accommodation of these on the substrate, allowing the generation of dense and homogeneously distributed layers of powder [7]. Nevertheless, it is possible to observe that as the size of the particle increases, its sphericity decreases. While particles smaller than 20 µm show high sphericity, particles larger than 63 µm begin to show a greater number of defects such as satellites, agglomerates, and splashes. To complement the information acquired by SEM, the powder samples were also analyzed by OM and DIA. Some of the information acquired through these techniques is mentioned below.

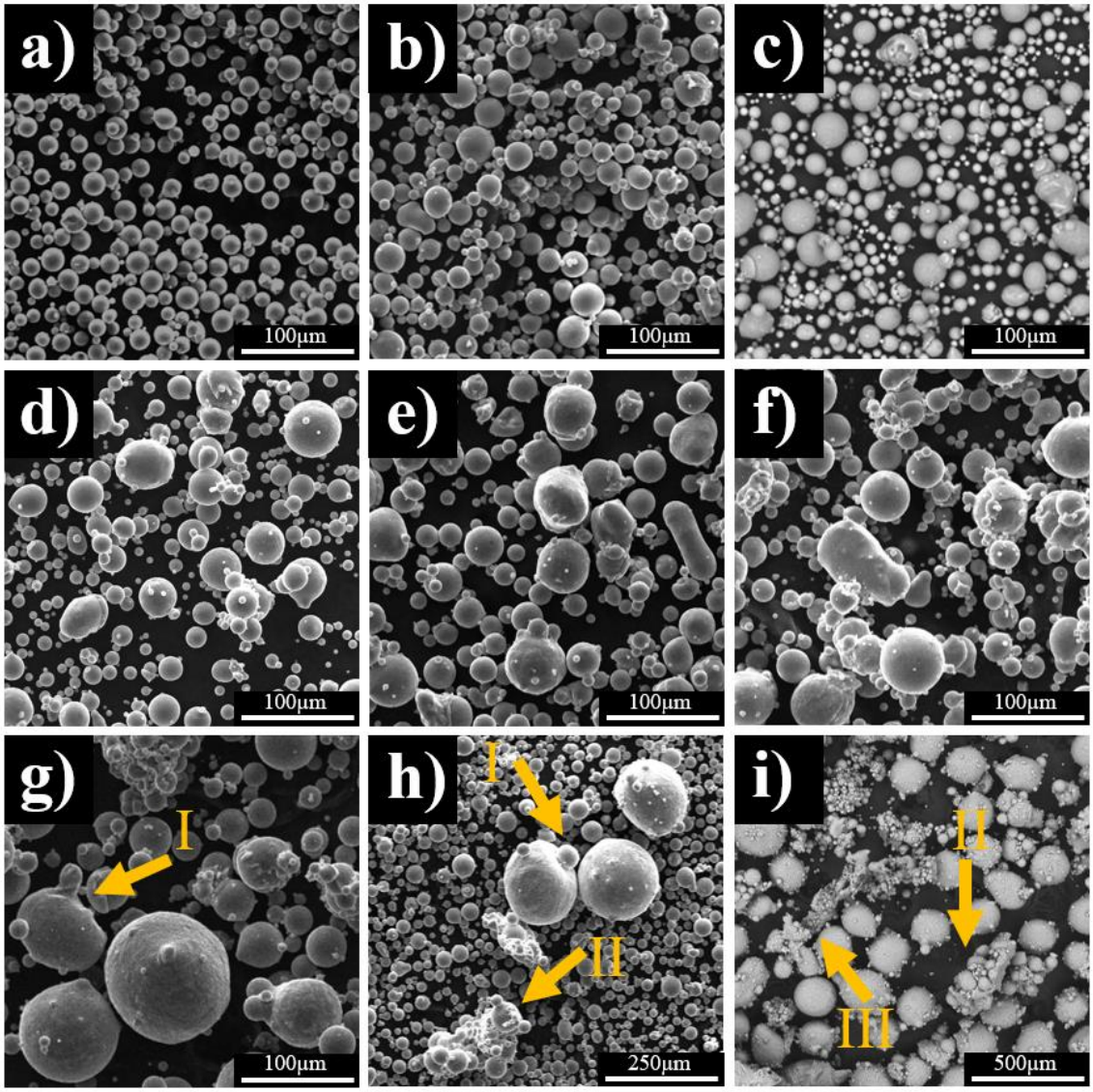

Figure 4. 29 – SEM-SE images of the M1_0Ce metal powders produced in this work. The powders were analyzed according to their particle size distribution. In a) <20 µm; b) 20 - 32 µm; c) 32 - 45 µm; d) 45 - 53 µm; e) 53 - 63 µm; f) 63 - 75 µm; g) 75 - 106 µm; h) 106 - 150 µm; and i) >150 µm. The SEM analysis allowed us to observe some defects in the particles such as I) satellites; II) agglomerates and III) splats.

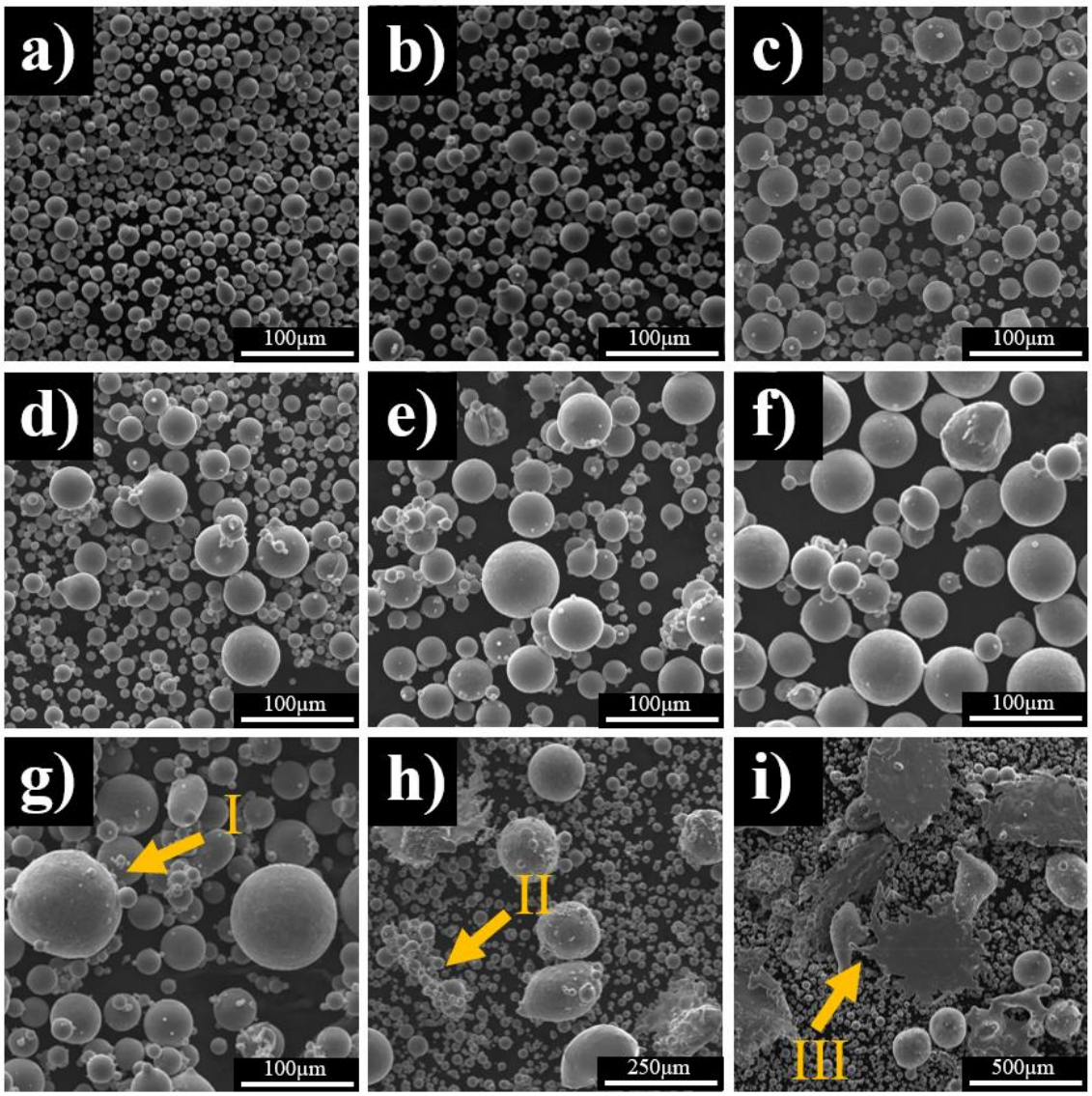

Figure 4. 30 – SEM-SE images of the M1_3Ce metal powders produced in this work. The powders were analyzed according to their particle size distribution. In a) <20 µm; b) 20 - 32 µm; c) 32 - 45 µm; d) 45 - 53 µm; e) 53 - 63 µm; f) 63 - 75 µm; g) 75 - 106 µm; h) 106 - 150 µm; and i) >150 µm. The SEM analysis allowed us to observe some defects in the particles such as I) satellites, II) agglomerates and III) splats.

4.3.2.2. Geometric anisotropy

Geometric anisotropy considers the difference in the average diameter of a particle [201][202]. In this sense, if the powder particle is completely spherical,

the diameter will be the same, regardless of the position in which it is measured. The diameter of a non-spherical particle will depend on the direction in which it is measured. Geometric anisotropy considers the maximum and minimum diameter values of the measured particles. The relationship between the maximum measured diameter and the geometric anisotropy of the particles is presented in **Figure 4.31**. An increase in the particle diameter favors a higher value of geometric anisotropy. Particles below 20 µm present an average anisotropy value between 0.82 - 0.95, while for particles larger than 150 µm these values are between 0.56 - 0.75. For the range of particles intended to be used by LPBF, these values are between 0.81 – 0.87 for composition M1_0Ce and between 0.8 – 0.9 for composition M1_3Ce. In general, using both techniques the particles present values greater than 0.8, which reflects that the powders are predominantly spherical.

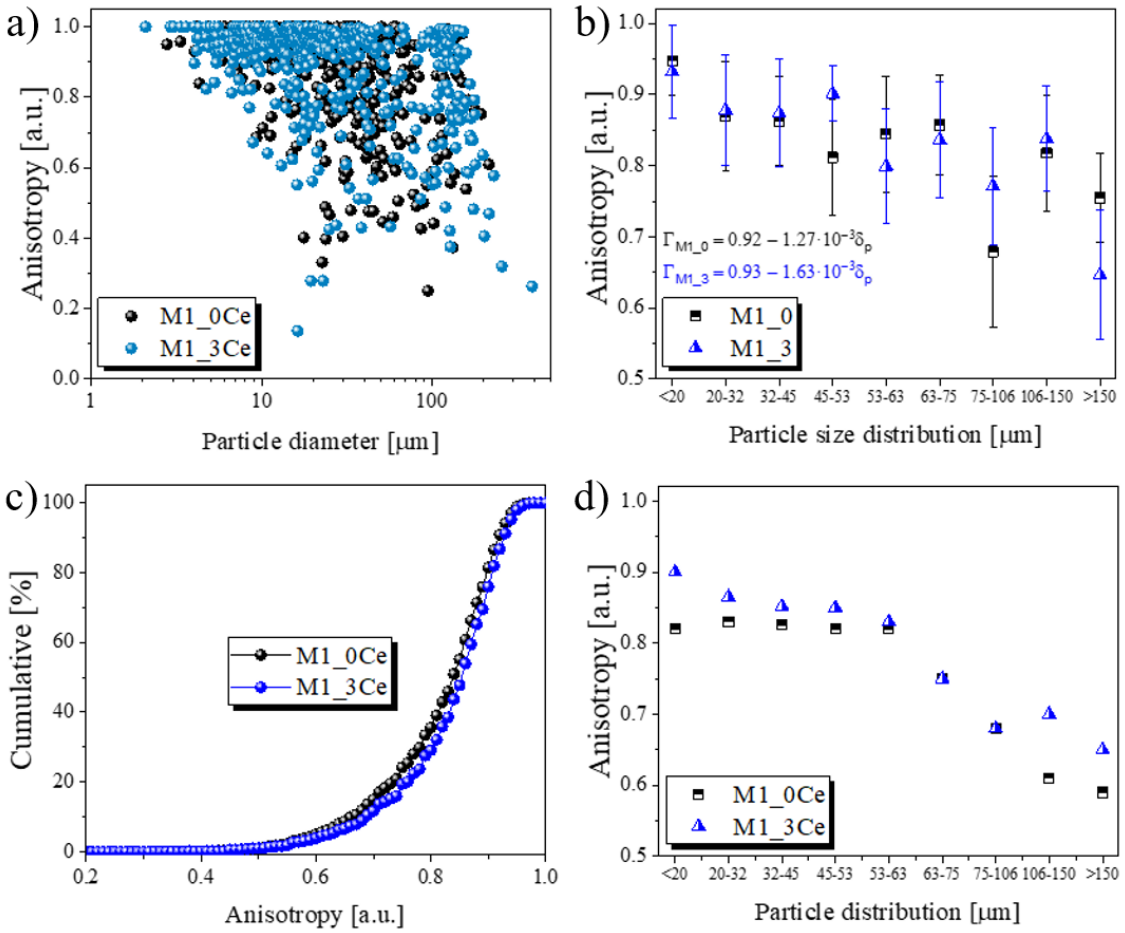

Figure 4. 31 – Geometric anisotropy in function of the particle size range for M1_0Ce and M1_3Ce powders. In a) data collected and b) anisotropy behavior obtained from optical microscopy. In c) cumulative values and d) anisotropy behavior obtained from dynamic image analysis.

4.3.2.3. Circularity

The circularity is directly linked to the roundness of the particle, which can be defined as the relationship between the surface area of the particle and the ideal area of a circle, considering the maximum diameter of the particle [203][202]. The circularity values estimated from the maximum diameter of the particle are presented in **Figure 4.32**. Similar to geometric asymmetry behavior, circularity decreases as particle size increases; however, it can be observed that the circularity in the different particle size ranges is more restricted. For the particle size distribution range of interest in this work (20-63 µm), the circularity values by OM for the M1_0Ce and M1_3Ce samples are between 0.96 – 0.98

and 0.96 – 0.99, respectively. Nevertheless, these values decrease to 0.65 – 0.91 for M1_0Ce and 0.6 – 0.95 for M1_3Ce composition. This is because the dynamic image analysis takes an average of all convex regions other than the outer circle of the particle. In contrast, through OM analysis only a 2D view of the particle is considered, selecting only the minimum and maximum diameter values. Both techniques show that the particles of interest for this work have circularity values greater than 0.85, which is useful for their application within AM processes.

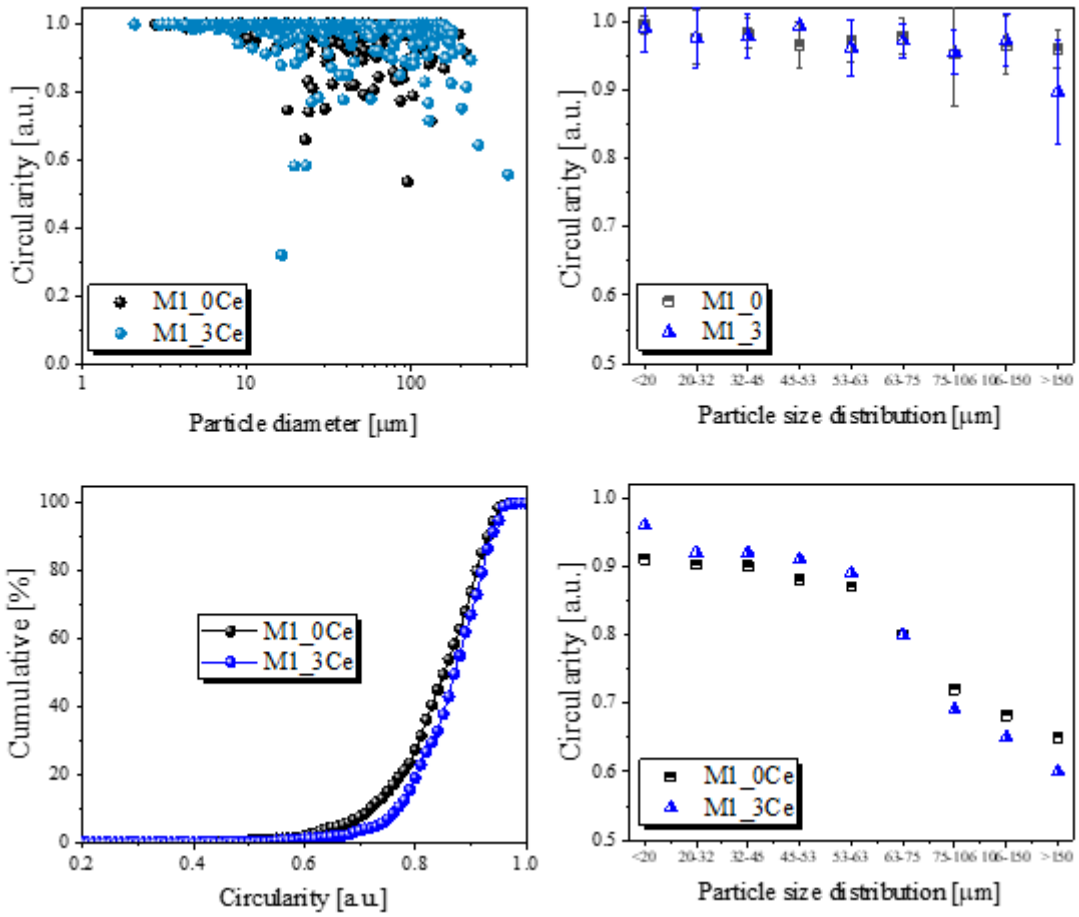

Figure 4. 32 – Geometric circularity behavior in function of the particle size range for M1_0Ce and M1_3Ce powders. In a) Data collected and b) circularity behavior obtained from optical microscopy. In c) cumulative values and d) circularity behavior obtained from dynamic image analysis.

4.3.2.4. Sphericity

Sphericity presents the relationship between the surface area of a sphere and the area of a particle, to determine how spherical an object is [204]. Although there are different ways to determine the sphericity of an object, the mathematical relationships proposed by Krumbein (**eq. 5**) and Wadell (**eq. 6**) are the most widely used [202]. The sphericity values obtained in this research are presented in **Figure 4.33**.

$$\Psi = \sqrt[3]{\frac{c^2}{a \cdot b}} \tag{5}$$

$$\Psi = \frac{S_n}{S} = \sqrt[3]{\frac{36 \cdot \pi \cdot V^2}{S}} \tag{6}$$

Where ***a***, ***b***, and ***c*** correspond to the diameters of the particle in coordinates X, Y, and Z; ***V*** is the projected volume of the particle and ***S*** is its surface area.

The first mathematical relationship corresponds to a relative sphericity and is obtained by using the three main axes of the object as observed in **eq**. (**1**) [205]. In contrast, the true sphericity proposed by Wadell is obtained from the volume and surface measurements as observed in **eq**. (**2**) [206]. It should be noted that the circularity index is the 2D equivalent of the true sphericity index proposed by Wadell [204]. This is because Wadell´s Model also considered the characteristics of the particle surface and not only the dimensions of its main axes.

Considering that the sphericity values presented were obtained from the information collected by optical microscopy, they are considered only as an estimate of the morphology of the particles to observe the sphericity trend of metallic powders concerning the particle size distribution. From dynamic image analysis (DIA), it is also possible to measure the sphericity of the particles. Although various models make it possible to determine sphericity, during the DIA,

the model presented in **eq**. **7** was used, where Pe is the perimeter of the equivalent circle of the particle and Pr is the real perimeter.

$$\Psi = \frac{P_e}{P_r} = 2 \cdot \frac{\sqrt{\pi \cdot S}}{P_r} \quad (7)$$

It can be seen that this model is consistent with the other two mathematical models. As the particle size increases, the circularity values decrease. This may be due to various factors; however, in this research, we consider that a decrease in the sphericity of the particles as their size increases is mainly due to a greater probability of forming satellites. The surface area increases for a larger particle, which increases the chance of intercepting small particles that weld to it during the solidification process. Likewise, a larger size could generate a greater instability of the particle, favoring less sphericity.

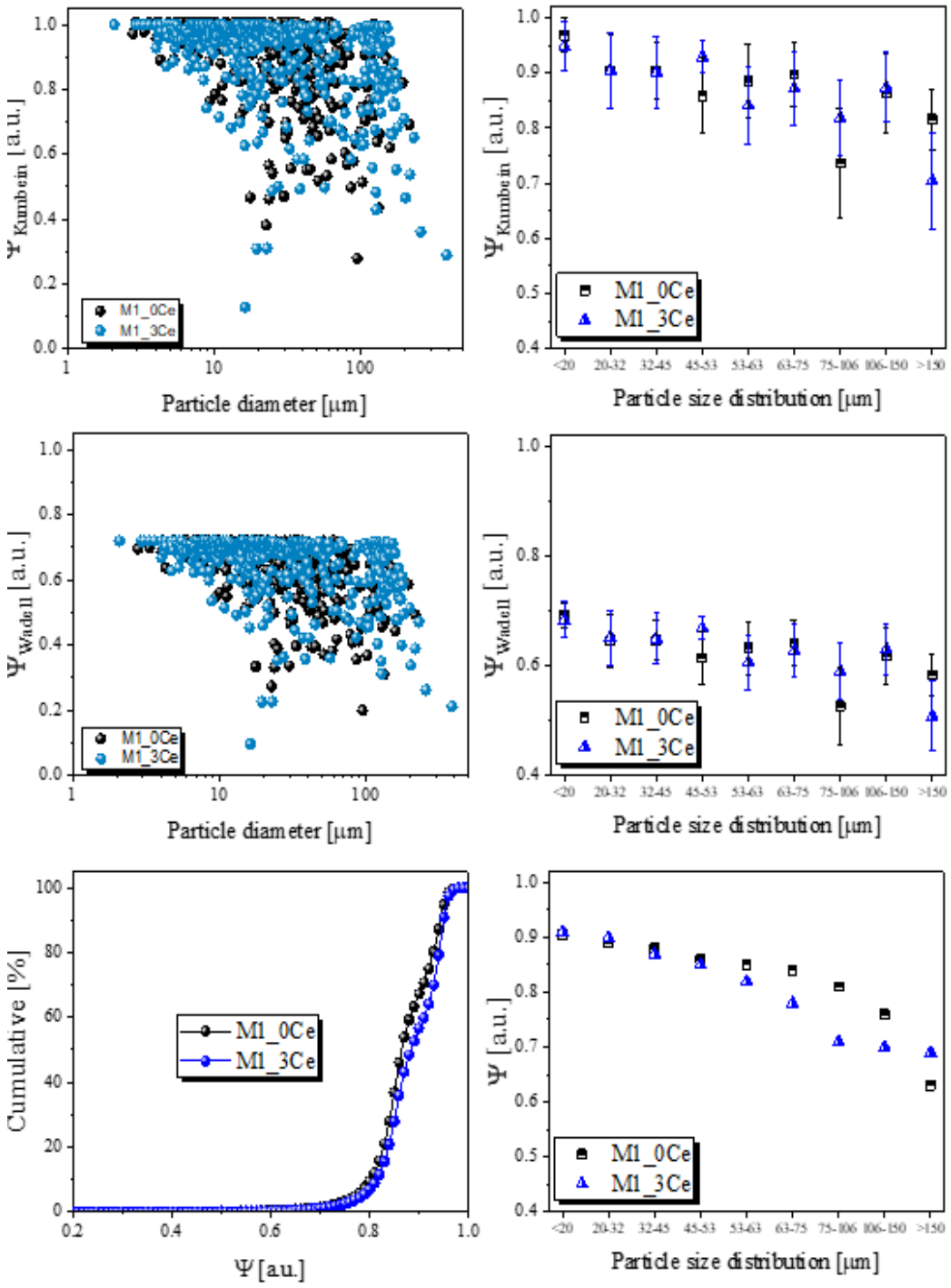

Figure 4. 33 – Sphericity as a function of the particle size range for M1_0Ce and M1_3Ce metal powders. In a, c) data collected and b, d) sphericity behavior obtained from optical microscopy. In e) cumulative values and f) sphericity behavior obtained from dynamic image analysis.

4.3.3. Physical properties

4.3.3.1. Moisture

Moisture measurements were carried out inside a controlled atmosphere oven, varying the temperature from 80 °C – 200 °C at 24 h intervals. The 50 g samples were deposited in 15 cm^2 basins to increase the surface area of the sample. The percent moisture removal for both powder samples is presented in **Figure 4.34**. Both compositions presented a similar behavior in which an increase in temperature favors greater moisture reduction, removing up to 1 wt. % moisture in the samples dried at 200 °C, although the moisture in the M1_3Ce samples is slightly lower.

Generally, metal powders from reactive alloys, such as aluminum, are easily contaminated by environmental humidity due to their high surface area and affinity for oxygen, with the formation of oxides on the powder surface [41]. The presence of moisture in aluminum powders makes it difficult to process by LPBF, reducing the free-flowing and requiring higher energy densities to break the alumina layer generated, in addition to favoring defects in the built parts, e.g. unmolten zones, evaporative porosity, and oxide disruption in the molten pool [207].

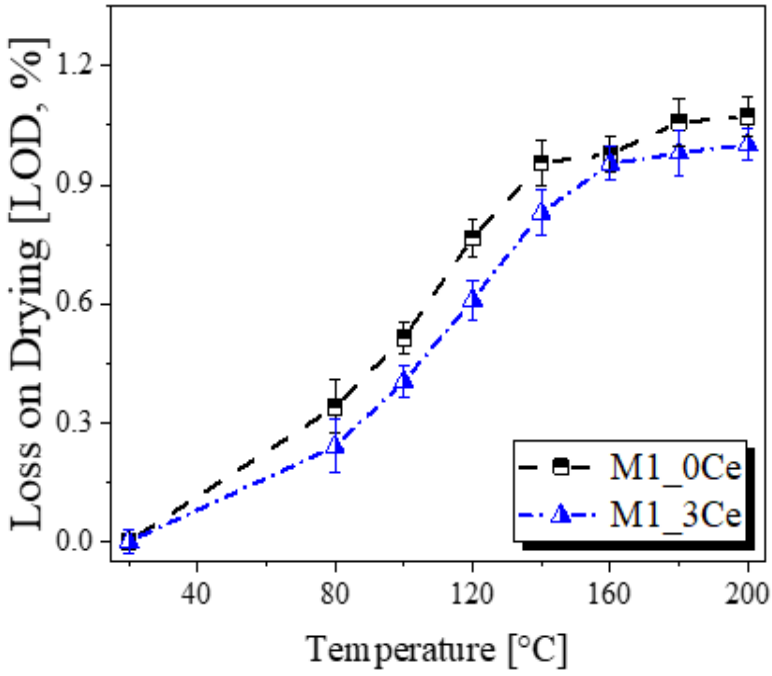

Figure 4. 34 – LOD values of M1_0Ce and M1_3Ce metal powders.

The samples dried at 200°C were cooled in an argon atmosphere and later analyzed using the Karl-Fischer technique. This technique offers greater precision in determining the remaining moisture content in powder samples [208]. Measurements made on 2 g samples (3 replicates per composition) show that the powder samples M1_0Ce and M1_3Ce still contain 0.03 wt.% and 0.04 wt.% of moisture, respectively.

4.3.3.2. Free-flowing

The fluidity of the M1_0Ce and M1_3Ce compositions was analyzed using the Hall and Carney funnels. Tests showed that the samples in undried condition did not flow through both funnels. The low fluidity of the powders is mainly attributed to the presence of a large number of fine particles, which obstruct and clog the funnel, thus preventing the fluidity of the sample [209-212]. Likewise, the presence of satellites in the powder reduces the free-flowing of metallic powders [213].

Moisture is also another factor that influences the fluidity of the material. Due to this, the samples were dried at 80°C for 24 hours to remove part of the moisture, reduce the degree of cohesion between particles, and, thus, improve the free-flowing of the metal powders. Although these dried samples did not present fluidity in the Hall funnel, both samples presented a fluidity of 15.12 ± 1.03 $s \cdot 50g^{-1}$ using the Carney funnel. Nevertheless, the flow of the powder in some measurements was not continuous and the funnel had to be tapped more than 2 times to remove the clogging, therefore these measurements were not considered. According to ASTM B417, the funnel can be tapped a maximum of two times, so if the sample does not flow after this, it is considered that the powder does not present free fluidity.

In this sense, it is established that the powder samples lack good free-flowing. The fluidity values obtained in this work are similar to those reported by Muñiz-Lerma *et al.* [209] for AlSi7Mg powder samples with irregular morphology (15.3 $s \cdot 50g^{-1}$) and a high content of fine particles (d10 = 14 µm, d50 = 31 µm; d90 = 58 µm). In comparison, powder samples with more spherical morphology and larger particle sizes (d10 = 48 – 54 µm; d50 = 63 -70 µm; d90 = 83-91 µm) had a flowability of 6.1 $s \cdot 50g^{-1}$ using a Carney funnel.

4.3.3.3. Angle of repose in static condition

The angle of repose is a characteristic of particles that relates their resistance to movement between them [214]. The angle of repose allows for indicating the fluidity of a material [215]. Measurements were made with dry and undried powder samples, making 6 measurements per sample. It was observed that the piles of the M1_0Ce and M1_3Ce powders without drying presented an angle of repose of 34.44° and 33.75°, respectively, with traces of accumulated material in the form of agglomerates (**Figure 4.35**(**a**)). In contrast, the dry samples presented a more uniform distribution, free of agglomerations (**Figure 4.35**(**b**)), and with an angle of repose of 30.58° for M1_0Ce and 28.16° for M1_3Ce.

According to the European Pharmacopeia [216], powder samples with an angle of repose between 25° – 30° usually show excellent fluidity, while powders

with angles of repose between 31° – 35° show good fluidity. Nevertheless, the fluidity tests carried out in this work with Hall and Carney funnels demonstrated that the powder samples produced present low fluidity. This is because other factors must be considered such as the Hausner ratio and the dynamic cohesive index, which must be between 1.00 - 1.11 and <5, respectively, to obtain excellent fluidity and between 1.12 - 1.18 and between 5 - 10 for good fluency [215-217]. Unfortunately, in this work, the angle of repose in dynamic conditions was not measured, so it is not possible to compare these characteristics of the powder with the data reported in the literature and have a better idea of how these parameters influence the fluidity of the material.

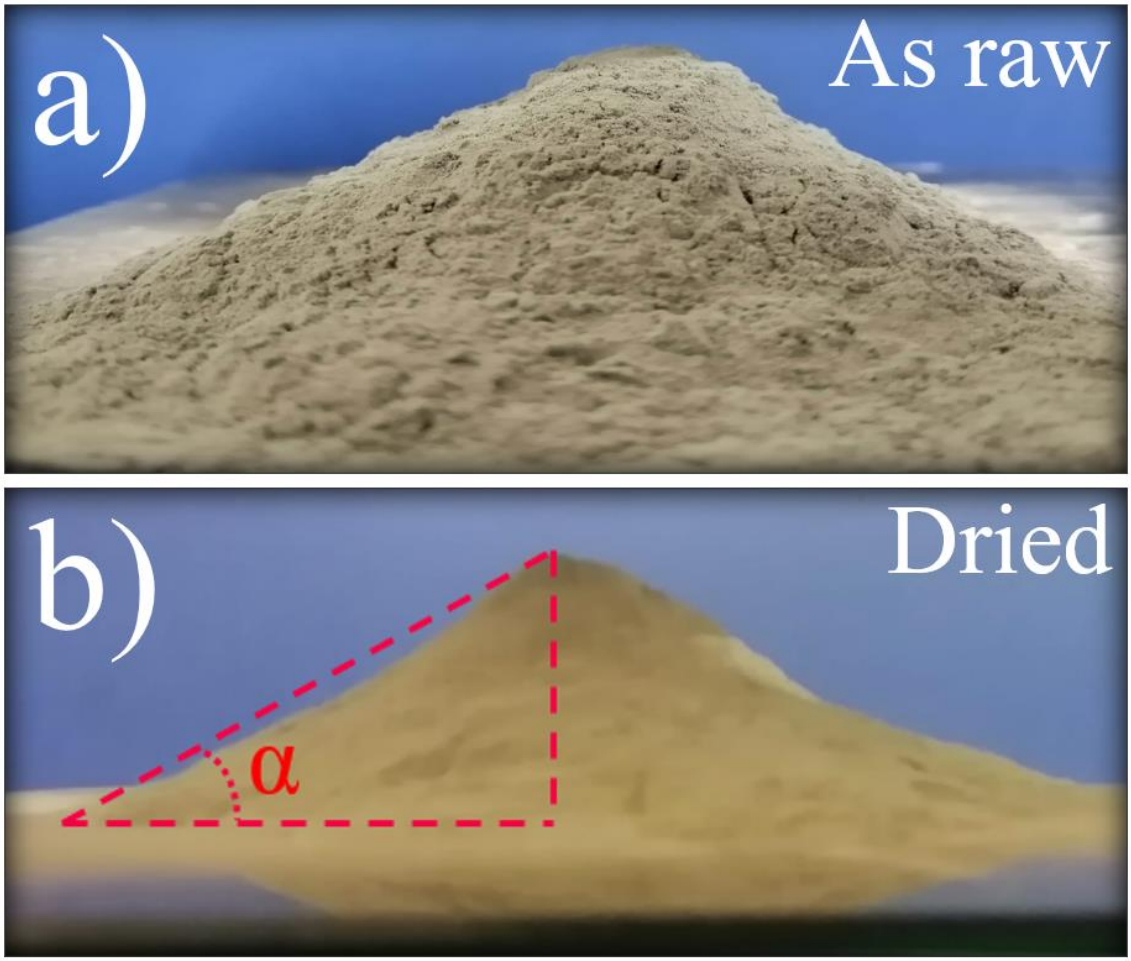

Figure 4. 35 – Static angle of repose of a) undried and b) dried M1_3Ce metal powder samples.

4.3.3.4. Density

The density of the powders used in this work was analyzed using different techniques: 1) Tapping Density, 2) Bulk Density, and 3) skeletal Density. The density of the metallic powders influences other characteristics of the material such as its fluidity, storage capacity, and distribution of the particles on the substrate, which will interfere with the density of the parts built by AM [218]. Various methods have been designed to measure the density of metal powders in storage, feeders, and even the density of the various layers of powder that are deposited on the substrate [219, 220]. The density of the powder is related to the particle size distribution and its morphology, preferring the use of spherical particles since they allow a greater fluidity of the powder [218]. Although there are various methods to determine the density of gas-atomized powder samples, this work only focused on these three methods. The results obtained are presented in **Table 4.6**.

Table 4. 6 – Density of M1_0Ce and M1_3Ce powders by different measuring methods. The densities values obtained by Hall/Carney funells and Arnold meter correspond to the bulk density.

Composition	Theoretical density	Hall Funnel	Carney Funnel	Arnold Meter	Tap Density	Skeletal density
M1_0Ce	2.76	1.36	1.41	1.43	1.81	2.72
M1_3Ce	2.82	1.45	1.48	1.49	1.87	2.76

The tapping density measurements were carried out according to the ASTM B527-15 standard. The data obtained showed that both samples obtained their maximum compaction after 500 blows, increasing the density by 18 ± 0.7 % and 17 ± 0.4 % for powders of composition M1_0Ce and M1_3Ce, respectively. These values were maintained in the dried powder samples. Both samples presented a Hausner Index of 1.2, which partially explains the low fluidity of the powder samples due to a high cohesive force between particles.

Bulk density is determined by Hall and Carney funnels, as well as by Arnold's method. Although this last method is not commonly used in the measurement of the density and fluidity of metal powders destined for AM

processes, it is representative of equipment whose powder supply is carried out by gravity, as reported by [209, 221]. Similar density values were obtained by applying these three methods, increasing slightly as the diameter of the funnel increased from 2.54 mm and 5.08 mm in Hall and Carney funnels to 31.6 mm using the Arnold's method.

Finally, the skeletal density measurement was carried out according to ASTM B923-22. The results revealed values similar to the theoretical density of each composition (98.6% and 97.9% for M1_0 and M1_3Ce compositions, respectively). It suggests that the gas-atomized powders produced in this work present a low internal porosity.

4.3.3.5. Reflectivity

Laser reflectivity was measured by diffuse reflectance UV–Vis spectroscopy (DRS). **Figure 4.36** shows the reflectivity of the powder samples using 1064 nm wavelength. Although the d_{50} values of the powder samples M1_0Ce and M1_3Ce are higher than other compositions reported in the literature, it can be observed that the reflectivity values are similar to those of AA7075 and AA2024 samples with d_{50} close to 30 µm and 40 µm, respectively. In contrast, particles with a smaller size, e.g. pure Al particles (d_{50} < 10 µm) or superficially modified by the addition of ceramic particles like AA2024 dopped with CaB_6 particles shall present a lower reflectivity. A reduction in the particle size favors a reduction of reflectivity, from 77.4 % for M1_0Ce powders to 71.8 % for M1_3Ce powders. A greater absorptivity allows the use of a lower energy density for the melting and deposition of the different powder layers during the printing of parts by LPBF. Consequently, it is possible to reduce build time by applying higher scanning speeds.

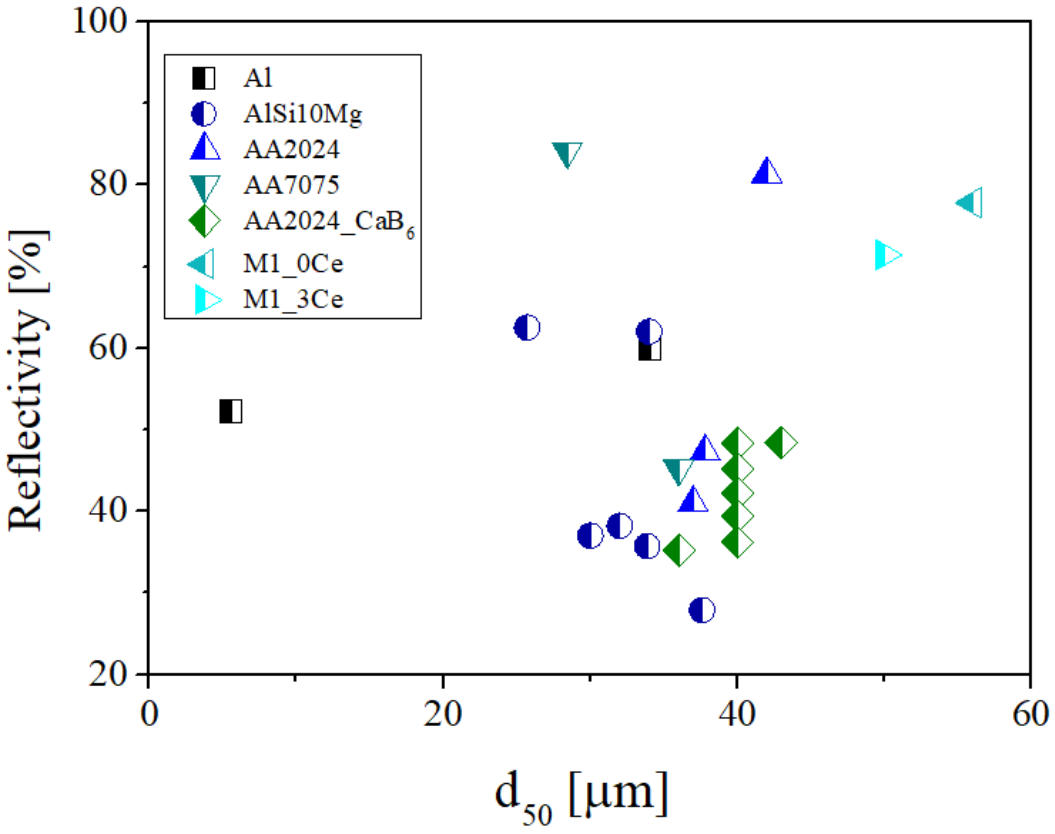

Figure 4. 36 – Reflectivity values of different aluminum powders used in AM processes. The data was quarried from the literature for Al [16, 222-227], AlSi10Mg [93, 228-234], AA2014 [106, 107, 136], AA7075 [78, 238], and AA2024 decorated with CaB_6 (0.1 – 2.0 wt. %) [106]. The reflectivity values for M1_Ce and M1_3Ce were obtained in this project.

4.3.4. Microstructural characterization

The powder samples were analyzed using the synchrotron XRD (Desy, Germany) and DSC techniques. **Figure 4.37** shows the XRD pattern of the M1_0Ce and M1_3Ce gas atomized powders, identifying the Al_2Cu phase (ICSD n° 42517, space group I4/mcm (140, Tetragonal) for the composition M1_0Ce and the Al_8CeCu_4 (ICSD n° 169061, space group I4/mmm (140), Tetragonal) and Al_3CeCu (ICSD n° 190993, space group I4mm (107)) phases for the M1_3Ce. The XRD - synchrotron results are in agreement with the XRD results previously mentioned for the cast samples.

Note that most of the phases suggested within the thermodynamic calculations were not detected by XRD. This may be because these phases coexist in a volume fraction that cannot be detected by this technique or due to the high cooling rates applied, which reduces the capacity for diffusion and formation of secondary phases during the solidification process. Likewise, the DSC curves shown in **Figure 4.38** did not reveal the presence of endothermic peaks. The formation of an exothermic peak was observed in the composition M1_0Ce at temperatures between 500 °C - 525 °C, characteristic of the formation of the Al2Cu phase, while for the composition M1_3Ce only the peaks are formed that reveal the presence of a composition close to eutectic.

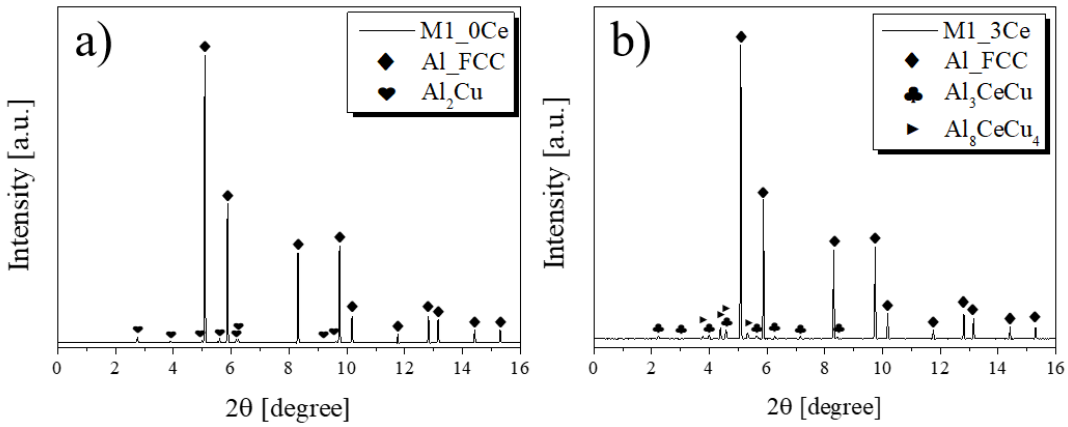

Figure 4. 37 – XRD synchrotron patterns for a) M1_0Ce and b) M1_3Ce gas atomized powders, with a particle size distribution between 20 – 63 µm.

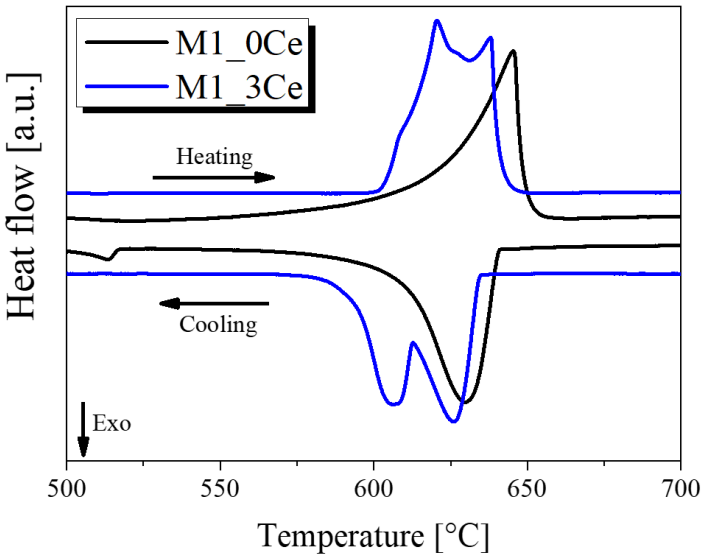

Figure 4. 38 – DSC curves for M1_0Ce (in black) and M1_3Ce (in blue) gas atomized powders.

4.3.5. Solidification Kinetics

The measurement of the secondary dendritic spacing in the powder particles of both alloys was performed by image analysis of approximately 1000 powder particles. **Figure 4.39** and **Figure 4.40** show an example of the microstructure of the powder samples at different particle sizes. **Figure 4.41** shows the relationship between particle size and average λ_2 for both compositions. An increase in the size of the particle generates a lower cooling rate, which favors the growth and thickening of the dendrites.

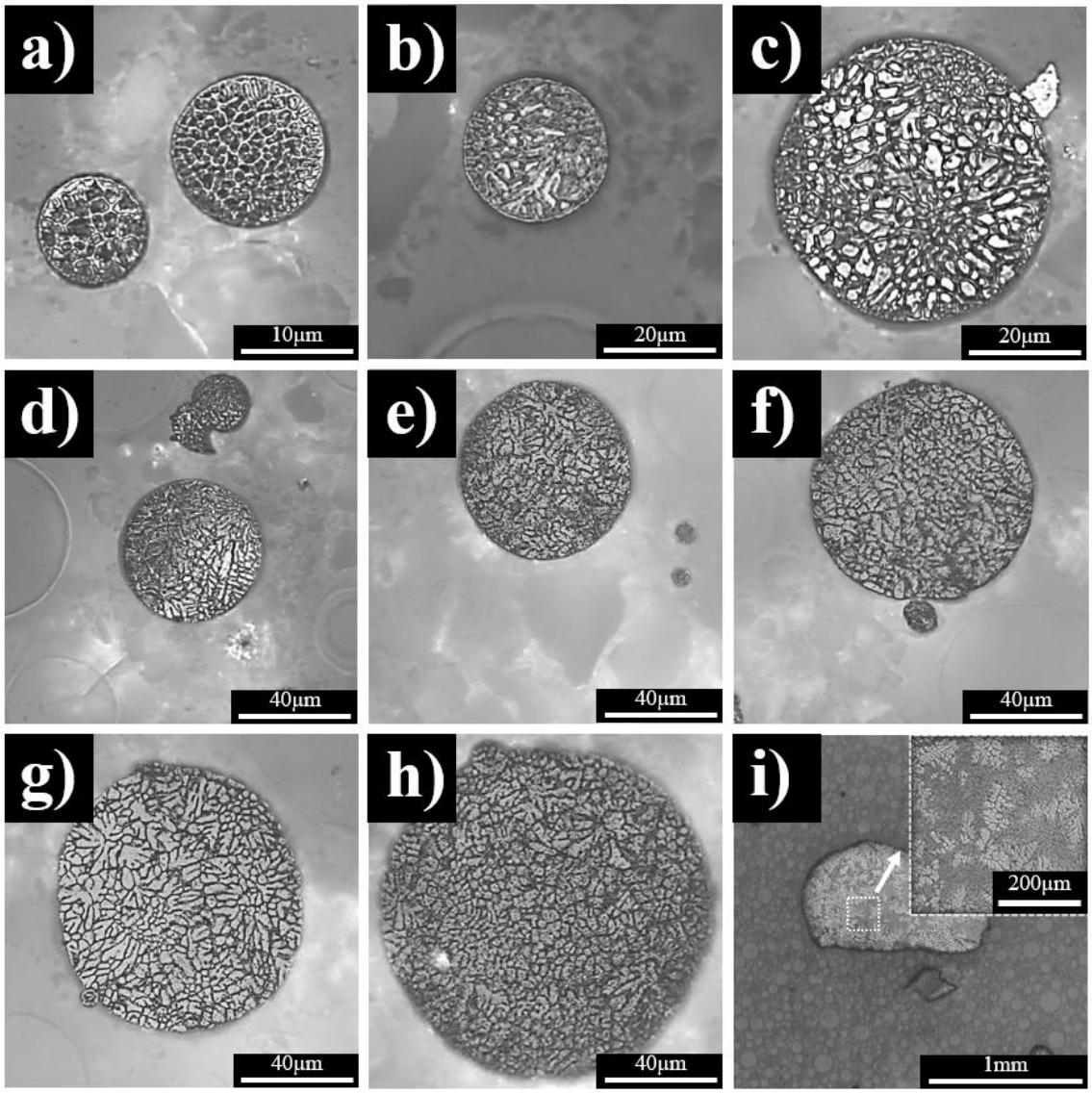

Figure 4. 39 – OM images of the M1_0Ce metal powders produced in this work showing the internal microstructure. The powders were analyzed according to their particle size range. In a) <20 µm; b) 20 - 32 µm; c) 32 - 45 µm; d) 45 - 53 µm; e) 53 - 63 µm; f) 63 - 75 µm; g) 75 - 106 µm; h) 106 - 150 µm; and i) >150 µm.

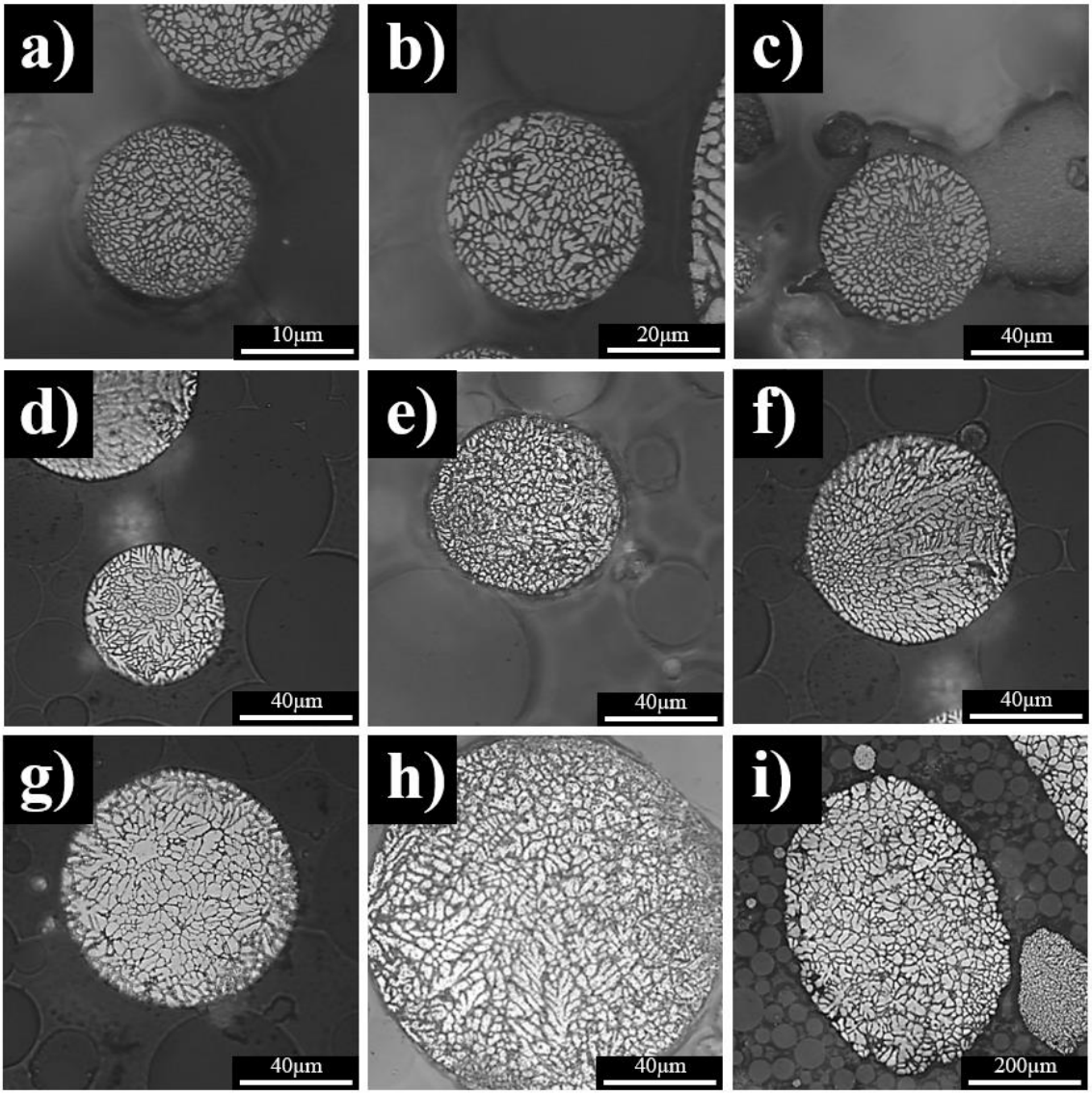

Figure 4. 40 – OM images of the M1_3Ce metal powders produced in this work showing the internal microstructure. The powders were analyzed according to their particle size range. In a) <20 µm; b) 20 - 32 µm; c) 32 - 45 µm; d) 45 - 53 µm; e) 53 - 63 µm; f) 63 - 75 µm; g) 75 - 106 µm; h) 106 - 150 µm; and i) >150 µm.

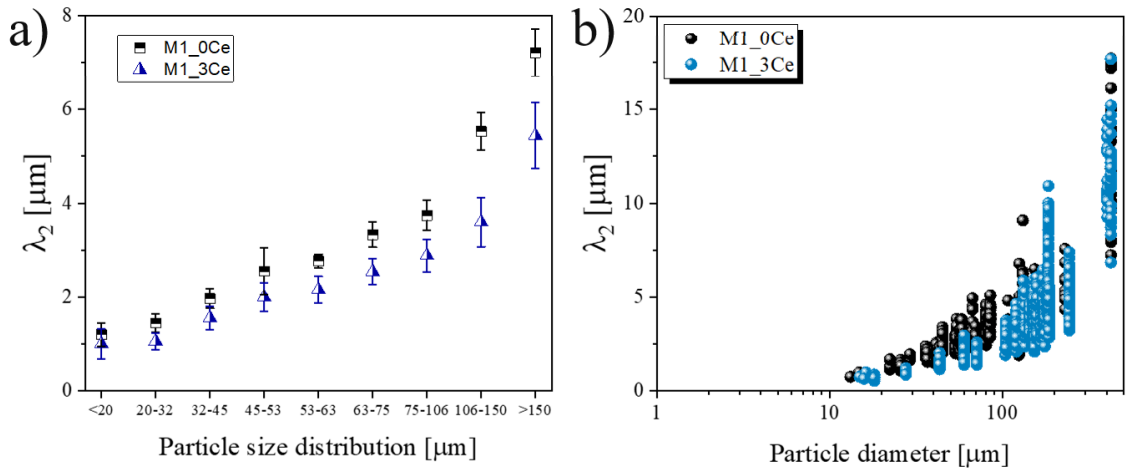

Figure 4. 41 – Secondary arm spacing of M1_0Ce and M1_3Ce metal powders versus a) the particle size range and b) particle diameter.

The cooling rate of metal powders produced by atomization is in the range of 10^2 – 10^7 °C·s^{-1} [236, 237]. Various authors have devoted part of their work to determining the solidification kinetics of atomized metal powders [238-243]. Nevertheless, from the mathematical models acquired through exploratory tests for directional solidification, it is also possible to determine the cooling rate of the particles, according to their size and composition. As seen in **Figure 4.42**, the mathematical models generated in this work are consistent with the mathematical models proposed by other authors, mainly for the M1_0Ce composition (**Figure 4.42**(**a**)), in which as the particle increases its size, it takes a longer time to solidify, remaining longer in a semi-solid state and favoring a greater probability of generating defects such as satellites due to collision and welding with smaller particles already solidified and loss of sphericity due to collision between particles or with the walls of the atomizer, among other factors.

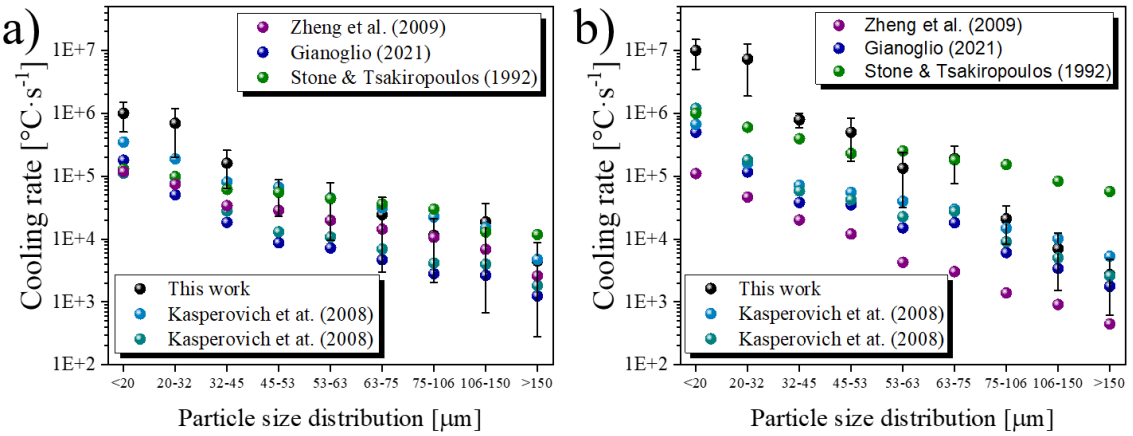

Figure 4. 42 – Estimation of the cooling rate as a function of the particle size range for a) M1_0Ce and b) M1_3Ce powders produced by gas atomization. The mathematical models used were obtained in this work and published previously by other authors [239-243].

4.4. Analysis of LPBF processing parameters

In order to select an optimal parameter combination to produce parts with high density and with the lowest possible density of defects, the DoE methodology was applied in this work, selecting the response surface method by applying a cubic design of face-centered (FCC, k = 3) [244]. The range of parameters used in this work (P, V, and H) are presented in **Table 3.1**. The response variables consisted of density, crack density, crack length, and microhardness values of the LPBF parts.

4.4.1. Density

Density values were obtained from image analysis using the free software ImageJ [153]. These values were used to determine the influence of the processing parameters. **Figure 4.43** shows the Pareto diagram of the standardized effects according to the density values obtained. In both compositions, the Laser Power (P) corresponds to the most influential parameter during the process followed by the Laser Scanning Speed (V), while hatching (H)

did not show a significant effect on the density of the parts built by LPBF. A similar behavior was reported during the processing of AlSi10Mg and AA6061 by LPBF and applying the surface response and full factorial DoE [245].

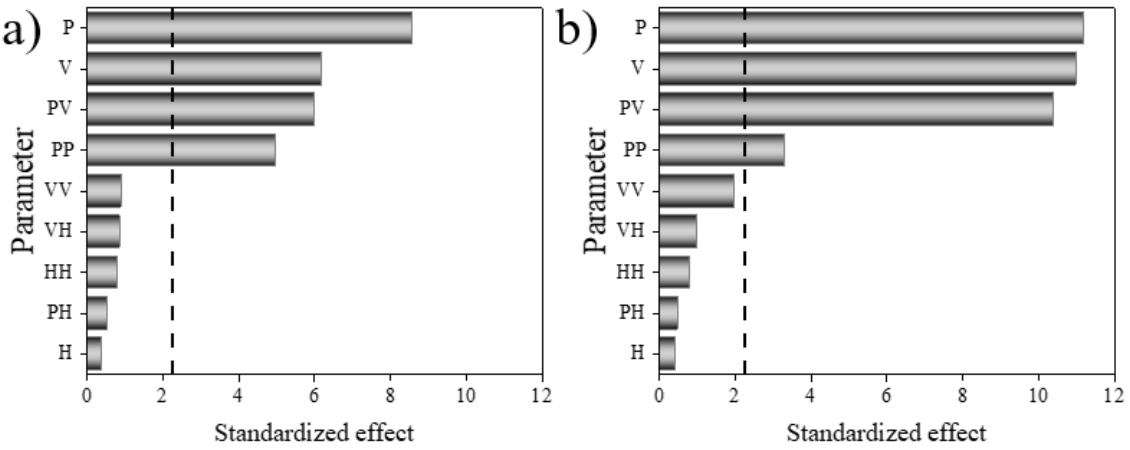

Figure 4. 43 – Pareto diagram of the standardized effects according to the density values obtained by OM for a) M1_0Ce and b) M1_3Ce compositions.

Figure 4.44 shows the interaction effect of laser power and laser scan speed on density values. The M1_3Ce shows a larger processing window than M1_0Ce, allowing building parts with a high density by applying higher scanning speeds. Parts with high density are favored by an increase in the applied laser power. Nevertheless, an excessive increase in laser power could cause internal defects in the as-built part, e.g. keyhole porosity, as reported by [245].

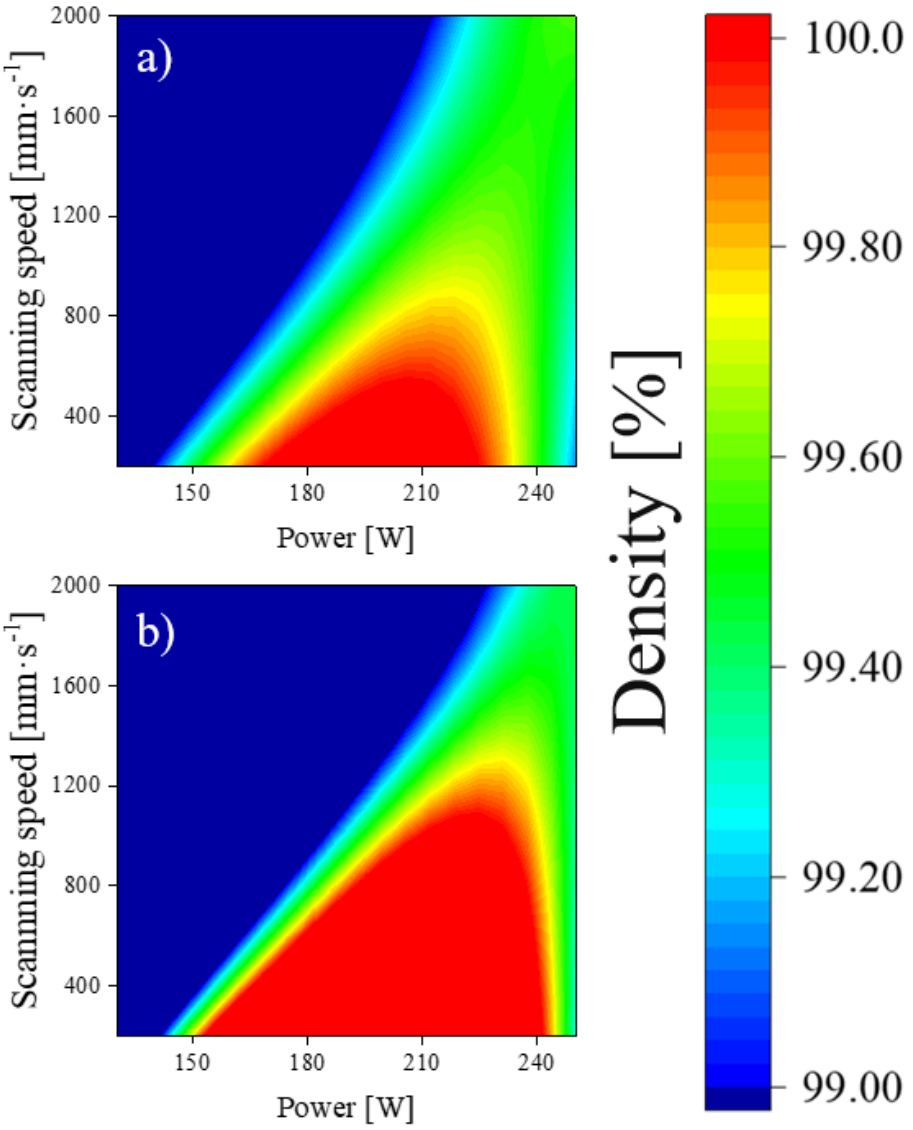

Figure 4. 44 – Density response surface plots for a) M1_0Ce and b) M1_3Ce compositions related to the variation of laser scanning speed and laser power applied during the LPBF process.

Figure 4.45 shows the microstructure obtained in M1_3Ce parts processed by LPBF using different processing parameters. **Figure 4.45**(**a**) shows the presence of incomplete fusion between adjacent layers (interlayer pores) due to the application of low power, which favors a lack of fusion [246, 247]. When low laser power is applied, the molten pool is not deep enough to melt and weld with the bottom layer; consequently, molten pools with a shallow depth are obtained as observed in **Figure 4.5**(**d**). The presence of porosity within individual

layers (intralayer pores) was not observed, which reinforces the idea that the hatching has not significant influence on the formation of pores in LPBF parts produced in this work, as corroborated in **Figure 4.44**.

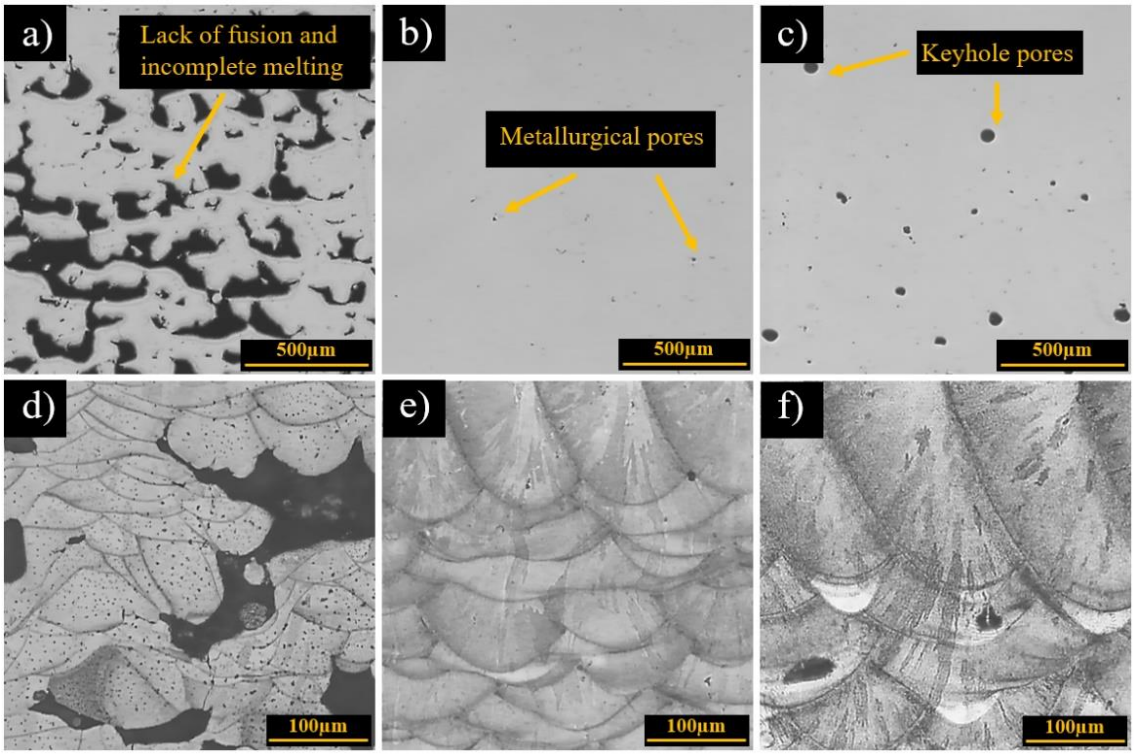

Figure 4. 45 – Microstructure and presence of defects in M1_3Ce parts processed by LPBF a - c) without and d - f) applying etching.

A higher energy density promotes the melt and union of deposited layers, favoring a reduction of porosity. As shown in **Figure 4.45**(**b**, **e**), by applying a higher energy density it is possible to obtain higher density values. For example, when applying energy densities of 160 J·m^2 and 280 J·m^2 using a laser power of 175 W, the density values are 96.26% and 97.4%, respectively; in contrast, an increase in laser power to 220 W allows obtaining parts with densities of 99.4% and 99.35%, applying the same energy densities. An excess in the applied laser power can cause a decrease in the density values due to the formation of keyhole porosities, as seen in **Figure 4.45**(**c**, **f**). The formation of these pores is caused by an excessive increase in the temperature of the melt pool, which favors the

evaporation of alloying elements and promotes the formation of spherical pores [248].

4.4.2. Hot cracking

Despite the important technological advances made recently to improve the processability of aluminum alloys within AM, the formation of defects such as hot cracks is one of the main challenges that hinder the incorporation of wrought aluminum alloys in processes such as LPBF. The main objective of this work focuses on adapting the composition of the AA2017 aluminum alloy to reduce its HCS during its processing by LPBF. Although density is a fundamental aspect when building parts using this technique, obtaining crack-free parts is also of great importance. Unlike other defects such as porosity, which can be reduced by applying secondary processes such as hot isostatic pressing (HIP) treatments, the cracks cannot be eliminated by these methods.

The results obtained in this work demonstrated that the modifications made in the composition of the AA2017 alloy and the addition of Ce as a new alloying element allowed obtaining crack-free LPBF parts, regardless of the selected parameter combination. In contrast, the parts built from the Ce-free composition show crack formation as seen in **Figure 4.46**. Note that the cracks are formed parallel to the building direction.

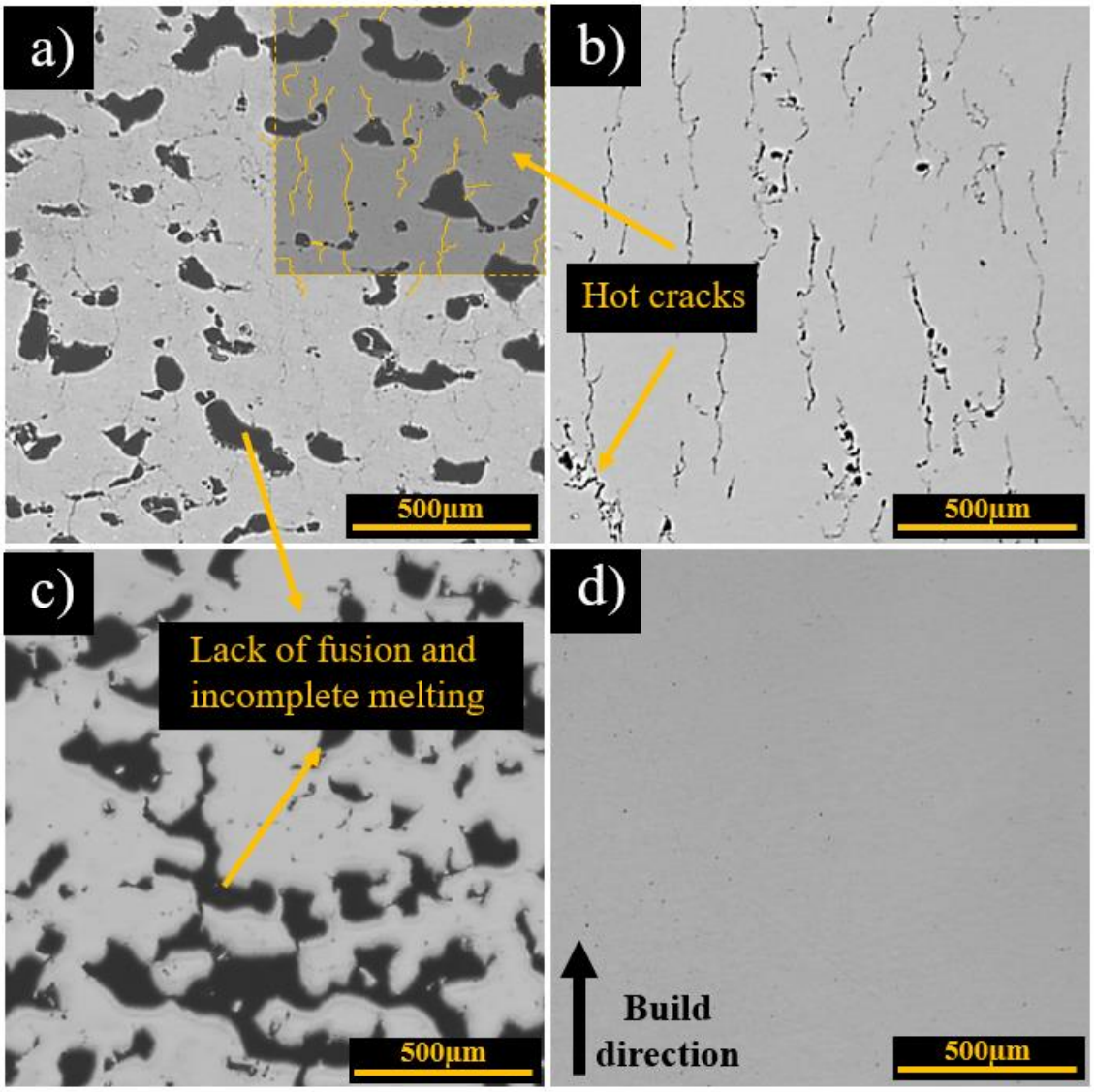

Figure 4. 46 – OM images of samples produced by LPBF using (a, c) worst and (b, d) optimal building parameters. The M1_0Ce parts (a, b) show the presence of hot cracks in both processing conditions while M1_3Ce (c, d) composition produced LPBF-parts without hot cracking

The formation of hot cracks is due to the intrinsic characteristics of wrought aluminum alloys as their wide solidification range, low permeability, and scarcity of liquid during the terminal stage of solidification, which favor a high HCS. This susceptibility is detrimentally increased during the building of LPBF parts due to the tendency for the formation of columnar microstructures caused by high thermal gradients (G) and cooling rates (R) [81].

Reducing the solidification interval of the alloy and increasing the amount of liquid available during the terminal stage of solidification can substantially reduce the HCS. Although the transformation from a columnar microstructure to an equiaxed one by adding inoculation agents that induce heterogeneous nucleation has proven to be an effective tool when obtaining crack-free metal parts [249, 250], this route was not contemplated in this research. In contrast, the addition of Ce favors a reduction in the solidification range and allows an increase in the amount of liquid during the final stage of solidification to fill the space between the grains, giving rise to the formation of eutectic zones [124].

Through image analysis, it was possible to determine the crack density and the average crack length in the M1_0Ce samples produced by LPBF. **Figure 4.47** shows the Pareto diagrams of the standardized effects according to the values of crack density and crack length. The length of the cracks is related to the three processing parameters (P, v, h) studied in this work, while the density of cracks is not drastically affected by the laser scanning speed. In both cases, the laser power is the most influential parameter. Haamoun *et al.* [245] have reported that an increase in energy density generates greater cracking in AA6061 parts built by LPBF. However, these authors attribute the scanning speed as the most influential parameter during crack formation for this alloy. Similar behavior has been observed in IN738LC superalloy parts processed by LPBF [251].

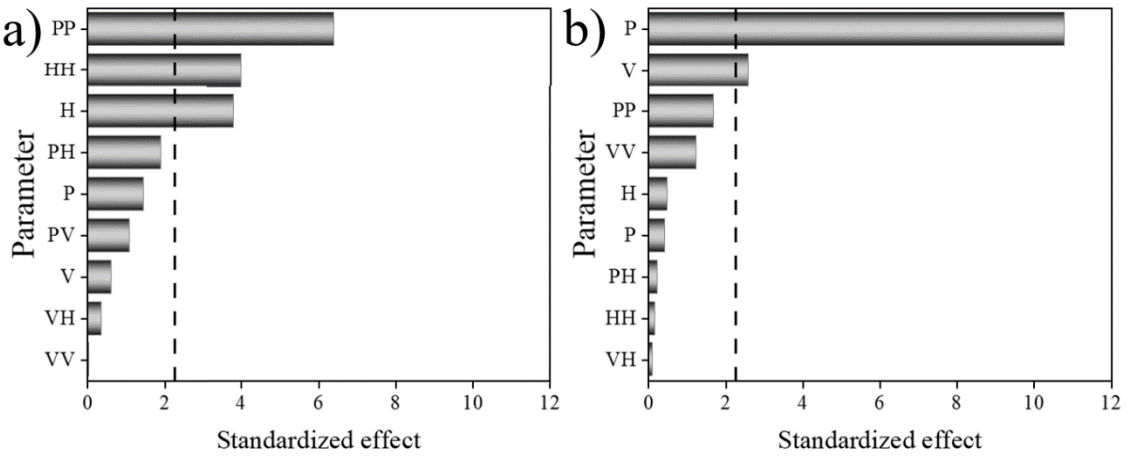

Figure 4. 47 – Pareto diagrams of the standardized effects according to the values of a) crack density and b) crack length for M1_0Ce composition.

Figure 4.48 shows the interaction effect of laser power, laser scan speed, and hatching on the characteristics of the cracks formed. It can be seen that laser power is the most influential parameter. The application of moderate powers (between 175 – 210W) could considerably reduce the density of cracks in the built part. A reduction in power favors obtaining cracks with a shorter length (**Figure 46**(**a**, **b**)); nevertheless, the values obtained in this work are related to the physical characteristics of the built parts. A reduction in power, as well as an increase in the hatching, leads to obtaining parts with a large proportion of unmelted regions due to an insufficient energy density applied [252]. These unmelted regions can act as barriers during the formation and propagation of cracks, which explains the presence of a high density of short cracks. In contrast, the parts with a higher density show cracks with a greater length, since these can propagate along the building direction. As previously mentioned, the processing of the Ce-free composition did not present an optimal combination of parameters that allows for obtaining crack-free parts.

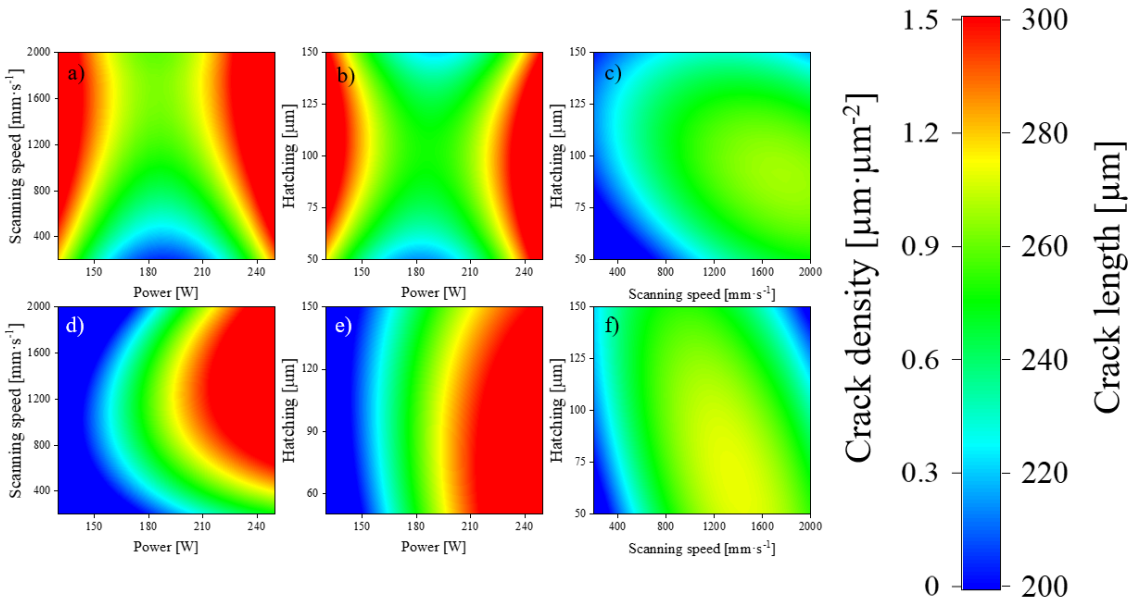

Figure 4. 48 – Surface response graphs for a - c) crack density and d - f) crack length in M1_0Ce parts built by LPBF.

4.4.3. Aspect ratio

The conditions in which the layer of metallic powder bed is melted play a fundamental role in the heat history, influencing the microstructural characteristics, the formation of defects, and the mechanical properties of LPBF parts. Conditional on the process parameters, the melting mode (keyhole or conduction modes) is different [247].

It has been reported that the type of porosity formed is highly dependent on the laser scanning speed due to the instability of the melt pool when high scanning speeds are applied [253]. However, **Figure 4.49** shows that the laser power is the parameter with the greatest influence when defining the characteristics of the melting well within the range of parameters studied in this work (*see* ***Table 3.1***). Sola and Noury [247] performed an extensive review of the literature on microstructural porosity in parts produced by AM, including work related to the processing of aluminum alloys. To reduce the porosity in as-built parts, the authors suggest using lower energy densities to reduce the formation of keyhole pores. They also advise adjusting the scanning strategy to rise the density of the as-built part. Likewise, it is recommended to carry out an adequate drying stage of the powders prior to their AM processing since one of the main causes of porosity in aluminum alloys is due to the trapping of gas from remaining moisture in the metal powder samples.

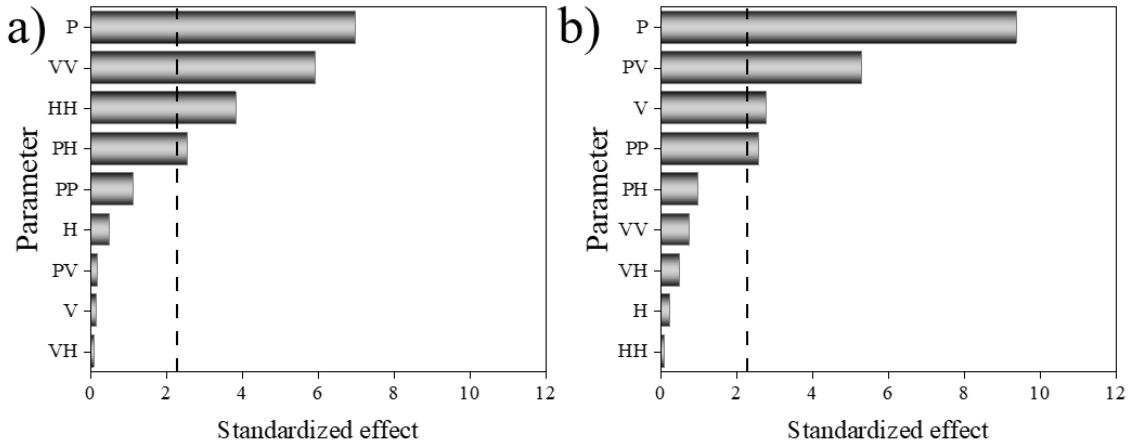

Figure 4. 49 – Pareto diagrams of the standardized effects according to the values of the aspect ratio of the melt pool in a) M1_0Ce and b) M1_3Ce LPBF-parts.

The application of low laser powers produces a small remelting region, favoring a conduction melting mode, which can induce a lack of fusion between the different layers if the laser power is insufficient to completely melt the powder bed [254]. In this sense, the depth of the molten pool well shall tend to be significantly less than its width as shown in **Figure 4.50**(**a**).

On the other hand, a keyhole melting mode (**Figure 4.50**(**d**)) shall present a larger remelted region that guarantees the union between the deposited layers [254], in addition to favoring a greater energy absorption due to an increase in laser reflections within it [255]. Nevertheless, this melting mode shall generate a change in the microstructure with deeper melt pools, in addition to increasing the probability of forming defects such as porosity caused by the partial boiling of the material [256, 257]; therefore, defining the threshold for the keyhole from an optimal combination of parameters is decisive to obtain parts with a low density of defects [81, 254, 255]. Considering this, it is recommended to work in a transition zone below the keyhole mode threshold as shown in **Figure 4.50**(**b**, **c**).

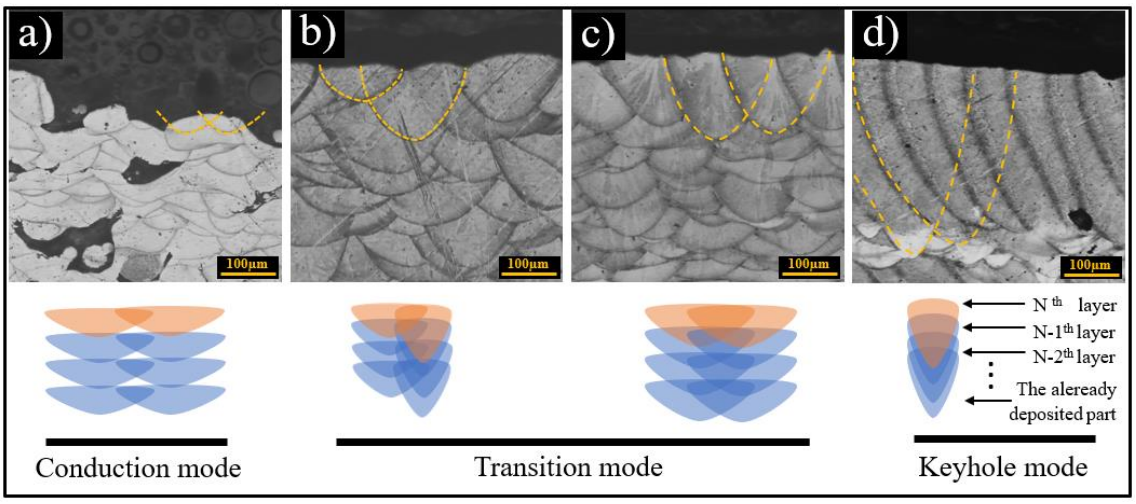

Figure 4. 50 – OM images and schematic representation of conduction-keyhole modes transition.

Figure 4.51 shows the interaction effect of processing parameters on the L/W ratio characteristics. Within this work, it has been established that the transition region from conduction mode to keyhole is obtained with a L/W ratio between 0.5 – 0.7. The transition range is determined empirically and shall depend on the process conditions, related to the characteristics of the machine and the raw material used, i.e. this relationship should be taken as a guide based on experimental data and not as a restriction when is selected an optimal processing parameter combination. L/W values have been reported to separate conduction mode from keyhole mode in S355 mild steel parts (0.4 [258]), AISI 409 steel (0.4 [259]), AA1100 aluminum (0.2 [259]), as well as AA7050 LPBF parts (0.5 – 1.2 [78]).

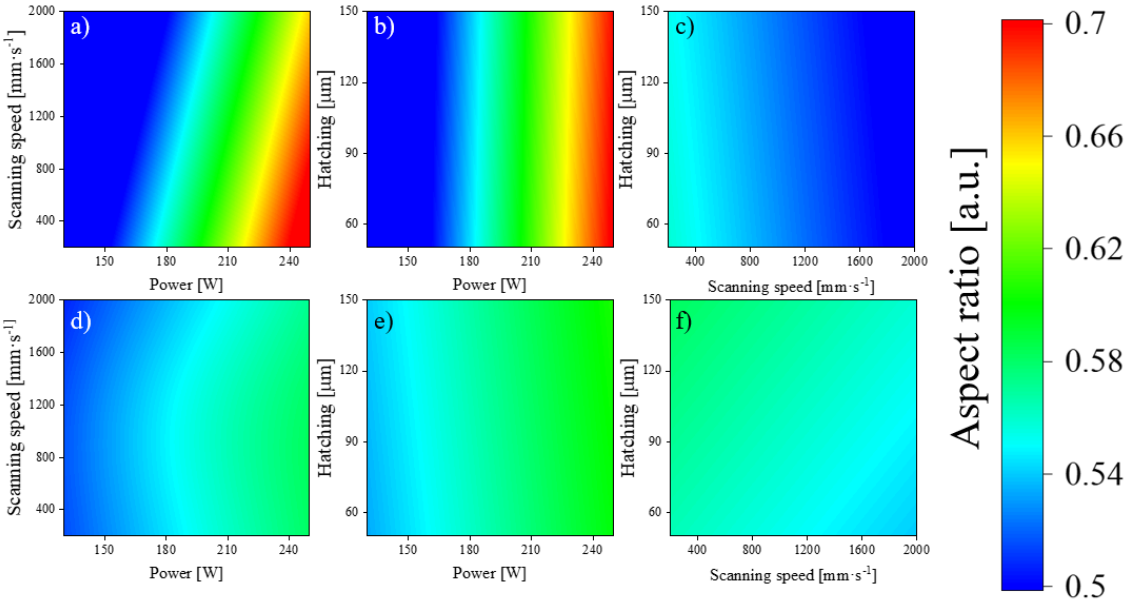

Figure 4. 51 – Surface response graphs of the aspect ratio in melt pools of a, c) M1_0Ce and d, f) M1_3Ce parts built by LPBF.

Although the L/W ratio works as an indicator to determine the type of molten pool formed, this is only an empirical relationship and it shall depend on the intrinsic characteristics of the material and the process. M.Cloots *et al.* [255] have established that in IN738LC parts built by LPBF, the keyhole mode is only elicited with melt pit depths greater than 100 µm, promoting the formation of keyhole porosity. In contrast, during this work, for both M1_0Ce and M1_3Ce compositions, it was shown that the variation in laser scanning speeds from 600 to 1200 mm·s^{-1}, applying a constant laser power (200 W), molten pools with a depth near 100 µm are obtained without forming keyhole porosity. On the other hand, increasing the laser scanning speed reduced the W and L values from 200 µm and 100 µm (L/W = 0.5) to approximately 115 µm and 55 µm (L/W = 0.5), respectively, causing the conduction mode.

4.4.4. Microhardness

In order to establish an adequate combination of parameters that allows obtaining optimal mechanical properties, the Vickers microhardness values of the parts were determined using a load of 200 gf and during 15 seconds. **Figure 4.52** allows us to glimpse that both the laser power and the scanning speed are the most influential parameters. **Figure 4.53** shows the interaction effect of processing parameters on microhardness values. In general, it can be observed that the addition of Ce within the composition of the AA2017 alloy significantly favors an increase in the microhardness of the material. The microhardness values for the M1_3Ce composition are favored by an increase in the power of the laser while, for M1_0Ce Composition, the microhardness is mostly influenced by the laser scanning speed.

The application of high laser power guarantees the melting and union of the different layers that make up M1_3Ce LPBF parts, while the application of high laser scanning speeds and greater hatching prevents excessive heat-trapping inside the part. In contrast, the Ce-free parts are mostly influenced by the laser scanning speed. An increase in microhardness values is obtained by applying low laser scanning speeds (close to 400 $mm \cdot s^{-1}$) and a laser power between 180 W – 210 W. In addition, the values for M1_0Ce LPBF parts are significantly lower than those for M1_3Ce LPBF parts.

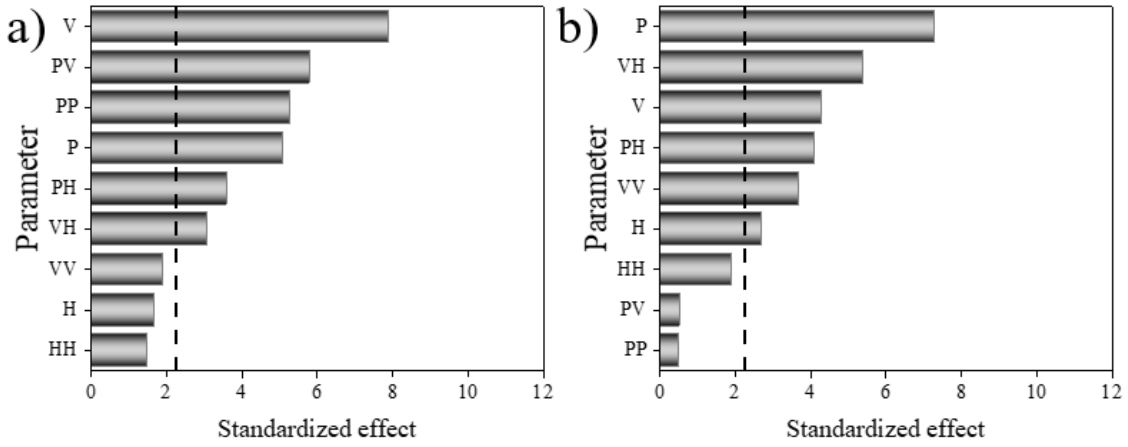

Figure 4. 52 – Pareto diagrams of the standardized effects according to the values of microhardness behavior in a) M1_0Ce and b) M1_3Ce LPBF-parts.

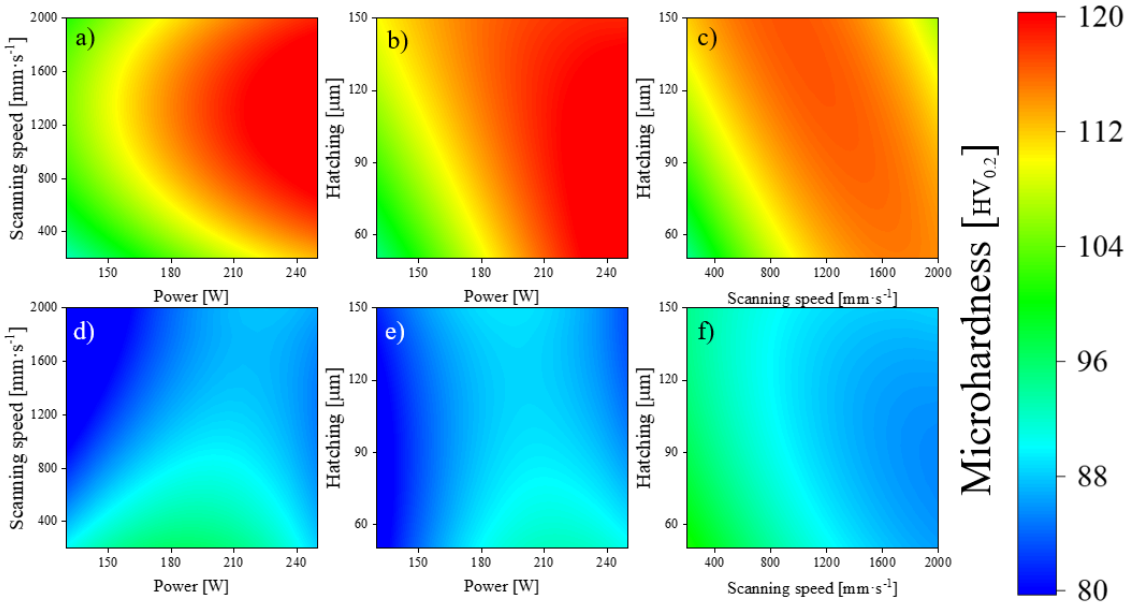

Figure 4. 53 – Surface response graphs of microhardness behavior of a-c) M1_3Ce and d-f) M1_0Ce parts built by LPBF.

4.4.5. DoE Validation and selection of optimal parameters for LPBF

From the results obtained previously, it is possible to obtain mathematical models that allow predicting the selected response variables, i.e. density, crack density, crack length, aspect ratio, and microhardness. As observed in the Pareto diagrams, some of the terms are not very relevant. Backward elimination was used to eliminate insignificant terms and obtain a reduced mathematical model without superfluous predictions. **Table 4.7** shows the coefficients obtained for each of the response variables. The general mathematical model developed in this stage of the research is presented below:

$$Variable\ of\ Response = C + a \cdot P + b \cdot V + c \cdot H + d \cdot P^2 + e \cdot V^2 + f \cdot H^2 + g \cdot P \cdot V + h \cdot P * H + i \cdot V * H \quad (3)$$

Table 4. 7 – Table of coefficients for each of the response variables considered in this work.

M1_0Ce

Response		C	P	V	H	P·P	V·V	H·H	P·V	P·H	V·H
Density	%	7E+01	3E-01	-1E-01	0E+00	-8E-04	5E-05	0E+00	0E+00	0E+00	0E+00
Crack Density	µm·µm-2	7E+00	-8E-02	0E+00	5-E2	2E-04	0E+00	-2E-04	0E+00	-5E-05	0E+00
Crack Length	µm	-2E+02	2E+00	1E-01	7E-01	0E+00	-3E-05	0E+00	0E+00	0E+00	-6E-04
Aspect ratio	a.u.	3E-01	1E-04	2E-04	2E-03	0E+00	-5E-07	-2E-05	0E+00	6E-06	0E+00
Microhardness	HV	4E+01	7E-01	-3E-02	9E-02	-2E-03	4E-06	0E+00	8E-05	-9E-04	5E-05

M1_3Ce

Response		C	P	V	H	P·P	V·V	H·H	P·V	P·H	V·H
Density	%	9E+01	2E-01	-1E-02	0E+00	-5E-04	-1E-06	0E+00	6E-05	0E+00	0E+00
Crack Density	µm·µm-2	0E+00	0E+00	0E+00	0E+00	0E+00	0E+00	0E+00	0E+00	0E+00	0E+00
Crack Length	µm	0E+00	0E+00	0E+00	0E+00	0E+00	0E+00	0E+00	0E+00	0E+00	0E+00
Aspect ratio	a.u.	7E-01	-5E-03	3E-04	0E+00	2E-05	0E+00	0E+00	-2E-06	0E+00	0E+00
Microhardness	HV	5E+00	3E-01	4E-02	9E-02	0E+00	-1E-05	-2E-03	0E+00	-2E-03	-1E+04

To validate the obtained mathematical model, samples with a random combination of parameters were produced. **Figure 4.54** shows the correlation between the theoretical values obtained from the mathematical models and the data collected from the characterization of the parts (in black). It can be observed that the validation points (in red) are coupled to the mathematical model made for the different response variables, remaining within the reliability region.

The juxtaposition of the different response surface maps allows for determining an optimal region, whose combination of parameters allows for obtaining the desired mechanical properties and microstructural characteristics in parts built by LPBF. Considering that only the composition with Ce presented crack-free parts; hence, parameter optimization was performed only for this alloy, seeking to maximize each of the response variables analyzed. **Figure 4.55** shows the optimal region selected, i.e. with a high density, hardness, and aspect ratio to build LPBF parts for mechanical analysis. From this graph, the following combination of parameters was selected: W=230W, v=1000 $mm \cdot s^{-1}$ and H= 100µm.

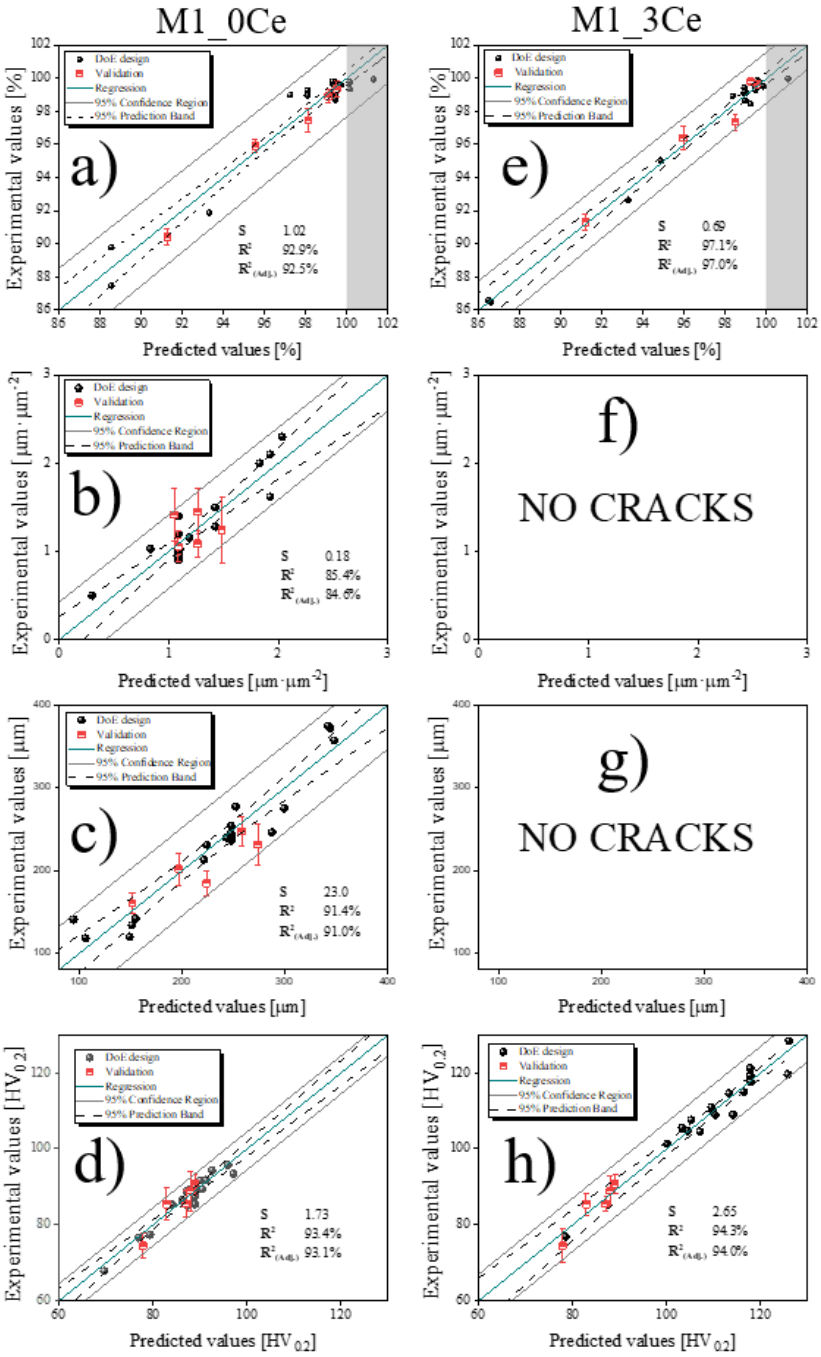

Figure 4. 54 – Plots of measured and predicted microstructural and mechanical characteristics in (a, d) M1_0Ce and (e, h) M1_3Ce LPBF parts. In a, e) density; b, f) crack density; c, g) crack length; and d, h) microhardness.

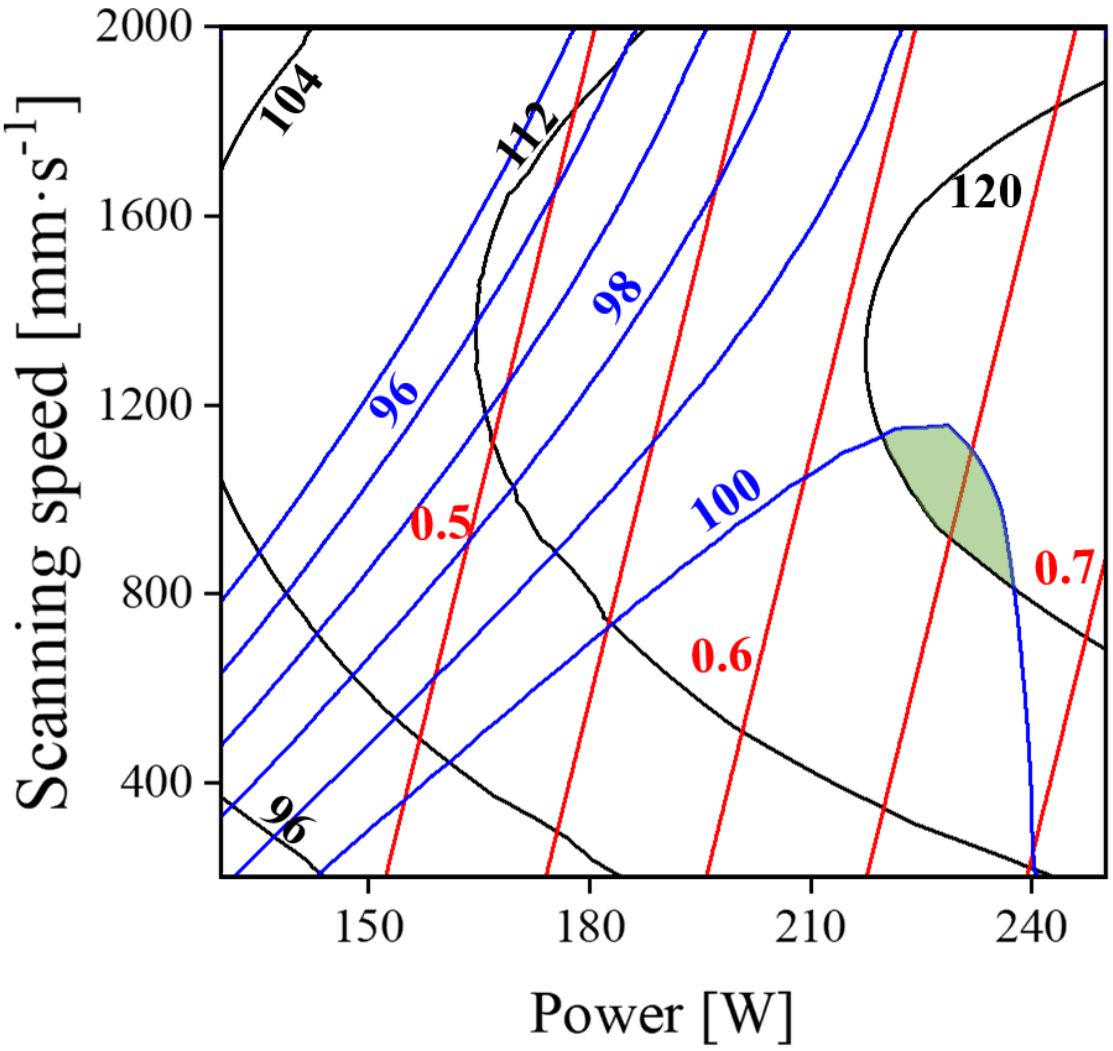

Figure 4. 55 – Overlaid contour plots of density (blue), aspect ratio (red), and microhardness behavior (black) of M1_3Ce parts considering the laser power and scanning speed range used in this work. For all the conditions is maintained a hatching of 100 µm. The green highlighted zone represents the optimal region to build parts with a high relative density and high microhardness, i.e. by applying a laser power between 220 – 240 W and laser scanning speed between 800 – 1150 mm·s^{-1}, maintaining a laser hatching of 100 µm.

4.5. Microstructural characterization

4.5.1. DSC

LPBF parts of the compositions M1_0Ce and M1_3Ce were analyzed by DSC. For comparison, both samples were built with the same processing parameters (W=230W, v=1000 mm·s^{-1} and H= 100µm). The DSC curves obtained are presented in **Figure 4.56**. Similar to the DSC curves presented in **Figure 4.10** in parts produced during the preliminary test and in **Figure 4.38** for gas-atomized powder samples, the Ce-free composition (M1_0Ce) presents a single peak during sample heating, which represents the solid-liquid transition of the material. Additionally, a peak is observed between 160 – 230°C corresponding to the formation of the Al_2Cu_θ phase, characteristic of Al-Cu base alloys [147]. The formation of this phase can also be observed in the cooling curves between 150 – 200°C. However, new peaks are found in the samples processed by LPBF, which stand out in the cooling curve between 480 – 520°C indicating the formation of the GP and θ′′ phases as previously reported in the literature [260].

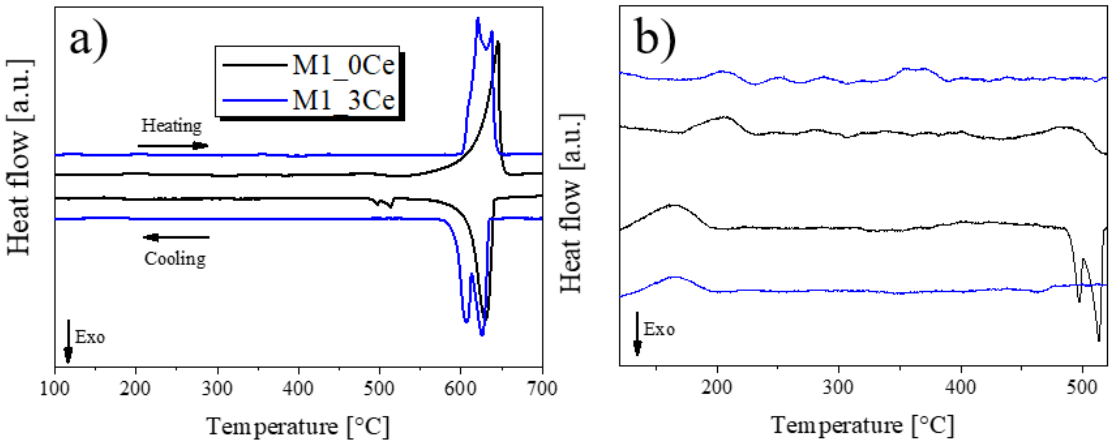

Figure 4. 56 – DSC curves of M1_0Ce and M1_3Ce LPBF parts processed using the best processing parameters, i.e. W = 230 W, V = 1000 mm·s^{-1}, and H = 100 µm. a) Full DSC spectrum and b) region between 120 °C and 150 °C, where the transformation peaks at low temperatures are detailed.

The DSC curves for the M1_3Ce samples reflect the two characteristic peaks of a "eutectic–like" composition, based in Al + Al_3CeCu phases, during the transition from solid to liquid. Likewise, the reduction of the solidification interval

caused by the addition of Ce in the composition M1 is corroborated, which favors a reduction of HCS. The heating curves allow us to observe the presence of various peaks between 200 °C – 400 °C. However, these peaks could not be detected in the cooling curves. This suggests the formation of secondary phases from alloying elements present in supersaturated solid solution due to high cooling rates [8]. Although the peak around 200°C may represent the formation of the Al_2Cu_θ phase, similar to M1_0Ce, the transformation that occurs at the 400°C peak is unknown, which may be connected to the formation of secondary phases.

4.5.2. XRD

The diffraction patterns of the M1_0Ce and M1_3Ce LPBF parts are presented in **Figure 4.57**. Both samples show the characteristic peaks of the Al_α phase, which is the main constituent of both alloys. For the M1_0Ce sample, the formation of the Al_2Cu_θ phase is observed. Although the high cooling rates offered during LPBF promote a supersaturated solid solution, the continuous deposition and melting of the different layers result in an intrinsic heat treatment. The continuous heating/cooling during the building process, as well as the presence of high Cu content in the alloy (4 wt. %Cu), can favor the formation of precipitates in the form of Al_2Cu. For the M1_3Ce samples, the Al_3CeCu and Al_8CeCu_4 phases were detected. The phases identified in the LPBF samples agree with the data obtained in AMI, SC, and LR samples, which suggests that the conditions of the LPBF process are not influential enough to create new metastable or secondary phases produced by intrinsic heat treatment processes.

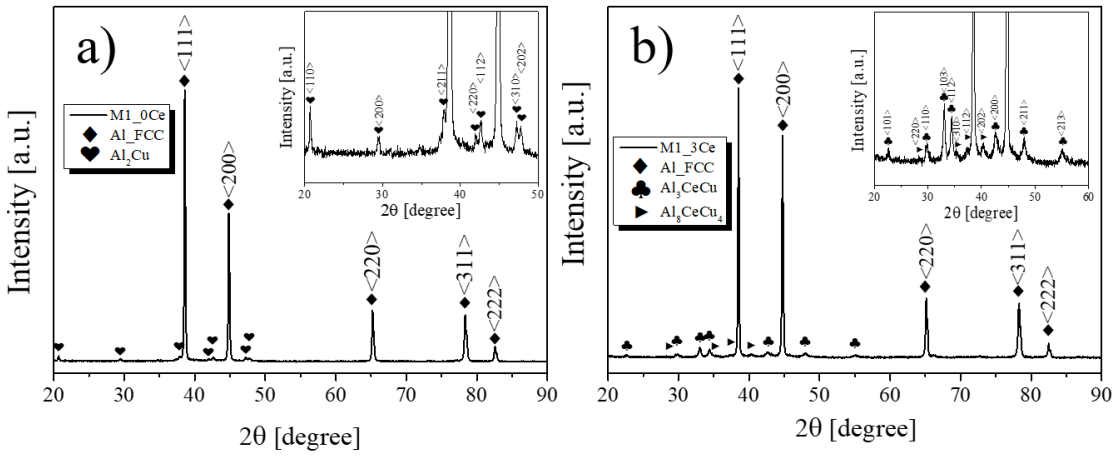

Figure 4. 57 – XRD patterns of M1_0Ce and M1_3Ce LPBF-parts processed using the best processing parameters, i.e. W = 230 W; v = 1000 mm·s^{-1}; H = 100 µm.

LPBF parts of the M1_3C composition were also analyzed by synchrotron XRD. This allowed obtaining an XRD pattern with higher signal tto noise ratio, revealing the peaks in greater detail. The XRD pattern obtained is shown in **Figure 4.58**. The analysis demonstrates that the LPBF samples present the same phases detected in the gas-atomized powder with a slight shift of the peaks towards the left part of the graph (around 0.01 °). Likewise, the highest intensity peak changes from <111> to <200>. The peaks of the secondary phases Al_3CeCu and Al_8Cu_4Ce are present with a lower intensity due to a lower volume fraction within this sample. The low concentration of these phases may be due to the high cooling rates applied during the process, with a lower time for diffusion. Even so, it is not possible to obtain a completely monophasic microstructure, i.e. solely composed of Al_FCC. This is because the high content of alloying elements (around 9 wt. %) reduces the possibility of generating a completely supersaturated microstructure. During the final stage of solidification, the remaining liquid, rich in alloying elements, solidifies around the aluminum cells forming a network similar to those observed in Al-Si(Mg) parts produced by AM, in which a fine Si network surrounds the Al cells (*See **4.5.3 Section***). Likewise, the constant thermal cycles during the processing promote intrinsic heat treatments allowing the formation of secondary phases detected by synchrotron

XRD. The presence of these phases represents an improvement in mechanical strength, acting as reinforcement phases, similar to what has been observed in the samples produced by AMI, SC, LR, and DS.

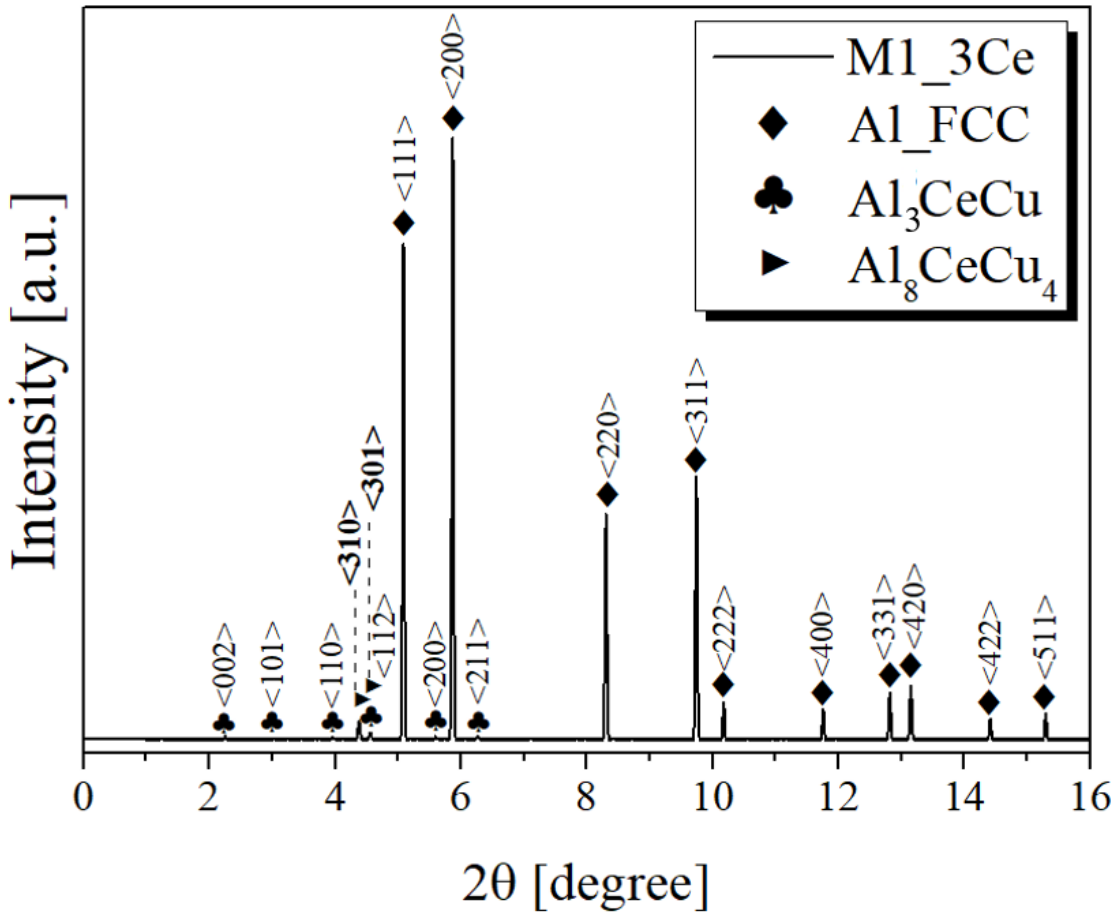

Figure 4. 58 – XRD synchrotron pattern for the M1_3Ce sample built by LPBF technique.

To analyze in greater detail the microstructural characteristics of the LPBF parts, as well as the possible formation of other secondary phases, the samples were analyzed by SEM-EDX, SEM-EBSD, and SAED-TEM techniques.

4.5.3. OM and SEM

The M1_0Ce and M1_3Ce LPBF parts were analyzed by scanning electron microscopy (SEM), using the EDX and EBSD techniques. Before using these techniques, samples produced with the same combination of parameters

(P = 230 W; V = 1000 mm·s^{-1}; H = 100 µm) were previously analyzed by optical microscopy (OM) as shown in **Figure 4.59**. It can be observed that both alloys present columnar grains, parallel to the direction of construction. For M1_0Ce composition, hot cracks mainly grow through the melt pools and between the grains (intergranular hot crack). Since both samples present a highly refined microstructure, it was not possible to analyze in detail the molten pools and the microstructure generated. For this reason, an analysis by SEM was performed.

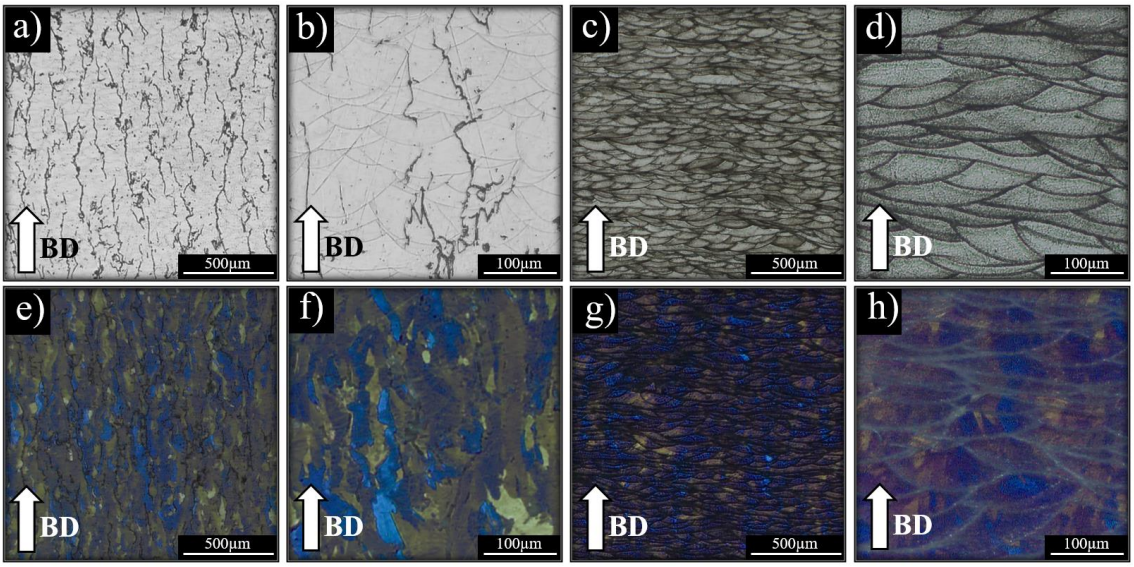

Figure 4. 59 – OM images in (a-d) true color light and (e-h) polarized light conditions. In (a, b, e, f) M1_0Ce and (c, d, g, h) M1_3Ce LPBF parts.

Figure 4.60 shows the microstructure and hot cracks formed in the M1_0Ce composition. In **Figure 4.60**(**a**) it is possible to see how the grains are arranged through the melt pool. In **Figure 4.60**(**a**–**c**) it is verified that the cracks are mainly formed on the grain boundaries due to a lack of liquid during the final stage of solidification, while in **Figure 4.60**(d, e) it is shown solidification microstructure at high magnifications. The hot crack grows and propagates through the build direction as new layers are deposited. In as-built parts, the propagation of intergranular cracks (along the edge of the fusion pool) or transgranular (through the melting pool) coexist in a smaller proportion. This behavior has been observed in different aluminum alloys parts processed by AM, e.g. on AA6063 parts produced by LPBF [261].

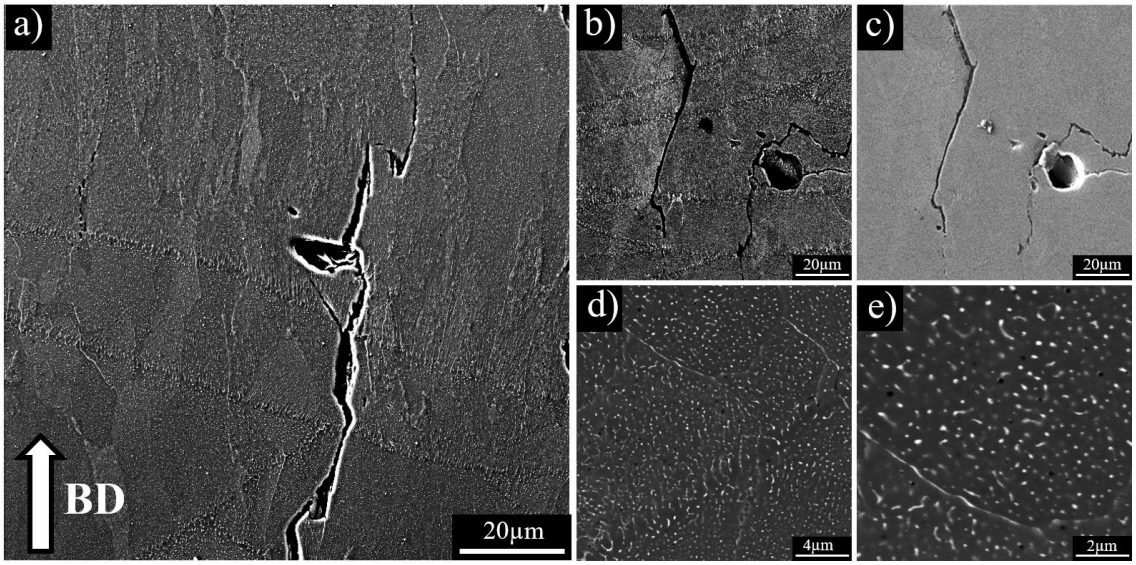

Figure 4. 60 – SEM images at different magnifications for M1_0Ce LPBF parts. In a) it is possible to observe the formation of intergranular hot cracking. In b, c) SEM in BSE and SE conditions, respectively, where it is possible to observe the formation of intergranular and transgranular hot cracks and porosity. In d) and e) the microstructure in higher magnification.

The microstructural characteristics of the M1_0Ce parts produced by LPBF were determined by the EBSD technique. **Figure 4.61** shows the inverse pole figure (IPF) map. The M1_0Ce part exhibits a weak texture, as observed in the (001) pole figures (**Figure 4.61**(**b**)), with a maximum intensity of 2.32, while the inverse pole figures show a maximum intensity of 2.035 over the plane [001]. The microstructure presented a mean grain size of 13.23 µm. **Figure 4.62** shows the aspect ratio (AR) and circularity (CR) of the measured grains. It can be seen that the grains presents mean values of AR and CR of 0.36 and 0.33, respectively. This is coherent with the thermal history of the sample and the manufacturing process (LPBF) where the high GxR applied produces elongated grains parallel to the direction of heat extraction.

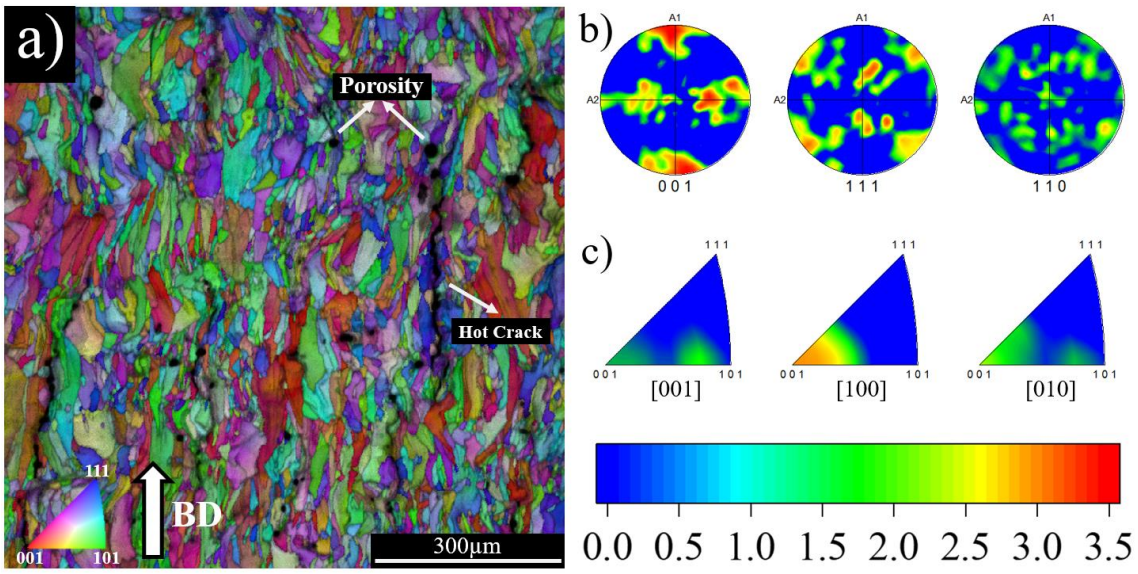

Figure 4. 61 – EBSD analysis of M1_0Ce composition processed by LPBF. In a) IPF-IQ map; b) pole; and c) inverse pole texture graphs.

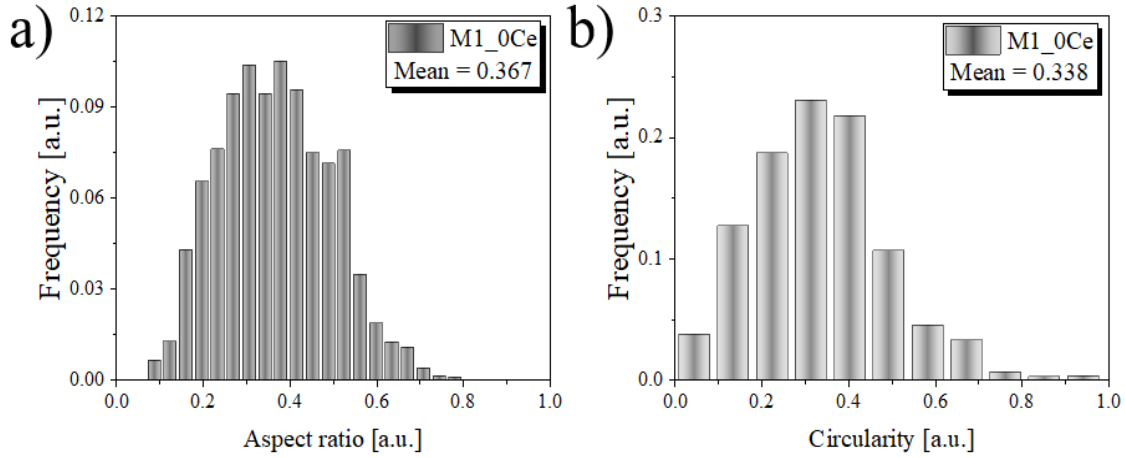

Figure 4. 62 – Grain characteristics by EBSD analysis of M1_0Ce LPBF-parts. In a) aspect ratio and b) circularity.

Figure 4.63 shows the kernel average misorientation maps for the composition M1_0Ce. Although the images show that the misorientation degree is greater near the hot cracks, the sample presents a fairly homogeneous disorientation of the grains. **Figure 4.63**(**d**) highlights how the grains with a high internal misorientation degree [1° – 1.5°] coincide with regions with cracks. Furthermore, an analysis in 3 different positions shown in **Figure 4.63**(**a**) of the sample was performed to observe the variation of the disorientation. As shown in

Figure 4.64, the regions close to the hot crack present an increase in the misorientation degree. In contrast, position (I), free of cracks, presents an average misorientation. It has been reported that an increase in the misorientation degree favors a higher hot cracking probability in AA6061 [261] and Ni-base Superalloy [262] parts built by additive manufacturing.

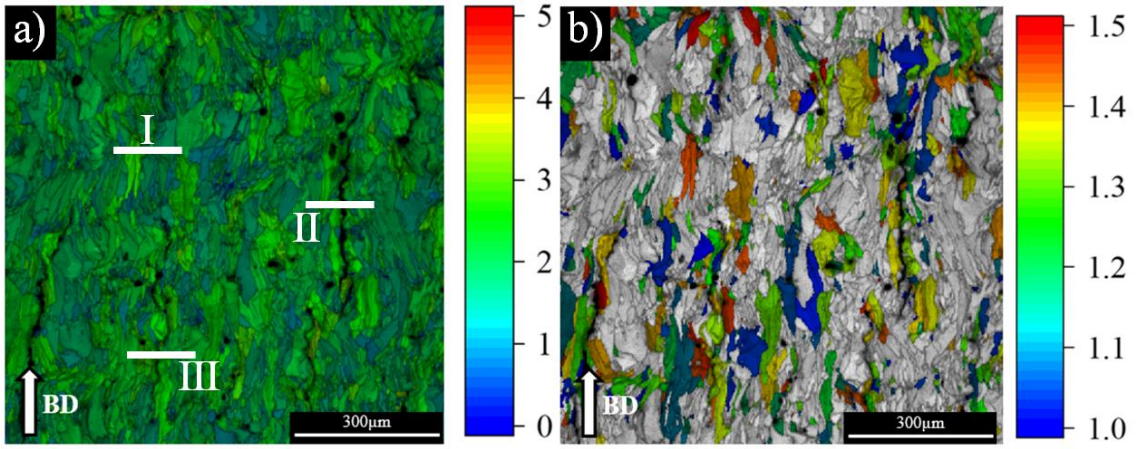

Figure 4. 63 – The KAM analysis of M1_0Ce LPBF-parts. In a) using misorientation angle intervals between a) 0 – 5° and b) 1 – 1.5°. In the I, II, and III positions highlighted in Figure 4.63(a) were carried out misorientation profile measurements to determinate its correlation with the formation of hot cracks.

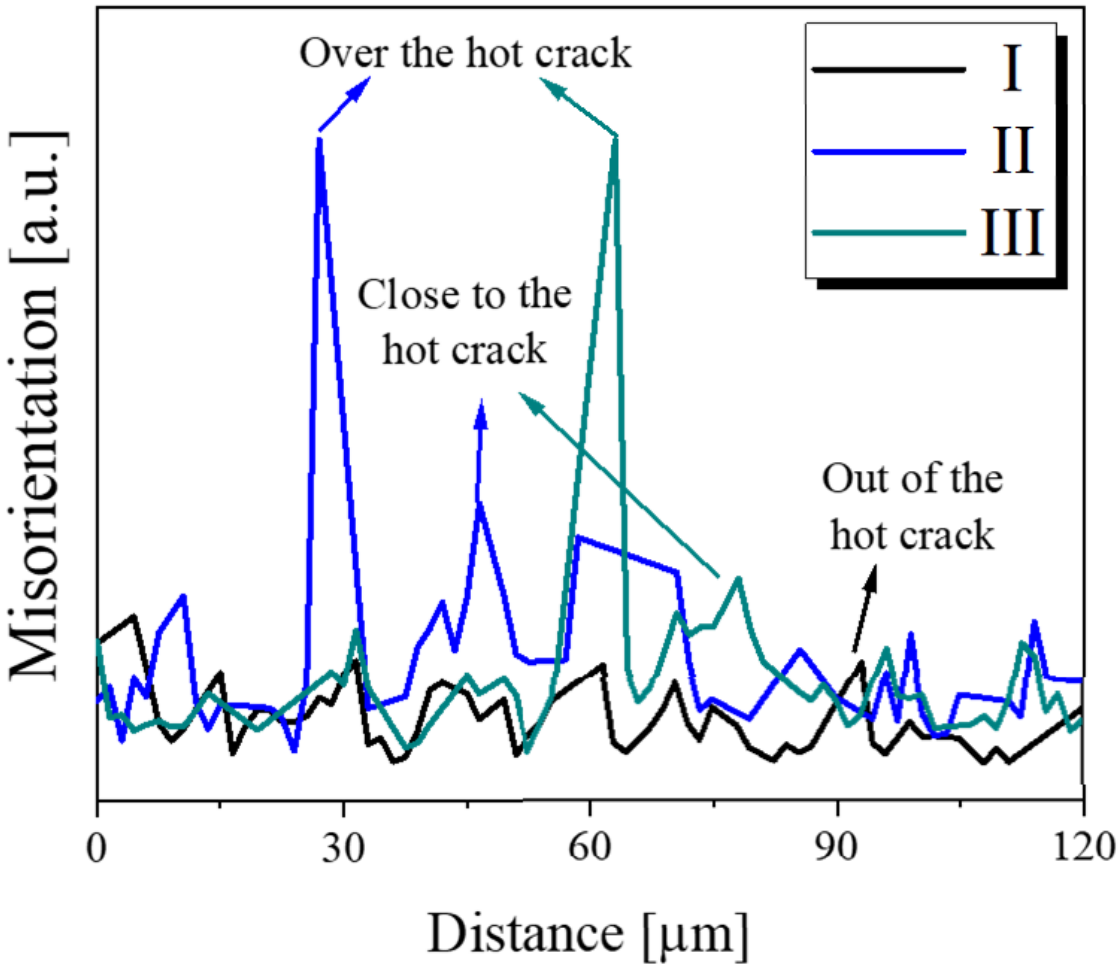

Figure 4. 64 – Misorientation profiles of the I, II, and III positions highlighted in Fig. 4.63 a).

To verify if the hot cracking is also formed by the segregation of the alloying elements, EDX mapping was performed in the area analyzed by EBSD. However, as depicted in **Figure 4.65**, a detailed examination of the segregation of alloying elements near the cracked regions is not feasible. To ascertain the presence of such segregation, employing more sophisticated techniques with higher precision is recommended, as described by Zhou *et al.* [262] where it was applied the electron probe X-ray microanalysis (EPMA) technique to observe the segregation of Al and Ti on the dendrite contour of MC2 (Ni-based Superalloy) components manufactured via DED, which can promote crack formation.

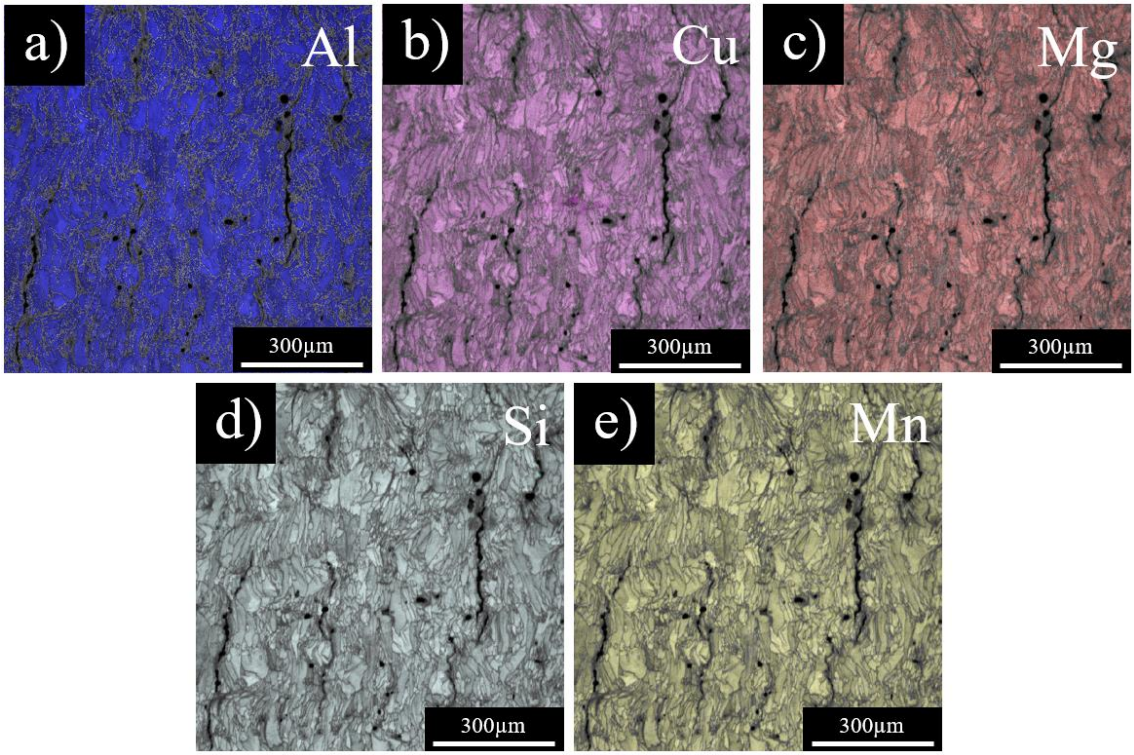

Figure 4. 65 – EBSD-EDX mapping of M1_0Ce compositions processed by LPBF. In a) Al, b) Cu, c) Mg, d) Si, and e) Mn.

Figure 4.66 shows the SEM-BSE images of the M1_3Ce parts produced by LPBF. The as-built part presents a homogeneous and highly refined microstructure. Furthermore, it can be seen that the solidification microstructure of the M1_3Ce part is more refined (average grain size of 9.17 µm) compared to the microstructure of the M1_0Ce composition (*see* ***Figure 4.59***). Although Plotkowskia *et al.* [121] have reported the presence of three different microstructures in laser-remelted parts within the melt pool, in the present work, only two of these regions could be recognized.

The edge of the molten pool, presents coarse cells growth to the center of the molten pool. This region, shown in **Figure 4.66**(**b**, **c**), presents a width of between 4 µm – 6 µm. As the molten pool solidifies, the thermal gradient decreases and the growth rate increases, resulting in a highly refined cell-like microstructure. Within this work, the formation of defined transition regions was not observed. Nevertheless, before the molten pool, a small region can be observed, with grains slightly larger than the cellular microstructure present in the

layer previously deposited, but more refined than the structure of the edge of the melt pool with coarser grains, considered as the heat affected zone (HAZ). The microstructure obtained in the parts produced by LPBF is highly refined. This prevented a detailed analysis of the distribution of the alloying elements by SEM-EDX technique. Nevertheless, it is presumed that the white regions surrounding the aluminum cells correspond to eutectic regions formed during the solidification of the material.

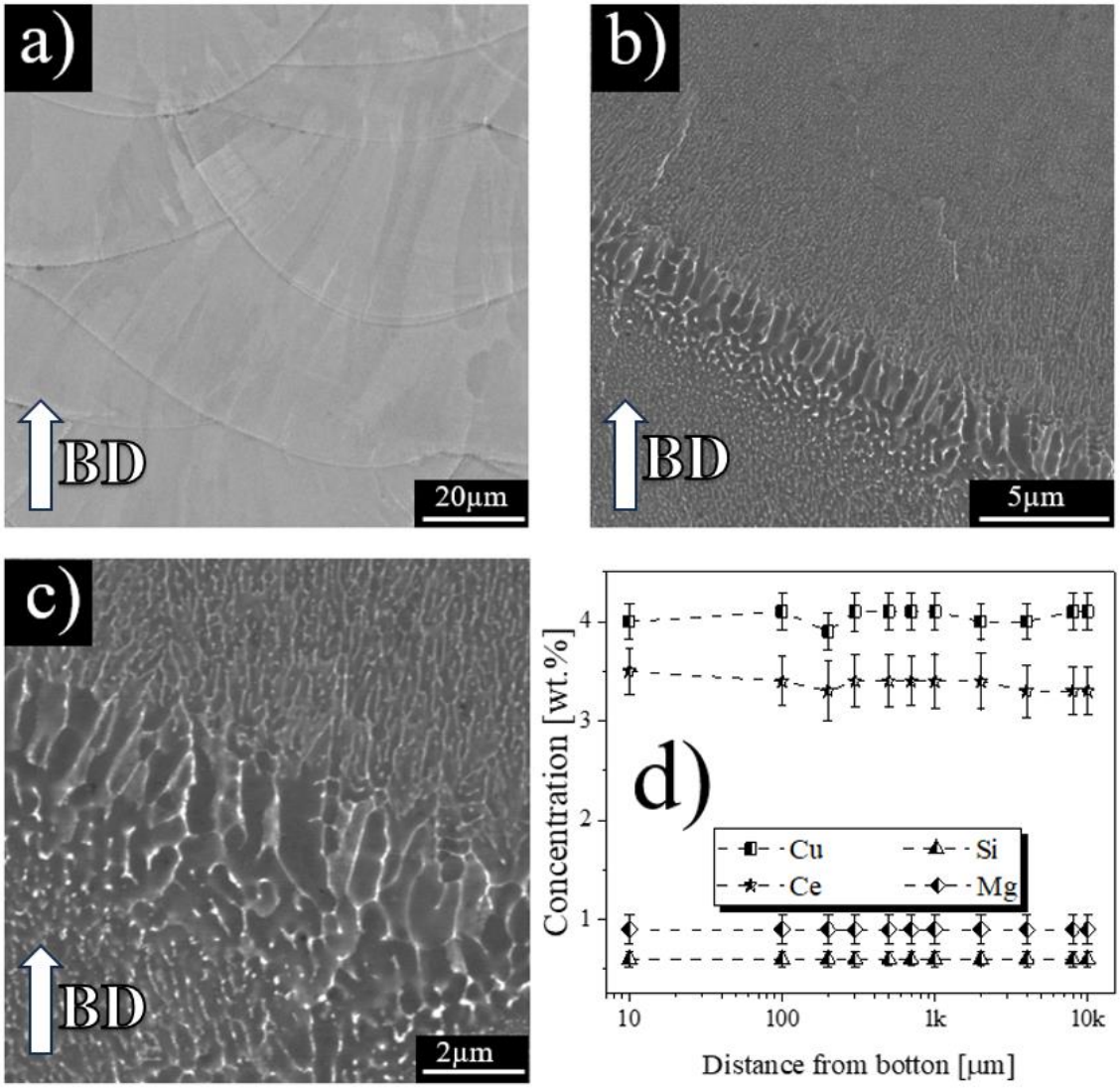

Figure 4. 66 – SEM-BSE using different magnifications and elemental EDX analysis in M1_3Ce LPBF-parts at different positions. In a) it is possible to observe the formation of grains through the melt pools; in b) and c) melt pool edge at 10000x of magnification; and in d) the alloying element concentration at

different positions from the bottom to the top of the as-built part (cube of 10cm^3). The compositions shown in Figure 4.55(d) must be interpreted qualitatively and not quantitatively.

To determine the existence of representative variations in the concentration of the alloying elements throughout the built part, EDX measurements (in areas of approximately 0.02 mm^2) at different heights of the part were performed. The results are presented in **Figure 4.66**(**d**). Measurements show that the concentration of the main alloying elements tends to be quite homogeneous, showing slight variations in Cu and Ce concentrations. However, Si and Mg concentrations tend to be stable along the direction of construction. This demonstrates optimal thermal stability of the alloy and the alloying elements, in which a loss of elements caused by diffusion or evaporation was not detected, as is usually reported for low melting point elements such as Mg [263].

The M1_3Ce parts presented a more refined solidification microstructure compared to the parts of the M1_0Ce composition and the microstructures reported by Plotkowskia *et al.* [121] in laser-remelted Al-Ce parts. Due to the high refinement of the obtained microstructure, it was not possible to perform EDX mapping to determine the distribution of alloying elements within the melt pool. Considering the above, at this stage, it was decided to carry out a linear analysis on the red line demarcated in **Figure 4.67**(**a**). A slight variation in the content of Ce and Cu generated in the melt pool was observed. The concentration of these elements is usually constant throughout the measurement. It is noted that the measurement peaks coincide with the brightest regions of the image (eutectic region), while the lowest values of the concentration of these elements coincide with the darker regions (Al). This behavior becomes more noticeable on the melt pool edge. A subsequent point analysis was carried out in the light and dark areas of the region demarcated with a dashed white line in **Figure 4.67**(**a**) and whose results are presented in **Figure 4.67**(**b**).

The Mg concentration along the measurement line shows most uniform distribution as shown in **Figure 4.67**(**a**). In contrast, the Si concentration varies significantly along the measurement line in which, towards the edge of the melt

pool, Si shows the lowest concentration values, while towards the center of the melt pool its concentration increases, demonstrating the diffusion of this element during the melting and solidification of the different tracks.

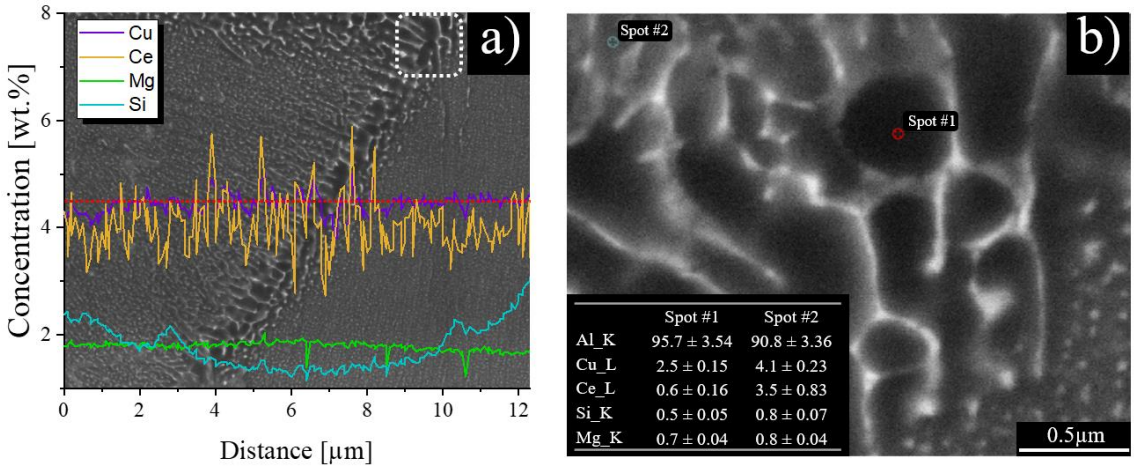

Figure 4. 67 – EDX analysis on the melt pool of the M1_3Ce composition processed by LPBF. In a) is shown the Line-EDX analysis carried out through the red line. In b), the point-EDX analysis on the light and dark areas of the region demarcated with a dashed white line in a). The compositions in both images must be interpreted qualitatively and not quantitatively.

The inverse pole figure (IPF) map for the composition M1_3Ce is shown in **Figure 4.68**. Although the texture is weak, it is slightly higher than what was observed in the M1_0Ce sample. The pole (001) and inverse pole figure on the plane [001] showed a maximum intensity of 2.85. The microstructure of the composition M1_3Ce also presented a slightly more refined grain size, with a mean value of 9.17 µm and mean values of AR and CR (**Figure 4.68**(**d**, **e**)) of 0.37 and 0.38, i.e. grains slightly more spherical than that seen in the composition M1_0Ce. Finally, **Figure 4.68**(**f**) shows the kernel average misorientation. The degree of misorientation of the samples tends to be quite homogeneous and with an average value of local misorientation of 0.7 and Kernel misorientation of 0.78. Nevertheless, the grain average misorientation is above 2°. In contrast, the higher values found in M1_0Ce LPBF-parts were between 1° - 1.5° close to the hot-cracked zones. These results suggest that, although the M1_3Ce parts present a high degree of disorientation, which could favor a higher probability of cracking

compared to the M1_0Ce composition, the formation of eutectic regions within the microstructure of the M1_3Ce parts prevents cracking of the M1_3Ce during solidification, demonstrating the effectiveness of Ce in improving the processability of the alloy within LPBF.

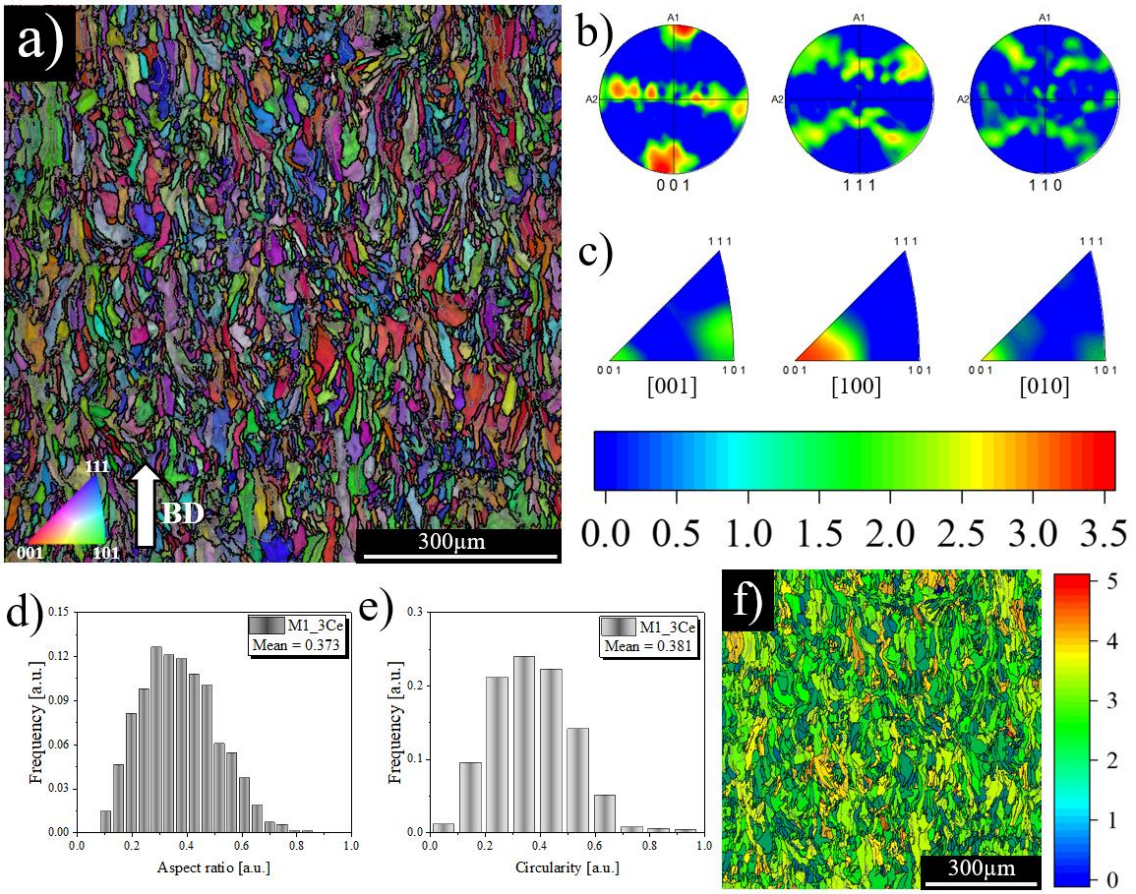

Figure 4. 68 – EBSD analysis of M1_3Ce composition processed by LPBF. In a) IPF-IQ map; b) pole; and c) inverse pole texture graphs. The frequency graphs, corresponding to the aspect ratio and circularity of the grains are shown in d) and e), respectively. The KAM analysis of the selected area is shown in f) using a misorientation angle between 0° – 5°.

4.5.4. TEM

Samples of M1_0Ce and M1_3Ce LPBF parts were analyzed by Transmission Electron Microscopy (TEM) technique in scanning (S-TEM), High-angle annular dark-field (HAADF-STEM), high resolution (HRTEM), and ASTAR

conditions to obtain a more precise analysis of the microstructure and phases formed during the solidification. As previously mentioned in the SEM analyses, both compositions present a highly refined microstructure and because of that, it was not possible to obtain details of the phases present. Therefore, this stage is focused on the more comprehensive analysis of the microstructure and the formation of possible secondary phases in LPBF parts.

LPBF sample of the M1_0Ce composition was analyzed near regions with the presence of hot cracks, as shown in **Figure 4.69**. When the material solidifies, the FCC cells formed undergo a great contraction stress, separating from each other. The lack of liquid material to fill the space between the cells allows the formation of the crack, which tends to propagate vertically in both directions (up and down according to the image). The presence of a large precipitate (200 nm long and 40 nm thick) restricts crack propagation. However, in **Figure 4.69**(**b**), it can be seen that the two cracks interconnect through a precipitate. The analyses carried out by EDX corroborate that both precipitates are rich in Cu and with a similar content of Mg (6 – 7 wt.%) and Si (4.1 – 4.6 wt.%), discarding the possibility of being two different phases. The authors suggest that the propagation of the hot crack through the precipitate may be due to different factors in which the size of the precipitate and the characteristics of the part produced by LPBF stand out.

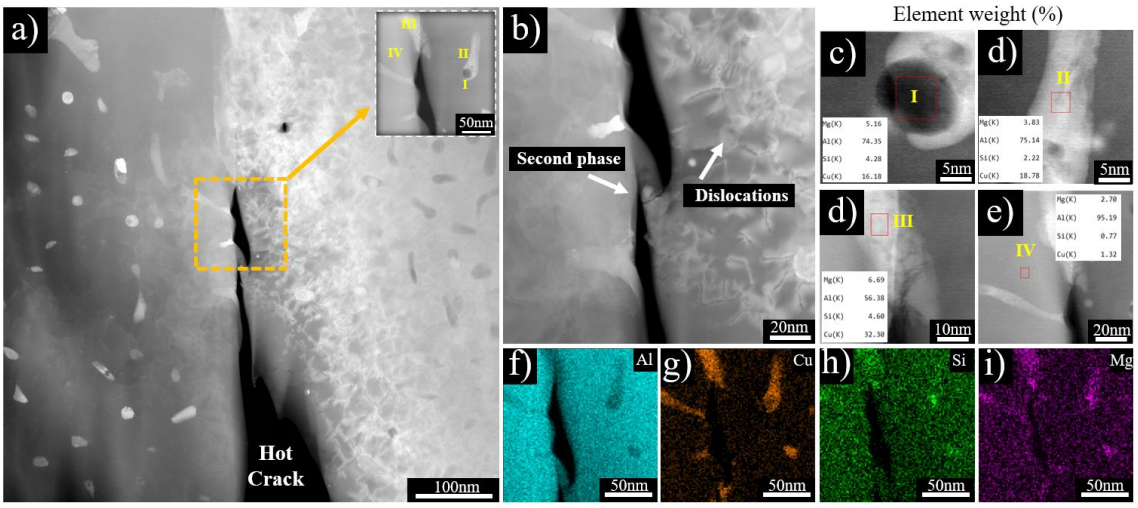

Figure 4. 69 – Microstructural analysis by TEM of LPBF M1_0Ce part. In a) HAADF image of two hot cracks, interconnected from the fracture of a precipitate.

Greater detail of the fractured precipitate is presented in b). In c – e) the EDX point analyses of the regions marked in (a) are presented. In f – i) the EDX maps of the region highlighted in Fig. (a) are shown. It can be seen that the precipitates are mainly composed of Cu, followed by a smaller amount of Mg and Si.

The Al_2Cu phase presents a coherent interface with the FCC matrix of aluminum, favoring an increase in mechanical strength; nevertheless, the coherence of both phases, in addition to the high density of residual stresses generated during the solidification of the alloy, drastically reduces the mobility of the dislocations within the matrix. Likewise, the smaller precipitate (roughly 20 nm) is unable to withstand the stresses generated during cracking, resulting in its fracture. In such circumstances, the crack finds it easier to propagate through the precipitate rather than circumvent it.

The ASTAR analysis was carried out to corroborate the possible phases generated in LPBF parts of the M1_0Ce composition. The results obtained are presented in **Figure 4.70**. Considering that this technique requires a long time to collect and analyze the data, a representative region of approximately 150 x 150 nm^2 was chosen. The ASTAR data were analyzed considering the phases detected by synchrotron XRD, ***see Section 4.5.2***. The microstructure analyzed by ASTAR is mainly formed by an Al_FCC matrix with some Al_2Cu precipitates, which agree with the XRD patterns. The indexed Al_2Cu region protrudes from the particle outline. This is because the area analyzed must present electron diffraction patterns with optimal quality and low noise to obtain optimal phase indexing. Other possible phases were not detected by TEM–ASTAR. This can be explained by the process conditions. High cooling rates reduce the segregation capacity of the alloying elements within the microstructure, prioritizing the formation of an supersaturated aluminum matrix. In addition, it should be considered that the composition M1_0Ce presents a low concentration of alloying elements, i.e. 0.8 wt. %Mg and 0.4 wt. %Si, which reduces the ability to form other secondary phases.

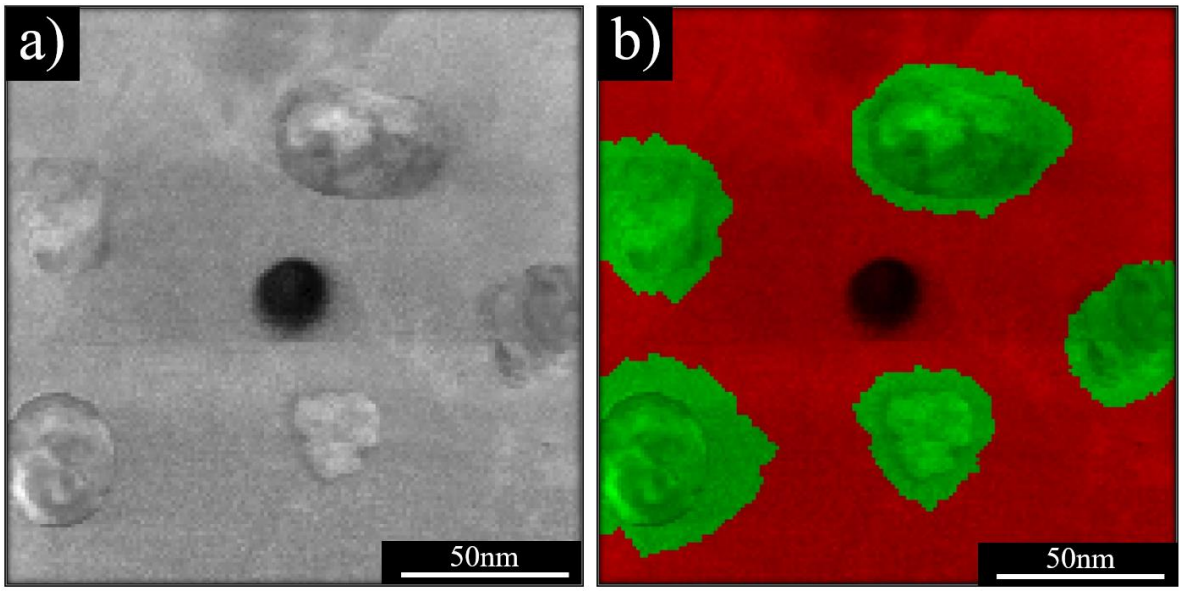

Figure 4. 70 – ASTAR analysis of sample M1_0Ce produced by LPBF. In a) the collected area is presented and in b) the analysis is carried out through phase indexing. The analyses allowed us to detect and corroborate the presence of precipitates of the Al_2Cu phase (in green) arranged within an aluminum matrix (in red).

TEM analysis for the M1_3Ce LPBF sample was performed on a melt pool as shown in **Figure 4.71**. It can be observed that on the edge of the melt pool the Al_FCC cells are coarser than those found on the center of the pool or outside it, similar to what was observed by SEM analysis. The secondary phase surrounding the FCC matrix was analyzed by point EDX and EDX maps, corroborating that this is a region rich in Cu and Ce, being mainly composed of the Al_3CeCu phase.

Similar to the M1_0Ce samples analyzed by TEM, the TEM – EDX analyses did not reveal the formation of the Al_8CeCu_4 phase, previously detected by synchrotron XRD. TEM analysis was performed up to 79.000 magnifications (79kx), this being the maximum magnification reached in the HAADF condition to obtain images with optimal resolution. Even so, it was not possible to detect the formation of micro or nano cracks produced during the solidification process, corroborating the effectiveness of the alloy to be processed within additive manufacturing.

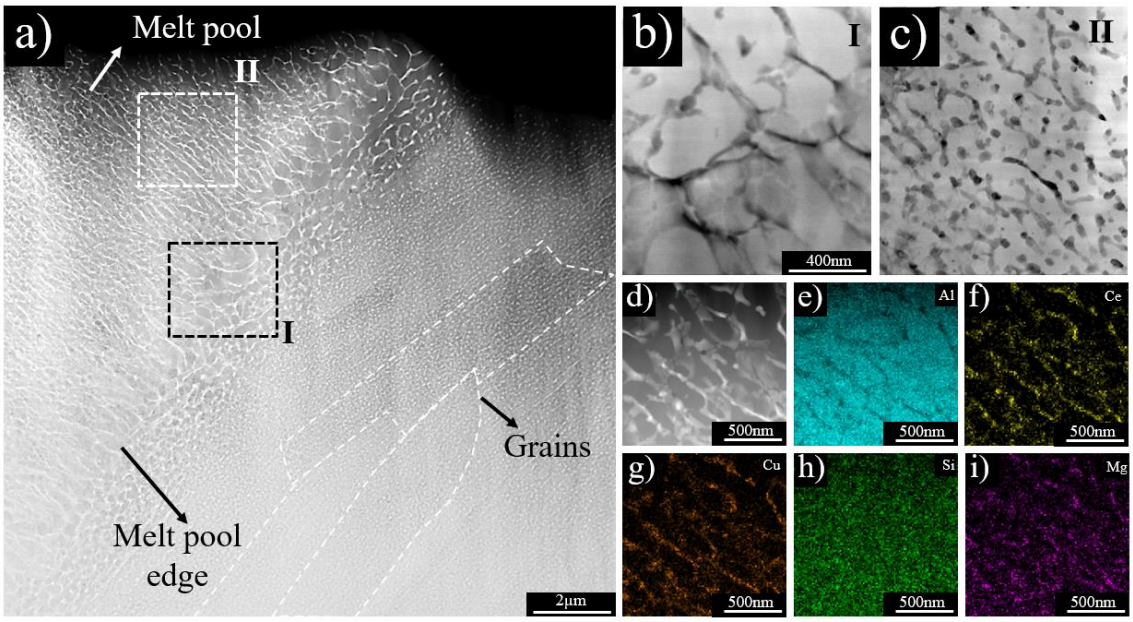

Figure 4. 71 – TEM analysis of the M1_3Ce composition processed by LPBF. In a) a melt pool image in HAADF condition is presented. Regions I and II are presented in b) and c), respectively, in BF condition. An EDX map analysis of region II is presented in d – i) where it is possible to observe that the matrix is composed mainly of Al and, in turn, it is surrounded by regions rich in Cu – Ce, mainly. Some regions are rich in Mg and Si is distributed homogeneously in the analyzed area.

The ASTAR analysis was performed in a region of 120 x 120 nm^2. The results are presented in **Figure 4.72**, where it is confirmed that the microstructure is mainly made up of an aluminum matrix (in red) and the Al_3CeCu phase (in green) which promotes the formation of eutectic regions. Unfortunately, some regions were not fully indexed, possibly due to the low quality of the electron diffraction patterns or the superposition of both phases within the diffraction pattern, prioritizing the Al phase over Al_3CeCu.

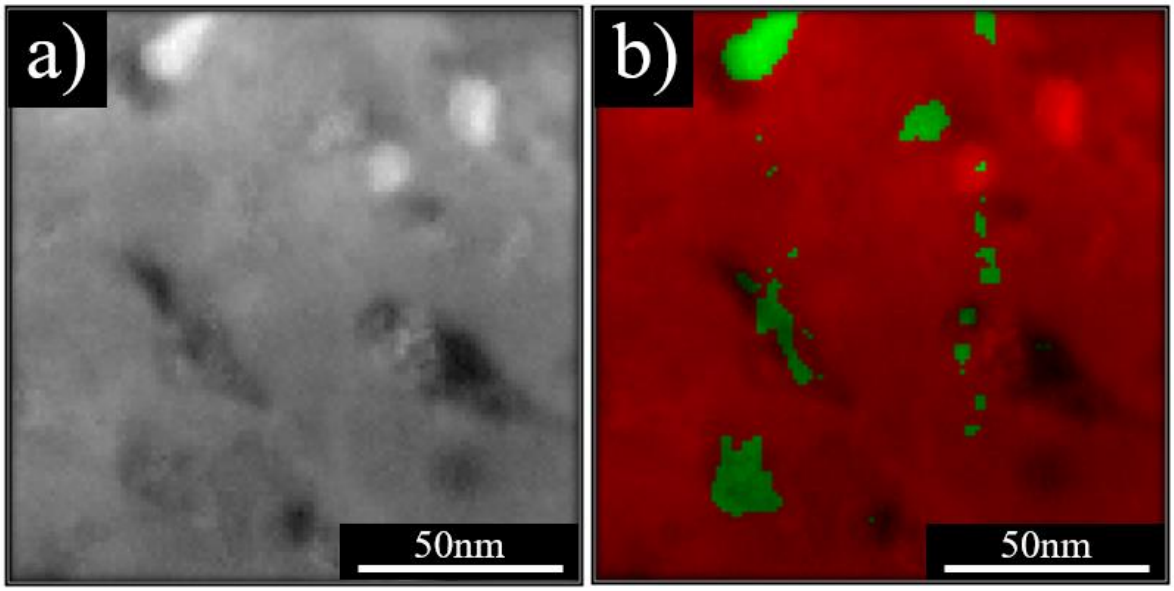

Figure 4. 72 – ASTAR analysis of sample M1_3Ce produced by LPBF. In a) the collected area is presented and in b) the analysis is carried out through phase indexing. The analyses allowed detection and corroboration of the presence of precipitates of the Al_3CeCu phase (in green) arranged within an aluminum matrix (in red). The Al_8Cu_4Ce phase detected by synchrotron XRD were not detected by TEM-ASTAR.

In order to detect the possible formation of other secondary phases, the sample was analyzed using the HR-TEM and SAED techniques. **Figure 4.73** shows some of the results obtained. **Figure 4.73** (**a**) represents the material matrix. The presence of quite fine secondary phases is observed, approximately d = 0.3 nm thick, up to L = 3.0 nm long. By comparing the interatomic spacing “d” value with the CIF of the possible phases proposed by thermodynamic calculations and the phases found by XRD, it was possible to determine that these precipitates may correspond to the Al_2Cu phase. Due to the minimum aperture offered during the SAED analysis to obtain the electron diffraction patterns, it was not possible to detect the phase that corresponding the precipitates, as seen in **Figure 4.73** (**b**). However, using ImageJ software it was possible to generate an electron diffraction pattern by FFT of the area of interest where was possible to observe characteristic signals of the Al_2Cu phase as shown in **Figure 4.73** (**a**), where the interplanar distance measured is consistent

with the interplanar distance measured in the HR-TEM image. **Figure 4.73**(**c**) shows the interface between the eutectic zone (left part of the image) and the matrix (right part). The electron diffraction pattern of the analyzed area is shown in **Figure 4.73**(**d**). From the measurement of the interatomic space, the Al_3CeCu phase was corroborated. Other phases were not detected by TEM for the M1_3Ce composition.

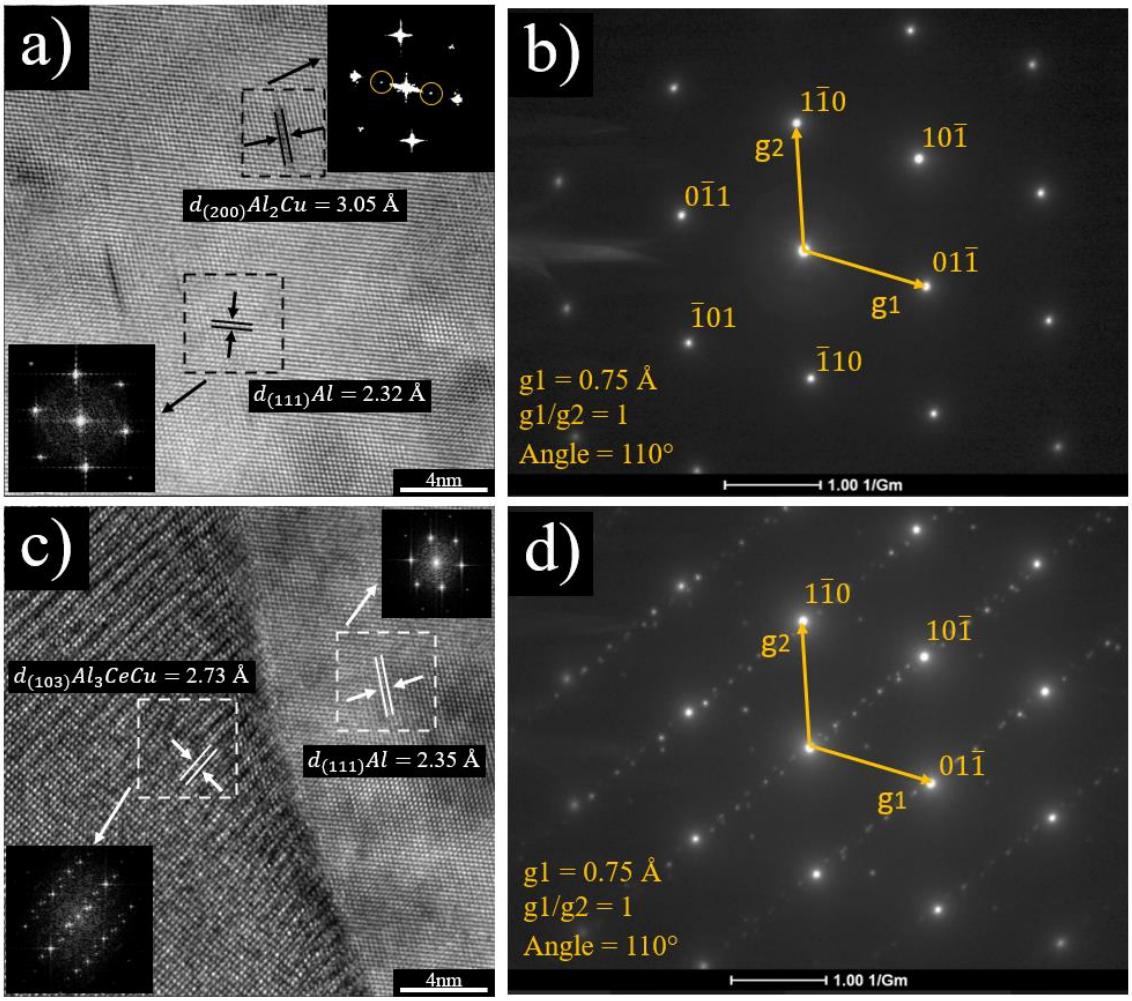

Figure 4. 73 – HR–TEM (a, c) and SAED (b, d) images of the M1_3Ce composition processed by LPBF. In a) the aluminum matrix and b) the interface between the eutectic region (Al + Al_3CeCu) and the Al matrix. The electron diffraction patterns, constructed by the Fast Fourier transform (FFT) method of the highlighted areas, are found in the insets of **Fig. 4.73** (**a**, **c**).

4.6. Effect of applying heat treatments on the microhardness behavior

M1_3Ce LPBF samples were subjected to heat treatment. The heat treatment conditions were selected from the DSC curves presented in **Figure 4.56** for M1_0Ce and M1_3Ce compositions. It is observed a first peak in both compositions at 200 °C in the DSC curve, corresponds to the Al_2Cu phase formation, typical of Al-Cu base alloys. Nevertheless, the composition M1_3Ce also presents a second peak between 350 °C – 400 °C. According to the thermodynamic calculations carried out by the CALPHAD method, this peak corresponds to the formation of the $AlCeSi_2$ phase, which was found previously by SEM-EDX analysis in directionally solidified parts.

Considering the above, it was decided to carry out the heat treatments between 150 °C – 190 °C and 350 °C – 350 °C, corresponding to temperatures for aging and annealing heat treatments, respectively. Although the annealing heat treatment supposes a softening by stress relief in the part, the presence of the second peak could represent the formation of reinforcement phases that increase the mechanical strength of the material. For this reason, heat treatments in both temperature ranges were considered. The heat treatment conditions are presented in **Table 4.8**. To validate the influence of the heat treatment applied on the mechanical properties of the LPBF part, microhardness measurements were performed.

Table 4. 8 – Parameters used in this work for direct aging and annealing heat treatments.

Heat treatment temperatures [°C]											
Direct aging							**Annealing**				
150			170		190		250		300		350
Time of the heat treatments [h]											
0	0.5	1	2	3	6	9	12	24	48	72	96

The microhardness curves for the direct aging condition are presented in **Figure 4.74**(**a**). The as-built LPBF samples presented an average microhardness

of 127 $HV_{0.2}$ (highlighted by a red dashed line). The application of heat treatment for aging at 150 °C allows a slight increase in the microhardness values, presenting its maximum peak of 134 ± 0.6 $HV_{0.2}$ between 360 – 720 min (3 – 12 h) of treatment. The application of heat treatments at 170 °C and 190 °C generated a reduction in hardness values by overaging up to values of 88 $HV_{0.2}$ for samples treated at 190 °C for 1440 – 2880 min (24 – 48 h).

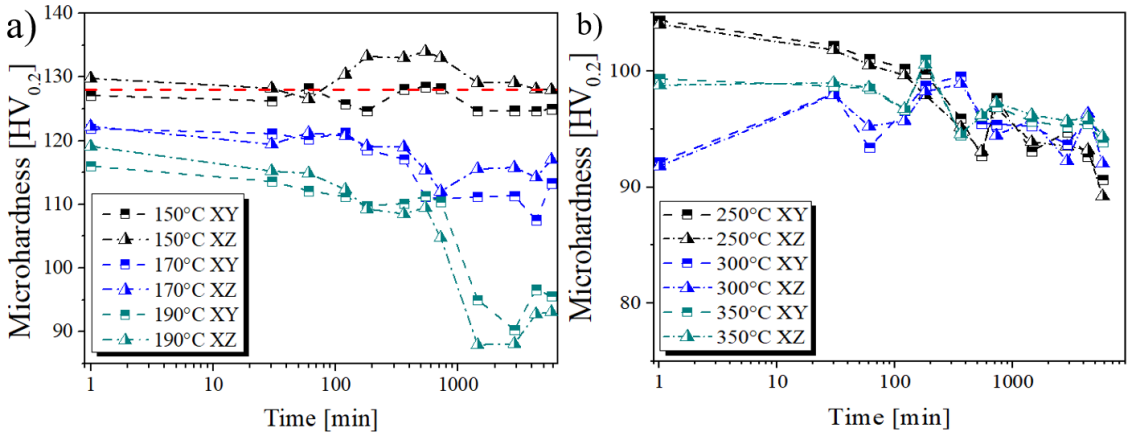

Figure 4. 74 – Microhardness behavior of M1_3Ce parts processed by LPBF and subsequently heat treated. In a) effect of applying direct artificial aging heat treatment at 150 °C, 170 °C, and 190 °C. In b) effect of applying annealing heat treatment at 250 °C, 300 °C, and 350 °C. All the tests were developed with holding times between 0 h and 96 h.

The heat treatments carried out in an annealing temperature range (i.e. 250 °C – 350 °C) are presented in **Figure 4.74**(**b**). A significant and continuous decrease in the microhardness values for parts annealed at 250 °C and 350 °C was observed. In contrast, the samples were annealed at 300 °C where a low increase is seen until reaching values close to 100 $HV_{0.2}$ after 6h of treatment before decaying again. Nevertheless, these values are significantly lower compared to as-built parts (127 $HV_{0.2}$).

LPBF technique is characterized by applying higher cooling rates. It favors a highly refined microstructure and a high volume internal stresses in as-built condition. Both factors significantly favor an increase in the mechanical strength

of the material, compared to parts manufactured by conventional processes, e.g. sand casting. By applying an annealing temperature an inherent stress relief is generated which softens the part.

Although it can be confirmed that the composition M1_3Ce can be hardened by applying heat treatments at 300°C, presenting an increase in microhardness values when a period between 0.5h and 9h of treatment is applied, it should be considered that the hardness obtained at 300°C during 1min of treatment (92 $HV_{0.2}$) is significantly lower than the hardness of parts in as-built condition (127 $HV_{0.2}$). This indicates that, although the alloy can be heat treated by aging at high temperatures, the stress relief effect of applying a high treatment temperature is more influential in M1_3Ce parts built by LPBF.

Some authors such as Li *et al.* [264] and Zhang *et al.* [265] have reported that applying solution heat treatments (SHT) and subsequent aging can favor a substantial increase in mechanical properties in Al-5Si-Cu-Mg and Al-4.24Cu-1.97Mg-0.56Mn (wt%) parts produced by LPBF and DED, respectively. For this, SHT at temperatures between 480 °C and 560 °C was performed during 1 h and subsequent water cooling. The results obtained are presented in **Figure 4.75**. The SHT generates a drop in the hardness values, similar to what was observed in the parts annealed. The condition of 500°C/1h showed the least loss in microhardness values. Likewise, the application of 0.5 h and 1.5 h at this temperature also reduced the microhardness. Although the results presented by these authors promised the possibility of further improving the mechanical strength of the material, the microhardness results obtained in this work for the M1_3Ce composition demonstrate the opposite behavior.

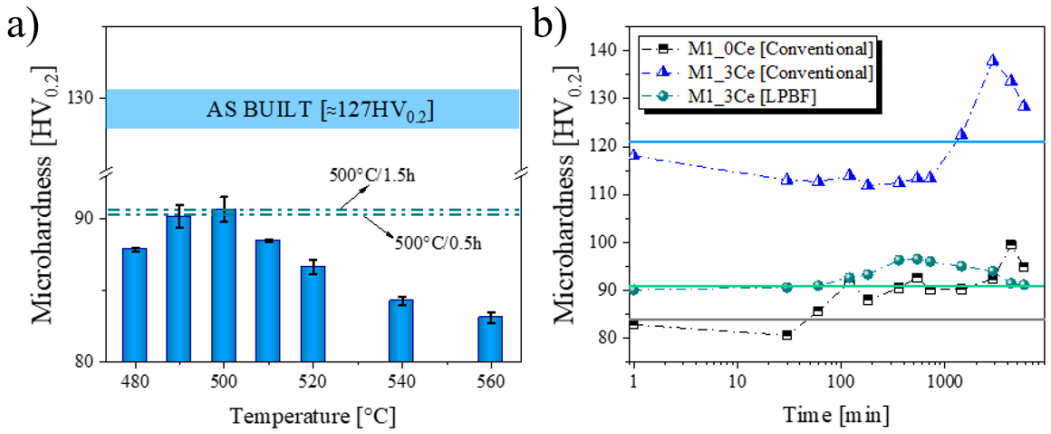

Figure 4. 75 – Microhardness behavior of M1_3Ce parts processed by LPBF and subsequently heat treated. In a) effect of applying solution heat treatment at different temperatures and holding times. In b) effect of T6 heat treatment (500 °C during 1 h, water cooling (20°C), and subsequent artificial aging at 150 °C at different times. The effect of solution and T6 heat treatments was compared with M1_0Ce and M1_3Ce parts manufactured by conventional method (casted ingot).

Considering the results shown in **Figure 4.75**, heat treatments in T6 condition (Solubilization 510°C/1h/WQ and subsequent artificial aging at 150 °C) were performed on parts M1_0Ce and M1_3Ce produced by conventional manufacturing process (from an ingot sample) and parts M1_3Ce built by LPBF. The results obtained for this treatment show that the alloy still can be hardenable by precipitation, as seen in **Figure 4.75**(**b**).

The presence of Ce in the alloy could reduce the hardening of parts by direct artificial aging. It has been reported that the addition of Ce favors greater thermal stability in aluminum alloys. Although this behavior has been widely reported in parts produced by ceramic/graphite mold casting [140, 266], it has also been reported for Al-Ce-Sc-Zr [267], Al-Ce-Mn [190], and Al-Ce-Cu [19] parts produced by LPBF. The low diffusion coefficient and solubility of Ce in Al, the eutectic regions and intermetallic phases produced by adding this element, e.g. $Al_{11}Ce_3$, also have high thermal stability and high melting point, reducing the heat-treatment effect in the LPBF parts.

The conventionally produced samples suffered softening during the first hours of treatment. Although the phenomenon of softening due to aging is poorly studied, the gradual loss in hardness of Al-Si pistons subjected to temperatures of 150°C has been reported [268]. It is reported that this phenomenon is an intrinsic property caused by the composition, which was solved by adding copper and applying aging treatments for long periods, favoring a delay in softening due to aging [268].

Another hypothesis considered in this work is based on the conditions in which the T6 treatment was carried out. The application of water cooling during the SHT is usually done to avoid the precipitation of intermetallics before the application of artificial aging treatments. However, this “abrupt” cooling can generate residual stresses within the material [145]. In this sense, the first hours of the heat treatment are likely to produce a stress-relieving effect that further softens the material before exhibiting an increase in hardness values. In contrast, the LPBF parts subjected to the T6 condition only showed this drop-in hardness at 0.1 h of aging.

Within this work, a longer heat-treatment time represented an increase in hardness values, reaching 99.5 $HV_{0.2}$ for M1_0Ce parts and 137.9 $HV_{0.2}$ for M1_3Ce parts. This last value is comparable with the maximum hardness peak reached in M1_3Ce LPBF parts aged directly at the same temperature. In general, these results suggest that regardless of the treatment conditions applied, the microhardness values in M1_3Ce parts produced by LPBF shall hardly increase more than 10 – 15 HV, compared with as-built parts. Likewise, as previously stated, the addition of Ce already produces a considerable increase in hardness in the as-prepared state, increasing from mean values of 90 HV for M1_0Ce parts to values up to 120 HV in M1_3Ce LPBF parts.

4.7. Mechanical properties

4.7.1. Microhardness

Although the microhardness tests were carried out to observe the influence of heat treatments on the mechanical properties of M1_3Ce LPBF-parts, this section seeks a more detailed analysis of the relationship between the

microstructural characteristics of the material and the microhardness behavior. For this, the different parts produced in this work were analyzed by applying different indentation loads. Heat-treated samples are not considered in this section.

Varying the applied indentation load can cause variations in the mean hardness value, which is known as the Indentation Size Effect (ISE). Due to this, small loads are usually used when carrying out this test (< 1 kgf, according to ASTM E384 and ISO 6507 [269]). Nevertheless, to determine the absolute hardness of the M1_3Ce parts, the microhardness measurements were made by applying loads of 0.01, 0.1, 0.2, 0.3, 0.5, 1, and 3 kgf.

Before determining the absolute hardness, preliminary measurements in different areas of the samples were made for the samples produced by LPBF. The microhardness maps are presented in **Figure 4.76**. Both samples present a high homogeneity maintaining similar hardness values between the different measurement points. This guarantees that measurements made at different loads will be representative of the entire built part.

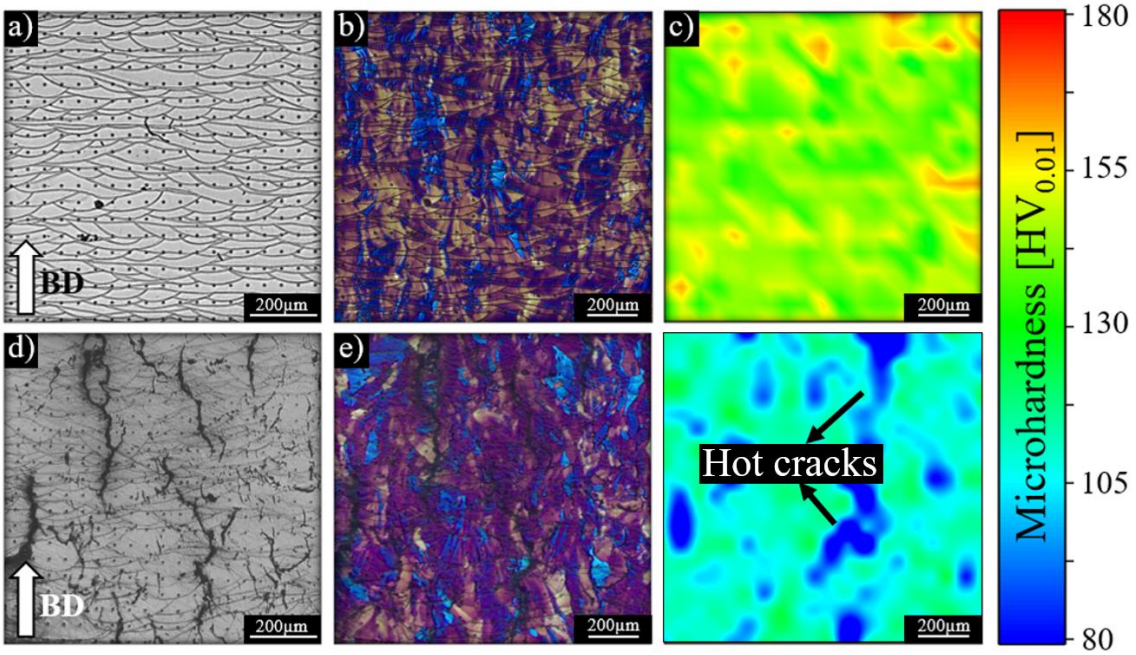

Figure 4. 76 – Microhardness maps for M1_3Ce (a – c) and M1_0Ce (d – f) LPBF samples. The color light (a, d) and polarized light (b, e) images show the melt pools and grains in the building direction.

It has been indicated that the application of low indentation loads generates an increase in hardness values (normal ISE), which can be determined using the Meyer index from **eq. 8** [270].

$$F = k \cdot d^m \quad (8)$$

Where,

F is the applied load,

k is an indentation coefficient,

d is the average indentation size,

m is the Meyer Index (usually < 2).

Figure 4.77(**a**) shows the microhardness behavior of M1_3Ce parts produced by different manufacturing processes. From the curves presented in **Figure 4.77**(**b**), it is possible to determine the value of the Meyer indices as shown in **Figure 4.77**(**c**). Finally, **Figure 4.**77(d) shown the correlation between the grain size and the microhardness. It can be seen that, as the cooling rate increases (i.e. grain refinement is obtained), the value of the Meyer index also increases. Likewise, the K coefficient shows a behavior similar to "m", indicating that, depending on the process, the material will tend to maintain high hardness values as the load increases.

According to Kick's law [$F = k \cdot d^2$], there should be a linear relationship between different types of hardness (i.e. Vickers, Knoop, Brinell, Rockwell, and Meyer measurements) [269]. For this, the Meyer index should be equal to 2. The results obtained show that regardless of the type of processing, the samples present a Meyer index < 2, indicating a normal ISE. Grain refinement caused by an increase in cooling rates favors obtaining a higher hardness with m values closer to 2. Zubacky and DebRoy [271] also reported a similar behavior for different alloys. In Al-Cu base alloys, an increase in Cu concentration favors a greater increase in hardness values as the cooling rate increases. Nevertheless,

the values published by this author present cooling rates lower than those usually obtained in LPBF (10^4 °C·s^{-1}).

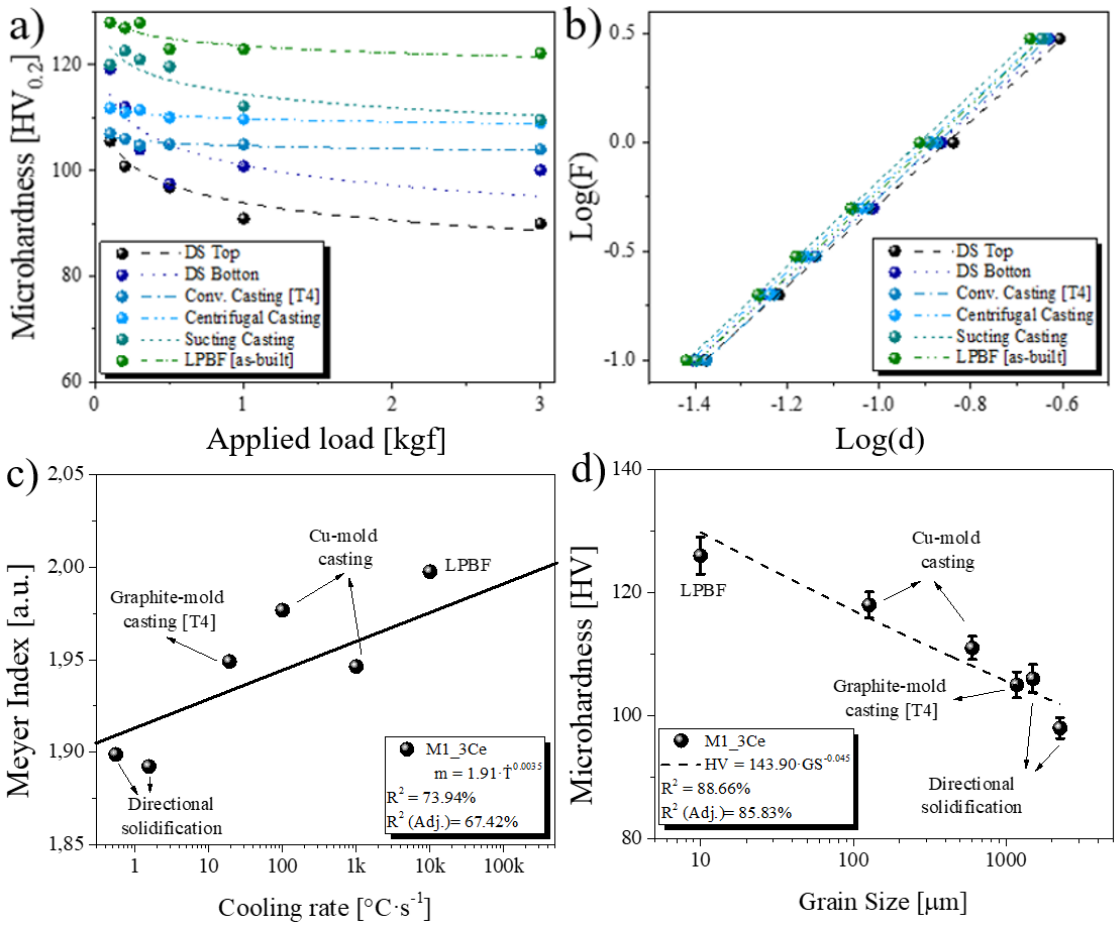

Figure 4. 77 – Correlation between the Meyer index, microhardness, cooling rate, and grain size of M1_3Ce parts processed by different manufacturing methods. In a) effect of the applied indentation load on the microhardness values; b) Log(d) – Log(F) curves to determine the Meyer index and K coefficient; c) Meyer index as a function of cooling rate; and d) Microhardness behavior in function of grain size. The microhardness measurements were carried out for M1_3Ce samples processed by directional solidification, graphite– (conventional) and copper–mold (suction and centrifugal) casting, and LPBF techniques.

Different mathematical models have been developed to establish the "absolute hardness" of a material [269, 272]. Luo and Kitchen [273] have studied different mathematical models to establish the ISE effect on the absolute

hardness of austenitic Hadfield steel parts. The results presented by the authors show that the microhardness measurements obey Meyer's law instead of Kick's law. In addition, the results obtained by these authors show that the Nix-Gao model presented a better fitting to understand the behavior observed in the different Hadfield steel parts.

In this work, the absolute hardness of the M1_3Ce parts obtained in different manufacturing processes was determined. Although new mathematical models related to ISE have been proposed [270], the application of these models shall depend on the manufacturing process; therefore, one model shall be more appropriate than another to correlate the microhardness values [274]. Considering this, only the models reported by Luo and Kitchen [273], presented in **Table 4.9**, were applied. The components of the different mathematical models are extracted from the regression curves shown in **Figure 4.78**.

Table 4. 9 – Mathematical models used in this work [270].

Author	**Year of publication**	**Mathematical model**
Hays-Kendal	1973	$F - W = A_0 d^2$
Bull	1989	$F = A_0 \cdot (d + d_0)^2$
Li-Bradt	1993	$F = A_0 d + B_0 d^2$
Nix-Gao	1998-1999	$\frac{H}{H_0} = \left(1 + \frac{h^*}{h}\right)^{\frac{1}{2}}$

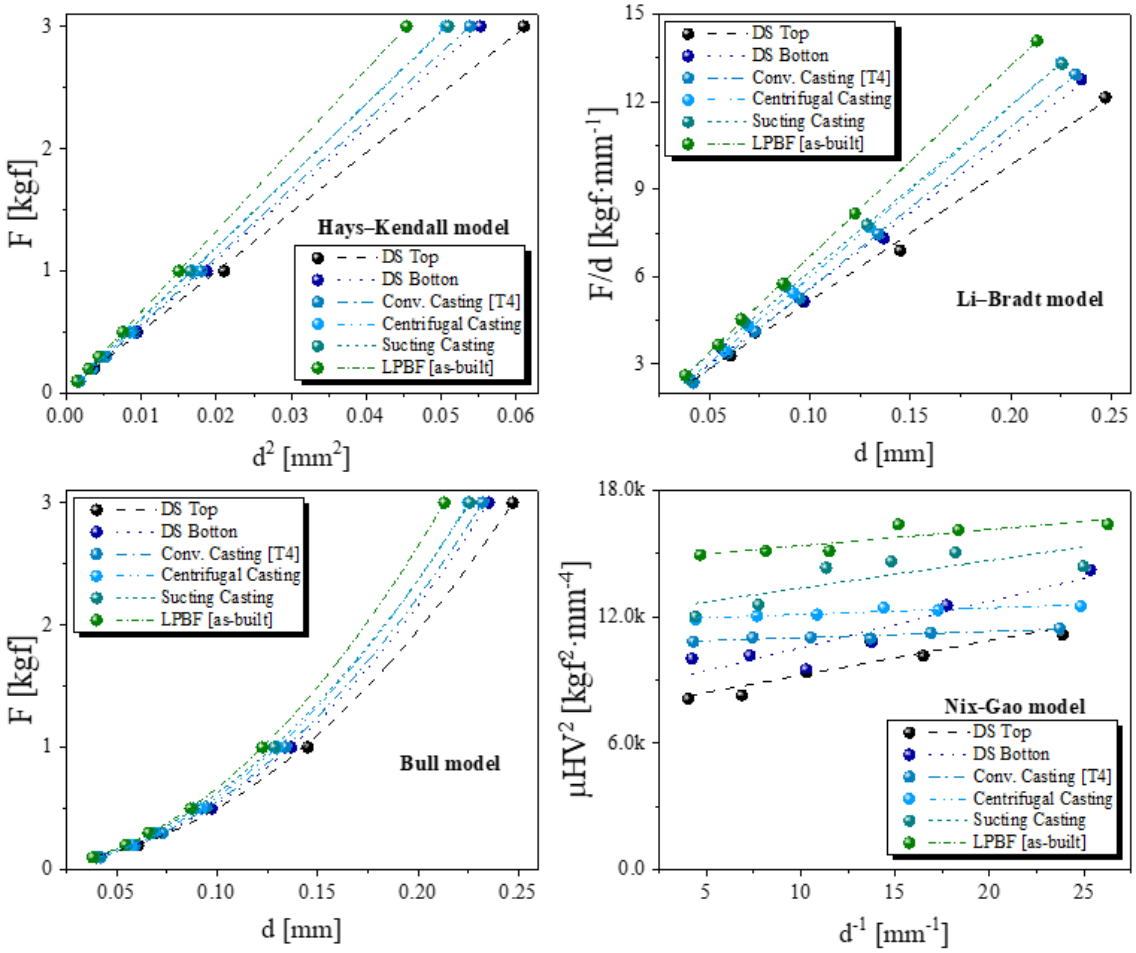

Figure 4. 78 – Mathematical models by linear regression method used to determine the absolute hardness of M1_3Ce parts processed by different manufacturing methods. In a) Hays-Kendal, b) Li-Brad, c) Bull, and d) Nix-Gao mathematical models. The mathematical models were carried out for M1_3Ce samples processed by directional solidification, grafite and copper mold casting, and LPBF techniques.

The Hays-Kendal model presented the best fit (R^2 and $R^2_{(adj.)}$ > 99.9%). This can be corroborated by observing the behavior of the ISE significance coefficient ($\eta = \frac{H_{measured} - H_{absolute}}{H_{absolute}}$) for the LPBF parts as shown in **Figure 4.79(a)**. When is used a low applied load, the value of η increases, indicating that the ISE loses influence on the measurement due to an increase in the value of “m”. **Figure 4.78(b)** shows the relationship between the measured microhardness values and "true hardness" obtained from the different mathematical models. In

all the models used, a lower hardness is observed than the values measured in the laboratory. Nevertheless, this work shall only consider the Hays-Kendal model, since this was the model that best matched the results obtained. For LPBF parts, it can be seen that the absolute hardness value is 122HV, which is still considerably high compared to the other parts produced by different manufacturing processes.

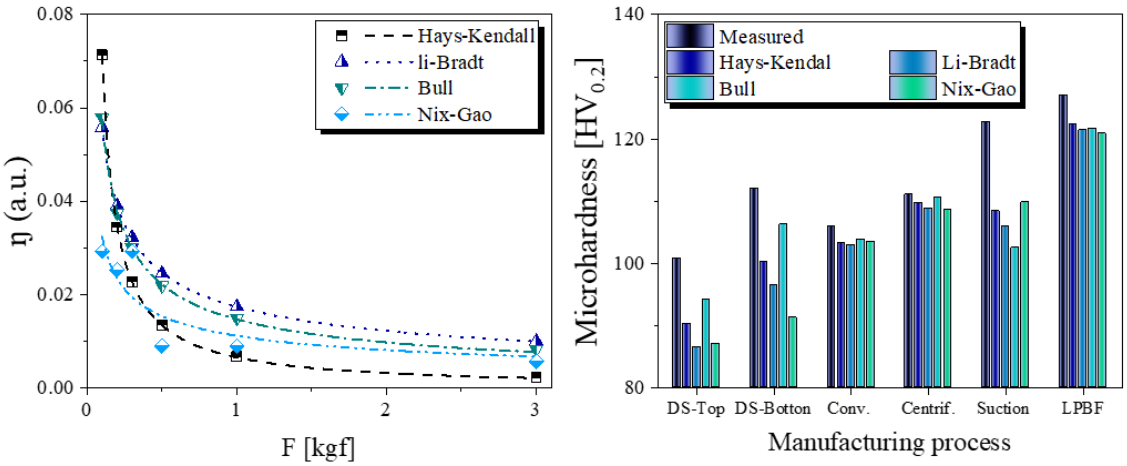

Figure 4. 79 – Determination of absolute hardness of M1_3Ce parts processed by different manufacturing methods. In a) η – ISE coefficient in the function of the applied indentation load and b) the absolute hardness values obtained applying the different mathematical models presented in **Table 4.9.**

4.7.2. Compression test

The M1_0Ce and M1_3Ce compositions underwent compression tests, with specimens produced using different manufacturing techniques to achieve a range of grain sizes. For LPBF parts, specimens were created at 0 °, 45 °, and 90 ° related to the substrate. **Figure 4.80** illustrates compression curves for both compositions. **Figure 4.81** depicts the relationship between grain size and compression mechanical properties.

Overall, M1_3Ce parts exhibit superior mechanical behavior compared to M1_0Ce parts, regardless of the manufacturing method. As grain size decreases, yield strength (YS), elastic modulus (E), deformation at failure (ε_{rup}), and ultimate tensile strength (UTS) generally increase in M1_3Ce parts. On the other hand,

M1_0Ce parts show an opposite trend, particularly in LPBF parts where the presence of hot cracks leads to premature failure. **Table 4.10** correlates YS values and UTS at 15% deformation for LPBF parts produced in this study and Al-Cu-based LPBF parts. In most cases, M1_3Ce samples exhibit higher YS and UTS values, while M1_0Ce samples demonstrate behavior similar to that reported in the literature. Although Al-XCu samples (X = 40, 33, and 20 wt.% Cu) boast higher YS values compared to M1_3Ce samples, they display significantly lower ductility, fracturing at strains of 1.5%, 2.5%, and 8%, respectively. In contrast, M1_3Ce LPBF parts fracture at strains exceeding 25%.

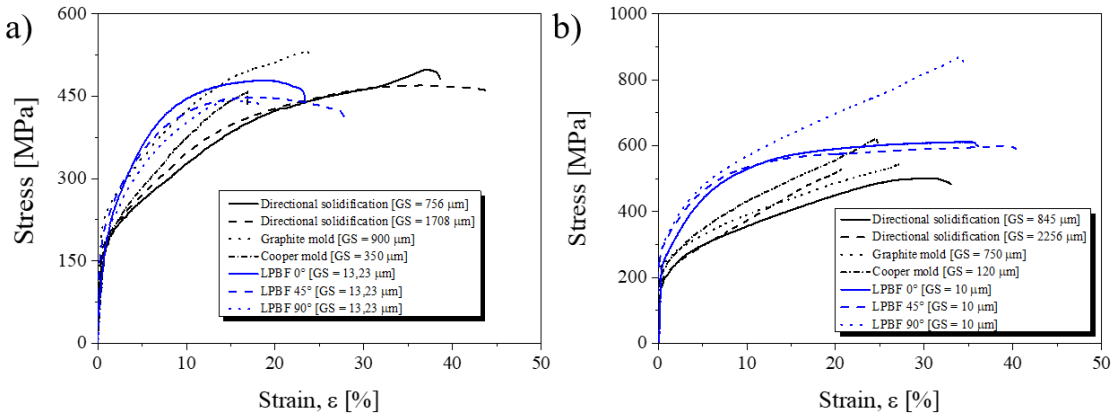

Figure 4. 80 – Typical compression curves registered for the **a**) M1_0Ce and **b**) M1_3Ce compositions processed by different manufacturing techniques used in this work.

Table 4. 10 – Values of YS and UTS at 15 % of deformation at compression form M1_0Ce and M1_3Ce LPBF parts produced in this work and values reported in the literature.

Alloy	Condition	YS MPa	UTS (15 %) MPa	Ref.
AA2024	As-built	157	350	[88]
AA2024	T6	378	460	
TiB_2/AA2024	As-built	191	450	
TiB_2/AA2024	T6	401	540	
Al–14Cu–7Ce	As-built	257	280	[19]
Al-40wt.%Cu	As-built	1000	Failed at 1.5%	[275]
Al-33wt.%Cu	As-built	1020	Failed at 2.5%	

Al-20wt.%Cu	As-built	850	Failed at 8.0%	
Al-6.0wt.%Cu	As-built	450	380	
Al-4.5wt.%Cu	As-built	350	300	
Al-Cu-Mg	As-built	251	460	[136]
Al-Cu-Mg-Y	As-built	267	550	
Al-Cu-Mg-Y	T6	241	460	
M1_0Ce	As-built	177 - 225	458 - 472	This work
M1_3Ce	As-built	255 - 282	575 - 665	This work

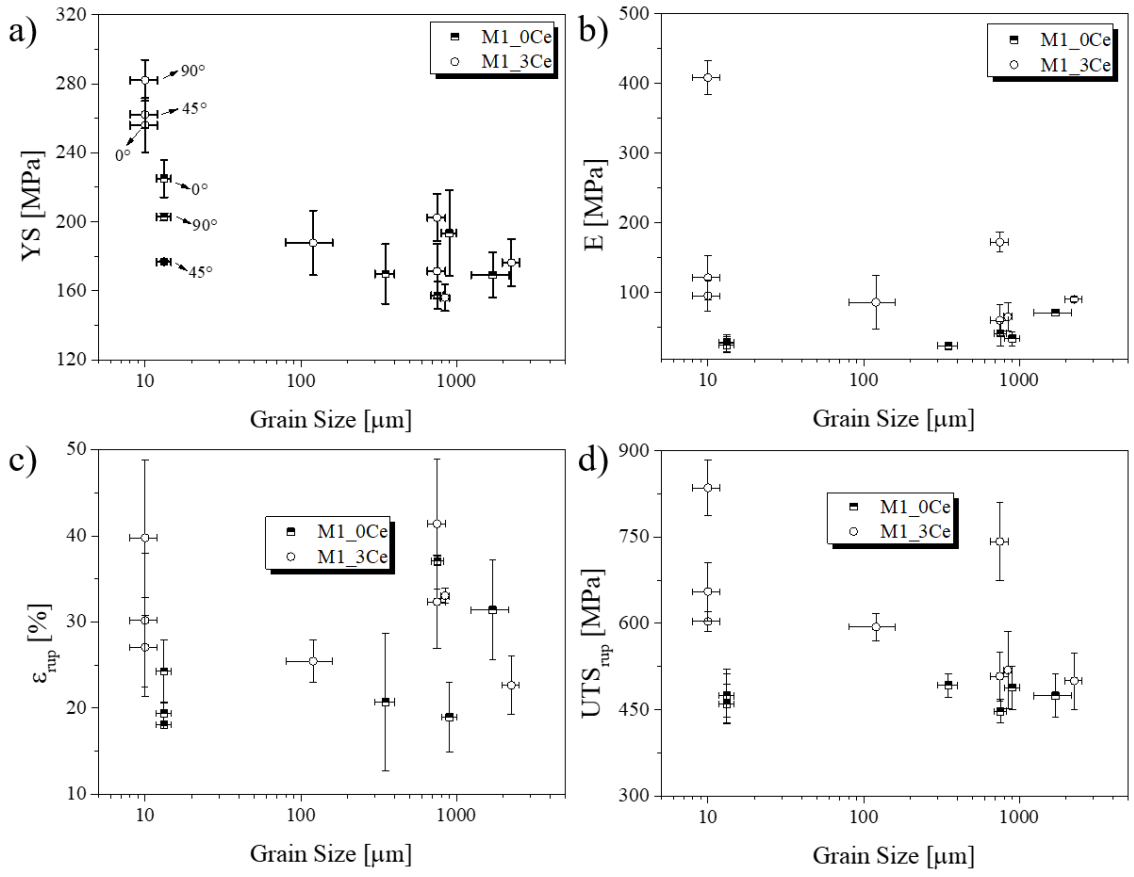

Figure 4. 81 – Experimental correlations between the **a**) yield strength; **b**) elastic modulus; **c**) elongation at fracture; and **d**) compressive strength as a function of the grain sizes for the M1_0Ce and M1_3Ce compositions.

Figure 4.82 depicts the fracture morphology of M1_0Ce and M1_3Ce parts in both LPBF and as-cast conditions. During compression tests, all samples fractured at 45 °. Throughout the compression process, the surface experienced significant deformation, Shear forces that break the samples apart, around 45º,

in the plane of maximum shear stress. M1_0Ce and M1_3Ce LPBF samples displayed pronounced cleavage planes. Conversely, samples produced by graphite mold casting reveal the formation of dimples.

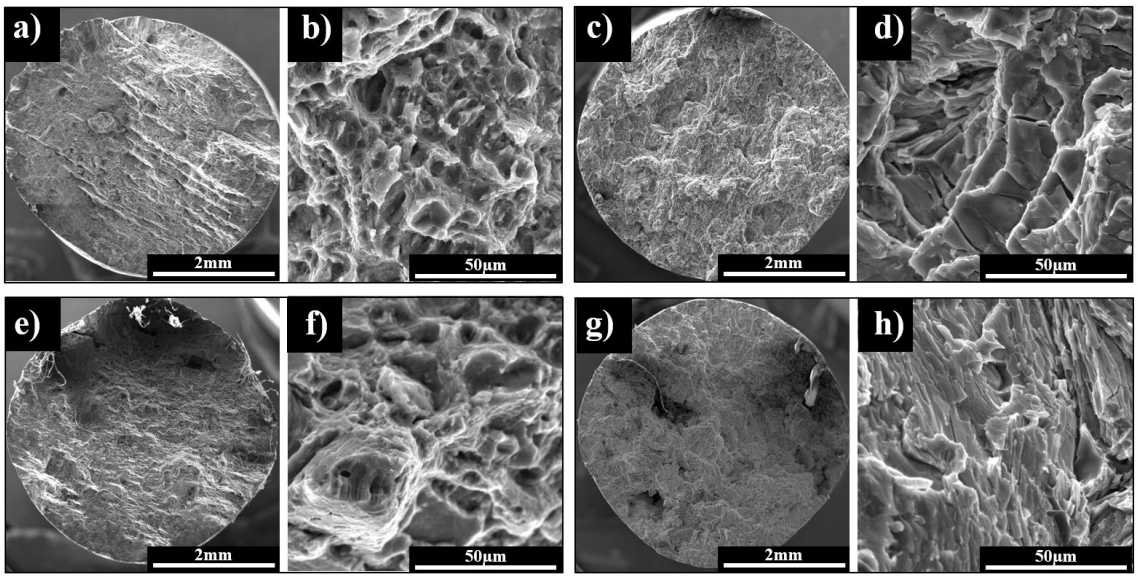

Figure 4. 82 – Compressive fracture surface characteristics of M1_0Ce (a – d) and M1_3Ce (e – h) parts processed by LPBF (a-b, e-f) and graphite casting (c-d, g-h) manufacturing techniques.

4.7.3. Tensile test

Tensile tests were conducted using both rectangular and cylindrical specimens, as previously mentioned. Rectangular specimens were primarily utilized to compare the mechanical properties of M1_0Ce and M1_3Ce parts produced through the different manufacturing techniques used in this research. **Figure 4.83** displays tensile test curves for both compositions, while **Figure 4.84** illustrates the relationship between grain size and tensile mechanical properties, derived from rectangular specimens. Similar to the compression tests, M1_3Ce exhibits superior mechanical performance compared to M1_0Ce, especially evident in LPBF parts, where hot cracks significantly degrade the mechanical properties of M1_0Ce parts. Grain refinement enhances YS and UTS, while E values remain relatively constant regardless of grain size; nevertheless, ductility, resilience, and toughness values decrease.

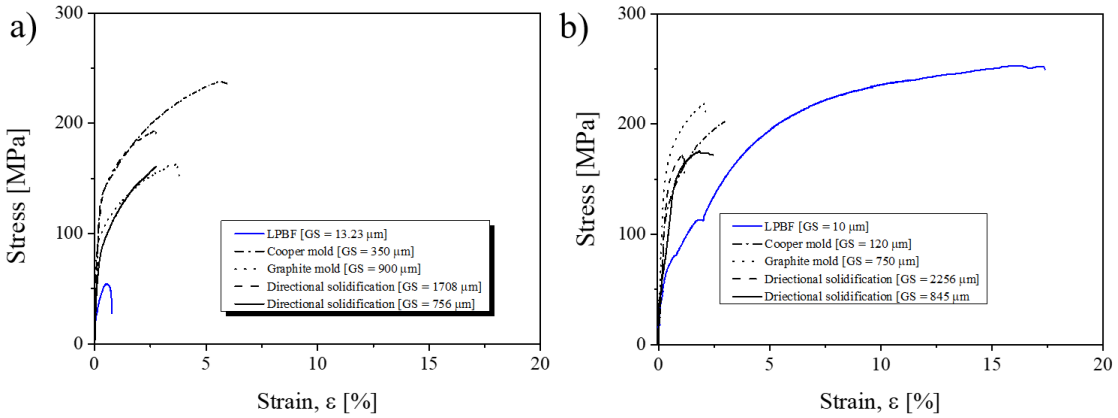

Figure 4. 83 – Typical tensile curves registered for the **a**) M1_0Ce and **b**) M1_3Ce compositions processed by different manufacturing techniques. The tensile tests were carried out using samples with a rectangular geometry.

By applying the Hollomon and Ludwik exponential model, the strain-hardening coefficient (n) and strength coefficient (k) of the material were determined (Figures 4.8 g and4.8 h). Ideally, high values of n and k are desirable, indicating strong mechanical strength requiring high tensile forces to initiate material necking. Although n and k values in LPBF parts are slightly lower than those in conventionally produced parts, they still fall within acceptable ranges. **Figure 4.85** depicts fracture analyses of rectangular M1_0Ce and M1_3Ce specimens in both LPBF and as-cast conditions. While both compositions exhibit predominantly brittle fractures in both conditions, M1_3Ce displays a tendency toward more ductile fracture behavior where small dimples on the fracture surface, typical of brittle fractures, are observed.

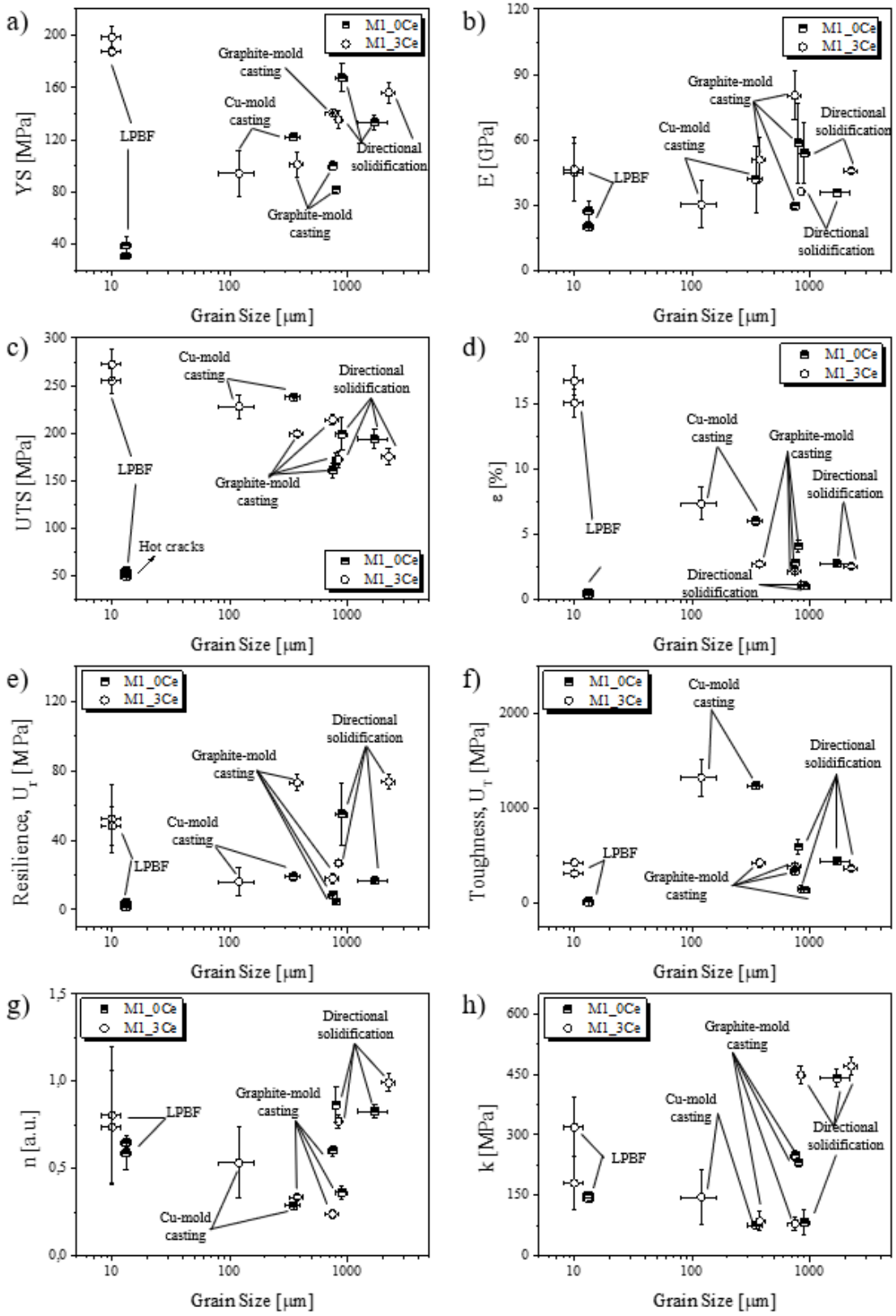

Figure 4. 84 – Experimental correlations between the **a**) yield strength; **b**) elastic modulus; **c**) ultimate tensile strength; **d**) elongation at fracture; **e**) resilience; **f**)

toughness; **g**) strain-hardening coefficient; and **h**) strength coefficient as a function of the grain sizes for the M1_0Ce and M1_3Ce parts processed by the different manufacturing techniques applied in this work.

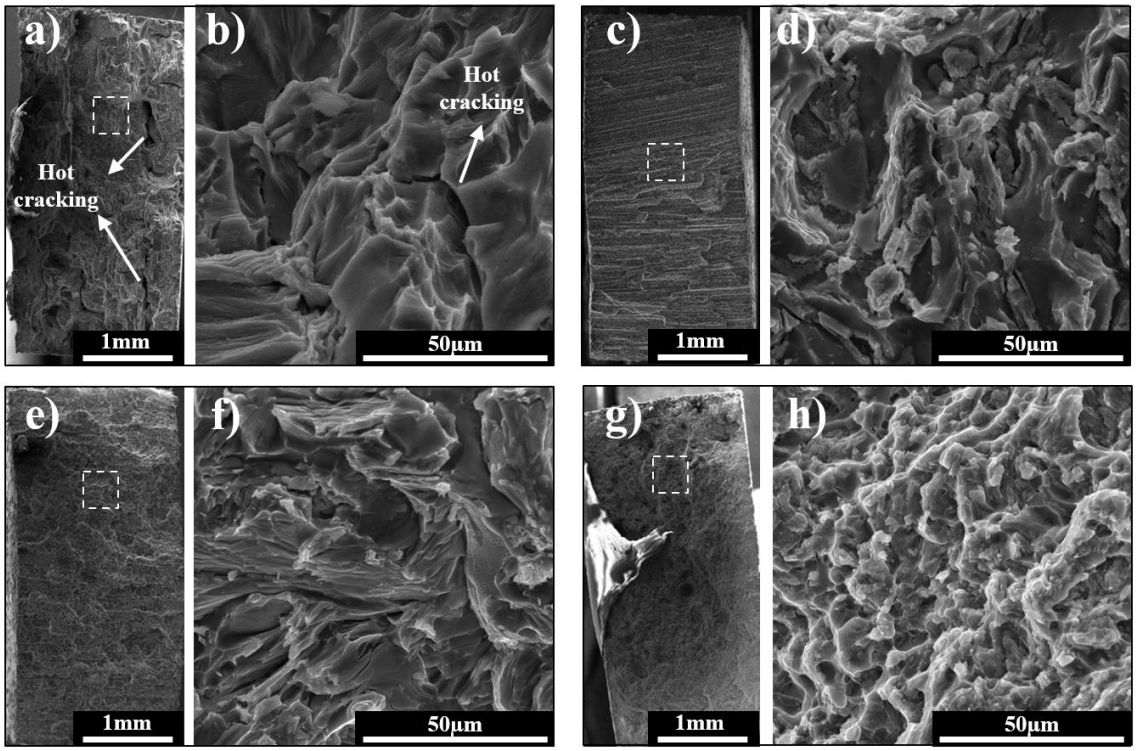

Figure 4. 85 – Tensile fracture surface characteristics of M1_0Ce (a – d) and M1_3Ce (e – h) parts processed by LPBF (a-b, e-f) and graphite casting (c-d, g-h) manufacturing techniques using specimens with a rectangular geometry.

Due to the high density of hot cracks of M1_0Ce LPBF parts, conducting tensile tests with cylindrical specimens was unfeasible. Samples failed prematurely either during machining or the tensile tests, preventing the measurement of any mechanical property. Consequently, only the M1_3Ce composition in the LPBF condition was considered. **Figure 4.86** illustrates tensile curves for cylindrical specimens, showing a substantial increase in mechanical properties compared to rectangular specimens, with yield strength (YS), ultimate tensile strength (UTS), and ductility reaching 283 MPa, 430 MPa, and 13.8%, respectively.

The n and k values also were calculated. For reference, AA2017 and AA2024 samples produced by graphite -mold casting exhibit n = 0.03 – 0.08 and k = 151 – 532 MPa for AA2017 (this research), and n = 0.17 and k = 701.6 MPa for AA2024 [276]. LPBF parts of AA2024 inoculated with Ti nanoparticles reportedly have n = 0.009 – 0.057 [277]. In contrast, LPBF M1_3Ce parts demonstrate significantly higher values of n = 0.2 and k = 874.68 MPa in cylindrical geometry samples.

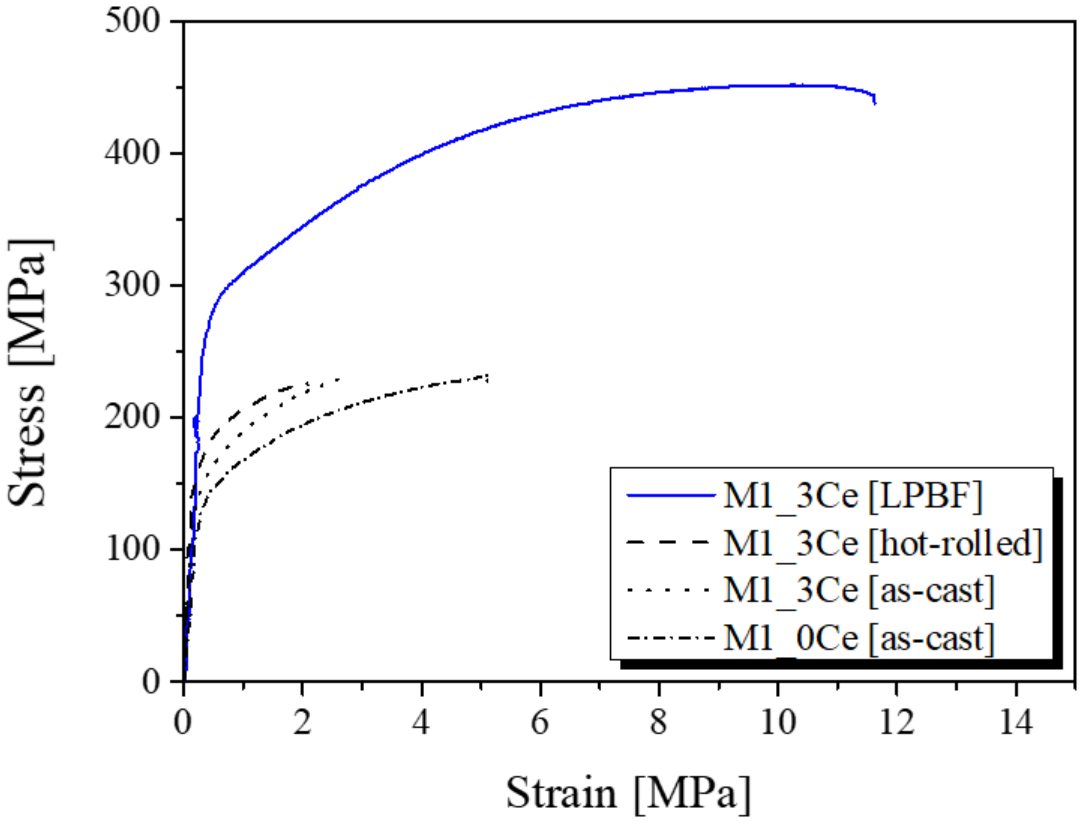

Figure 4. 86 – Typical tensile curves registered for M1_3Ce parts in LPBF, hot-rolled, and as-cast conditions, as well as the M1_0Ce part in the as-cast condition. The tensile tests were carried out using samples with a cylindrical geometry.

Figure 4.87 displays the fracture surface analysis of cylindrical geometry specimens. Similar to rectangular specimens, M1_0Ce cylindrical specimens exhibit brittle behavior, with premature failure in LPBF samples characterized by

sharp cleavage planes aligning with hot crack presence. In as-cast condition, M1_0Ce samples show less pronounced cleavage. In contrast, M1_3Ce in as-cast condition feature larger and more abundant dimples, indicating greater material ductility. Nevertheless, the LPBF parts shows the presence of cleavage planes but less pronounced than the M1_0Ce LPBF parts.

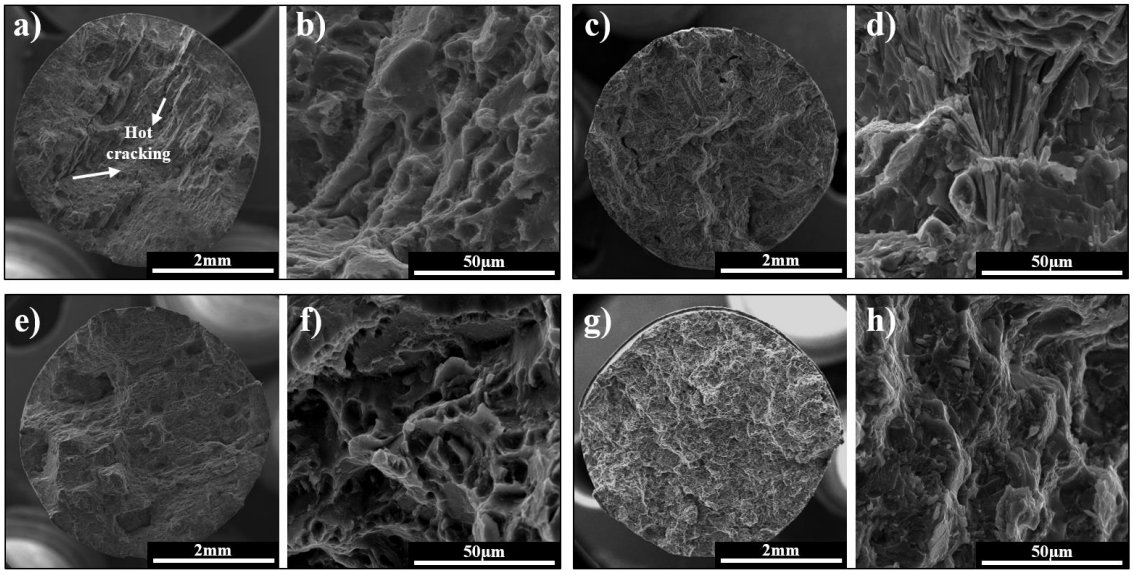

Figure 4. 87 – Tensile fracture surface characteristics of M1_0Ce (a – d) and M1_3Ce (e – h) parts processed by LPBF (a-b, e-f) and graphite casting (c-d, g-h) manufacturing techniques using specimens with a cylindrical geometry.

Figure 4.88 illustrates a comparison of YS, UTS, and ductility values with data from the literature [19, 136, 142, 265, 275-286]. It's evident that the M1_3Ce composition shares similar YS-UTS and Ductility-UTS relationships with Al-Cu compositions reinforced by inoculants and manufactured through additive processes. This suggests that M1_3Ce LPBF parts possess good mechanical properties without requiring reinforcing particles.

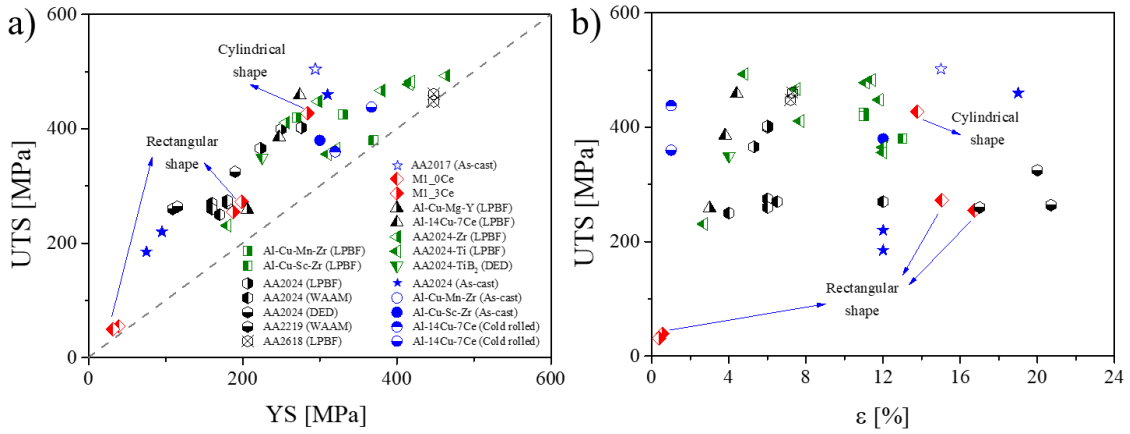

Figure 4. 88 – a) UTS vs YS and b) UTS vs ductility (ε) values at tensile tests of LPBF parts produced in this work. The values are compared with the tensile mechanical properties reported in the literature for Al-Cu-based alloys processed by additive manufacturing and conventional manufacturing techniques. The data was collected from [19, 136, 142, 165, 275-286].

4.8. Defects produced during LPBF

Until now, the methodology and procedure carried out for the proper development of this work have been presented, highlighting the most relevant results and the best processing conditions obtained. However, although we discussed in this work some of the defects typically found in parts produced by additive manufacturing such as porosity, lack of fusion, and hot cracking, other types of defects can also occur due to a poor selection of parameters or caused by geometry and size of parts processed by LPBF. Although a detailed analysis of the formation of this type of defect by DoE was not carried out, it is good to take them into account when thinking about building metal parts by LPBF.

One of the main defects in the parts that were obtained during the selection of parameters was the lack of fusion of the different layers that make up the built part. An example of defective parts due to this cause is presented in **Figure 4.89**. This defect was generated by an insufficiency in the applied energy density (low power, high scanning speeds, and a wide hatch distance), and the intrinsic characteristics of the metallic powder and the laser source like the reflectivity of the powders and the wavelength of the laser, causing the depth of the well to melt

is not able to penetrate the previously deposited layer and, consequently, the layers cannot be melted and welded properly [287].

Likewise, in the course of this project's development, flaws in both the CAD code and the machine software contributed to the occurrence of this defect. For instance, certain prints had to be redone because of the deposition of successive powder layers without proper melting, resulting in the accumulation of thicker powder layers that couldn't be fully melted by the laser. Consequently, this led to the formation of sheets that shifted across the substrate, impeding the construction of other components.

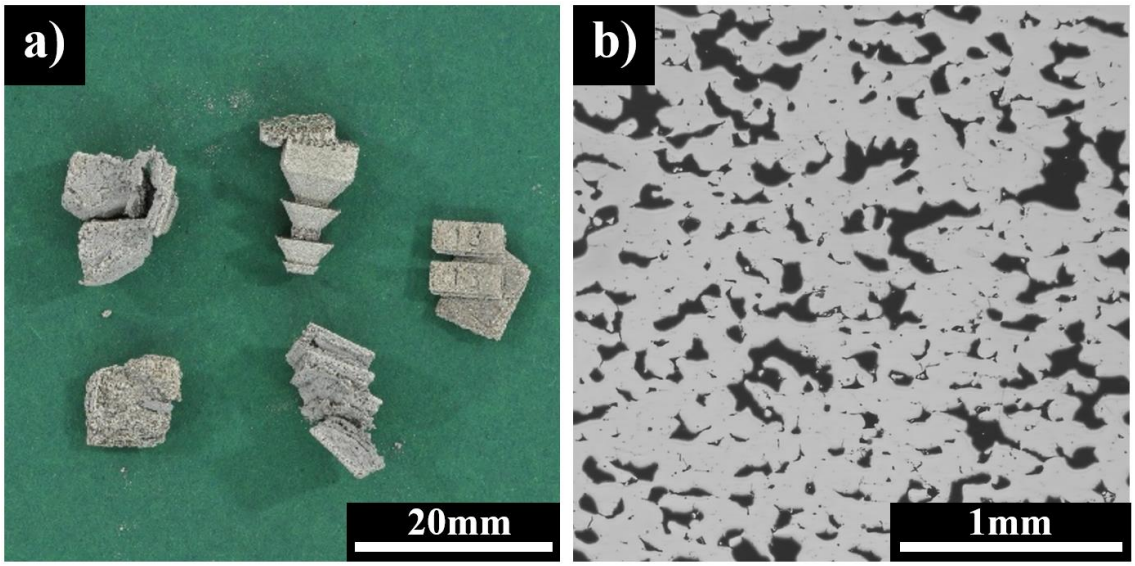

Figure 4. 89 – Effect of a wrong parameters selection on the a) welding between powder layers and b) lack of fusion of parts processed by LPBF.

Shape distortion is one of the most common defects in parts built by LPBF as reported by Aboulkhair *et al.* [7]. The high density of residual stresses caused during the construction of the part can generate distortion and delamination. As reported by Buchbinder *et al.* [288], during the melting of the powder layer, compressive plastic stresses are formed at the beginning of the scanned track, while towards the end of the track, tensile stresses are formed, distorting the deposited layer. If a high density of internal stresses is generated, the newly deposited layer can detach from the previous layer, thus generating delamination [289].

The tendency to generate this type of defect increases as the dimensions of the constructed part increase. In this work, the parts built as cubes of different dimensions did not present traces of delamination; however, distortion was observed in the dimensions of cylindrical bars with a greater length (12 cm, diameter of 1 cm) compared to bars of shorter length (5 cm, diameter of 1 cm) due to a greater difference between the dimensions of the part built, as seen in **Figure 4.90**.

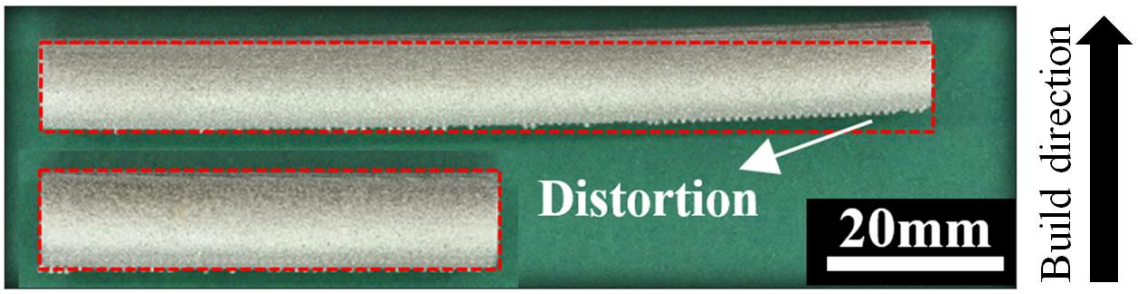

Figure 4. 90 – Shape distortion in M1_3Ce cylinders built by LPBF. A significant difference between the dimensions of each axis, i.e. diameter/length of the cylinder, in this case, produces a shape distortion by the effect of the internal stresses generated during the building of the LPBF part.

The formation of internal defects such as porosity and hot cracking also tends to increase due to an increase in the dimensions of the built part. Koutny *et al.* [290] have shown that an increase in AA2618 parts built by LPBF causes an increase in porosity and crack formation. The porosity values increased from 0.03 % in 0.5 mm cubes to 5.95 % in 13 mm edge cubes. In this study, cubes of the composition M1_3Ce with 5 mm, 8 mm, 12 mm, and 15 mm edges were printed. As observed in **Figure 4.91**, the built parts did not present a significant variation in the porosity values. Likewise, the formation of cracks was not detected, verifying the optimal behavior of this composition within LPBF. Although other types of defects can be formed during the construction of parts by AM, e.g. surface defects such as spatter, roughness, satellites, and balling, these were unfortunately not analyzed in this work. The authors will consider the analysis of this type of defect in future works.

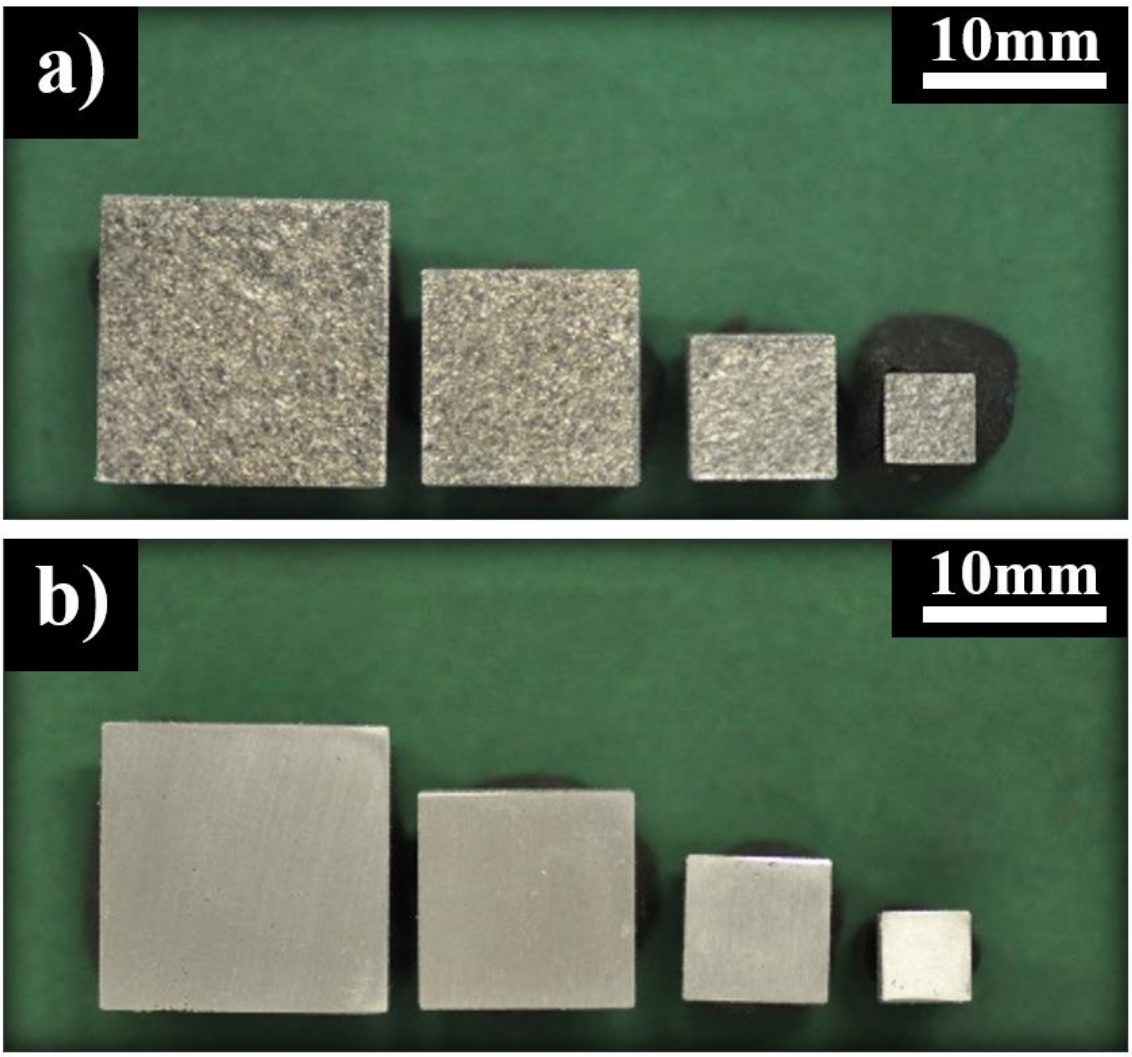

Figure 4. 91 – Effect of the M1_3Ce LPBF cube size on the formation of surface roughness, porosity, and hot cracking defects. As shown in a) the samples do not show changes in the as-built surface of the different cubes. In b) it is shown the polished cubes until 3 µm. It was not possible to observe a representative increase in porosity by applying higher dimensions to produce bigger cubes. Likewise, independent of the cube size, M1_3Ce LPBF parts did not present hot cracks.

5. CONCLUSIONS

This research focused on tailoring the AA2017 composition to improve its processability by LPBF. The main results obtained are summarized below:

Selection of candidate compositions: Thermodynamic calculations using the CALPHAD method were conducted to analyze the solidification process of the AA2017 composition and its impact on hot cracking susceptibility (HCS). Using the Pandat software, a suitable composition for additive manufacturing was determined (M1_3Ce). The AA2017 alloy comprises Al-Cu-Mg-Si elements, with Cu and Si significantly widening its solidification range, thus enhancing HCS. Optimal concentrations of these elements reduce HCS by narrowing the solidification interval and increasing the remaining eutectic liquid during the solidification's terminal stage. Cerium emerged as an excellent candidate to enhance the processability of the AA2017 alloy, with a 3 wt.%Ce addition representing an ideal concentration to ensure crack-free part manufacturing.

Preliminary tests: Candidate compositions identified through thermodynamic calculations underwent processing via various techniques to assess their microstructure and phase formation. This step ensured that the composition proposed in this study, namely M1_3Ce, exhibits the lowest HCS. This is primarily attributed to a reduced solidification range and the formation of eutectic regions primarily composed of Al + Al_3CeCu. Furthermore, the addition of Ce promotes a refining and strengthening effect, enhancing the material's mechanical strength, as evidenced in directionally solidified, suction-cast, and laser-remelted parts. Directional solidification tests were instrumental in elucidating the solidification behavior of the compositions investigated in this study and determining the phases that can emerge at different cooling rates for both M1_0Ce and M1_3Ce compositions.

Atomization of metal powders: The raw material was produced via gas atomization. Various techniques were employed to characterize the metal

powders, focusing on morphology, defect formation, and physicochemical behavior crucial for additive manufacturing applications. Optical microscopy, scanning electron microscopy, and dynamic image analysis revealed a direct relationship between particle size, morphology, microstructure, and cooling rate. Smaller particles exhibit rapid cooling, resulting in a highly refined microstructure and predominantly spherical morphology. As particle size increases, the morphology changes, leading to reduced sphericity and increased defect formation such as agglomerations, satellites, and splashes. Directional solidification tests and mathematical models from existing literature were employed to correlate particle size with cooling rate. Physicochemical characterization unveiled low fluidity due to high cohesion among particles, attributed to the low density of aluminum alloy particles and a high concentration of fine particles (20 - 63 μm) in the powder samples intended for LPBF processing.

Production of metallic parts by LPBF: Cubic samples of M1_0Ce and M1_3Ce compositions were fabricated using a Design of Experiments (DoE) and Analysis of Variance (ANOVA) approach to investigate the influence of process variables (laser power, scanning speed, and hatch size) on microstructural characteristics and mechanical properties of the built parts. This facilitated the development of mathematical models to determine optimal parameter combinations for producing parts with superior quality—specifically, high density, crack-free structure and enhanced mechanical strength.

It was observed that, regardless of the parameter combination used, M1_0Ce composition exhibited high susceptibility to cracking. In contrast, no crack formation was observed in any of the samples manufactured from the M1_3Ce composition, highlighting its excellent processability in additive manufacturing. Characterization of the Laser Powder Bed Fusion (LPBF) parts through Scanning Electron Microscopy (SEM), Transmission Electron Microscopy (TEM), and X-ray Diffraction (XRD) revealed that the exceptional printability of M1_3Ce composition stemmed from the formation of eutectic regions rich in Al + Al_3CeCu, which mitigated hot cracking susceptibility.

Mechanical properties: Parts made from M1_0Ce and M1_3Ce compositions underwent various manufacturing techniques, including Laser Powder Bed Fusion (LPBF). Mechanical properties were validated through microhardness, compression, and tension tests. Results revealed that M1_3Ce composition exhibited greater mechanical strength, reaching hardness values of up to 130 HV in LPBF parts, while M1_0Ce parts achieved a maximum hardness of 110 HV. Application of solution and annealing heat treatments reduced ductility values for M1_3Ce composition. Furthermore, although aging treatments at 150 °C for 3 – 12 h increased hardness values, the difference compared to as-built parts was merely 5 HV.

Compression and tensile tests showcased that M1_3Ce composition outperforms M1_0Ce in mechanical strength and ductility. Poor ductility in LPBF M1_0Ce parts primarily stemmed from crack presence, initiating fracture. Conversely, LPBF-produced M1_3Ce parts demonstrated an optimal balance of yield strength (YS), ultimate tensile strength (UTS), and ductility. Correlation of these properties with literature data indicated optimal mechanical behavior, with YS and UTS values comparable to those of additive manufacturing parts of Al-Cu-based alloys reinforced with particles or inoculant elements, while ductility tended to be superior.

Finally, cubic and cylindrical samples of M1_3Ce composition were produced in random sizes. Although some defects like shape distortion were observed, this composition did not exhibit delamination or crack formation reported in other aluminum alloys processed via LPBF when scaling up part size. This finding underscores the superior printing capability of this composition compared to previously tested aluminum alloys in additive manufacturing processes.

6. REFERENCES

[1] J. Koch and J. Mazumder, *Apparatus and methods for monitoring and controlling multi-layer laser cladding*. 2000.

[2] H. Y. Jung *et al.*, “Fabrication of Fe-based bulk metallic glass by selective laser melting: A parameter study,” *Mater Des*, vol. 86, pp. 703–708, Dec. 2015, doi: 10.1016/j.matdes.2015.07.145.

[3] S. Pauly *et al.*, “Processing metallic glasses by selective laser melting,” *Materials Today*, vol. 16, no. 1–2, pp. 37–41, Jan. 2013, doi: 10.1016/j.mattod.2013.01.018.

[4] X. P. Li *et al.*, “A selective laser melting and solution heat treatment refined Al–12Si alloy with a controllable ultrafine eutectic microstructure and 25% tensile ductility,” *Acta Mater*, vol. 95, pp. 74–82, Aug. 2015, doi: 10.1016/j.actamat.2015.05.017.

[5] M. Seifi, A. Salem, J. Beuth, O. Harrysson, and J. J. Lewandowski, “Overview of Materials Qualification Needs for Metal Additive Manufacturing,” *JOM*, vol. 68, no. 3, pp. 747–764, Mar. 2016, doi: 10.1007/s11837-015-1810-0.

[6] I. Polmear, D. StJohn, J.-F. Nie, and M. Qian, “Novel Materials and Processing Methods,” in *Light Alloys*, Elsevier, 2017, pp. 461–514. doi: 10.1016/B978-0-08-099431-4.00008-7.

[7] N. T. Aboulkhair, M. Simonelli, L. Parry, I. Ashcroft, C. Tuck, and R. Hague, “3D printing of Aluminium alloys: Additive Manufacturing of Aluminium alloys using selective laser melting,” *Prog Mater Sci*, vol. 106, p. 100578, Dec. 2019, doi: 10.1016/j.pmatsci.2019.100578.

[8] K. G. Prashanth and J. Eckert, “Formation of metastable cellular microstructures in selective laser melted alloys,” *J Alloys Compd*, vol. 707, pp. 27–34, Jun. 2017, doi: 10.1016/j.jallcom.2016.12.209.

[9] J. H. Martin, B. D. Yahata, J. M. Hundley, J. A. Mayer, T. A. Schaedler, and T. M. Pollock, “3D printing of high-strength aluminium alloys,” *Nature*, vol. 549, no. 7672, pp. 365–369, Sep. 2017, doi: 10.1038/nature23894.

[10] D. Zhang *et al.*, “Additive manufacturing of ultrafine-grained high-strength titanium alloys,” *Nature*, vol. 576, no. 7785, pp. 91–95, Dec. 2019, doi: 10.1038/s41586-019-1783-1.

[11] I. Rosenthal, A. Stern, and N. Frage, “Microstructure and Mechanical Properties of AlSi10Mg Parts Produced by the Laser Beam Additive Manufacturing (AM) Technology,” *Metallography, Microstructure, and Analysis*, vol. 3, no. 6, pp. 448–453, Dec. 2014, doi: 10.1007/s13632-014-0168-y.

[12] R. Xiao and X. Zhang, “Problems and issues in laser beam welding of aluminum–lithium alloys,” *J Manuf Process*, vol. 16, no. 2, pp. 166–175, Apr. 2014, doi: 10.1016/j.jmapro.2013.10.005.

[13] S. Lathabai, “Additive Manufacturing of Aluminium-Based Alloys and Composites,” in *Fundamentals of Aluminium Metallurgy*, Elsevier, 2018, pp. 47–92. doi: 10.1016/B978-0-08-102063-0.00002-3.

[14] P. Wang, H. C. Li, K. G. Prashanth, J. Eckert, and S. Scudino, “Selective laser melting of Al-Zn-Mg-Cu: Heat treatment, microstructure and mechanical properties,” *J Alloys Compd*, vol. 707, pp. 287–290, Jun. 2017, doi: 10.1016/j.jallcom.2016.11.210.

[15] T. Minasyan and I. Hussainova, “Laser Powder-Bed Fusion of Ceramic Particulate Reinforced Aluminum Alloys: A Review,” *Materials*, vol. 15, no. 7, p. 2467, Mar. 2022, doi: 10.3390/ma15072467.

[16] F. Chang, D. Gu, D. Dai, and P. Yuan, “Selective laser melting of in-situ Al4SiC4 + SiC hybrid reinforced Al matrix composites: Influence of starting SiC particle size,” *Surf Coat Technol*, vol. 272, pp. 15–24, Jun. 2015, doi: 10.1016/j.surfcoat.2015.04.029.

[17] M. Wang, B. Song, Q. Wei, and Y. Shi, “Improved mechanical properties of AlSi7Mg/nano-SiCp composites fabricated by selective laser melting,” *J Alloys Compd*, vol. 810, p. 151926, Nov. 2019, doi: 10.1016/j.jallcom.2019.151926.

[18] R. Chen *et al.*, “Exposure, assessment and health hazards of particulate matter in metal additive manufacturing: A review,” *Chemosphere*, vol. 259, p. 127452, Nov. 2020, doi: 10.1016/j.chemosphere.2020.127452.

[19] D. R. Manca *et al.*, “Microstructure and Properties of Novel Heat Resistant Al–Ce–Cu Alloy for Additive Manufacturing,” *Metals and Materials International*, vol. 25, no. 3, pp. 633–640, May 2019, doi: 10.1007/s12540-018-00211-0.

[20] Z. C. Sims *et al.*, “Cerium-Based, Intermetallic-Strengthened Aluminum Casting Alloy: High-Volume Co-product Development,” *JOM*, vol. 68, no. 7, pp. 1940–1947, Jul. 2016, doi: 10.1007/s11837-016-1943-9.

[21] Z. C. Sims, O. Rios, S. K. McCall, T. Van Buuren, and R. T. Ott, “Characterization of Near Net-Shape Castable Rare Earth Modified Aluminum Alloys for High Temperature Application,” in *Light Metals 2016*, Cham: Springer International Publishing, 2016, pp. 111–114. doi: 10.1007/978-3-319-48251-4_19.

[22] D. Weiss, “Improved High-Temperature Aluminum Alloys Containing Cerium,” *J Mater Eng Perform*, vol. 28, no. 4, pp. 1903–1908, Apr. 2019, doi: 10.1007/s11665-019-3884-2.

[23] Y. Wu, J. Xiong, R. Lai, X. Zhang, and Z. Guo, “The microstructure evolution of an Al–Mg–Si–Mn–Cu–Ce alloy during homogenization,” *J Alloys Compd*, vol. 475, no. 1–2, pp. 332–338, May 2009, doi: 10.1016/j.jallcom.2008.07.032.

[24] F. Czerwinski, “Cerium in aluminum alloys,” *J Mater Sci*, vol. 55, no. 1, pp. 24–72, Jan. 2020, doi: 10.1007/s10853-019-03892-z.

[25] M. Karg, B. Ahuja, and M. Schimidt, “Processability of High Strength Aluminium-Copper Alloys AW-2022 and 2024 by Laser Beam Melting in Powder Bed,” in *Proceedings of the 25th Solid Freeform Fabrication Symposium (SFF)*, 2014, pp. 420–436.

[26] R. Casati, M. Coduri, M. Riccio, A. Rizzi, and M. Vedani, “Development of a high strength Al–Zn–Si–Mg–Cu alloy for selective laser melting,” *J Alloys Compd*, vol. 801, pp. 243–253, Sep. 2019, doi: 10.1016/j.jallcom.2019.06.123.

[27] K. Schmidtke, F. Palm, A. Hawkins, and C. Emmelmann, “Process and Mechanical Properties: Applicability of a Scandium modified Al-alloy for

Laser Additive Manufacturing," *Phys Procedia*, vol. 12, pp. 369–374, 2011, doi: 10.1016/j.phpro.2011.03.047.

[28] P. K. Dos Santos Bomfim, "Efeito do inoculante Al-Nb-B na microestrutura e propriedades mecânicas da liga AA2017 fabricada por fusão em leito de pó a laser," Federal University of São Carlos, 2023.

[29] T. DebRoy *et al.*, "Additive manufacturing of metallic components – Process, structure and properties," *Prog Mater Sci*, vol. 92, pp. 112–224, 2018, doi: https://doi.org/10.1016/j.pmatsci.2017.10.001.

[30] A. V. Pozdniakov, A. Y. Churyumov, I. S. Loginova, D. K. Daubarayte, D. K. Ryabov, and V. A. Korolev, "Microstructure and properties of novel AlSi11CuMn alloy manufactured by selective laser melting," *Mater Lett*, vol. 225, pp. 33–36, 2018, doi: 10.1016/j.matlet.2018.04.077.

[31] J. O. Milewski, "Additive manufacturing of metals," in *From Fundamental Technology to Rocket Nozzles, Medical Implants, and Custom Jewelry*, 2017, pp. 134–157.

[32] G. Gong *et al.*, "Research status of laser additive manufacturing for metal: a review," *Journal of Materials Research and Technology*, vol. 15, pp. 855–884, Nov. 2021, doi: 10.1016/j.jmrt.2021.08.050.

[33] H. Asgari, C. Baxter, K. Hosseinkhani, and M. Mohammadi, "On microstructure and mechanical properties of additively manufactured AlSi10Mg_200C using recycled powder," *Materials Science and Engineering: A*, vol. 707, pp. 148–158, Nov. 2017, doi: 10.1016/j.msea.2017.09.041.

[34] R. F. Hamilton, B. A. Bimber, M. Taheri Andani, and M. Elahinia, "Multi-scale shape memory effect recovery in NiTi alloys additive manufactured by selective laser melting and laser directed energy deposition," *J Mater Process Technol*, vol. 250, pp. 55–64, Dec. 2017, doi: 10.1016/j.jmatprotec.2017.06.027.

[35] P. C. Collins, D. A. Brice, P. Samimi, I. Ghamarian, and H. L. Fraser, "Microstructural Control of Additively Manufactured Metallic Materials," *Annu Rev Mater Res*, vol. 46, no. 1, pp. 63–91, Jul. 2016, doi: 10.1146/annurev-matsci-070115-031816.

[36] D. Jafari and W. W. Wits, “The utilization of selective laser melting technology on heat transfer devices for thermal energy conversion applications: A review,” *Renewable and Sustainable Energy Reviews*, vol. 91, pp. 420–442, Aug. 2018, doi: 10.1016/j.rser.2018.03.109.

[37] D. D. Gu, W. Meiners, K. Wissenbach, and R. Poprawe, “Laser additive manufacturing of metallic components: materials, processes and mechanisms,” *International Materials Reviews*, vol. 57, no. 3, pp. 133–164, May 2012, doi: 10.1179/1743280411Y.0000000014.

[38] Y. Tang, H. T. Loh, Y. S. Wong, J. Y. H. Fuh, L. Lu, and X. Wang, “Direct laser sintering of a copper-based alloy for creating three-dimensional metal parts,” *J Mater Process Technol*, vol. 140, no. 1–3, pp. 368–372, Sep. 2003, doi: 10.1016/S0924-0136(03)00766-0.

[39] D. Gu and Y. Shen, “Balling phenomena during direct laser sintering of multi-component Cu-based metal powder,” *J Alloys Compd*, vol. 432, no. 1–2, pp. 163–166, Apr. 2007, doi: 10.1016/j.jallcom.2006.06.011.

[40] S. Das, “Physical Aspects of Process Control in Selective Laser Sintering of Metals,” *Adv Eng Mater*, vol. 5, no. 10, pp. 701–711, Oct. 2003, doi: 10.1002/adem.200310099.

[41] E. O. Olakanmi, R. F. Cochrane, and K. W. Dalgarno, “A review on selective laser sintering/melting (SLS/SLM) of aluminium alloy powders: Processing, microstructure, and properties,” *Prog Mater Sci*, vol. 74, pp. 401–477, Oct. 2015, doi: 10.1016/j.pmatsci.2015.03.002.

[42] N. K. Tolochko, Y. V. Khlopkov, S. E. Mozzharov, M. B. Ignatiev, T. Laoui, and V. I. Titov, “Absorptance of powder materials suitable for laser sintering,” *Rapid Prototyp J*, vol. 6, no. 3, pp. 155–161, Sep. 2000, doi: 10.1108/13552540010337029.

[43] N. Takata, H. Kodaira, K. Sekizawa, A. Suzuki, and M. Kobashi, “Change in microstructure of selectively laser melted AlSi10Mg alloy with heat treatments,” *Materials Science and Engineering: A*, vol. 704, pp. 218–228, Sep. 2017, doi: 10.1016/j.msea.2017.08.029.

[44] L. Thijs, K. Kempen, J.-P. Kruth, and J. Van Humbeeck, “Fine-structured aluminium products with controllable texture by selective laser melting of

pre-alloyed AlSi10Mg powder," *Acta Mater*, vol. 61, no. 5, pp. 1809–1819, Mar. 2013, doi: 10.1016/j.actamat.2012.11.052.

[45] T. Kimura and T. Nakamoto, "Microstructures and mechanical properties of A356 (AlSi7Mg0.3) aluminum alloy fabricated by selective laser melting," *Mater Des*, vol. 89, pp. 1294–1301, Jan. 2016, doi: 10.1016/j.matdes.2015.10.065.

[46] E. Louvis, P. Fox, and C. J. Sutcliffe, "Selective laser melting of aluminium components," *J Mater Process Technol*, vol. 211, no. 2, pp. 275–284, Feb. 2011, doi: 10.1016/j.jmatprotec.2010.09.019.

[47] D. Schreuder, *Outdoor Lighting: Physics, Vision and Perception*. Dordrecht: Springer Netherlands, 2008. doi: 10.1007/978-1-4020-8602-1.

[48] G. S. (George S. Brady, H. R. Clauser, and J. A. Vaccari, *Materials handbook : an encyclopedia for managers, technical professionals, purchasing and production managers, technicians and supervisors.* McGraw-Hill, 2002.

[49] G. Welsch, R. Boyer, and E. W. Collings, *Materials properties handbook: titanium alloys*. ASM International, 1993.

[50] M. Bauccio, *Metals reference book*. ASM International, 1993.

[51] M. Boivineau *et al.*, "Thermophysical Properties of Solid and Liquid Ti-6Al-4V (TA6V) Alloy," *Int J Thermophys*, vol. 27, no. 2, pp. 507–529, Mar. 2006, doi: 10.1007/PL00021868.

[52] M. Zavala-Arredondo *et al.*, "Laser diode area melting for high speed additive manufacturing of metallic components," *Mater Des*, vol. 117, pp. 305–315, Mar. 2017, doi: 10.1016/j.matdes.2016.12.095.

[53] D. Buchbinder, H. Schleifenbaum, S. Heidrich, W. Meiners, and J. Bültmann, "High Power Selective Laser Melting (HP SLM) of Aluminum Parts," *Phys Procedia*, vol. 12, pp. 271–278, 2011, doi: 10.1016/j.phpro.2011.03.035.

[54] B. Ahuja, M. Karg, K. Yu. Nagulin, and M. Schmidt, "Fabrication and Characterization of High Strength Al-Cu Alloys Processed Using Laser Beam Melting in Metal Powder Bed," *Phys Procedia*, vol. 56, pp. 135–146, 2014, doi: 10.1016/j.phpro.2014.08.156.

[55] C. Kamath, B. El-dasher, G. F. Gallegos, W. E. King, and A. Sisto, “Density of additively-manufactured, 316L SS parts using laser powder-bed fusion at powers up to 400 W,” *The International Journal of Advanced Manufacturing Technology*, vol. 74, no. 1–4, pp. 65–78, Sep. 2014, doi: 10.1007/s00170-014-5954-9.

[56] J. C. Ion, *Laser processing of engineering materials: principles, procedure and industrial application*. Elsevier, 2005.

[57] W. Yuan, H. Chen, T. Cheng, and Q. Wei, “Effects of laser scanning speeds on different states of the molten pool during selective laser melting: Simulation and experiment,” *Mater Des*, vol. 189, p. 108542, Apr. 2020, doi: 10.1016/j.matdes.2020.108542.

[58] H. L. Wei, J. Mazumder, and T. DebRoy, “Evolution of solidification texture during additive manufacturing,” *Sci Rep*, vol. 5, no. 1, p. 16446, Dec. 2015, doi: 10.1038/srep16446.

[59] N. T. Aboulkhair, I. Maskery, C. Tuck, I. Ashcroft, and N. M. Everitt, “The microstructure and mechanical properties of selectively laser melted AlSi10Mg: The effect of a conventional T6-like heat treatment,” *Materials Science and Engineering: A*, vol. 667, pp. 139–146, Jun. 2016, doi: 10.1016/j.msea.2016.04.092.

[60] L. N. Carter, C. Martin, P. J. Withers, and M. M. Attallah, “The influence of the laser scan strategy on grain structure and cracking behaviour in SLM powder-bed fabricated nickel superalloy,” *J Alloys Compd*, vol. 615, pp. 338–347, Dec. 2014, doi: 10.1016/j.jallcom.2014.06.172.

[61] M. Xia, D. Gu, G. Yu, D. Dai, H. Chen, and Q. Shi, “Porosity evolution and its thermodynamic mechanism of randomly packed powder-bed during selective laser melting of Inconel 718 alloy,” *Int J Mach Tools Manuf*, vol. 116, pp. 96–106, May 2017, doi: 10.1016/j.ijmachtools.2017.01.005.

[62] S. A. Khairallah, A. T. Anderson, A. Rubenchik, and W. E. King, “Corrigendum to ‘Laser powder-bed fusion additive manufacturing: Physics of complex melt flow and formation mechanisms of pores, spatter, and denudation zones’ [Acta Mater. 108 (2016) 36–45],” *Acta Mater*, vol. 196, p. 30, Sep. 2020, doi: 10.1016/j.actamat.2020.06.034.

[63] D. Dai, D. Gu, R. Poprawe, and M. Xia, “Influence of additive multilayer feature on thermodynamics, stress and microstructure development during laser 3D printing of aluminum-based material,” *Sci Bull (Beijing)*, vol. 62, no. 11, pp. 779–787, Jun. 2017, doi: 10.1016/j.scib.2017.05.007.

[64] D. Wang, Y. Yang, R. Liu, D. Xiao, and J. Sun, “Study on the designing rules and processability of porous structure based on selective laser melting (SLM),” *J Mater Process Technol*, vol. 213, no. 10, pp. 1734–1742, Oct. 2013, doi: 10.1016/j.jmatprotec.2013.05.001.

[65] W. J. Sames, F. A. List, S. Pannala, R. R. Dehoff, and S. S. Babu, “The metallurgy and processing science of metal additive manufacturing,” *International Materials Reviews*, vol. 61, no. 5, pp. 315–360, Jul. 2016, doi: 10.1080/09506608.2015.1116649.

[66] P. Krakhmalev, I. Yadroitsava, G. Fredriksson, and I. Yadroitsev, “In situ heat treatment in selective laser melted martensitic AISI 420 stainless steels,” *Mater Des*, vol. 87, pp. 380–385, Dec. 2015, doi: 10.1016/j.matdes.2015.08.045.

[67] B. Zheng, Y. Zhou, J. E. Smugeresky, J. M. Schoenung, and E. J. Lavernia, “Thermal Behavior and Microstructural Evolution during Laser Deposition with Laser-Engineered Net Shaping: Part I. Numerical Calculations,” *Metallurgical and Materials Transactions A*, vol. 39, no. 9, pp. 2228–2236, Sep. 2008, doi: 10.1007/s11661-008-9557-7.

[68] S. Kou, *Welding metallurgy*. New Jersey: John Wiley & Sons, Inc., 2003.

[69] G. P. Dinda, A. K. Dasgupta, and J. Mazumder, “Texture control during laser deposition of nickel-based superalloy,” *Scr Mater*, vol. 67, no. 5, pp. 503–506, Sep. 2012, doi: 10.1016/j.scriptamat.2012.06.014.

[70] S. Thapliyal *et al.*, “An integrated computational materials engineering-anchored closed-loop method for design of aluminum alloys for additive manufacturing,” *Materialia (Oxf)*, vol. 9, p. 100574, Mar. 2020, doi: 10.1016/j.mtla.2019.100574.

[71] S. Thapliyal *et al.*, “Damage-tolerant, corrosion-resistant high entropy alloy with high strength and ductility by laser powder bed fusion additive

manufacturing," *Addit Manuf*, vol. 36, p. 101455, Dec. 2020, doi: 10.1016/j.addma.2020.101455.

[72] D. G. Eskin, Suyitno, and L. Katgerman, "Mechanical properties in the semi-solid state and hot tearing of aluminium alloys," *Prog Mater Sci*, vol. 49, no. 5, pp. 629–711, Jan. 2004, doi: 10.1016/S0079-6425(03)00037-9.

[73] S. Kou, "A criterion for cracking during solidification," *Acta Mater*, vol. 88, pp. 366–374, Apr. 2015, doi: 10.1016/j.actamat.2015.01.034.

[74] J. R. Davis, "Light Metals and Alloys-Aluminum and Aluminum Alloys," in *Alloying: Understanding the Basics*, ASM International, 2001, pp. 351–416.

[75] D. S. Mackenzie, *Handbook of Aluminum*. New York: Marcel Dekker Inc., 2003.

[76] J. R. Kissell, S. G. Pantelakis, and G. N. Haidemenopoulos, "Aluminum and Aluminum Alloys," in *Uhlig's Corrosion Handbook*, 2011, pp. 715–745.

[77] N. T. Aboulkhair, N. M. Everitt, I. Maskery, I. Ashcroft, and C. Tuck, "Selective laser melting of aluminum alloys," *MRS Bull*, vol. 42, no. 04, pp. 311–319, Apr. 2017, doi: 10.1557/mrs.2017.63.

[78] T. Qi, H. Zhu, H. Zhang, J. Yin, L. Ke, and X. Zeng, "Selective laser melting of Al7050 powder: Melting mode transition and comparison of the characteristics between the keyhole and conduction mode," *Mater Des*, vol. 135, pp. 257–266, Dec. 2017, doi: 10.1016/j.matdes.2017.09.014.

[79] S. Kou, "A simple index for predicting the susceptibility to solidification cracking," *Welding research*, vol. 94, pp. 374–388, 2015, [Online]. Available: https://app.aws.org/wj/supplement/WJ_2015_12_s374.pdf

[80] R. LIU, Z. DONG, and Y. PAN, "Solidification crack susceptibility of aluminum alloy weld metals," *Transactions of Nonferrous Metals Society of China*, vol. 16, no. 1, pp. 110–116, Feb. 2006, doi: 10.1016/S1003-6326(06)60019-8.

[81] S. A. Khairallah, A. T. Anderson, A. Rubenchik, and W. E. King, "Laser powder-bed fusion additive manufacturing: Physics of complex melt flow and formation mechanisms of pores, spatter, and denudation zones," *Acta Mater*, vol. 108, pp. 36–45, Apr. 2016, doi: 10.1016/j.actamat.2016.02.014.

[82] D. Turnbull and B. Vonnegut, “Nucleation Catalysis,” *Ind Eng Chem*, vol. 44, no. 6, pp. 1292–1298, Jun. 1952, doi: 10.1021/ie50510a031.

[83] Q. Wei *et al.*, “Selective laser melting of stainless-steel/nano-hydroxyapatite composites for medical applications: Microstructure, element distribution, crack and mechanical properties,” *J Mater Process Technol*, vol. 222, pp. 444–453, Aug. 2015, doi: 10.1016/j.jmatprotec.2015.02.010.

[84] C. Han *et al.*, “Microstructure and mechanical properties of (TiB+TiC)/Ti composites fabricated in situ via selective laser melting of Ti and B4C powders,” *Addit Manuf*, vol. 36, p. 101466, Dec. 2020, doi: 10.1016/j.addma.2020.101466.

[85] L. Xi, D. Gu, S. Guo, R. Wang, K. Ding, and K. G. Prashanth, “Grain refinement in laser manufactured Al-based composites with TiB2 ceramic,” *Journal of Materials Research and Technology*, vol. 9, no. 3, pp. 2611–2622, May 2020, doi: 10.1016/j.jmrt.2020.04.059.

[86] J. Liu and S. Kou, “Crack susceptibility of binary aluminum alloys during solidification,” *Acta Mater*, vol. 110, pp. 84–94, May 2016, doi: 10.1016/j.actamat.2016.03.030.

[87] S. Otarawanna and A. K. Dahle, “Casting of aluminium alloys,” in *Fundamentals of Aluminium Metallurgy*, Elsevier, 2011, pp. 141–154. doi: 10.1533/9780857090256.1.141.

[88] P. Wang, C. Gammer, F. Brenne, T. Niendorf, J. Eckert, and S. Scudino, “A heat treatable TiB2/Al-3.5Cu-1.5Mg-1Si composite fabricated by selective laser melting: Microstructure, heat treatment and mechanical properties,” *Compos B Eng*, vol. 147, pp. 162–168, Aug. 2018, doi: 10.1016/j.compositesb.2018.04.026.

[89] X. Wen *et al.*, “Laser solid forming additive manufacturing TiB2 reinforced 2024Al composite: Microstructure and mechanical properties,” *Materials Science and Engineering: A*, vol. 745, pp. 319–325, Feb. 2019, doi: 10.1016/j.msea.2018.12.072.

[90] B. Jiang, L. Zhenglong, C. Xi, L. Peng, L. Nannan, and C. Yanbin, “Microstructure and mechanical properties of TiB2-reinforced 7075

aluminum matrix composites fabricated by laser melting deposition," *Ceram Int*, vol. 45, no. 5, pp. 5680–5692, Apr. 2019, doi: 10.1016/j.ceramint.2018.12.033.

[91] D. Gu, F. Chang, and D. Dai, "Selective Laser Melting Additive Manufacturing of Novel Aluminum Based Composites With Multiple Reinforcing Phases," *J Manuf Sci Eng*, vol. 137, no. 2, Apr. 2015, doi: 10.1115/1.4028925.

[92] Z. Fan, C. Li, H. Yang, and Z. Liu, "Effects of TiC nanoparticle inoculation on the hot-tearing cracks and grain refinement of additively-manufactured AA2024 Al alloys," *Journal of Materials Research and Technology*, vol. 19, pp. 194–207, Jul. 2022, doi: 10.1016/j.jmrt.2022.05.039.

[93] Z. Hu *et al.*, "Microstructure and mechanical behavior of cemented carbide with Al alloy binder fabricated by selective laser melting," *Int J Refract Metals Hard Mater*, vol. 108, p. 105916, Nov. 2022, doi: 10.1016/j.ijrmhm.2022.105916.

[94] D. Dai and D. Gu, "Influence of thermodynamics within molten pool on migration and distribution state of reinforcement during selective laser melting of AlN/AlSi10Mg composites," *Int J Mach Tools Manuf*, vol. 100, pp. 14–24, Jan. 2016, doi: 10.1016/j.ijmachtools.2015.10.004.

[95] X. Li, G. Li, M.-X. Zhang, and Q. Zhu, "Novel approach to additively manufacture high-strength Al alloys by laser powder bed fusion through addition of hybrid grain refiners," *Addit Manuf*, vol. 48, p. 102400, Dec. 2021, doi: 10.1016/j.addma.2021.102400.

[96] A. S. Konopatsky *et al.*, "Microstructure evolution during AlSi10Mg molten alloy/BN microflake interactions in metal matrix composites obtained through 3D printing," *J Alloys Compd*, vol. 859, p. 157765, Apr. 2021, doi: 10.1016/j.jallcom.2020.157765.

[97] K. Miao, H. Zhou, Y. Gao, X. Deng, Z. Lu, and D. Li, "Laser powder-bed-fusion of Si3N4 reinforced AlSi10Mg composites: Processing, mechanical properties and strengthening mechanisms," *Materials Science and Engineering: A*, vol. 825, p. 141874, Sep. 2021, doi: 10.1016/j.msea.2021.141874.

[98] S. Dadbakhsh and L. Hao, “Effect of Al alloys on selective laser melting behaviour and microstructure of in situ formed particle reinforced composites,” *J Alloys Compd*, vol. 541, pp. 328–334, Nov. 2012, doi: 10.1016/j.jallcom.2012.06.097.

[99] S. S. Razavi Tousi, R. Yazdani Rad, E. Salahi, I. Mobasherpour, and M. Razavi, “Production of Al–20 wt.% Al2O3 composite powder using high energy milling,” *Powder Technol*, vol. 192, no. 3, pp. 346–351, Jun. 2009, doi: 10.1016/j.powtec.2009.01.016.

[100] A. Maleki, N. Hosseini, and B. Niroumand, “A review on aluminothermic reaction of Al/ZnO system,” *Ceram Int*, vol. 44, no. 1, pp. 10–23, Jan. 2018, doi: 10.1016/j.ceramint.2017.09.168.

[101] S. Dadbakhsh, R. Mertens, K. Vanmeensel, J. Vleugels, J. Van Humbeeck, and J.-P. Kruth, “In situ alloying and reinforcing of Al6061 during selective laser melting,” *Procedia CIRP*, vol. 74, pp. 39–43, 2018, doi: 10.1016/j.procir.2018.08.009.

[102] P. Mair, L. Kaserer, J. Braun, N. Weinberger, I. Letofsky-Papst, and G. Leichtfried, “Microstructure and mechanical properties of a TiB2-modified Al–Cu alloy processed by laser powder-bed fusion,” *Materials Science and Engineering: A*, vol. 799, p. 140209, Jan. 2021, doi: 10.1016/j.msea.2020.140209.

[103] S. I. Shakil *et al.*, “Microstructural-micromechanical correlation in an Al–Cu–Mg–Ag–TiB2 (A205) alloy: additively manufactured and cast,” *Materials Science and Engineering: A*, vol. 832, p. 142453, Jan. 2022, doi: 10.1016/j.msea.2021.142453.

[104] M. Avateffazeli *et al.*, “Correlation between tensile properties, microstructure, and processing routes of an Al–Cu–Mg–Ag–TiB2 (A205) alloy: Additive manufacturing and casting,” *Materials Science and Engineering: A*, vol. 841, p. 142989, Apr. 2022, doi: 10.1016/j.msea.2022.142989.

[105] T. Sun *et al.*, “Achieving excellent strength of the LPBF additively manufactured Al–Cu–Mg composite via in-situ mixing TiB2 and solution

treatment," *Materials Science and Engineering: A*, vol. 850, p. 143531, Aug. 2022, doi: 10.1016/j.msea.2022.143531.

[106] P. Mair *et al.*, "Dependence of mechanical properties and microstructure on solidification onset temperature for Al2024–CaB6 alloys processed using laser powder bed fusion," *Materials Science and Engineering: A*, vol. 833, p. 142552, Jan. 2022, doi: 10.1016/j.msea.2021.142552.

[107] P. Mair *et al.*, "Laser powder bed fusion of nano-CaB6 decorated 2024 aluminum alloy," *J Alloys Compd*, vol. 863, p. 158714, May 2021, doi: 10.1016/j.jallcom.2021.158714.

[108] X. Liu, Y. Liu, Z. Zhou, K. Wang, Q. Zhan, and X. Xiao, "Grain refinement and crack inhibition of selective laser melted AA2024 aluminum alloy via inoculation with TiC–TiH2," *Materials Science and Engineering: A*, vol. 813, p. 141171, May 2021, doi: 10.1016/j.msea.2021.141171.

[109] L. Li, R. Li, T. Yuan, C. Chen, Z. Zhang, and X. Li, "Microstructures and tensile properties of a selective laser melted Al–Zn–Mg–Cu (Al7075) alloy by Si and Zr microalloying," *Materials Science and Engineering: A*, vol. 787, p. 139492, Jun. 2020, doi: 10.1016/j.msea.2020.139492.

[110] L. Deillon, F. Jensch, F. Palm, and M. Bambach, "A new high strength Al–Mg–Sc alloy for laser powder bed fusion with calcium addition to effectively prevent magnesium evaporation," *J Mater Process Technol*, vol. 300, p. 117416, Feb. 2022, doi: 10.1016/j.jmatprotec.2021.117416.

[111] Y. Liang, C. Guo, C. Li, and Z. Du, "Thermodynamic modeling of the Al–Cr system," *J Alloys Compd*, vol. 460, no. 1–2, pp. 314–319, Jul. 2008, doi: 10.1016/j.jallcom.2007.06.046.

[112] D. Schimbäck *et al.*, "Alloy design strategy for microstructural-tailored scandium-modified aluminium alloys for additive manufacturing," *Scr Mater*, vol. 207, p. 114277, Jan. 2022, doi: 10.1016/j.scriptamat.2021.114277.

[113] J. R. Croteau *et al.*, "Microstructure and mechanical properties of Al-Mg-Zr alloys processed by selective laser melting," *Acta Mater*, vol. 153, pp. 35–44, Jul. 2018, doi: 10.1016/j.actamat.2018.04.053.

[114] J. Røyset and N. Ryum, “Scandium in aluminium alloys,” *International Materials Reviews*, vol. 50, no. 1, pp. 19–44, Feb. 2005, doi: 10.1179/174328005X14311.

[115] M. E. van Dalen, D. C. Dunand, and D. N. Seidman, “Effects of Ti additions on the nanostructure and creep properties of precipitation-strengthened Al–Sc alloys,” *Acta Mater*, vol. 53, no. 15, pp. 4225–4235, Sep. 2005, doi: 10.1016/j.actamat.2005.05.022.

[116] J. Zhang *et al.*, “A novel crack-free Ti-modified Al-Cu-Mg alloy designed for selective laser melting,” *Addit Manuf*, vol. 38, p. 101829, Feb. 2021, doi: 10.1016/j.addma.2020.101829.

[117] N. Kang, P. Coddet, L. Dembinski, H. Liao, and C. Coddet, “Microstructure and strength analysis of eutectic Al-Si alloy in-situ manufactured using selective laser melting from elemental powder mixture,” *J Alloys Compd*, vol. 691, pp. 316–322, Jan. 2017, doi: 10.1016/j.jallcom.2016.08.249.

[118] T. Kimura, T. Nakamoto, M. Mizuno, and H. Araki, “Effect of silicon content on densification, mechanical and thermal properties of Al-xSi binary alloys fabricated using selective laser melting,” *Materials Science and Engineering: A*, vol. 682, pp. 593–602, Jan. 2017, doi: 10.1016/j.msea.2016.11.059.

[119] G. Boussinot, M. Döring, S. Hemes, O. Stryzhyboroda, M. Apel, and M. Schmidt, “Laser powder bed fusion of eutectic Al–Ni alloys: Experimental and phase-field studies,” *Mater Des*, vol. 198, p. 109299, Jan. 2021, doi: 10.1016/j.matdes.2020.109299.

[120] S. Thapliyal *et al.*, “Design of heterogeneous structured Al alloys with wide processing window for laser-powder bed fusion additive manufacturing,” *Addit Manuf*, vol. 42, p. 102002, Jun. 2021, doi: 10.1016/j.addma.2021.102002.

[121] A. Plotkowski *et al.*, “Evaluation of an Al-Ce alloy for laser additive manufacturing,” *Acta Mater*, vol. 126, pp. 507–519, Mar. 2017, doi: 10.1016/j.actamat.2016.12.065.

[122] A. Perrin *et al.*, “Phase stability in cast and additively manufactured Al-rich Al-Cu-Ce alloys,” *J Alloys Compd*, vol. 926, p. 166984, Dec. 2022, doi: 10.1016/j.jallcom.2022.166984.

[123] H. Hyer *et al.*, “Composition-dependent solidification cracking of aluminum-silicon alloys during laser powder bed fusion,” *Acta Mater*, vol. 208, p. 116698, Apr. 2021, doi: 10.1016/j.actamat.2021.116698.

[124] L. Aucott *et al.*, “A Three-Stage Mechanistic Model for Solidification Cracking During Welding of Steel,” *Metallurgical and Materials Transactions A*, vol. 49, no. 5, pp. 1674–1682, May 2018, doi: 10.1007/s11661-018-4529-z.

[125] M. L. Montero-Sistiaga *et al.*, “Changing the alloy composition of Al7075 for better processability by selective laser melting,” *J Mater Process Technol*, vol. 238, pp. 437–445, Dec. 2016, doi: 10.1016/j.jmatprotec.2016.08.003.

[126] B. Vrancken, L. Thijs, J.-P. Kruth, and J. Van Humbeeck, “Microstructure and mechanical properties of a novel β titanium metallic composite by selective laser melting,” *Acta Mater*, vol. 68, pp. 150–158, Apr. 2014, doi: 10.1016/j.actamat.2014.01.018.

[127] G. Li *et al.*, “Investigation of Solidification and Precipitation Behavior of Si-Modified 7075 Aluminum Alloy Fabricated by Laser-Based Powder Bed Fusion,” *Metallurgical and Materials Transactions A*, vol. 52, no. 1, pp. 194–210, Jan. 2021, doi: 10.1007/s11661-020-06073-9.

[128] R. Li, M. Wang, Z. Li, P. Cao, T. Yuan, and H. Zhu, “Developing a high-strength Al-Mg-Si-Sc-Zr alloy for selective laser melting: Crack-inhibiting and multiple strengthening mechanisms,” *Acta Mater*, vol. 193, pp. 83–98, Jul. 2020, doi: 10.1016/j.actamat.2020.03.060.

[129] A. B. Spierings *et al.*, “Microstructural features of Sc- and Zr-modified Al-Mg alloys processed by selective laser melting,” *Mater Des*, vol. 115, pp. 52–63, Feb. 2017, doi: 10.1016/j.matdes.2016.11.040.

[130] Q. Jia, P. Rometsch, S. Cao, K. Zhang, and X. Wu, “Towards a high strength aluminium alloy development methodology for selective laser melting,” *Mater Des*, vol. 174, p. 107775, Jul. 2019, doi: 10.1016/j.matdes.2019.107775.

[131] Q. Jia *et al.*, “Selective laser melting of a high strength Al Mn Sc alloy: Alloy design and strengthening mechanisms,” *Acta Mater*, vol. 171, pp. 108–118, Jun. 2019, doi: 10.1016/j.actamat.2019.04.014.

[132] R. Li *et al.*, “Selective laser melting of a novel Sc and Zr modified Al-6.2 Mg alloy: Processing, microstructure, and properties,” *Powder Technol*, vol. 319, pp. 117–128, Sep. 2017, doi: 10.1016/j.powtec.2017.06.050.

[133] J. Liu and S. Kou, “Susceptibility of ternary aluminum alloys to cracking during solidification,” *Acta Mater*, vol. 125, pp. 513–523, Feb. 2017, doi: 10.1016/j.actamat.2016.12.028.

[134] F. Zhang *et al.*, “Prediction of Cracking Susceptibility of Commercial Aluminum Alloys during Solidification,” *Metals (Basel)*, vol. 11, no. 9, p. 1479, Sep. 2021, doi: 10.3390/met11091479.

[135] X. Zhang, L. Li, Z. Wang, H. Peng, J. Gao, and Z. Peng, “A novel high-strength Al-La-Mg-Mn alloy for selective laser melting,” *J Mater Sci Technol*, vol. 137, pp. 205–214, Feb. 2023, doi: 10.1016/j.jmst.2022.07.046.

[136] Y. Chen *et al.*, “Microstructure characterization and mechanical properties of crack-free Al-Cu-Mg-Y alloy fabricated by laser powder bed fusion,” *Addit Manuf*, vol. 58, p. 103006, Oct. 2022, doi: 10.1016/j.addma.2022.103006.

[137] F. Czerwinski, “Critical Assessment 36: Assessing differences between the use of cerium and scandium in aluminium alloying,” *Materials Science and Technology*, vol. 36, no. 3, pp. 255–263, Feb. 2020, doi: 10.1080/02670836.2019.1702775.

[138] L. Zhou *et al.*, “Laser powder bed fusion of Al–10 wt% Ce alloys: microstructure and tensile property,” *J Mater Sci*, vol. 55, no. 29, pp. 14611–14625, Oct. 2020, doi: 10.1007/s10853-020-05037-z.

[139] B. Zhou, Z. Li, and C. Chen, “Global Potential of Rare Earth Resources and Rare Earth Demand from Clean Technologies,” *Minerals*, vol. 7, no. 11, p. 203, Oct. 2017, doi: 10.3390/min7110203.

[140] Z. C. Sims *et al.*, “High performance aluminum–cerium alloys for high-temperature applications,” *Mater Horiz*, vol. 4, no. 6, pp. 1070–1078, 2017, doi: 10.1039/C7MH00391A.

[141] F. Cecchinato *et al.*, “Influence of Magnesium Alloy Degradation on Undifferentiated Human Cells,” *PLoS One*, vol. 10, no. 11, p. e0142117, Nov. 2015, doi: 10.1371/journal.pone.0142117.

[142] Q. Tan *et al.*, “Inoculation treatment of an additively manufactured 2024 aluminium alloy with titanium nanoparticles,” *Acta Mater*, vol. 196, pp. 1–16, Sep. 2020, doi: 10.1016/j.actamat.2020.06.026.

[143] Tecnika4, “Aluminum 2017.” Accessed: Jun. 19, 2020. [Online]. Available: https://www.teknika4.com/es/aluminio-2017

[144] ASM-International, *ASM Handbook Volume 2: Properties and Selection: Nonferrous Alloys and Special-Purpose Materials*. ASM International, 1998.

[145] T. A. S. of M. ASTM, *ASM Handbook Volume 4: Heat treatment*. ASM International, 1998.

[146] A. May, L. Taleb, and M. A. Belouchrani, “Analysis of the cyclic behavior and fatigue damage of extruded AA2017 aluminum alloy,” *Materials Science and Engineering: A*, vol. 571, pp. 123–136, Jun. 2013, doi: 10.1016/j.msea.2013.01.079.

[147] S. K. Son, M. Takeda, M. Mitome, Y. Bando, and T. Endo, “Precipitation behavior of an Al–Cu alloy during isothermal aging at low temperatures,” *Mater Lett*, vol. 59, no. 6, pp. 629–632, Mar. 2005, doi: 10.1016/j.matlet.2004.10.058.

[148] S. P. Ringer and K. Hono, “Microstructural Evolution and Age Hardening in Aluminium Alloys,” *Mater Charact*, vol. 44, no. 1–2, pp. 101–131, Jan. 2000, doi: 10.1016/S1044-5803(99)00051-0.

[149] P. Kwolek, G. Mrówka-Nowotnik, and M. Wytrwal-Sarna, “Corrosion of structural constituents of 2017 aluminium alloy in acidic solutions containing inhibitors,” *Materials and Corrosion*, vol. 72, no. 5, pp. 888–903, May 2021, doi: 10.1002/maco.202012046.

[150] Z. Szklarz, H. Krawiec, and Ł. Rogal, “The effect of vacuum suction casting on the microstructure and corrosion behavior of aluminium alloy 2017,” *Materials Science and Engineering: B*, vol. 240, pp. 23–32, Jan. 2019, doi: 10.1016/j.mseb.2019.01.006.

[151] A. Mauduit, S. Pillot, and Gransac. Hervé, “Study of the suitability of aluminum alloys for additive manufacturing by laser powder bed fusion,” *Scientific Bulletin-University Politehnica of Bucharest, Series B*, vol. 79, no. 4, pp. 119–138, 2017.

[152] A. S. Silva, S. M. de Albuquerque Sousa, G. L. de Gouveia, A. Garcia, and J. E. Spinelli, “The influence of NbB inoculation on dendritic spacing and grain size of an aluminum 2017 alloy at different cooling rates,” *The International Journal of Advanced Manufacturing Technology*, vol. 125, no. 11–12, pp. 5681–5696, Apr. 2023, doi: 10.1007/s00170-023-11104-x.

[153] W. S. Rasband, “ImageJ,” Bethesda, Maryland, USA, 2018.

[154] X. Yan and J. C. Lin, “Prediction of hot tearing tendency for multicomponent aluminum alloys,” *Metallurgical and Materials Transactions B*, vol. 37, no. 6, pp. 913–918, Dec. 2006, doi: 10.1007/BF02735013.

[155] K. Buchanan, J. Ribis, J. Garnier, and K. Colas, “Identification of monoclinic θ-phase dispersoids in a 6061 aluminium alloy,” *Philos Mag Lett*, vol. 96, no. 4, pp. 121–131, Apr. 2016, doi: 10.1080/09500839.2016.1162911.

[156] X. Wang *et al.*, “High-ductility AA6061 alloys produced by combination of sub-rapid solidification and Cr-alloying,” *Journal of Materials Research and Technology*, vol. 18, pp. 1566–1577, May 2022, doi: 10.1016/j.jmrt.2022.03.034.

[157] K. Saito, K. Sugiyama, and K. Hiraga, “Al13M4-type structures and atomic models of their twins,” *Materials Science and Engineering: A*, vol. 294–296, pp. 279–282, Dec. 2000, doi: 10.1016/S0921-5093(00)01213-2.

[158] F.-Z. Liu *et al.*, “Precipitation of dispersoids in Al–Mg–Si alloys with Cu addition,” *Journal of Materials Research and Technology*, vol. 14, pp. 3134–3139, Sep. 2021, doi: 10.1016/j.jmrt.2021.08.123.

[159] K. Binnemans and P. T. Jones, “Rare Earths and the Balance Problem,” *Journal of Sustainable Metallurgy*, vol. 1, no. 1, pp. 29–38, Mar. 2015, doi: 10.1007/s40831-014-0005-1.

[160] Y. Birol, “The performance of Al–Ti–C grain refiners in twin-roll casting of aluminium foilstock,” *J Alloys Compd*, vol. 430, no. 1–2, pp. 179–187, Mar. 2007, doi: 10.1016/j.jallcom.2006.05.027.

[161] S. MIN, C. KANGHUA, and H. LANPING, “Effects of Ce and Ti on the microstructures and mechanical properties of an Al-Cu-Mg-Ag alloy,” *Rare Metals*, vol. 26, no. 1, pp. 28–32, Feb. 2007, doi: 10.1016/S1001-0521(07)60023-0.

[162] I. Vedel, A.-M. Redon, J.-M. Mignot, and J.-M. Leger, “Absence of discontinuity in the pressure-volume dependence of CeAl 2 and CeIn 3,” *Journal of Physics F: Metal Physics*, vol. 17, no. 4, pp. 849–856, Apr. 1987, doi: 10.1088/0305-4608/17/4/012.

[163] F. Theska, Y. Yang, K. D. Sisco, A. Plotkowski, and S. Primig, “On the high-temperature stability of the Al8Cu3Ce intermetallic in an additively manufactured Al-Cu-Ce-Zr alloy,” *Mater Charact*, vol. 191, p. 112109, Sep. 2022, doi: 10.1016/j.matchar.2022.112109.

[164] M. A. Pekok, R. Setchi, M. Ryan, Q. Han, and D. Gu, “Effect of process parameters on the microstructure and mechanical properties of AA2024 fabricated using selective laser melting,” *The International Journal of Advanced Manufacturing Technology*, vol. 112, no. 1–2, pp. 175–192, Jan. 2021, doi: 10.1007/s00170-020-06346-y.

[165] K. Sampath, “Transverse-Weld Tensile Properties of a New Al-4Cu-2Si Alloy as Filler Metal,” *J Mater Eng Perform*, vol. 18, no. 9, pp. 1218–1225, Dec. 2009, doi: 10.1007/s11665-009-9371-4.

[166] D. Fabregue, “Microstructure et fissuration à chaud lors du soudage laser d’alliages d’aluminium 6000,” Institut National Polytechnique de Grenoble - INPG, France, 2009.

[167] T. Soysal and S. Kou, “Predicting effect of filler metals on solidification cracking susceptibility of 2024 Al and 6061 Al,” *Science and Technology of Welding and Joining*, vol. 24, no. 6, pp. 559–565, Aug. 2019, doi: 10.1080/13621718.2019.1570683.

[168] S. M. de Albuquerque Sousa, G. L. de Gouveia, and J. E. Spinelli, “Evaluating grain size, dendritic scale, and tensile properties of a NbB-inoculated 6201 alloy using solidification rate,” *Materials Science and Engineering: A*, vol. 835, p. 142680, Feb. 2022, doi: 10.1016/j.msea.2022.142680.

[169] H. Becker, T. Bergh, P. E. Vullum, A. Leineweber, and Y. Li, “Effect of Mn and cooling rates on α-, β- and δ-Al–Fe–Si intermetallic phase formation in a secondary Al–Si alloy,” *Materialia (Oxf)*, vol. 5, p. 100198, Mar. 2019, doi: 10.1016/j.mtla.2018.100198.

[170] B. Hu, B. Quan, D. Li, X. Wang, Z. Li, and X. Zeng, “Solid solution strengthening mechanism in high pressure die casting Al–Ce–Mg alloys,” *Materials Science and Engineering: A*, vol. 812, p. 141109, Apr. 2021, doi: 10.1016/j.msea.2021.141109.

[171] J. Gröbner, D. Mirković, and R. Schmid-Fetzer, “Thermodynamic aspects of the constitution, grain refining, and solidification enthalpies of Al-Ce-Si alloys,” *Metallurgical and Materials Transactions A*, vol. 35, no. 11, pp. 3349–3362, Nov. 2004, doi: 10.1007/s11661-004-0172-y.

[172] Z. Liu, H. L. Luo, and Q. C. Chen, “The Refinement Mechanism of La-Ce Binary Alloy on Primary α Phase in A356 Alloy under Electromagnetic Stirring,” *Solid State Phenomena*, vol. 217–218, pp. 340–346, Sep. 2014, doi: 10.4028/www.scientific.net/SSP.217-218.340.

[173] G. MENG, B. JI, H. HAN, C. GU, R. LIN, and F. PENG, “Design and simulation of an innovative cylinder fabricated by selective laser melting,” *Chinese Journal of Aeronautics*, vol. 32, no. 1, pp. 133–142, Jan. 2019, doi: 10.1016/j.cja.2018.10.011.

[174] C. Didier, W. K. Pang, Z. Guo, S. Schmid, and V. K. Peterson, “Phase Evolution and Intermittent Disorder in Electrochemically Lithiated Graphite Determined Using in Operando Neutron Diffraction,” *Chemistry of Materials*, vol. 32, no. 6, pp. 2518–2531, Mar. 2020, doi: 10.1021/acs.chemmater.9b05145.

[175] A. Meetsma, J. L. De Boer, and S. Van Smaalen, “Refinement of the crystal structure of tetragonal Al2Cu,” *J Solid State Chem*, vol. 83, no. 2, pp. 370–372, Dec. 1989, doi: 10.1016/0022-4596(89)90188-6.

[176] M. Klicpera *et al.*, “Crystal structure and its stability in CeCuAl3 single crystal,” *Intermetallics (Barking)*, vol. 46, pp. 126–130, Mar. 2014, doi: 10.1016/j.intermet.2013.11.004.

[177] L. Pedersen and L. Arnberg, “The effect of solution heat treatment and quenching rates on mechanical properties and microstructures in AlSiMg foundry alloys,” *Metallurgical and Materials Transactions A*, vol. 32, no. 3, pp. 525–532, Mar. 2001, doi: 10.1007/s11661-001-0069-y.

[178] V. Fallah *et al.*, “Atomic-scale pathway of early-stage precipitation in Al–Mg–Si alloys,” *Acta Mater*, vol. 82, pp. 457–467, Jan. 2015, doi: 10.1016/j.actamat.2014.09.004.

[179] O. Gharbi *et al.*, “On the corrosion of additively manufactured aluminium alloy AA2024 prepared by selective laser melting,” *Corros Sci*, vol. 143, pp. 93–106, Oct. 2018, doi: 10.1016/j.corsci.2018.08.019.

[180] G. Del Guercio *et al.*, “Cracking behaviour of high-strength AA2024 aluminium alloy produced by Laser Powder Bed Fusion,” *Addit Manuf*, vol. 54, p. 102776, Jun. 2022, doi: 10.1016/j.addma.2022.102776.

[181] J. Lu, B. Chen, X. Liu, F. Yang, and I. K. Robinson, “3D microstructure reconstruction of casting aluminum alloy based on serial block-face scanning electron microscopy,” *J Alloys Compd*, vol. 778, pp. 721–730, Mar. 2019, doi: 10.1016/j.jallcom.2018.11.188.

[182] X. Zhu, H. Yang, X. Dong, and S. Ji, “The effects of varying Mg and Si levels on the microstructural inhomogeneity and eutectic Mg2Si morphology in die-cast Al–Mg–Si alloys,” *J Mater Sci*, vol. 54, no. 7, pp. 5773–5787, Apr. 2019, doi: 10.1007/s10853-018-03198-6.

[183] W. A. Phelan *et al.*, “Crystal Growth, Structure, and Physical Properties of LnCu 2 (Al,Si) 5 (Ln = La and Ce),” *Inorg Chem*, vol. 51, no. 2, pp. 920–927, Jan. 2012, doi: 10.1021/ic2019378.

[184] H. Hyer *et al.*, “High strength aluminum-cerium alloy processed by laser powder bed fusion,” *Addit Manuf*, vol. 52, p. 102657, Apr. 2022, doi: 10.1016/j.addma.2022.102657.

[185] M. Hesselmann, D. Knoop, J. Epp, V. Uhlenwinkel, A. von Hehl, and A. Toenjes, “Effect of precipitation-forming elements in a near-eutectic Al-Ce alloy for Laser Powder Bed Fusion,” *Addit Manuf*, vol. 57, p. 102959, Sep. 2022, doi: 10.1016/j.addma.2022.102959.

[186] J. U. Rakhmonov, D. Weiss, and D. C. Dunand, “Solidification microstructure, aging evolution and creep resistance of laser powder-bed fused Al-7Ce-8Mg (wt%),” *Addit Manuf*, vol. 55, p. 102862, Jul. 2022, doi: 10.1016/j.addma.2022.102862.

[187] K. Sisco *et al.*, “Microstructure and properties of additively manufactured Al–Ce–Mg alloys,” *Sci Rep*, vol. 11, no. 1, p. 6953, Mar. 2021, doi: 10.1038/s41598-021-86370-4.

[188] H. B. Henderson *et al.*, “Enhanced thermal coarsening resistance in a nanostructured aluminum-cerium alloy produced by additive manufacturing,” *Mater Des*, vol. 209, p. 109988, Nov. 2021, doi: 10.1016/j.matdes.2021.109988.

[189] S. Bahl *et al.*, “Al-Cu-Ce(-Zr) alloys with an exceptional combination of additive processability and mechanical properties,” *Addit Manuf*, vol. 48, p. 102404, Dec. 2021, doi: 10.1016/j.addma.2021.102404.

[190] A. Plotkowski *et al.*, “Microstructure and properties of a high temperature Al–Ce–Mn alloy produced by additive manufacturing,” *Acta Mater*, vol. 196, pp. 595–608, Sep. 2020, doi: 10.1016/j.actamat.2020.07.014.

[191] K. Gabrysiak *et al.*, “Development and characterization of a metastable Al-Mn-Ce alloy produced by laser powder bed fusion,” *Additive Manufacturing Letters*, vol. 1, p. 100017, Dec. 2021, doi: 10.1016/j.addlet.2021.100017.

[192] O. S. Zarechnyuk, P. I. Kripyakevich, I. F. Kolobnev, and E. E. Cherkashin, “The quaternary compound Ce3 Mn Cu8 Al24 and its crystal structure,” *Izvestiya Akademii Nauk SSSR, Neorganicheskie Materialy*, vol. 2, pp. 182–183, 1967.

[193] E. O. Hall, “The Deformation and Ageing of Mild Steel: III Discussion of Results,” *Proceedings of the Physical Society. Section B*, vol. 64, no. 9, pp. 747–753, Sep. 1951, doi: 10.1088/0370-1301/64/9/303.

[194] D. H. Xiao, J. N. Wang, D. Y. Ding, and H. L. Yang, “Effect of rare earth Ce addition on the microstructure and mechanical properties of an Al–Cu–Mg–Ag alloy,” *J Alloys Compd*, vol. 352, no. 1–2, pp. 84–88, Mar. 2003, doi: 10.1016/S0925-8388(02)01162-3.

[195] Y. Liu, R. A. Michi, and D. C. Dunand, “Cast near-eutectic Al-12.5 wt.% Ce alloy with high coarsening and creep resistance,” *Materials Science and Engineering: A*, vol. 767, p. 138440, Nov. 2019, doi: 10.1016/j.msea.2019.138440.

[196] C. Brito *et al.*, “High cooling rate cells, dendrites, microstructural spacings and microhardness in a directionally solidified Al–Mg–Si alloy,” *J Alloys Compd*, vol. 636, pp. 145–149, Jul. 2015, doi: 10.1016/j.jallcom.2015.02.140.

[197] C. A. Siqueira, N. Cheung, and A. Garcia, “Solidification thermal parameters affecting the columnar-to-equiaxed transition,” *Metallurgical and Materials Transactions A*, vol. 33, no. 7, pp. 2107–2118, Jul. 2002, doi: 10.1007/s11661-002-0042-4.

[198] W. Kurz and D. J. Fisher, *Fundamentals of solidification*, 3rd ed. Trans Tech Publications, 1990.

[199] K. A. Jackson and J. D. Hunt, “Lamellar and Rod Eutectic Growth,” *Transactions of the Metallurgical Society of AIME*, vol. 236, pp. 1129–1142, 1996.

[200] L. Zhen-kuan *et al.*, “Effect of Pure Cerium on Microstructure of Eutectic and Hypereutectic Al-Si Alloy,” *Foundry technology*, vol. 78, no. 11, pp. 1210–1213, 2006.

[201] H. J. Feise, “A review of induced anisotropy and steady-state flow in powders,” *Powder Technol*, vol. 98, no. 3, pp. 191–200, Aug. 1998, doi: 10.1016/S0032-5910(98)00064-3.

[202] I. Cruz-Matías *et al.*, “Sphericity and roundness computation for particles using the extreme vertices model,” *J Comput Sci*, vol. 30, pp. 28–40, Jan. 2019, doi: 10.1016/j.jocs.2018.11.005.

[203] Ż. Garczyk and S. Stach, “Three-dimensional model for assessing the pore volume of biomaterials intended for implantation,” in *Computational Modelling of Biomechanics and Biotribology in the Musculoskeletal System*, Elsevier, 2021, pp. 305–358. doi: 10.1016/B978-0-12-819531-4.00013-4.

[204] B. Guo, X. Liu, and X. Tan, “Hydraulic Fracturing,” in *Petroleum Production Engineering*, Elsevier, 2017, pp. 389–501. doi: 10.1016/B978-0-12-809374-0.00014-3.

[205] E. D. Sneed and R. L. Folk, “Pebbles in the lower Colorado River, Texas a study in particle morphogenesis,” *J Geol*, vol. 66, no. 2, pp. 114–150, 1958.

[206] H. Wadell, “Volume, shape, and roundness of quartz particles,” *J Geol*, vol. 43, no. 3, pp. 250–280, 1935.

[207] J. Zhang, B. Song, Q. Wei, D. Bourell, and Y. Shi, “A review of selective laser melting of aluminum alloys: Processing, microstructure, property and developing trends,” *J Mater Sci Technol*, vol. 35, no. 2, pp. 270–284, Feb. 2019, doi: 10.1016/j.jmst.2018.09.004.

[208] P. Mellin, T. Zavalis, L. Tingo, H. Brodin, J. Wndel, and S. Berg, “Moisture Content Analysis Of Metal Powders, Using Oven Desorption Followed By Karl Fischer Titration,” in *Euro PM2018 Congress & Exhibition*, Bilbao, 2018, pp. 1–6.

[209] J. Muñiz-Lerma, A. Nommeots-Nomm, K. Waters, and M. Brochu, “A Comprehensive Approach to Powder Feedstock Characterization for Powder Bed Fusion Additive Manufacturing: A Case Study on AlSi7Mg,” *Materials*, vol. 11, no. 12, p. 2386, Nov. 2018, doi: 10.3390/ma11122386.

[210] D. Herzog, V. Seyda, E. Wycisk, and C. Emmelmann, “Additive manufacturing of metals,” *Acta Mater*, vol. 117, pp. 371–392, Sep. 2016, doi: 10.1016/j.actamat.2016.07.019.

[211] A. Aversa *et al.*, “Effect of Process and Post-Process Conditions on the Mechanical Properties of an A357 Alloy Produced via Laser Powder Bed Fusion,” *Metals (Basel)*, vol. 7, no. 2, p. 68, Feb. 2017, doi: 10.3390/met7020068.

[212] F. Chu *et al.*, “Influence of satellite and agglomeration of powder on the processability of AlSi10Mg powder in Laser Powder Bed Fusion,” *Journal of Materials Research and Technology*, vol. 11, pp. 2059–2073, Mar. 2021, doi: 10.1016/j.jmrt.2021.02.015.

[213] S. Dietrich, M. Wunderer, A. Huissel, and M. F. Zaeh, “A New Approach for a Flexible Powder Production for Additive Manufacturing,” *Procedia Manuf*, vol. 6, pp. 88–95, 2016, doi: 10.1016/j.promfg.2016.11.012.

[214] J. Clayton, “An Introduction to Powder Characterization,” in *Handbook of Pharmaceutical Wet Granulation*, Elsevier, 2019, pp. 569–613. doi: 10.1016/B978-0-12-810460-6.00021-X.

[215] G. Lumay *et al.*, “Measuring the flowing properties of powders and grains,” *Powder Technol*, vol. 224, pp. 19–27, Jul. 2012, doi: 10.1016/j.powtec.2012.02.015.

[216] EDQM, “Powder Flow,” in *European Pharmacopoeia*, 7th ed., European Directorate for the Quality of Medicines & HealthCare of the Council of Europe (EDQM), 2010, p. 308.

[217] F. Boschini, V. Delaval, K. Traina, N. Vandewalle, and G. Lumay, “Linking flowability and granulometry of lactose powders,” *Int J Pharm*, vol. 494, no. 1, pp. 312–320, Oct. 2015, doi: 10.1016/j.ijpharm.2015.08.030.

[218] S. Kumar, “Selective Laser Sintering/Melting,” in *Comprehensive Materials Processing*, Elsevier, 2014, pp. 93–134. doi: 10.1016/B978-0-08-096532-1.01003-7.

[219] J. W. Carson, B. H. Pittenger, and J. & J. Inc., “Bulk properties of powders,” in *ASM Handbook, Volume 7: Powder Metal Technologies and Applications*, 1998, pp. 287–301. doi: 10.1361/asmhba0001530.

[220] M. Li, W. Du, A. Elwany, Z. Pei, and C. Ma, “Metal Binder Jetting Additive Manufacturing: A Literature Review,” *J Manuf Sci Eng*, vol. 142, no. 9, Sep. 2020, doi: 10.1115/1.4047430.

[221] L. Marchetti and C. Hulme-Smith, “Flowability of steel and tool steel powders: A comparison between testing methods,” *Powder Technol*, vol. 384, pp. 402–413, May 2021, doi: 10.1016/j.powtec.2021.01.074.

[222] J. Yi, X. Zhang, J. H. Rao, J. Xiao, and Y. Jiang, “In-situ chemical reaction mechanism and non-equilibrium microstructural evolution of (TiB2 + TiC)/AlSi10Mg composites prepared by SLM-CS processing,” *J Alloys Compd*, vol. 857, p. 157553, Mar. 2021, doi: 10.1016/j.jallcom.2020.157553.

[223] W. Zhou *et al.*, “In situ formation of uniformly dispersed Al4C3 nanorods during additive manufacturing of graphene oxide/Al mixed powders,” *Carbon N Y*, vol. 141, pp. 67–75, Jan. 2019, doi: 10.1016/j.carbon.2018.09.057.

[224] K. Geng, S. Li, Y. F. Yang, and R. D. K. Misra, “3D printing of Al matrix composites through in situ impregnation of carbon nanotubes on Al powder,” *Carbon N Y*, vol. 162, pp. 465–474, Jun. 2020, doi: 10.1016/j.carbon.2020.02.087.

[225] J. Cui *et al.*, “Printability enhancement and mechanical property improvement via in situ synthesis of carbon nanotubes on aluminium powder,” *Powder Technol*, vol. 413, p. 118038, Jan. 2023, doi: 10.1016/j.powtec.2022.118038.

[226] K. Geng, Y. Yang, S. Li, R. D. K. Misra, and Q. Zhu, “Enabling high-performance 3D printing of Al powder by decorating with high laser absorbing Co phase,” *Addit Manuf*, vol. 32, p. 101012, Mar. 2020, doi: 10.1016/j.addma.2019.101012.

[227] K. Geng, Y. Yang, S. Li, R. D. K. Misra, and Q. Zhu, “A General Strategy for Enhancing 3D Printability of High Laser Reflectivity Pure Aluminum Powder,” *Metallurgical and Materials Transactions A*, vol. 50, no. 11, pp. 4970–4976, Nov. 2019, doi: 10.1007/s11661-019-05436-1.

[228] Z. Hu, Z. Zhao, X. Deng, Z. Lu, J. Liu, and Z. Qu, “Microstructure and mechanical behavior of TiCN reinforced AlSi10Mg composite fabricated by selective laser melting,” *Mater Chem Phys*, vol. 283, p. 125996, May 2022, doi: 10.1016/j.matchemphys.2022.125996.

[229] C. Gao, Z. Xiao, Z. Liu, Q. Zhu, and W. Zhang, “Selective laser melting of nano-TiN modified AlSi10Mg composite powder with low laser reflectivity,” *Mater Lett*, vol. 236, pp. 362–365, Feb. 2019, doi: 10.1016/j.matlet.2018.10.126.

[230] C. Gao, W. Wu, J. Shi, Z. Xiao, and A. H. Akbarzadeh, “Simultaneous enhancement of strength, ductility, and hardness of TiN/AlSi10Mg nanocomposites via selective laser melting,” *Addit Manuf*, vol. 34, p. 101378, Aug. 2020, doi: 10.1016/j.addma.2020.101378.

[231] M. Dong, W. Zhou, K. Kamata, and N. Nomura, “Microstructure and mechanical property of graphene oxide/AlSi10Mg composites fabricated by laser additive manufacturing,” *Mater Charact*, vol. 170, p. 110678, Dec. 2020, doi: 10.1016/j.matchar.2020.110678.

[232] X. Zhao, D. Gu, C. Ma, L. Xi, and H. Zhang, “Microstructure characteristics and its formation mechanism of selective laser melting SiC reinforced Al-based composites,” *Vacuum*, vol. 160, pp. 189–196, Feb. 2019, doi: 10.1016/j.vacuum.2018.11.022.

[233] X. P. Li *et al.*, “Selective laser melting of nano-TiB2 decorated AlSi10Mg alloy with high fracture strength and ductility,” *Acta Mater*, vol. 129, pp. 183–193, May 2017, doi: 10.1016/j.actamat.2017.02.062.

[234] W. Cheng, Y. Liu, X. Xiao, B. Huang, Z. Zhou, and X. Liu, “Microstructure and mechanical properties of a novel (TiB2+TiC)/AlSi10Mg composite prepared by selective laser melting,” *Materials Science and Engineering: A*, vol. 834, p. 142435, Feb. 2022, doi: 10.1016/j.msea.2021.142435.

[235] W. Wu, C. Gao, Z. Liu, K. Wong, and Z. Xiao, “Laser powder bed fusion of crack-free TiN/Al7075 composites with enhanced mechanical properties,” *Mater Lett*, vol. 282, p. 128625, Jan. 2021, doi: 10.1016/j.matlet.2020.128625.

[236] J. J. Dunkley, “Metal Powder Atomisation Methods for Modern Manufacturing,” *Johnson Matthey Technology Review*, vol. 63, no. 3, pp. 226–232, Jul. 2019, doi: 10.1595/205651319X15583434137356.

[237] D. G. White, *Volume 7: Powder Metal Technology and Applications*. ASM International, 2006. doi: 10.31399/asm.hb.v07.9781627081757.

[238] F. C. da Silva, M. L. de Lima, and G. F. Colombo, “Evaluation of a Mathematical Model Based on Lubanska Equation to Predict Particle Size for Close-Coupled Gas Atomization of 316L Stainless Steel,” *Materials Research*, vol. 25, 2022, doi: 10.1590/1980-5373-mr-2021-0364.

[239] D. Gianoglio, N. Ciftci, S. Armstrong, V. Uhlenwinkel, and L. Battezzati, “On the Cooling Rate-Microstructure Relationship in Molten Metal Gas Atomization,” *Metallurgical and Materials Transactions A*, vol. 52, no. 9, pp. 3750–3758, Sep. 2021, doi: 10.1007/s11661-021-06325-2.

[240] B. Zheng, Y. Lin, Y. Zhou, and E. J. Lavernia, “Gas Atomization of Amorphous Aluminum: Part I. Thermal Behavior Calculations,” *Metallurgical and Materials Transactions B*, vol. 40, no. 5, pp. 768–778, Oct. 2009, doi: 10.1007/s11663-009-9276-5.

[241] B. Zheng, Y. Lin, Y. Zhou, and E. J. Lavernia, “Gas Atomization of Amorphous Aluminum Powder: Part II. Experimental Investigation,” *Metallurgical and Materials Transactions B*, vol. 40, no. 6, pp. 995–1004, Dec. 2009, doi: 10.1007/s11663-009-9277-4.

[242] G. Kasperovich, T. Volkmann, L. Ratke, and D. Herlach, “Microsegregation during Solidification of an Al-Cu Binary Alloy at Largely Different Cooling Rates (0.01 to 20,000 K/s): Modeling and Experimental Study,” *Metallurgical and Materials Transactions A*, vol. 39, no. 5, pp. 1183–1191, May 2008, doi: 10.1007/s11661-008-9505-6.

[243] I. C. Stone and P. Tsakiropoulos, “Cooling rates in gas atomised Al-4wt%Cu alloys powders,” *International journal of rapid solidification*, vol. 7, no. 3, pp. 177–190, 1992.

[244] D. C. Montgomery, “Response Surface Methods and Designs,” in *Design and Analysis of Experiments*, Hoboken, New Jersey, U.S.: John Wiley & Sons, Inc., 2013, pp. 458–543.

[245] A. Maamoun, Y. Xue, M. Elbestawi, and S. Veldhuis, “Effect of Selective Laser Melting Process Parameters on the Quality of Al Alloy Parts: Powder Characterization, Density, Surface Roughness, and Dimensional Accuracy,” *Materials*, vol. 11, no. 12, p. 2343, Nov. 2018, doi: 10.3390/ma11122343.

[246] X. Su and Y. Yang, “Research on track overlapping during Selective Laser Melting of powders,” *J Mater Process Technol*, vol. 212, no. 10, pp. 2074–2079, Oct. 2012, doi: 10.1016/j.jmatprotec.2012.05.012.

[247] A. Sola and A. Nouri, “Microstructural porosity in additive manufacturing: The formation and detection of pores in metal parts fabricated by powder bed fusion,” *J Adv Manuf Process*, vol. 1, no. 3, Jul. 2019, doi: 10.1002/amp2.10021.

[248] W. E. King *et al.*, “Observation of keyhole-mode laser melting in laser powder-bed fusion additive manufacturing,” *J Mater Process Technol*, vol. 214, no. 12, pp. 2915–2925, Dec. 2014, doi: 10.1016/j.jmatprotec.2014.06.005.

[249] X. Nie, H. Zhang, H. Zhu, Z. Hu, L. Ke, and X. Zeng, “Effect of Zr content on formability, microstructure and mechanical properties of selective laser melted Zr modified Al-4.24Cu-1.97Mg-0.56Mn alloys,” *J Alloys Compd*, vol. 764, pp. 977–986, Oct. 2018, doi: 10.1016/j.jallcom.2018.06.032.

[250] L. Zhou *et al.*, “Microstructure and tensile property of a novel AlZnMgScZr alloy additively manufactured by gas atomization and laser powder bed fusion,” *Scr Mater*, vol. 158, pp. 24–28, Jan. 2019, doi: 10.1016/j.scriptamat.2018.08.025.

[251] M. Vilanova, R. Escribano-García, T. Guraya, and M. San Sebastian, “Optimizing Laser Powder Bed Fusion Parameters for IN-738LC by Response Surface Method,” *Materials*, vol. 13, no. 21, p. 4879, Oct. 2020, doi: 10.3390/ma13214879.

[252] M. Brandt, *Laser Additive Manufacturing: MAaterials, Design, Technologies, and Applications*. Matthew Deans, 2017.

[253] N. T. Aboulkhair, N. M. Everitt, I. Ashcroft, and C. Tuck, “Reducing porosity in AlSi10Mg parts processed by selective laser melting,” *Addit Manuf*, vol. 1–4, pp. 77–86, Oct. 2014, doi: 10.1016/j.addma.2014.08.001.

[254] J. Yang *et al.*, “Role of molten pool mode on formability, microstructure and mechanical properties of selective laser melted Ti-6Al-4V alloy,” *Mater Des*, vol. 110, pp. 558–570, Nov. 2016, doi: 10.1016/j.matdes.2016.08.036.

[255] M. Cloots, P. J. Uggowitzer, and K. Wegener, “Investigations on the microstructure and crack formation of IN738LC samples processed by selective laser melting using Gaussian and doughnut profiles,” *Mater Des*, vol. 89, pp. 770–784, Jan. 2016, doi: 10.1016/j.matdes.2015.10.027.

[256] D. B. Hann, J. Iammi, and J. Folkes, “A simple methodology for predicting laser-weld properties from material and laser parameters,” *J Phys D Appl Phys*, vol. 44, no. 44, p. 445401, Nov. 2011, doi: 10.1088/0022-3727/44/44/445401.

[257] J. Metelkova, Y. Kinds, K. Kempen, C. de Formanoir, A. Witvrouw, and B. Van Hooreweder, “On the influence of laser defocusing in Selective Laser Melting of 316L,” *Addit Manuf*, vol. 23, pp. 161–169, Oct. 2018, doi: 10.1016/j.addma.2018.08.006.

[258] E. Assuncao, S. Williams, and D. Yapp, “Interaction time and beam diameter effects on the conduction mode limit,” *Opt Lasers Eng*, vol. 50, no. 6, pp. 823–828, Jun. 2012, doi: 10.1016/j.optlaseng.2012.02.001.

[259] D. C. Weckman, H. W. Kerr, and J. T. Liu, “The effects of process variables on pulsed Nd:YAG laser spot welds: Part II. AA 1100 aluminum and comparison to AISI 409 stainless steel,” *Metallurgical and Materials Transactions B*, vol. 28, no. 4, pp. 687–700, Aug. 1997, doi: 10.1007/s11663-997-0043-1.

[260] Z. Chen, Y. Zhao, and Z. Zhang, “Theoretical and experimental study of precipitation and coarsening kinetics of θ′ phase in Al–Cu alloy,” *Vacuum*, vol. 189, p. 110263, Jul. 2021, doi: 10.1016/j.vacuum.2021.110263.

[261] F. Li, T. Zhang, Y. Wu, C. Chen, and K. Zhou, “Microstructure, mechanical properties, and crack formation of aluminum alloy 6063 produced via laser powder bed fusion,” *J Mater Sci*, vol. 57, no. 21, pp. 9631–9645, Jun. 2022, doi: 10.1007/s10853-022-06993-4.

[262] Z. Zhou, L. Huang, Y. Shang, Y. Li, L. Jiang, and Q. Lei, “Causes analysis on cracks in nickel-based single crystal superalloy fabricated by laser powder deposition additive manufacturing,” *Mater Des*, vol. 160, pp. 1238–1249, Dec. 2018, doi: 10.1016/j.matdes.2018.10.042.

[263] L. Zhou *et al.*, “Microstructure and mechanical properties of Zr-modified aluminum alloy 5083 manufactured by laser powder bed fusion,” *Addit Manuf*, vol. 28, pp. 485–496, Aug. 2019, doi: 10.1016/j.addma.2019.05.027.

[264] J. Li, X. Cheng, Z. Li, X. Zong, S.-Q. Zhang, and H.-M. Wang, “Improving the mechanical properties of Al-5Si-1Cu-Mg aluminum alloy produced by laser additive manufacturing with post-process heat treatments,” *Materials Science and Engineering: A*, vol. 735, pp. 408–417, Sep. 2018, doi: 10.1016/j.msea.2018.08.074.

[265] H. Zhang, H. Zhu, X. Nie, T. Qi, Z. Hu, and X. Zeng, “Fabrication and heat treatment of high strength Al-Cu-Mg alloy processed using selective laser melting,” B. Gu, H. Helvajian, and A. Piqué, Eds., Apr. 2016, p. 97380X. doi: 10.1117/12.2211362.

[266] F. Czerwinski, “Thermal stability of aluminum–cerium binary alloys containing the Al–Al11Ce3 eutectic,” *Materials Science and Engineering: A*, vol. 809, p. 140973, Mar. 2021, doi: 10.1016/j.msea.2021.140973.

[267] Z. Yang *et al.*, “An additively manufactured heat-resistant Al-Ce-Sc-Zr alloy: Microstructure, mechanical properties and thermal stability,” *Materials Science and Engineering: A*, vol. 872, p. 144965, May 2023, doi: 10.1016/j.msea.2023.144965.

[268] M. Jayamathy and R. Vasanth, “Aluminium Piston Alloy to Retard Age Softening Characteristics in Motorcycle Engines,” Nov. 2006. doi: 10.4271/2006-32-0030.

[269] E. Broitman, “Indentation Hardness Measurements at Macro-, Micro-, and Nanoscale: A Critical Overview,” *Tribol Lett*, vol. 65, no. 1, p. 23, Mar. 2017, doi: 10.1007/s11249-016-0805-5.

[270] D. Chicot, F. Roudet, A. Soom, and J. Lesage, “Interpretation of instrumented hardness measurements on stainless steel with different surface preparations,” *Surface Engineering*, vol. 23, no. 1, pp. 32–39, Jan. 2007, doi: 10.1179/174329407X161573.

[271] J. S. Zuback and T. DebRoy, “The Hardness of Additively Manufactured Alloys,” *Materials*, vol. 11, no. 11, p. 2070, Oct. 2018, doi: 10.3390/ma11112070.

[272] S. M. Walley, “Historical origins of indentation hardness testing,” *Materials Science and Technology*, vol. 28, no. 9–10, pp. 1028–1044, Oct. 2012, doi: 10.1179/1743284711Y.0000000127.

[273] Q. Luo and M. Kitchen, “Microhardness, Indentation Size Effect and Real Hardness of Plastically Deformed Austenitic Hadfield Steel,” *Materials*, vol. 16, no. 3, p. 1117, Jan. 2023, doi: 10.3390/ma16031117.

[274] J. Gong, J. Wu, and Z. Guan, “Examination of the indentation size effect in low-load vickers hardness testing of ceramics,” *J Eur Ceram Soc*, vol. 19, no. 15, pp. 2625–2631, Nov. 1999, doi: 10.1016/S0955-2219(99)00043-6.

[275] P. Wang, L. Deng, K. G. Prashanth, S. Pauly, J. Eckert, and S. Scudino, “Microstructure and mechanical properties of Al-Cu alloys fabricated by selective laser melting of powder mixtures,” *J Alloys Compd*, vol. 735, pp. 2263–2266, Feb. 2018, doi: 10.1016/j.jallcom.2017.10.168.

[276] S. Sabari, D. G. Andrade, C. Leitão, F. Simões, and D. M. Rodrigues, “Influence of the strain hardening behaviour on the tensile and compressive response of aluminium auxetic structures,” *Compos Struct*, vol. 305, p. 116472, Feb. 2023, doi: 10.1016/j.compstruct.2022.116472.

[277] S. Gairola, R. Jayaganthan, and J. Ajay, “Laser powder bed fusion on Ti modified Al 2024 alloy: Influence of build orientation and T6 treatment on mechanical behaviour, microstructural features and strengthening mechanisms,” *Materials Science and Engineering: A*, vol. 896, p. 146296, Mar. 2024, doi: 10.1016/j.msea.2024.146296.

[278] Y. Zhou, T. Chang, X. Fang, R. Chen, Y. Li, and K. Huang, “Tailoring the mechanical properties and thermal stability of additive manufactured micro-alloyed Al-Cu alloy via multi-stage heat treatment,” *Mater Des*, vol. 233, p. 112287, Sep. 2023, doi: 10.1016/j.matdes.2023.112287.

[279] H. Zhang, H. Zhu, T. Qi, Z. Hu, and X. Zeng, “Selective laser melting of high strength Al–Cu–Mg alloys: Processing, microstructure and mechanical properties,” *Materials Science and Engineering: A*, vol. 656, pp. 47–54, Feb. 2016, doi: 10.1016/j.msea.2015.12.101.

[280] X. Nie, H. Zhang, H. Zhu, Z. Hu, Y. Qi, and X. Zeng, “On the role of Zr content into Portevin-Le Chatelier (PLC) effect of selective laser melted high strength Al-Cu-Mg-Mn alloy,” *Mater Lett*, vol. 248, pp. 5–7, Aug. 2019, doi: 10.1016/j.matlet.2019.03.112.

[281] Z. Qi, B. Qi, B. Cong, H. Sun, G. Zhao, and J. Ding, “Microstructure and mechanical properties of wire + arc additively manufactured 2024 aluminum alloy components: As-deposited and post heat-treated,” *J Manuf Process*, vol. 40, pp. 27–36, Apr. 2019, doi: 10.1016/j.jmapro.2019.03.003.

[282] M. Arana, E. Ukar, D. Aguilar, and P. Álvarez, “Wire arc additive manufacturing of nanomodified 2024 alloy,” *Mater Lett*, vol. 348, p. 134712, Oct. 2023, doi: 10.1016/j.matlet.2023.134712.

[283] J. Gu, M. Gao, S. Yang, J. Bai, Y. Zhai, and J. Ding, “Microstructure, defects, and mechanical properties of wire + arc additively manufactured Al Cu4.3-Mg1.5 alloy,” *Mater Des*, vol. 186, p. 108357, Jan. 2020, doi: 10.1016/j.matdes.2019.108357.

[284] P. Wang *et al.*, “Microstructure and mechanical properties of a heat-treatable Al-3.5Cu-1.5Mg-1Si alloy produced by selective laser melting,” *Materials Science and Engineering: A*, vol. 711, pp. 562–570, Jan. 2018, doi: 10.1016/j.msea.2017.11.063.

[285] F. Belelli, R. Casati, M. Riccio, A. Rizzi, M. Y. Kayacan, and M. Vedani, “Development of a Novel High-Temperature Al Alloy for Laser Powder Bed Fusion,” *Metals (Basel)*, vol. 11, no. 1, p. 35, Dec. 2020, doi: 10.3390/met11010035.

[286] B. Chen, X. Xi, T. Gu, C. Tan, and X. Song, “Influence of heat treatment on microstructure evolution and mechanical properties of TiB2/Al 2024 composites fabricated by directed energy deposition,” *Journal of Materials Research and Technology*, vol. 9, no. 6, pp. 14223–14236, Nov. 2020, doi: 10.1016/j.jmrt.2020.10.014.

[287] W. Wang, J. Ning, and S. Y. Liang, “Prediction of lack-of-fusion porosity in laser powder-bed fusion considering boundary conditions and sensitivity to laser power absorption,” *The International Journal of Advanced Manufacturing Technology*, vol. 112, no. 1–2, pp. 61–70, Jan. 2021, doi: 10.1007/s00170-020-06224-7.

[288] D. Buchbinder, W. Meiners, N. Pirch, K. Wissenbach, and J. Schrage, “Investigation on reducing distortion by preheating during manufacture of aluminum components using selective laser melting,” *J Laser Appl*, vol. 26, no. 1, p. 012004, Feb. 2014, doi: 10.2351/1.4828755.

[289] H.-S. Park and D.-S. Nguyen, “Study on Flaking Behavior in Selective Laser Melting Process,” *Procedia CIRP*, vol. 63, pp. 569–572, 2017, doi: 10.1016/j.procir.2017.03.146.

[290] D. Koutny *et al.*, “Influence of Scanning Strategies on Processing of Aluminum Alloy EN AW 2618 Using Selective Laser Melting,” *Materials*, vol. 11, no. 2, p. 298, Feb. 2018, doi: 10.3390/ma11020298.